Mechanisms and Machine Science 38

Hannes Bleuler
Mohamed Bouri
Francesco Mondada
Doina Pisla
Aleksandar Rodić
Patrick Helmer *Editors*

New Trends in Medical and Service Robots

Assistive, Surgical and Educational Robotics

Springer

Mechanisms and Machine Science

Volume 38

More information about this series at http://www.springer.com/series/8779

Hannes Bleuler · Mohamed Bouri
Francesco Mondada · Doina Pisla
Aleksandar Rodić · Patrick Helmer
Editors

New Trends in Medical and Service Robots

Assistive, Surgical and Educational Robotics

Springer

Editors
Hannes Bleuler
LSRO—Robotic Systems Laboratory
Ecole Polytechnique Federale de Lausanne
Lausanne
Switzerland

Mohamed Bouri
Ecole Polytechnique Federale de Lausanne
Lausanne
Switzerland

Francesco Mondada
Ecole Polytechnique Federale de Lausanne
Lausanne
Switzerland

Doina Pisla
Research Center for Industrial Robots
Technical University of Cluj-Napoca
Cluj-Napoca
Romania

Aleksandar Rodić
Robotics Laboratory
Mihailo Pupin Institute
Belgrade
Serbia

Patrick Helmer
Force Dimension
Nyon
Switzerland

ISSN 2211-0984 ISSN 2211-0992 (electronic)
Mechanisms and Machine Science
ISBN 978-3-319-23831-9 ISBN 978-3-319-23832-6 (eBook)
DOI 10.1007/978-3-319-23832-6

Library of Congress Control Number: 2015949263

Springer Cham Heidelberg New York Dordrecht London

Printed on acid-free paper

Springer International Publishing AG Switzerland is part of Springer Science+Business Media (www.springer.com)

Preface

Medical and Service Robotics are entering a phase of very vigorous growth. An—obviously incomplete—list of "hot" topics would include surgery robotics, assist devices, rehabilitation technology, surgical instrumentation, Brain–Machine Interface (BMI) as examples for medical robotics, autonomous cleaning, tending, logistics, surveying and rescue robots and elderly and healthcare robots as topics from service robotics.

A relatively small single-session workshop such as MeSRob, held for the third time in July 2014 at EPFL, cannot cover all these fields. It gives, however, with its 120 participants from a dozen countries, a representative snapshot of activities, especially in the three partner countries of the SCOPES funding scheme of the Swiss SNF, Romania, Serbia and Switzerland, along with a growing number of participants from Europe and Asia. Particularly promising is the fact that MeSRob 2015 is already well on track and will be held in July in Nantes, France. This is proof of the timely character and growing interest of the MeSRob topics. As a matter of fact, every large industrial robotics company is now entering the biomedical market, the number of start-up companies in medical and service robotics is impressing and many are successful.

The topics presented at MeSRob 2014 can be classified into three topical parts:

(1) Wearable, Assistive and Rehabilitation Devices (8 Chapters)
(2) Surgical Robotics, Instrumentation, Biomechanical Modeling (6 Chapters)
(3) Educational and Service Robotics (6 Chapters)

Far from claiming anything near a complete coverage of medical and service robotic topics, the papers presented here nevertheless give a good impression of current research directions and fields of interest. Most papers are strongly anchored on collaborations between technical and medical actors, engineers, surgeons and clinicians. The larger field of biomedical technology and rapid growth in service automation has clearly overtaken the "classical" industrial robotics and automatic control centered activity familiar to the older generation of roboticists. While this might be true for the application fields, more theoretical topics such as kinematics, parallel link mechanisms and similar subjects now find new applications in biomechanics and biomedical robotics. At the same time, new transdisciplinary fields are emerging, e.g. intersections between psychology, psychiatry, cognitive neurosciences on one hand and robotics on the other hand. Brain-Machine interface and haptic interfaces will grow in importance. Many of these topics are relatively new and publications are under way or have been presented at keynotes, but are not yet mature enough for publication in these proceedings. We may however look forward to upcoming MeSRob workshops to report on an increasing number of submission in this direction.

Finally, the organizers wish to thank the main sponsors of this event, the Swiss National Foundation for Science, IFToMM, EPFL to the team of reviewers (most of whom were not participants in MeSRob) and to the scientific and organizing Committees.

Hannes Bleuler
Mohamed Bouri
Francesco Mondada
Doina Pisla
Aleksandar Rodić

Contents

Part II Surgical Robotics

Part III Educational and Service Robotics

Part I
Assistive and Rehabilitation Devices

Study and Choice of Actuation for a Walking Assist Device

Y. Aoustin, C. Chevallereau and V. Arakalian

Abstract A walking assist device (WAD) with bodyweight support reduces energy expenditure of a walking person. However, it is also important that the location of actuators in the WAD will be optimally chosen. For this purpose a wearable assist device composed of a bodyweight support, legs and shoes articulated with hip (upper joint), knee (middle joint), and ankle (lower joint) is discussed. Since human walk involves large displacements only in sagittal plane, a planar model is considered. In order to evaluate the optimal distribution of input torques, a bipedal model of a seven-link system with several walking velocities is coupled with the mentioned WAD. To study the efficiency of the WAD and to choose an appropriate actuation, the torque cost is evaluated when the same walking pattern are tracked with and without a WAD. The paper deals with the torque cost for the human and the WAD with several types of actuation. It is shown that full actuation with six motors or partial actuation with two motors located at the upper joints are two more efficient solutions while an actuation at the middle joints or lower joints only is ineffective. The numerical simulations carried out for several walking velocities confirm the mentioned observations.

Keywords Assist device · Walking gait · Optimization · Torque costs · Biped fully assisted · Biped partially assisted

Y. Aoustin (✉) · C. Chevallereau · V. Arakalian
L'UNAM, Institut de Recherche en Communications et Cybernétique de Nantes, UMR 6597, CNRS, École Centrale de Nantes, Université de Nantes, 92101 1 rue de la Noë, 44321 Nantes, France
e-mail: Yannick.Aoustin@irccyn.ec-nantes.fr

C. Chevallereau
e-mail: Christine.Chevallereau@irccyn.ec-nantes.fr

V. Arakalian
e-mail: Vigen.Arakalian@irccyn.ec-nantes.fr

H. Bleuler et al. (eds.), *New Trends in Medical and Service Robots*, Mechanisms and Machine Science 38, DOI 10.1007/978-3-319-23832-6_1

1 Introduction

Musculoskeletal disorders for workers and/or elderly people are actually social worries. As a consequence during the last few years, several biomechanic studies and realizations of walking assist devices have been carried out. For example, Priebe and Kram [1] compared the metabolic power consumption for ten young adults walkingwithout assistance and using two-wheeled, four-wheeled and four-footed walker devices. Zhang and Hashimoto [2] presented a trajectory generation method for a robotic suit to assist walking by supporting the hip joints. Ikeuchi et al. [3] proposed a wearable walking assist device. This device, with a seat, segments, and two shoes is disposed along the inner side of the user's legs. It produces an assisting force directed from the center of pressure to the center of mass of the human using two actuators.

The design of a WAD remains an open problem since walking implies displacement of the mass and inertia of the WAD, the human walking must be facilitated and not perturbed. Human's walking is a complex coordination of muscle activity, actuator torques and joint motions. This is even more true for human's walking with an assist device, where closed kinematic chains has to be considered (see Aoustin [4]). This paper deals with the problem of the best distribution of actuators for a given wearable walking device which assists a seven-link planar biped during a given cyclic walking gait.

To evaluate the effect of WAD on the torque cost, reference walking gaits must previously be defined. For example the cart-model, or the linear inverted pendulum model, based on the zero moment point *ZMP* can be efficient to design a walking gait; see [5–7]. A walking gait based on capture point regulation is developed in [8, 9]. The capture point is the location on the ground where a biped needs to step in order to come to a stop. These approaches are largely used in humanoid robotics but do not produce human-like motion and thus are not well adapted in our context. Another approach employed to generate walking patterns for biped robots is based on central pattern generators (CPGs) and do not require any physical model of the biped; see [10, 11]. The reference motion of the biped can be based on record of human motion [12, 13]. In this paper walking patterns defined through an optimization algorithm.

To study the efficiency of the walking assist devices, the torques of the model of human without and with the wearable device will be compared. Several levels of assistance will be considered. These levels of assistance are respectively the biped fully assisted, the biped partially assisted through two motors located at the upper joints, at the middle joints or at the lower joints respectively. The structure of the paper is the following. In Sect. 2, the modeling of the biped and its walking assist device are defined. In Sect. 3, the design of reference gaits is shortly presented. Section 4 is devoted to the statement of the considered problem. In Sect. 5, the numerical tests are discussed. Section 6 offers our conclusion and perspectives.

2 Studied Biped with Its Wearable Walking Assist Device

The wearable walking assist device, drawn with thick lines in Fig. 1, is composed of a seat, attached to the waist, segments, and two shoes. It has six joints in the sagittal plane, i.e. two upper joints between the seat and the upper legs, two middle joints between the upper legs and the lower legs, and two lower joints between the the lower

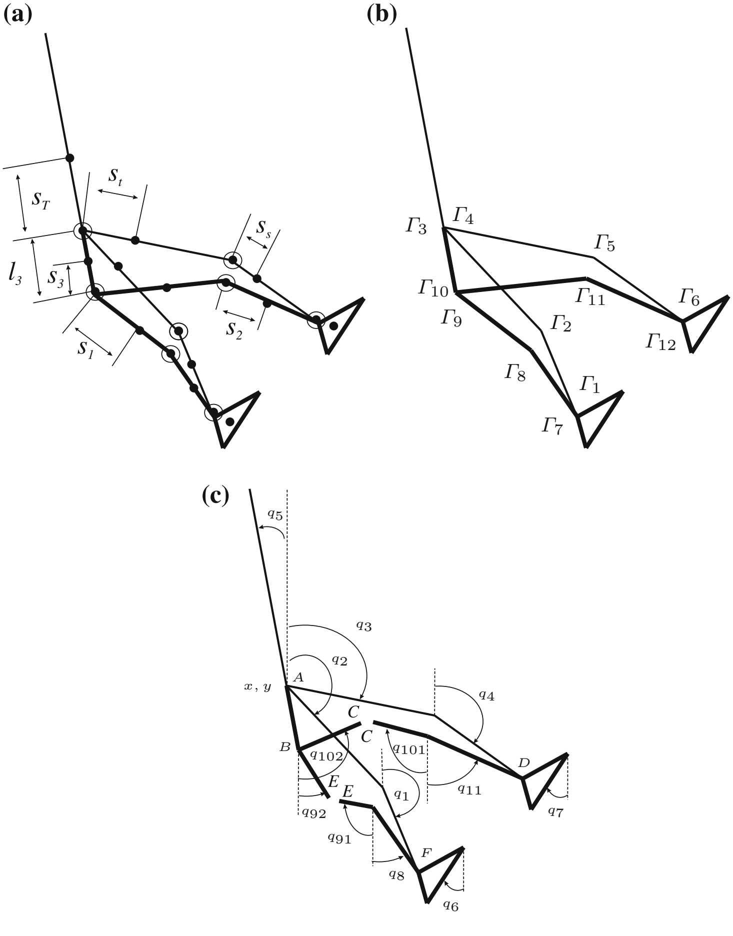

Fig. 1 Planar model of human with its walking assist device. The model of human is depicted in fine line, the coordinates, which are used to describe the human configuration include the position and orientation of the trunk defined by *x, y,* q_5 and the orientation of the thigh, shin and feet defined by q_1, q_2, q_3, q_4, q_6, q_7. The WAD shown in *thick line* is attached to the waist of the human, and the articulation of the seat is below the human hip with a distance l_3 along the trunk. The WAD is also attached to the human throughout the feet. Mechanical loops are thus created and the modeling required to cut these closed loops virtually 0 and to introduce the coordinates q_8, q_{91}, q_{92}, q_{101}, q_{102}, q_{11} to describe the WAD configuration

legs and the feet. The wearable device has a similar shape than of human with two shins, femurs and shoes. The connection of the wearable walking assist device with human corresponds to the complete feet and to the base of the trunk according to Fig. 1. The parameters of the human model is taken from the literature [14]. The whole mass of the biped is 75 kg, its height is 1.75 m. Table 1 summarizes the parameters of the model of human and the WAD. The arms and head of the human are taken into account in the parameters of the trunk.

The model of the human equipped with the walking assist device includes mechanical closed loops due to the multiple connections between the human and the WAD. The generalized configuration vector $\mathbf{x}$ is

$$\mathbf{x} = [q_1, q_2, q_3, q_4, q_5, q_6, q_7, q_8, q_{91}, q_{92}, q_{101}, q_{102}, q_{11}, x, y]^\top. \quad (1)$$

where the configuration variables are described in Fig. 1.

The dynamic model is calculated using the equivalent tree structure and adding the external forces and moments between the cut links as external forces and moments [15]. Let us define by $\mathbf{f}_{c_i} = [f_{x_i}, f_{y_i}, m_{z_i}]^\top$, $i = 1{,}2$, the vectors composed of the external forces and moments for both loop closures denote action torsors. Through the virtual work principle, these vectors contribute into the dynamic model by adding terms $\mathbf{J}_i^\top \lambda_i$, where $\mathbf{J}_i$ is the 3×15 Jacobian matrix describing how the action torsor acts on the system.

The model of human and its WAD is also subject of external forces and moments exerted by the ground in the stance feet. The complete dynamic model can be written as:

$$\mathbf{A}(\mathbf{x})\,\ddot{\mathbf{x}} + \mathbf{h}(\mathbf{x}, \dot{\mathbf{x}}) = \begin{bmatrix} \mathbf{D_h} & \mathbf{D_W} & \mathbf{J}_1^\top & \mathbf{J}_2^\top \end{bmatrix} \begin{bmatrix} \boldsymbol{\Gamma}_\mathbf{h} \\ \boldsymbol{\Gamma}_\mathbf{W} \\ \mathbf{f}_{c1} \\ \mathbf{f}_{c2} \end{bmatrix} + \mathbf{J}_{\mathbf{r}_1}^\top \begin{bmatrix} \mathbf{r}_1 \\ \mathbf{m}_{1_z} \end{bmatrix} + \mathbf{J}_{\mathbf{r}_2}^\top \begin{bmatrix} \mathbf{r}_2 \\ \mathbf{m}_{2_z} \end{bmatrix}, \quad (2)$$

with the constraint equations,

Table 1 Parameters for the seven-link biped and the walking assist device

	Mass (kg)	Length (m)	Inertia (kg m^2)	Center of mass (m)
Foot and shoe	$m_f = 0.678$	$L_p = 0.207$	$I^f = 0.012$	$s_{px} = 0.0135$
		$l_p = 0.072$		$s_{py} = 0.0321$
		$H_p = 0.064$		
Shin	$m_s = 4.6$	$l_s = 0.497$	$I^s = 0.0521$	$s_s = 0.3240$
Thigh	$m_t = 8.6$	$l_t = 0.41$	$I^t = 0.7414$	$s_t = 0.18$
Trunk	$m_T = 16.5$	$l_T = 0.625$	$I^T = 11.3$	$s_T = 0.3860$
Seat	$m_3 = 2.0$	$l_3 = 0.1$	$I^T = 0.3$	$s_3 = 0.050$
Upper link	$m_1 = 3.0$	$l_1 = 0.392$	$I^1 = 0.04$	$s_1 = 0.1127$
Lower link	$m_2 = 2.0$	$l_2 = 0.3645$	$I^2 = 0.02$	$s_2 = 0.169$

$$\mathbf{J}_{\mathbf{r}_i}\ddot{\mathbf{x}} + \dot{\mathbf{J}}_{\mathbf{r}_i}\dot{\mathbf{x}} = \mathbf{0} \text{ for } i = 1 \text{ to } 2,$$
$$\begin{bmatrix}\mathbf{J}_1\\ \mathbf{J}_2\end{bmatrix}\ddot{\mathbf{x}} + \begin{bmatrix}\dot{\mathbf{J}}_1\\ \dot{\mathbf{J}}_2\end{bmatrix}\dot{\mathbf{x}} = \mathbf{0}. \quad (3)$$

$[\mathbf{r}_i \mathbf{m}_{i_z}]^\top$, with $i = 1$ to 2, are the resultant action torsors of the contact efforts with the ground reaction in both feet. $\mathbf{J}_{r_1}$ and $\mathbf{J}_{r_2}$ are the 3 × 15 Jacobian matrices for the constraint equations in position and orientation for both feet, respectively. $\mathbf{A}(\mathbf{x})$ is the 15 × 15 symmetric positive definite inertia matrix, $\mathbf{h}(\mathbf{x}, \dot{\mathbf{x}})$ is the (15 × 1) vector, which groups the centrifugal, Coriolis effects, and the gravity forces. The (15 × 6) constant matrix $\mathbf{D_h}$, describes the action of the torque $\Gamma_\mathbf{h}$ of the human model on the system. The (15 × n_a) constant matrix $\mathbf{D_W}$, describes how the torque $\Gamma_\mathbf{W}$ of the WAD act on the system, here n_a is the number of actuators $2 \leq n_a \leq 6$. In the single support, with a stance foot and with flat foot contact on the ground the number of degrees of freedom is six, since the constraints (3) have to be satisfied.

3 The Reference Cyclic Walking Gait

The goal of this study is to compare the energy consumption for a given reference walking gait adopted by the biped alternately without and with its wearable assist device.

Initially, the reference walking gait is computed for the biped without the WAD. This walking gait is cyclic, i.e. all steps are identical. Each step is composed of a single support phase and an impact. In single support the stance foot has a flat contact with the ground. When the swing foot impacts the ground the other foot takes off. The evolution of each joint of the biped is prescribed with a third order polynomial function, of which the coefficients are calculated through a parametric optimization algorithm. The criterion for minimization is the integral of the square of torques for a given walking step length at several velocities; see [16, 17]. The cyclic walking gait is defined such that the conditions of the flat contact for the stance foot are satisfied without sliding nor rotation of this stance foot. This gait has been chosen for its simplicity, more complex gait with double support phase can be considered in future.

4 Study of the Optimal Distribution of the Torques for the Biped with the Wearable Assist Device

The biped equipped of a WAD tracks the walking cyclic gait defined in Sect. 3. The optimal distribution of the torques for the biped and its walking assist device is studied for the four following cases. Firstly the biped is fully assisted, the WAD provides six torques. The three other cases are defined such as the WAD provides two torques (Γ_7 and Γ_8), (Γ_9 and Γ_{10}), or (Γ_{11} and Γ_{12}). For each case, at each sampling time during one step of the cyclic gait, an optimization algorithm is stated to define the torque distribution between human and WAD.

Let us multiply the dynamic model (2) with the matrix $\mathbf{J}^{\perp}(12 \times 15) = \begin{bmatrix} \mathbf{J}_{\mathbf{r}_1}^{\top} & \mathbf{J}_{\mathbf{r}_2}^{\top} \end{bmatrix}^{\perp}$ to obtain a model, which does not depend on the ground reaction on the stance foot:

$$\mathbf{J}^{\perp}\mathbf{A}(\mathbf{x})\ddot{\mathbf{x}} + \mathbf{J}^{\perp}\mathbf{h}(\mathbf{x},\dot{\mathbf{x}}) = \mathbf{J}^{\perp}\begin{bmatrix} \mathbf{D} & \mathbf{J}_1^{\top} & \mathbf{J}_2^{\top} \end{bmatrix}\begin{bmatrix} \Gamma_{\mathbf{h}} \\ \Gamma_{\mathbf{W}} \\ \mathbf{f}_{c1} \\ \mathbf{f}_{c2} \end{bmatrix}. \tag{4}$$

The left hand side of (4) depends only of the reference walking gait, and thus is known. The objective is now to find the forces and moments $\mathbf{f}_{c1}$, $\mathbf{f}_{c2}$ and the torques $\Gamma_{\mathbf{h}}$, $\Gamma_{\mathbf{W}}$ that produce the desired motion. It exists an infinite number of solutions since Eq. (4) is a system of 12 equations and 12 + n_a unknowns, with a full rank matrix $\begin{bmatrix} \mathbf{D} & \mathbf{J}_1^{\top} & \mathbf{J}_2^{\top} \end{bmatrix}$. The dimension of over-actuation is n_a, the number of actuators of the WAD.

Two criteria will be considered depending on the objective of the use of the WAD. For people with disabilities, the minimisation of the human action is an obvious criterion

$$C_1 = \Gamma_{\mathbf{h}}^{\top}\Gamma_{\mathbf{h}}. \tag{5}$$

For valid people, the minimisation of the human and WAD torques can also be used:

$$C_2 = \Gamma_{\mathbf{h}}^{\top}\Gamma_{\mathbf{h}} + \Gamma_{\mathbf{W}}^{\top}\Gamma_{\mathbf{W}}. \tag{6}$$

The weighted combination of the two criteria can be considered, but as illustration the two extreme cases C_1 and C_2 will only be studied. Constraints are defined to limit the efforts of each loop closure between the human and its assist advice, to ensure that the vertical component of the ground reaction on the stance foot is positive. Furthermore a constraint of no rotation of the stance foot is also taken into account.

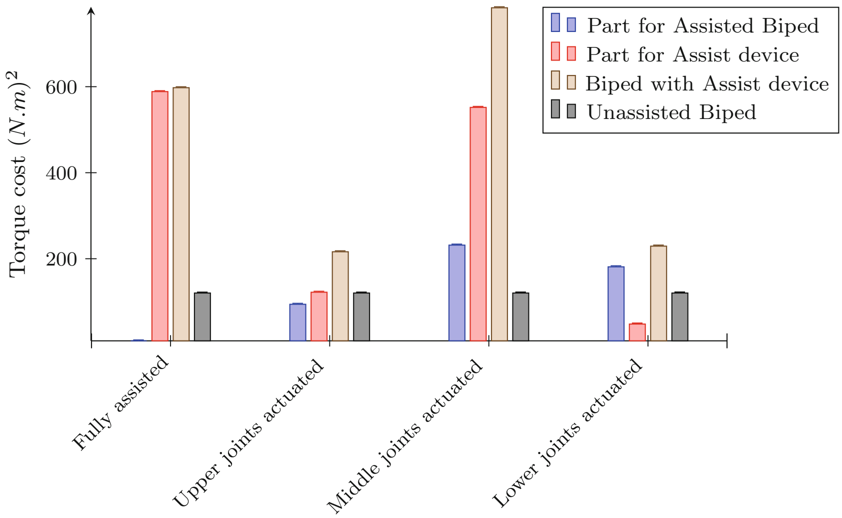

Fig. 2 Histogram of torque cost for the different distributions of the actuation of the WAD, and minimization of criterion C_1 (Only the human torques are minimized)

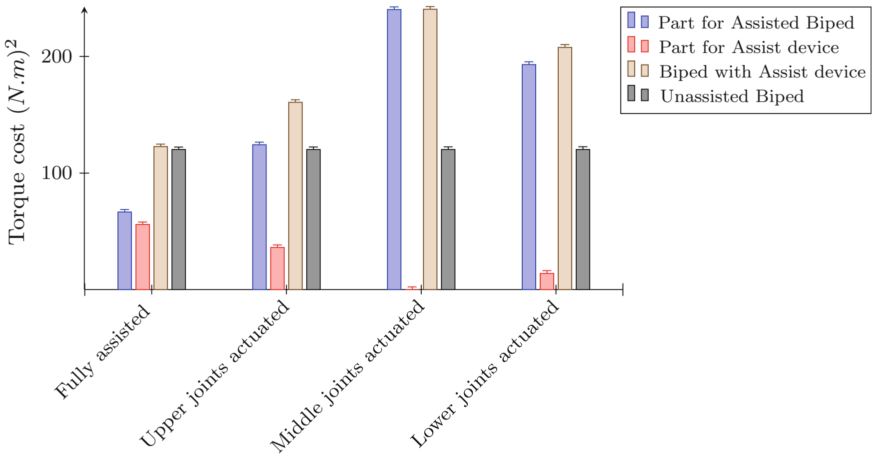

Fig. 3 Histogram of torque cost for the different distributions of the actuation of the WAD, and minimization of criterion C_2 (The torques of the biped and walking assist device are minimized)

5 Results

The results are presented for a walking speed 0.65 m/s (2.34 km/h) of the biped, considering the optimization criteria, respectiveley C_1 and C_2 given in Figs. 2 and 3.

Four different cases of actuation of the WAD are considered: the WAD is fully actuated, or partially actuated through the actuated upper joints only ($\Gamma_9 = 0$, $\Gamma_{10} = 0$, $\Gamma_{11} = 0$ and $\Gamma_{12} = 0$), the actuated middle joints only ($\Gamma_7 = 0$, $\Gamma_8 = 0$, $\Gamma_{11} = 0$ and $\Gamma_{12} = 0$), and the upper joints only ($\Gamma_7 = 0$, $\Gamma_8 = 0$, $\Gamma_9 = 0$ and $\Gamma_{10} = 0$). The results are compared to the case of the walking without assistance. In this case the biped is not equipped with the WAD, thus the weight of the walking assist device is not taken into account. These results correspond to the nominal case for the definition of the cyclic walking (see Sect. 3). The shown results correspond to the following cases.

1. The torque cost for the model of human expressed as $\frac{1}{d}\int_0^T \Gamma_h^\top \Gamma_h \mathrm{d}t$, where d is the walking step length when the human is equipped with the WAD,
2. The torque cost for the WAD expressed as $\frac{1}{d}\int_0^T \Gamma_W^\top \Gamma_W \mathrm{d}t$,
3. The sum of these two quantities,
4. The torque cost for the model of human expressed as $\frac{1}{d}\int_0^T \Gamma_h^\top \Gamma_h \mathrm{d}t$, when the human is not equipped with the WAD.

Based on the obtained results, we following observations can be made

1. An actuation of the middle joints or of the lower joints only are not appropriate since the torque cost for the human increases with these types of assistance.
2. A complete actuation of the WAD, allows a displacement of the human without any human torque if necessary (see Fig. 2). In this case, the cost to be produced by the WAD is high. A decrease of the human torque cost with respect to an unassisted case can be obtained with a very low increase of the total torque cost when criterion C_2 is minimized. The human torque cost can be adjusted between 0 and this value through the use of a weighted criterion $C_1 + \alpha C_2$.
3. The solution of the assistance in the upper joints only seems efficient to help the biped in good health, the device at least compensates for its weight, it can also reduce the burden of the human according to the optimized criterion.

Figure 4a–d presents the torque cost previously studied, as function of the motion velocity V of the biped with and without its WAD. The velocities vary between 0.4 and 0.9 m/s (1.44 and 3.24 km/h). Figure 4a, b are relative to the fully assisted biped for the optimized criteria C_1 and C_2 respectively. The cost torque for the model of human of the fully assisted biped is smaller than without assistance. When C_{1k} is the optimization criterion, the torque cost of the WAD is high. However the torques of the model of human are not equal to zero and even increase when the velocity is over 0.6 m/s (2.88 km/h). This is due to the fact that the reference trajectory is adapted to the autonomous biped and not to the biped with its WAD. In case of a paralyzed human using a walking assist device, the gait has to be adapted to the complete system. Figure 4c, d are relative to the model of human equipped of the WAD actuated at the upper joint level only, for the optimized criterion C_1 and C_2 respectively. Depending of the criterion minimized, the torque cost for the human can be reduced or almost unchanged with respect to the case of

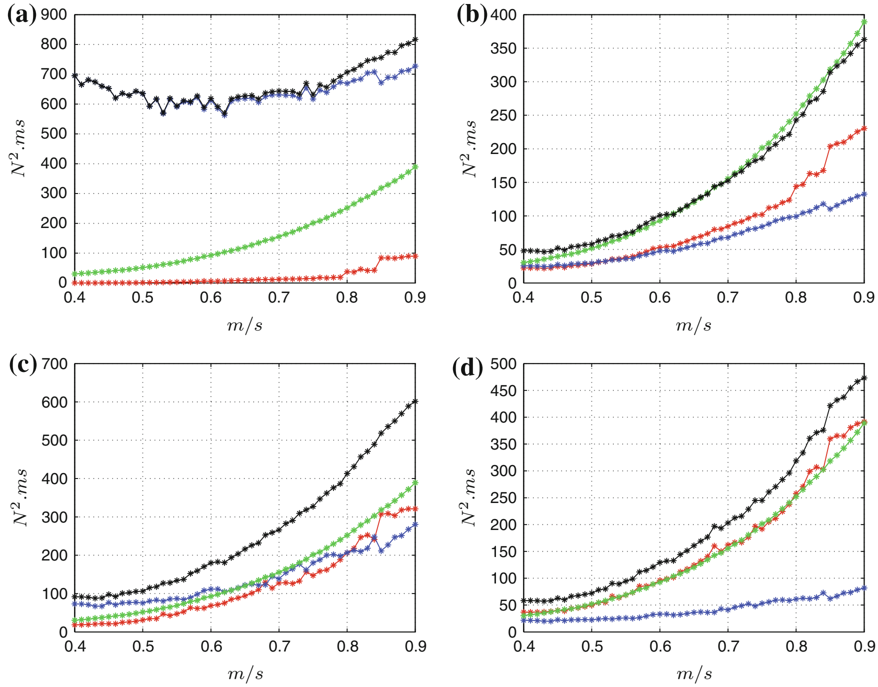

Fig. 4 Torque cost as function of the motion velocities: biped without assistance (*green*), part for the WAD (*blue*), part for the human model (*red*), addition of the WAD and model of human parts (*black*). **a** Fully actuated WAD, optimized criterion C_1; **b** fully actuated WAD, optimized criterion C_2; **c** upper joint actuation of the WAD only, optimized criterion C_1; **d** upper joint actuation of the WAD only, optimized criterion C_2

the human not equipped with a WAD. These curves confirm that to increase the autonomy of the biped the assistance in the upper joints only is a good compromise.

6 Conclusion

The paper presented a comparative analysis of the torque cost of walking with several actuations of a WAD in the case of simple walking gait with single support phases and impacts. It has been shown that the WAD fully actuated and the WAD actuated only at the upper joints are two interesting proposals. The WAD only actuated at the middle joints or at the lower joints are ineffective. A study for several walking velocities confirmed these results. It is an initial step to start the process of conception of a walking assist device. The perspective is a deeper study of the optimal placement of the actuators by introducing more complex and anthropomorphic walking gaits and the extension to the introduction of passive element to store energy.

Acknowledgments This work is supported by Ministry of Education and Science of Russian Federation and by Région des Pays de la Loire, Project *LMA* and Gérontopôle Autonomie Longévité des Pays de la Loire.

References

1. Priebe JR, Kram R (2011) Why is walker-assisted gait metabolically expensive? Gait Posture 34:265–269
2. Zhang X, Hashimoto M (2012) Synchronization-based trajectory generation method for a robotic suit using neural oscillators for hip joint support in walking. Mechatronics 22:33–44
3. Ikeuchi Y, Ashihara J, Hiki Y, Kudoh H, Noda T (2010) Walking assist device with bodyweight support system. In: Proceedings of IEEE/RSJ international conference on intelligent robots and systems, St Louis, pp 4073–4079
4 Aoustin Y (2015) Walking gait of a biped with a wearable walking assist device. Int J HR 12 (2):1550018-1–11550018-20
5. Vukobratovic M, Borovac B (2004) Zero-moment point-thirty five years of its life. Int J Hum Robot 1(1):157–173
6. Kaneko K, Kanehiro F, Kajita S, Hirukawa H, Kawasaki T, Hirata M, Akachi K, Isozumi T (2004) Humanoid robot hrp-2. In: Proceedings of IEEE international conference on robotics and automation ICRA, New-Orleans, Louisiana, pp 1083–1090
7. Kuo AD, Donelan JM, Ruina A (2005) Energetic consequences of walking like an inverted pendulum: step-to-step transitions. Exerc Sport Sci Rev 33(2):88–97
8. Englsberger J, Ott C, Roa MA, Albu-Shäffer A, Hirzinger G (2001) Bipedal walking control based on capture point dynamics. In: Proceedings of international conference on intelligent robots and systems (IROS), San Francisco, pp 4420–4427
9. Pratt JE, Koolen T, de Boer T, Rebula JR, Cotton S, Carff J, Johnson M, Neuhaus PD (2012) Capturability-based analysis and control of legged locomotion, part 2: application to m2v2, a lower-body humanoid. Int J Robot Res 31(10):1117–1133
10. Behnke S (2006) Online trajectory generation for omnidirectional biped walking. In: Proceedings of international conference on robotics and automation (ICRA), Orlando, pp 1597–1603
11. Graf C, Häryl A, Röfer T, Laue T (2009) A robust closed-loop gait for the standard platform league humanoid. In: Proceedings of workshop on humanoid soccer robots of the IEEE-RAS international conference on humanoid robots, Paris, France, pp 30–37
12. Powell MJ, Heraeid A, Ames AD (2013) Speed regulate in 3d robotic walking through motion transitions between human-inspired partial hybrid zero dynamics. In: Proceedings of IEEE international conference on robotics and automation (ICRA), Karlsruhe, Germany, pp 4803–4810
13. Tomic M, Vassallo C, Chevallereau C, Rodic A, Potkonjak V (2014) Arms motion of a humanoid inspired by human motion. In: Proceedings of international conference on medical and service robotics (MESROB 2014), Lausanne, Switzerland
14. Formalskii AM (1982) Locomotion of Anthropomorphic Mechanisms. Nauka, Moscow, Russia (in Russian)
15. Khalil W, Dombre E (2002) Modeling, identification and control of robots. Butterworth Heinemann
16. Beletskii VV, Chudinov PS (1977) Parametric optimization in the problem of bipedal locomotion. Izv. An SSSR. Mekhanika Tverdogo Tela [Mechanics of Solids], no 1, pp 25–35
17. Chevallereau C, Aoustin Y (2001) Optimal reference trajectories for walking and running of a biped. Robotica 19(5):557–569

Design of a Hybrid Adaptive Support Device for FES Upper Limb Stroke Rehabilitation

Giuseppe Cannella, Dina S. Laila and Christopher T. Freeman

Abstract A novel design of a low cost non-powered orthosis device for home-based upper limb stroke rehabilitation is proposed. The design allows the device to be integrated with a dual robotic and electrical stimulation control scheme. This enables exploitation of the motor relearning principles which underpin both robotic therapy and Functional Electrical Stimulation (FES) based stroke rehabilitation. This work focuses on the mechanical design of the non-powered orthosis, based on gravity balancing theory and provides preliminary dynamic simulations of the 3D CAD model.

Keywords Passive orthosis · Gravity balancing theory · FES · Stroke rehabilitation · Multibody dynamics

1 Introduction

Stroke patients can relearn how to use impaired parts of their body by progressive goal-based physical exercise programmes. New therapies often employ expensive and complex robotic devices to train patients. Another widely used technology in the field of stroke rehabilitation is Functional Electrical Stimulation (FES), which contracts muscles through short electrical pulses in the same way as those produced by the central nervous system [3].

G. Cannella (✉) · D.S. Laila
Faculty of Engineering and the Environment, University of Southampton, Southampton, UK
e-mail: gc2g12@soton.ac.uk

D.S. Laila
e-mail: d.laila@soton.ac.uk

C.T. Freeman
Electronics and Computer Science, University of Southampton, Southampton, UK
e-mail: cf@ecs.soton.ac.uk

H. Bleuler et al. (eds.), *New Trends in Medical and Service Robots*,
Mechanisms and Machine Science 38, DOI 10.1007/978-3-319-23832-6_2

In this research it was chosen to combine FES with an adjustable low cost support device, controlling both with a model-based controller. This represents a novel non-conventional therapy and the overall device can be defined as hybrid adaptive low cost support for home-based stroke rehabilitation. The design of the mechanical support device is based on gravity balancing theory [4]. This theory allows a low cost arm support to be designed to carry the weight of the patient's arm during training throughout their whole range of motion, allowing them to use their residual muscle strength to perform the rehabilitation task. Moreover, the system is integrated with an adjustment balancing mechanism which allows variation of the support given to a patient's arm according to their inertial characteristics. These project specifications are addressed in this paper which develops a 3D CAD model of the mechanical support, whose dynamic performance is evaluated in Sect. 4.

2 Non-Conventional Rehabilitation Therapies

In non-conventional rehabilitation therapy the manual assistance of the physiotherapist is augmented or entirely replaced by a rehabilitative device. These specific devices are usually classified as: robotics, powered and non-powered orthoses. Robotic devices and powered orthoses consist of complex robots and active mechanical systems operating under computer control. Their design features mean they can be personalised for each patient's anatomy, but this often results in a complex and expensive device. On the other hand, non-powered orthoses are much simpler devices that provide gravitational support to the specific limb that needs to be trained, helping the patient to perform rehabilitation tasks. Their design and usage complexity is lower compared to that of robots and active orthoses. The only restriction for non-powered orthoses is that they need to be actuated by the patient's neuromuscular effort, since they only provide gravitational support. Hence they can only be employed for the rehabilitation of subjects with residual force in their muscles. Two examples of existing non-powered orthoses are the Wilmington Robotic Exoskeleton (WREX) [7] and the Armon Orthosis [5, 6]. WREX is a body-powered orthosis that provides gravitational support to the patient's arm thanks to a light exoskeleton mechanism that is counterbalanced by means of elastic bands. The Armon Orthosis is non-powered and designed to be mounted on a wheelchair or on a table, providing gravitational support to the patient's arm. It exploits gravity balancing theory, combining a parallelogram linkage and zero-free length springs.

In this research, we propose a novel design that combines gravity balancing based non-powered orthotic support and muscular stimulation by means of FES, in order to increase the effectiveness of therapy without sacrificing the low cost home-based philosophy.

3 Mechanical Design

In Fig. 1 the mechanism chosen to meet the device specifications for the purpose of this research is shown. It comprises a planar 2 degrees of freedom (d.o.f.) kinematic chain made of a parallelogram linkage combined with two zero-free length springs, where each spring balances each d.o.f. of the mechanism.

Zero-free length springs are useful components within gravity balanced systems since they have linear characteristics; the force acting on the spring is directly proportional to its deflection, and this feature simplifies the mechanical analysis of the systems in which they are employed. Moreover, the parallelogram linkage in this particular configuration allows the device to be in contact with just a small area of the forearm of the patient, identified by the Combined Center of Mass (CCM). Performing both a potential energy and moment equilibrium analysis [1] yields the following balancing conditions for the mechanism:

$$\begin{cases} (m+m_4)gL + m_3gr_{m3} + m_1gr_{m1} = k_2ar \\ mgL + m_4gr_{m4} - m_2gr_{m2} - m_3gr = k_1ar. \end{cases} \quad (1)$$

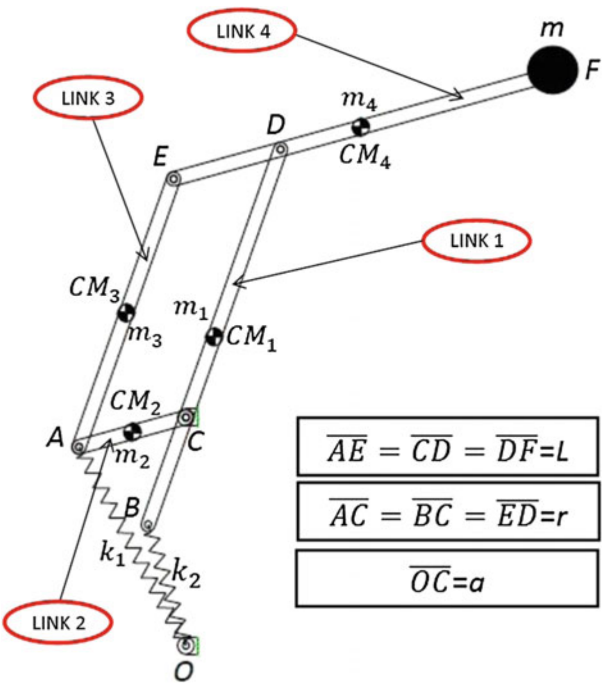

Fig. 1 Kinematic chain of the arm support

Fig. 2 3D CAD model and subcomponent labels

This system is a linear mechanical model, which will later simplify the analysis. Moreover, the rehabilitative device has to be adaptive and the above system contains all the variables of the mechanism that can be varied in order to adjust the mechanical behaviour of the system according to different patient anatomic characteristics and their progress in the rehabilitation programme. Among all the inertial and spring parameters, a was chosen to be varied. This choice allows the adjustment mechanism to be placed below the linkage and it does not directly affect the inertia parameters of the links.

In Fig. 2 the 3D CAD model of the orthosis is shown. It consists of a parallelogram linkage, with a light weight interface connection for the user's arm (Fig. 3), a balancing mechanism (Fig. 4), an adjustment system (Fig. 5) and a frame. In total it has 5 d.o.f. divided as follows: 2 d.o.f. for the interface connection, 2 d.o.f. for the parallelogram linkage and 1 d.o.f. for the vertical axis of rotation of the mechanism. For more details about the 3D CAD model refer to [1].

Deep groove ball bearings were selected to be mounted in the joints of the device in order to reduce friction and thereby improve the mechanical performance of the overall system. The linkage links are made of aluminium in order to reduce the overall inertia of the mechanical device. The same approach has been used for the interface connection in order to produce a light weight component which does not introduce additional dynamics to the overall linkage. The lower part of the linkage is connected to the springs via a string-pulley arrangement. The linear system (1) results from the assumption of zero-free length springs, however the proposed solution allows them to be replaced with normal extension springs, significantly reducing the cost of the device. The balancing behaviour of the device

Fig. 3 Detailed view of the two revolute joints of the interface connection

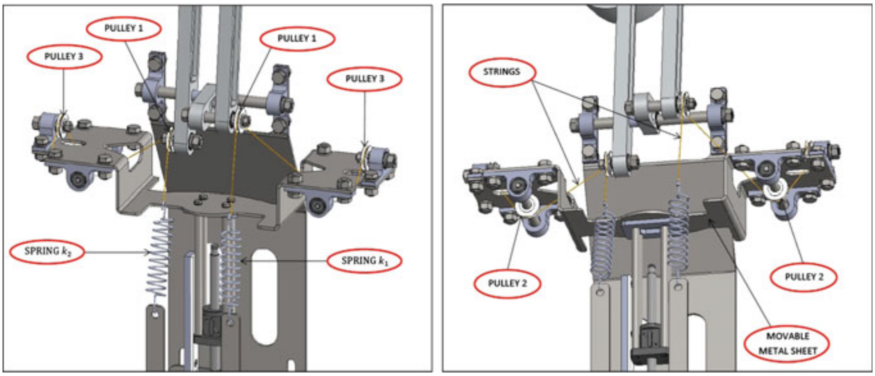

Fig. 4 Detailed views of the gravity balancing mechanism. *Left* view from above. *Right* view from below

Fig. 5 Detailed view of the adjustment system

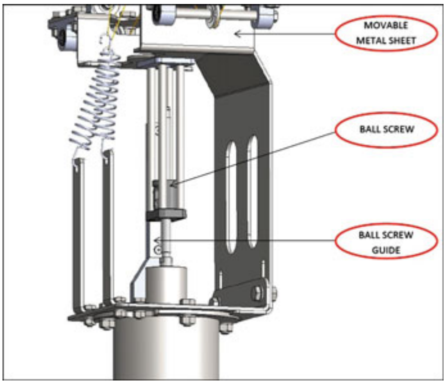

can be varied by an adjustment system comprising a ball screw connected to an electric motor. This electromechanical solution will be controlled by a model-based FES controller which automatically varies the amount of support needed by the patient by changing the value of a. The placing of the balancing mechanism and the adjustment systems between the linkage and the 5th revolute joint allows the overall inertia of the system to be reduced about the vertical axis of rotation. Since the device may need to be moved between different environments, four casters with brakes have been installed at its base.

4 3D CAD Model Dynamic Simulation

In this section the dynamic simulation of the 3D CAD model is carried out in SolidWorks using the Motion Analysis module. The study is performed by analysing the displacement of the centre of mass of the interface connection, when a specific payload is carried by it. For the sake of simplicity the 2 d.o.f. of the interface connection are locked during the simulations. The device can adapt its balancing behaviour for a range of different payloads. It was chosen to perform four simulations where the values of the payload and the distance a have been calculated according to the linear relationship (1): first simulation $m = 0$ kg and $a = 3.5$ mm; second simulation $m = 1$ kg and $a = 19$ mm, third simulation $m = 2$ kg and $a = 34.5$ mm, fourth simulation $m = 3$ kg and $a = 50$ mm, which corresponds to the maximum arm weight. The stiffness of the two springs is calculated by a Matlab code based on the gravity balancing condition (1), and the values are $k_1 = 4048$ N/mm and $k_2 = 5035$ N/mm, which are kept constant during all four simulations. Since the joints have been designed using bearings, the static friction is $\mu_s = 0.0024$ and the dynamic friction is $\mu_d = 0.0012$. The simulations are run for a duration of 20s. The coordinates of the centre of mass of the interface connection are shown in Figs. 6, 7 and 8. The results show how the dynamic behaviour of the device improves when the payload increases. The reason is that the stiffness of the springs is a fixed parameter that has been calculated for the case of the maximum payload, $m = 3$ kg. Moreover the oscillatory trend of the centre of mass is due to the lack of damping and to the fact that the stiffness of the springs and the parameter a were set using a static gravity balancing analysis. These confirm that the device is able to support a payload with only a minor level of oscillation, but indicate that a controller is required in order to overcome this drawback. It should be also taken into account that on the real prototype, these oscillations will be mitigated by the additional natural damping introduced by the patient's arm.

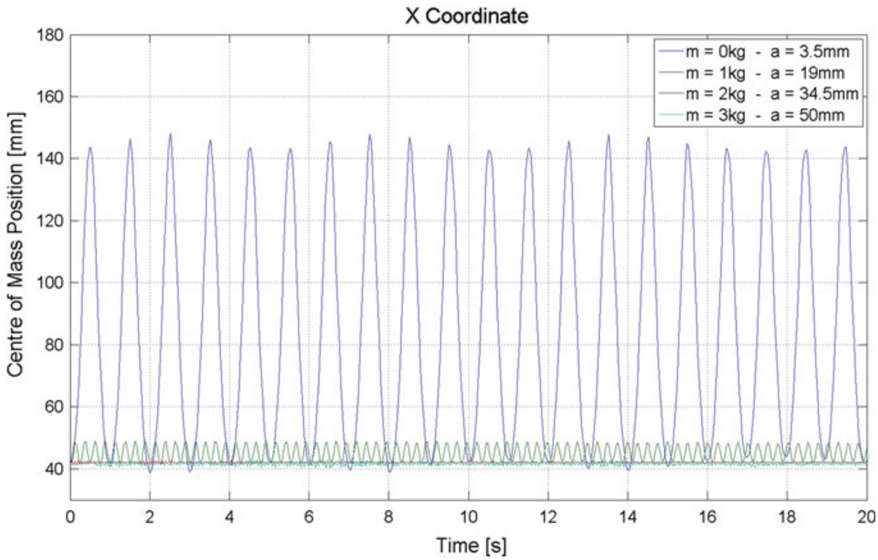

Fig. 6 X coordinate of the position of the centre of mass

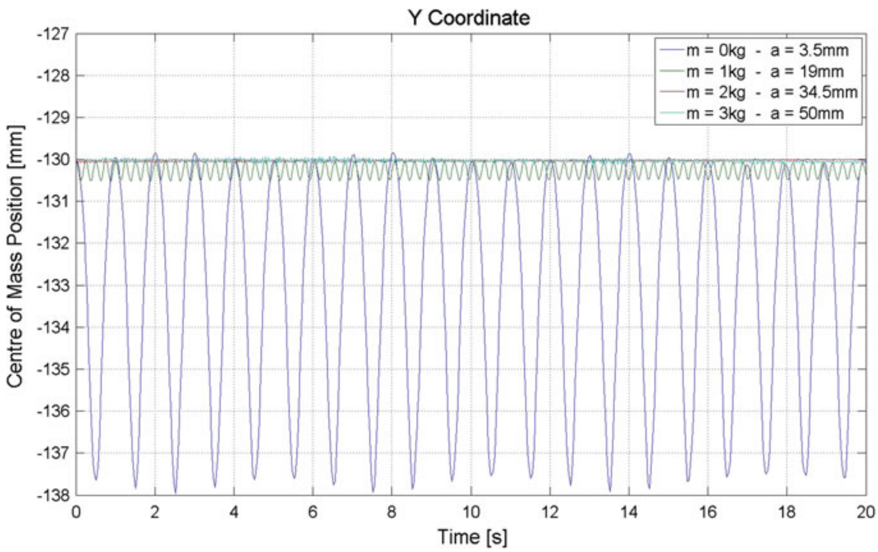

Fig. 7 Y coordinate of the position of the centre of mass

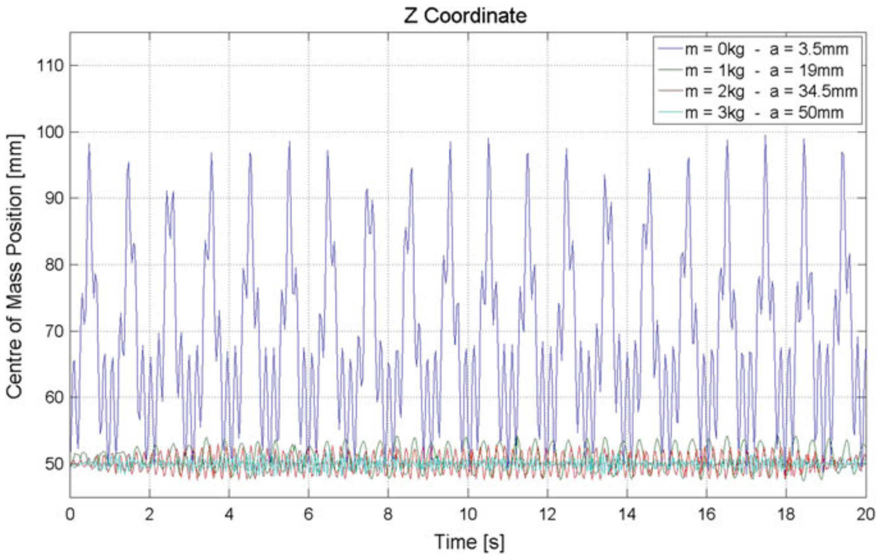

Fig. 8 Z coordinate of the position of the centre of mass

5 Hybrid Control Scheme

During therapeutic application, the support device will be used simultaneously with FES applied to clinically relevant muscles groups in the patient's upper limb. This will enable a greater level of support than either can provide when acting alone, and is expected to translate into more effective clinical outcome measures. This section presents details of the hybrid control scheme that will be employed to assist upper limb tasks using a combination of mechanical and FES modalities.

From [3], a dynamic model of the human arm with FES applied to a subset of joints is given by

$$B(\Phi(t))\ddot{\Phi}(t) + C(\Phi(t), \dot{\Phi}(t))\dot{\Phi}(t) + F(\Phi(t), \dot{\Phi}(t)) + G(\Phi(t)) = \tau(u(t), \Phi(t), \dot{\Phi}(t)) \quad (2)$$

where $B(\cdot)$, $C(\cdot)$ are inertial and Coriolis matrices respectively, $F(\cdot)$ and $G(\cdot)$ are friction and gravitational vectors respectively, and $\Phi(t)$ contains the joint angles of the human arm. Vector $\tau(u(t))$ comprises the moment produced through application of FES signal $u(t) = [u_1(t), \cdots, u_n(t)]^{\mathrm{T}}$ to actuate n muscles, and $\Phi(t)$ contains the anthropomorphic joint angles. Application of gravity balancing to this arm model produces a moment, $v(a(t), \Phi(t))$, about the anthropomorphic joint axes which is added to the right hand side. In addition, the dynamic properties of the mechanical support can also be incorporated into the terms B and C if deemed significant (see [3] for details).

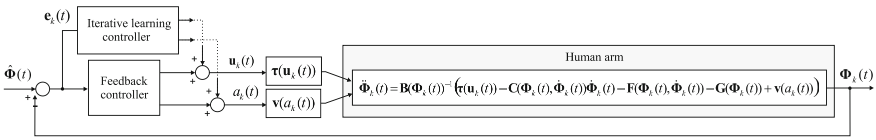

Fig. 9 Hybrid control scheme

The control task is to select gravity support parameter $a(t)$, and FES signal $u(t)$ in order to assist the user in tracking a joint reference signal $\hat{\Phi}(t)$. To achieve this, consider the quadratic minimisation problem

$$\min_{u,a} J(u,a), \quad J(u,a) = \|\hat{\Phi} - \Phi\|^2 + \|a\|^2_{W_a} + \|u\|^2_{W_u} \tag{3}$$

in which $\|x\|^2_W = x^{\mathrm{T}}Wx$, and weighting matrices W_a, W_u are positive definite. Selection of FES signals $u(t)$, $a(t)$ to minimise (3) over the task duration can be computed using any iterative minimisation procedure. In the rehabilitation setting the user has multiple attempts at performing the task and hence (3) can be solved in an iterative manner using data collected over these attempts. Denoting each attempt with the subscript k, this naturally leads to an Iterative Learning Control (ILC) scheme, with an appropriate control scheme shown in Fig. 9. Note that explicit feedback and ILC structures are derived in [2, 3].

The support, τ, provided by FES acts around each joint axis, while the gravity balancing support, v, acts against the gravity term $G(\Phi)$. In particular, if the system mass were concentrated solely at the end-effector, then $a(t)$ can be stipulated such that $G(\Phi) - v(a(t), \Phi(t)) = \beta(t)G(\Phi)$, $\beta \in [0, 1]$. Hence $a(t)$ solely regulates support against against gravity by acting on the term $G(\Phi)$ while FES assists the remaining human arm dynamics. This effectively partitions the control system and prevents/suppresses interaction between controlled variables. Simpler control strategies are also possible by employing constraints within (3), for example if $a_k(t) = a_k$ is fixed during each attempt then the level of gravity balancing is only updated between task attempts.

6 Conclusion and Future Work

The kinematics and the 3D CAD model of the device have been analysed. Then the dynamic analysis of the 3D CAD has been carried out and confirms satisfactorily dynamic behaviour with only minor oscillation of the arm support for realistic upper limb masses.

The next step for this research program is to complete further dynamic analyses and FEA of the 3D CAD model. Then the first prototype of the support will be manufactured and tested. To integrate the device with FES, parameters in the model of the supported stimulated upper limb (2) will be identified, and the proposed optimal control strategy will be employed to implement a hybrid control system which controls FES and mechanical support in order to balance voluntary effort and performance to maximise therapeutic effect. Once the overall design is completed, the device will be tested with both unimpaired and neurologically impaired subjects to evaluate its performance and optimize its function.

References

1. Cannella G, Laila DS, Freeman CT (2015) Mechanical design of an affordable adaptive gravity balanced orthosis for upper limb stroke rehabilitation. Mech Based Des Struct Mach Int J. doi:10.1080/15397734.2015.1054513
2. Freeman CT (2014) Newton-method based iterative learning control for robot-assisted rehabilitation using FES Mechatronics 24:934–943
3. Freeman CT (2015) Upper limb electrical stimulation using input-output linearization and iterative learning control. IEEE Transactions on Control Systems Technology 23(4):1546–1554
4. Herder JL (2001) Energy-free systems: Theory, conception, and design of statically balanced mechanisms. Ph.D. thesis, Delft University of Technology
5. Herder JL (2005) Development of a statically balanced arm support: Armon. In: 9th international conference on rehabilitation robotics, Chicago, 281–286
6. Mastenbroek B, de Haan E, van den Berg M, Herder JL (2007) Development of a mobile arm support (Armon): Design evolution and preliminary user experience. In: Proceedings of IEEE 10th international conference on rehabilitation robotics, Noordwijk, 1114–1120
7. Rahman T, Sample W, Jayakumar S, King MM, Wee JY, Seliktar R, Alexander M, Scavina M, Clark A (2006) Passive exoskeletons for assisting limb movement. J Rehabil Res Dev 43:583–590

Motion Control Algorithm of Walking Assist Machine Using Crutches to Achieve Variable Gait Style and Step Length

D. Matsuura, R. Inose and Y. Takeda

Abstract A new scheme to determine actuator input trajectory for a walking assist machine using crutches to achieve various desired step length will be discussed. First of all, two different gaits, swing-to and dragging gait and typical patterns of actuator input trajectory regarding those two gaits were defined. Secondly, some dominant parameters, maximum stroke and amplitude of acceleration of linear actuator in the phase to get off the ground, were investigated to find reasonable parameter region called gait feasible region to achieve the above-proposed gaits safely. In addition, initial condition of the apparatus to start walking were also determined. By using a prototype walking device, effectiveness of the proposed scheme has been demonstrated by achieving several different desired step lengths in the swing-to and dragging gaits.

Keywords Walking machine · Walking assist · Actuator input trajectory · Initial configuration · Parametric analysis

1 Introduction

Assistance for handicapped people's daily mobility is highly required in many countries for establishing sustainable aged society. In Japan, for example, there are 0.83 million people having disability issues in their lower limbs [1], and many of them are using wheelchairs. Although wheelchair is safe and easy to use, users are not completely satisfied because of its large foot print, difficulty in ascending/descending or getting over steps, lower eye level and arm reach and poor visibility from others. To solve these problems and help handicapped people to lead

D. Matsuura (✉) · R. Inose · Y. Takeda
Tokyo Institute of Technology, Meguro, Japan
e-mail: matsuura@mech.titech.ac.jp

Y. Takeda
e-mail: takeda@mech.titech.ac.jp

H. Bleuler et al. (eds.), *New Trends in Medical and Service Robots*,
Mechanisms and Machine Science 38, DOI 10.1007/978-3-319-23832-6_3

independent daily lives, upright-type walking assist machines are suitable. Although some exoskeleton-type walking assist machines have come in early stage of commercial use [2–5], they tend to have complicated structure and sensor/control system and thus expensive. Some alternative approaches such as a biped-robot walking chair using spatial parallel mechanism [6], coupled planar parallel mechanisms connected by orthogonal joints [7], or cable-based manipulator type walking assist device [8] have also been developed, but those mechanisms also tend to become complicated and heavy. In order to design a simple and lightweight walking assist machine for daily transportation assistance, our research group has been developing a very simple walking mechanism called walking assist machine using crutches (WAMC) [9]. This apparatus was designed under the consideration of the fact that many, especially young paraplegics are still maintaining healthy upper-limb function as same as able-bodied people. In such case, forearm crutches can be used not only for improving the stability by increasing the number of contact points but also for driving one's body by utilizing residual upper limb function. In the project, gaits on horizontal ground as fast as those of able-bodied people and climbing/descending steps up to 180 mm high have been achieved [9]. Those functions are essential to establish basic mobility, but not enough to provide practical walking assistance. In addition that, adjustment of walking speed and step length to achieve a gait according to surrounding environment/condition is also required.

In this paper, two different new gait styles called step-to and dragging gaits will be firstly proposed based on observation of able-bodied person and physical consideration of walking principle to establish variable small step length. Regarding those two gait options, relationship between the initial configuration of the mechanism, translation/velocity and acceleration of the linear actuator and resulting step length are quantitatively evaluated on the basis of kinetostatic model analysis. Relationship between some design parameters of the input trajectory for actuator and capability of gait achievement are investigated to distinguish dominant parameters to provide a simple and strategic scheme to denote actuator input, and to guarantee the stability of resulting gait. Various combinations of those dominant parameters and success/failure of resulting gait are investigated to plot the gait feasible region in which the walking assist machine can perform gait with desired step length successfully. By using the obtained map of gait feasible region and theoretical model, a motion control algorithm to achieve walking assist motion with commanded step length in different walking style will be figured out. Finally, experimental validation using a prototype apparatus will demonstrate the effectiveness of the proposed scheme by achieving several different step length in different gait style.

2 Walking Assist Machine Using Crutches (WAMC)

Composition of WAMC is as shown in Fig. 1, which has a single linear actuator to change the distance between the user's hip joint and foot plate. This actuator and two crutches forms tripod structure to supports user's body without any control.

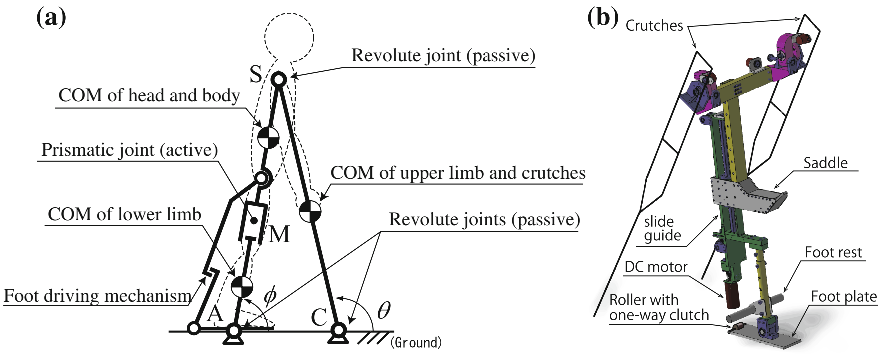

Fig. 1 Composition of WAMC. **a** Schematic drawing. **b** 3D-CAD drawing

The linear actuator is composed of a 48 V/150 W DC motor with planetary reducer of 1:10 reduction ratio, a ball spline and timing belt. Output stroke of the linear actuator is calculated from optical encoder signal, and exerted voltage for the motor is controlled based on a simple PID algorithm. During the motion control of the machine, user's upper limb function can be utilized not only for supporting his or her body but also for achieving gait motion together with the linear actuator. In addition, users can sit down on a saddle and put one's legs on a foot rest. Thanks to those components, tight harnesses are not necessary, and users can take rests on the saddle while using both arms freely whenever one wants. Furthermore, this design provides many other benefits such as a simple and lightweight structure, low energy consumption and enhancement of the user's health.

3 Algorithm to Achieve Variable Small Step Length

In order to determine the reasonable initial configuration of the apparatus and actuator input trajectory to achieve safe and adaptive gait with various step length, two different gait styles called swing-to and dragging gait are determined as shown in Fig. 2. Theoretical model for kinetostatic analysis was also determined as shown in Fig. 3. Typical step length which should be achieved by swing-to gait is up to half of initial step distance, L_{step}, namely approximately in-between 0.4 and 0.2 m. Dragging gait is used to achieve very small step length less than 0.2 m. Before theoretical analysis, gait of able-bodied subject using crutches, which is similar to swing-to gait, was experimentally analyzed. As the result, time-trajectory of the distance between the hip and ankle joint was obtained, and that was approximated into five linear sections as shown in the left side of Fig. 4. This was used as a desired actuator input trajectory in case of swing-to gate.

The desired length of the linear actuator, L, takes maximum value, L_1, during the third phase starting from the time $t_1 + t_2$ according to the diagram of Fig. 4. After

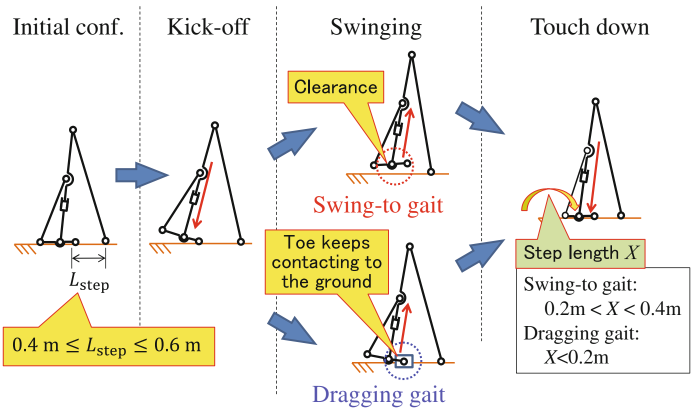

Fig. 2 Two gait styles to achieve small step length

Fig. 3 Analytical model of WAMC

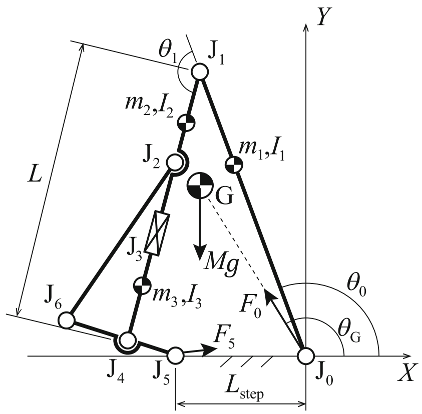

that, the linear actuator contracts at the acceleration of $\ddot{L}_3$ to take the foot plate off from the ground. While in the swinging phase, step length to be achieved depends on the height of the ankle joint, h, at the moment of taking off, and the value of h can be geometrically calculated from L_1. Whether the swing-to gait can be succeeded or not is dominated by the sign of the vertical element of ground reaction force (GRF), F_{4y}. When F_{4y} becomes minus, toe will take off. F_{4y} is written as

$$F_{4y} = \frac{-\left\{I - M\left(X_G^2 + Y_G^2\right) b_G \ddot{L} - MgX_G\right\}}{L_{step}} \qquad (1)$$

where X_G, Y_G, I, M and g are the position of the center of mass and inertia around that point, mass of WAMC and gravitational acceleration, respectively. $\ddot{L}$ and b_G are output acceleration of the linear actuator and a constant coefficient. In this paper,

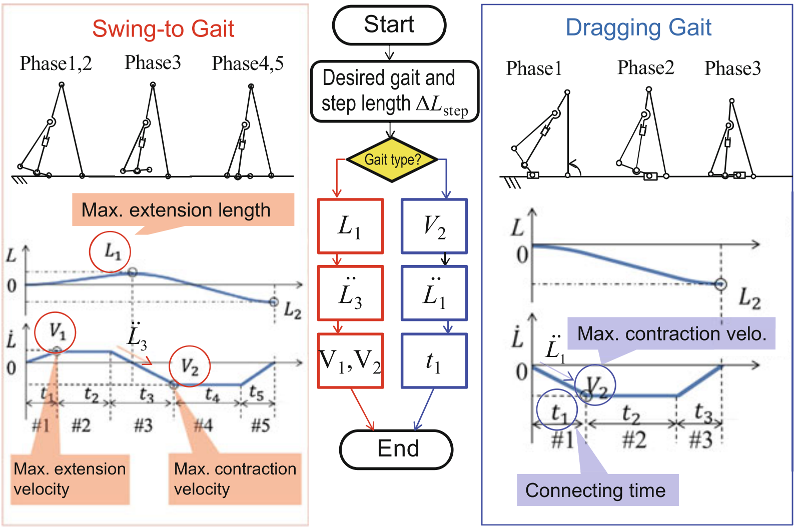

Fig. 4 Desired stroke, velocity and acceleration of linear actuator, corresponding mechanism configuration and order of parameter determination

the acceleration of the center of mass is assumed to be calculated from the linear actuator acceleration as $\ddot{\theta}_G = b_G \ddot{L}$. A desired step length, D, is given as a command value to be achieved, and the maximum actuator stroke, L_1, is geometrically calculated from it. Initial distance between the crutch tip and foot plate, L_{step}, is also given. After the assignment of those parameters, $\ddot{L}_3$ should be selected to satisfy the condition $F_{4y} < 0$. After the assignment of value for L_1, a gait feasible region in which the target gait can be achieved is obtained by performing number of dynamical analysis with different combination of V_1 and V_2. From this result, values of V_1 and V_2 are picked up from the center of the gait feasible region to guarantee maximum stability. As a numerical example, a gait feasible region for swing-to gait is shown in Fig. 5. Design parameters given in this calculation are shown in Table 1. In the figure, all the considered combination of V_1 and V_2 are plotted. White circle represents the conditions in which the machine can achieve swing-to gait, and a gait feasible region can be seen as an envelope of those markers. According to the above decision scheme, suitable V_1 and V_2 can be chose from the center of those white markers (black marker). Since range of $\ddot{L}_3$ is limited as

$$|\ddot{L}_3| > \left[\frac{V_2 - V_1}{t_2}\right]. \tag{2}$$

Thus $\ddot{L}_3$ can be determined as the minimum value which satisfies this inequality. In case of dragging gait, on the other hand, desired trajectory becomes simpler that only the last three-phases of swing-to gait were remaining. Essential condition to

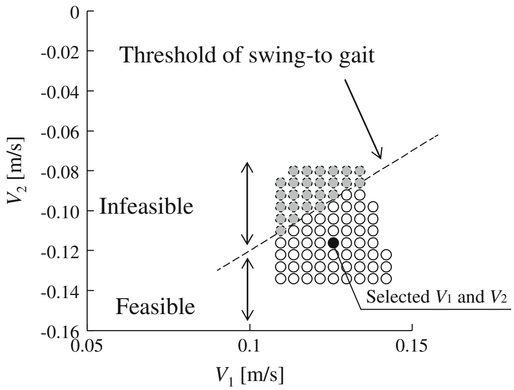

Fig. 5 Numerical example of gait feasible region

Table 1 Given design parameters

Inertia (kg m^2)		
I_1	I_2	I_3
0.60	0.69	1.90
Mass (kg)		
m_1	m_2	m_3
2.0	10.9	7.7
Link length (m)		
ℓ_{01}	ℓ_{12}	ℓ_{13}
1.28	0.55	0.59
ℓ_{45}	ℓ_{46}	
0.20	0.10	

success the dragging gait is that the sign of horizontal element of ground reaction force becomes zero.

From acceleration analysis and equilibrium condition of force, following equations can be obtained,

$$\begin{aligned} M\ddot{X}_G &= -F_{0x} + F_{4x},\ M\ddot{Y}_G = F_{0y} + F_{4y} - Mg, \\ \ddot{\theta}_0 &= a_0 + b_0\ddot{L}_1,\ \ddot{\theta}_1 = a_1 + b_1\ddot{L}_1,\ \ddot{\theta}_G = b_G\ddot{L}_1, \end{aligned} \tag{3}$$

where F_0 and F_4 are ground reaction forces at the end of crutch and toe, and $a_{0,1}$ and $b_{0,1 \text{ and } G}$ are constant terms determined by the linear actuator's displacement and velocity. These constants were obtained by performing line fitting to the numerical results of dynamical simulation. From above, condition to achieve dragging gait on the acceleration of linear actuator can be written as following,

$$\left|\ddot{L}_1\right| = \left[\frac{V_2}{t_1}\right]. \tag{4}$$

In case of dragging gait, resulting step length becomes smaller due to the influence of friction between the toe and ground. Velocity of the toe while dragging, V_2, thus should be chosen carefully not to become too small. Since the relationship between V_2 and resulting step length was almost linear, it was simply linear approximated to calculate suitable value to achieve desired step length, D.

4 Experimental Validation

In order to validate the proposed scheme for determining input trajectory to achieve various step length, motion control experiment using a prototype apparatus shown in Fig. 6a was performed. In order to guarantee the safeness and repeatability of condition, all experiments were done in unmanned apparatus. In the experiment, various input trajectories for the linear actuator were generated based on the proposed scheme corresponding to different desired step length between 0.1 and 0.45 m. Output motion of the prototype was measured by 3D optical motion capture system and force plates to measure ground reaction force at the end of the crutches and the foot plate.

Achieved gait style with respect to each trial was judged by ground reaction force such that when vertical term of GRF becomes very small or zero, it was judged as swing-to gait, and when it kept certain value, it was judged as dragging gait. Example of measured ground reaction force signals with two gait styles is shown in Fig. 7. Figure 6b, c plot the amplitude of contraction acceleration against the maximum actuator stroke, L_1, and established gait style at each trial. The experimentally obtained transition of gait style well agreed with the theoretical prediction based on the Eqs. (2) and (4). Figure 6c, on the other hand, plots the

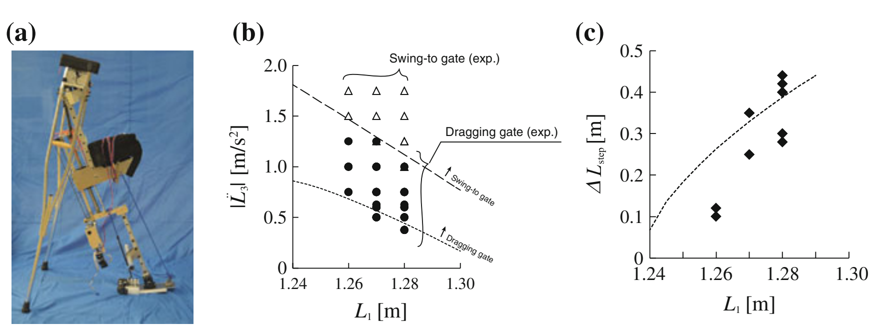

Fig. 6 Comparison between theoretical prediction and experimental result. **a** Prototype WAMC. **b** Max actuator stroke versus acc. **c** Max actuator stroke versus step length

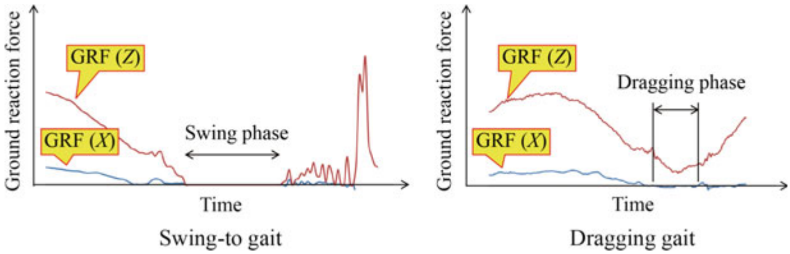

Fig. 7 Measurement results of ground reaction force during the experiments

relationship between L_1 and obtained step length, ΔL_{step}. In the previous section, it has been suggested that L_1 strongly dominates ΔL_{step}, and plots in Fig. 6c was actually close to a theoretical curve.

5 Conclusions

In order to realize adaptive locomotion of walking assist machine using crutches, determination scheme of actuator input trajectory to achieve various small step length was proposed, and the scheme was experimentally validated. Obtained results are summarized as followings.

(1) Based on the result of gait motion analysis of able-bodied subject, two different gait styles called swing-to and dragging gait were proposed. Range of step length to be achieved by those two gaits was also determined.
(2) In order to achieve each gait safely, essential condition was determined based on the dynamical analysis. Based on the obtained equations and numerical calculation, determination scheme of actuator input trajectory was established.
(3) The proposed scheme was experimentally validated by using a prototype apparatus. Effectiveness of the proposed scheme was proofed since desired step length in between 0.1 and 0.45 m was well agreed with obtained results.

References

1. Ministry of Health, Factual investigation of physically handicapped children and person in the year 2011, 2013 (In Japanese)
2. Lee S, Sankai Y (2002) Power assist control for walking aid with HAL-3 based on EMG and impedance adjustment around knee joint. In: Proceedings of the 2002 IEEE/RSJ international conference on intelligent robots and systems, pp 1499–1504

3. Kazerooni H et al (2005) On the control of the Berkeley Lower Extremity Exoskeleton (BLEEX). In: Proceedings of the 2005 IEEE international conference on robotics and automation (ICRA2005), pp 4353–4360
4. Farris RJ, Quintero HA, Goldfarb M (2011) Preliminary evaluation of a powered lower limb orthosis to aid walking in paraplegic individuals. IEEE Trans Neural Syst Rehabil Eng 19 (6):652–659
5. Swift TA (2011) Control and trajectory generation of a wearable mobility exoskeleton for spinal cord injury patients. UC Berkeley Electronic Theses and Dissertations
6. Sugahara Y, Ohta A, Hashimoto K, Sunazuka H, Kawase M, Tanaka C, Lim H, Takanishi A (2005) Walking up and down stairs carrying a human by a biped locomotor with parallel mechanism. In: Proceedings of international conference on intelligent robots and systems, 2005 (IROS 2005), pp 1489–1494
7. Yusa H, Tanaka E, Ikehara T, Ito K, Saegusa S, Hashimoto K, Sato Y, Yuge L (2010) Development of a walking assistance apparatus using a spatial parallel link mechanism and evaluation of muscle activity. In: Proceedings of 19th international symposium in robot and human interactive communication (RO-MAN2010), pp 151–158
8. Castelli G, Ottaviano E (2010) Modelling, simulation and testing of a reconfigurable cable-based parallel manipulator as motion aiding system. Appl Bion Biomech 7(4):253–268
9. Matsuura D, Funato R, Ogata M, Higuchi M, Takeda Y Efficiency improvement of walking assist machine using crutches based on gait-feasible region analysis. Mechanism Mach Theor 1–8. doi:10.1016/j.mechmachtheory.2014.02.011

On Developing Lightweight Robot-Arm of Anthropomorphic Characteristics

A. Rodić, B. Miloradović, S. Popić and Đ. Urukalo

Abstract Design of mechanical structure of the lightweight robot arm with anthropomorphic characteristics is considered in the paper with aim to achieve system performances and appearance closer to the physical properties and capabilities of human limb. In this goal, design solutions of contemporary lightweight robot arms are analyzed. New mechanical structure of robot arm is proposed in this study. The solution proposed takes into account the important biological aspects (structural as well physiological) to a greater extent than the existing constructive solutions. Main objective of the research regards to development of a bi-manual service robotic system of anthropomorphic characteristics. Tendon-driven, biologically-inspired, over-actuated 7 DOFs redundant robotic arm is presented in the paper. Compliant structure of robot arm is needed and enables safe and reliable human-robot interaction. Compliance in the system was achieved by introducing additional passive elastic and damping elements and by means of intelligent control that changes system impedance in a way inspired by human body. Corresponding control-block scheme and CAD-model of the robot-arm mechanical structure are presented in the paper. Simulation results of robot-arm model are presented, too, with aim to validate the concept and technical feasibility.

Keywords Bio-inspired anthropomimetic system · Lightweight robot-arm · Over-actuated system · Tendon-driven joint · Spherical joint

A. Rodić (✉) · B. Miloradović · S. Popić · Đ. Urukalo
Mihailo Pupin Institute, University of Belgrade, Belgrade, Serbia
e-mail: aleaksandar.rodic@pupin.rs

B. Miloradović
e-mail: branko.miloradovic@pupin.rs

S. Popić
e-mail: svemir.popic@pupin.rs

Đ. Urukalo
e-mail: djordje.urukalo@pupin.rs

H. Bleuler et al. (eds.), *New Trends in Medical and Service Robots*,
Mechanisms and Machine Science 38, DOI 10.1007/978-3-319-23832-6_4

1 Introduction

Human arm is one of the most sophisticated biological limbs known in the nature, capable to accomplish majority different and delicate sensory-motor tasks such as for example, lifting and carrying on payload, dexterous manipulation, symbolic gesticulation up to a fine sensitivity and tactile perception, pressure feeling, texture, temperature, moisture, sensing fluid stream, etc. A human arm with multi-finger hand has an exceptional dexterity and physical capabilities by virtue of its own naturally adjusted structure of the musculoskeletal system, sensitive perceptive system and fast and reactive nervous system whose peripheral terminations reach up the every segment of the limb [1].

Human body represents an exceptionally over actuated system that has much more muscles ($\sim$640) [2] than number of mechanical degrees of freedom ($\sim$256). The reasons for that are numerous. Primarily, humans for their motion utilize synergy of large number of muscles to perform motion. Muscles act by complementing each-other. In the case of fatigue or muscle injury the rest of complementing muscles take over the payload and biological system continues to operate with more effort even in difficult (non-regular) conditions. When a large number of complementing muscles work they distribute payload amongst them in a selective way and save energy consequently [3]. In the case of a small payload implemented on the limb it is not necessary all muscles to be activated in the same time and by full capacity. If it is necessary however, the muscles use their synergy to resist payload. This principle taken from the nature was utilized in the paper to design a lightweight robot arm of anthropomorphic structure. In this goal, the term "anthropomorphism" or "degree of anthropomorphism" is introduced as one of the criteria to be used in the process of design [20]. The term anthropomorphism used in the paper describes the property of a system that is a measure of the degree how the technical system applies biological methods and principles for its' operation as well as how it looks like the biological system as referent model.

The objective of the research presented in this paper regards to design of a conceptually novel mechanical structure of the lightweight robot arm even at the cost of some degradation of technical performances in order to achieve system of more anthropomorphic properties. The evolution process took thousands of years during which the human body underwent significant changes in accordance with the conditions and way of life. Human arm has a structure consisting of the upper arm and two forearm bones and large number of muscles as presented in Fig. 1.

2 State of the Art

Industrial robots (manipulators) are devices with rigid structure and high precision designed to carry out the tasks of accurate and repeatable end-effector positioning [4–7]. Contemporary service robots are made with *lightweight robotic-arms* (LWR

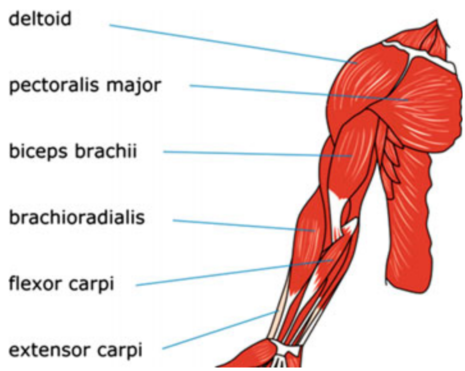

Fig. 1 Anatomy of human arm—the muscular system

or LWA) and robot hands integrated with aim to adapt the overall structure similar to human limb. Characteristics of such robotic structures are: decreased weight in comparison to the industrial LWR, payload capacity corresponds to human arm physical capabilities, compliant structure made according to the biological models, improved energy efficiency, etc. Industrial lightweight robot arms rely to the contemporary technology—miniature actuators with maximal capacity i.e. performance, embedded electronics, structure made of light and durable composite materials, built in harmonic-drives to improve accuracy, integrated mechanics and electronics [8], etc. In spite of that, the overall mass of the lightweight robots is still higher than human arms. Also the payload fraction (coefficient that quantifies robot weight and payload ratio [9]) overcomes those of human arms. Due to these facts, energy consumptions are still high because of inappropriately used actuators. This paper represents attempt to make next step towards new concept of design lightweight robot arms.

2.1 Industrial Lightweight Robot-Arms

When speak about LWRs we usually talk about two types of mechanisms. They can be categorized in lightweight manipulation systems for industrial purposes and service LWR systems which are usually made in a form of dual arm manipulation systems. The first type of LWR is mainly intended for industrial applications which demand high accuracy and repeatability (up to ±0.1 mm), payload (up to 10 kg) and composite speed of 3–5 m/s. These systems commonly have high stiffness (rigidity) and body weight (15–35 kg) and also require protected work areas in order to prevent collision with physical environment. These manipulators have stiff joints without compliance. World famous LWR manipulation systems are: KUKA KR Agilus 6 R700 [10], Shunk LWA Powerball [11], Mitsubishi LWAPA10 [12], Yaskawa-Motoman SIA5F [13], Denso VS-6577G-B [14], Barett robotic arm [15] etc. Exception in this case gives new outstanding KUKA LBR iiwa 7R800 [16] lightweight robotic arm, which satisfies the most rigorous technical criteria and also has soft joints which enables human robot interaction in the workspace of the robot.

2.2 Bi-Manual Robotic Systems

Parallel with permanent progress in development of LWRs dedicated to industrial purposes, intensive work on design bi-manual i.e. dual-arm manipulation systems for humanoids and service robots was accomplished in the recent years. Two technologically very advance realizations can be mentioned here: (i) the FRIDA dual arm system [11], and the Hizook Meka robot [17] developed at the MIT presented in Fig. 2a, b.

The concept robot FRIDA (Fig. 2a) was created in response to requests from ABB Robotics' [18] existing customer base to develop robotic solutions for manufacturing environments in which humans and robots would be able to work together. In addition, the robot is compact and intended to fit into spaces ergonomically designed for human workers.

The Meka A2 Compliant Manipulator is a lightweight seven degree-of-freedom force controlled arm. Engineered for compactness, safety, and reliability, the A2 system feature high-strength force controlled actuators, intrinsic physical compliance, zero-backlash Harmonic Drive gearheads, and the Meka M3 real-time manipulation control system. Each joint of the A2 manipulator utilizes a Series Elastic Actuator [19] where a spring is placed between the motor and the joint. It also makes the arm "intrinsically safe" for human-robot interaction.

Despite the undeniable progress in the design of the LWAs, the anthropomorphism degree as an important design indicator [20], is sacrificed and is still far away from the biological system. Anthropomorphic robot-arm ensures the following advantages with respect to the conventional industrial lightweight robot-arms:

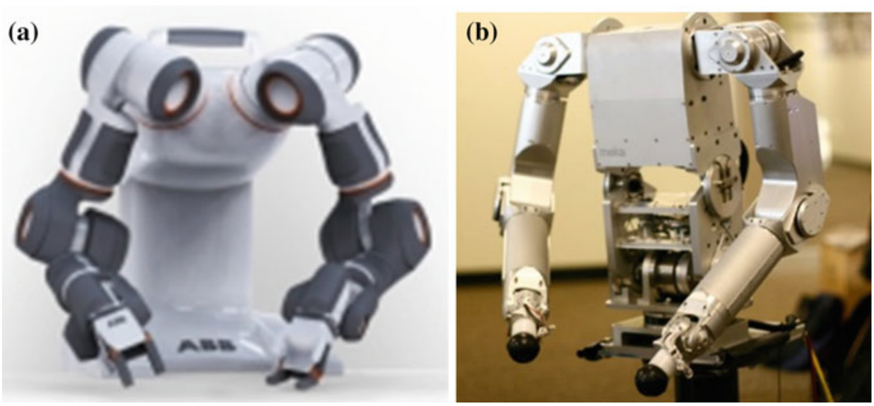

Fig. 2 **a** Concept dual-arm robot FRIDA; **b** the Meka A2 compliant manipulator with 7-DOFs

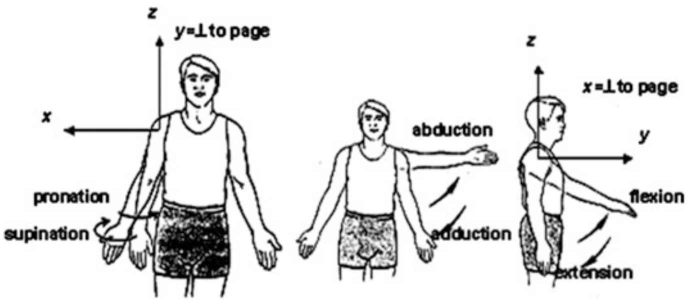

Fig. 3 Basic arm movements articulated by different groups of arm muscles

(i) appearance and functionality better fit model of the biological limb, (ii) better social acceptability in tasks of direct interaction with humans, (iii) energy saving, (iv) better ergonomic performances, etc. The main features of an anthropomorphic robot-arm are: (i) redundant kinematical structure with 7 degrees of freedom (DOFs), (ii) spherical shoulder joint applied instead three cylindrical sequentially arranged joints, (iii) poly-articular activation characteristic for over actuated systems, (iv) implementation of linear actuators as imitation of natural muscles, (v) utilization synergy of complementing actuators, (vi) light mechanical structure converging to the human arm weight, (vii) payload fraction (weight-payload ratio) close to value 1:1 that is characteristic to humans. The basic arm movements, expected from the new anthropomorphic robot arm to be performed in a human-like manner (skill), are: adduction/abduction, flexion and extension, pronation and supination as well as interior and exterior rotation (Fig. 3).

3 Concept and Design of Robot Arm

The novelties presented in the paper regard to robot design and especially searching for solutions how to decrease overall robot weight, increase payload fraction (the mass and payload ratio), introduce spherical (universal [21]) joint in the shoulder instead of corresponding cylindrical joints arranged in sequence [22], use of linear actuators (muscles-like) to move robot links, etc. By working on new robot design it was endeavored to keep trade-off between human manipulation accuracy, repeatability and speed from one side and degree of anthropomorphism from another side. Both features are very important for service robots. This criterion was achieved and explained in the text to follow.

If the principle of mono articulation (single joint—single actuator) is assumed for driving robot arm then powerful motors (which are of relatively large size and mass) need to be implemented in order to accomplish required operations. In the case when mono articulated robot has to cope with small payload then powerful actuators would be unnecessarily engaged, that causes energy wasting. In this case, we say that such a robot is unnecessarily oversized. As opposed to that case, the principle of poly-articulation (single joint—multiple actuators) ensures better use of power resources by introducing complementing motors in the system. This system is over actuated. Instead of single powerful motor a larger number of less powerful ones need to be utilized. While mono articulated systems have actuators commonly placed in the joints, the poly articulated [23] systems have actuators dislocated in the robot basis i.e. torso. The power transmission in this case is accomplished by non-tensile tendons. In such a way, the links' masses and moments of inertia are decreased and a lighter structure is obtained. Such mechanical structure ensures less energy consumption, saves actuators and prolongs the duty-cycle of device. Bearing in mind that the key objective of research in this paper regards to development of new robot design with high degree of similarity and functionality with biological model, it was set the following criteria to be fulfilled by design:

- Repeatability of robot-arm (1 mm),
- End-tip speed of robot-arm (3 m/s), and
- Payload in position of full abduction (3 kg).

Proposed mechanism of robotic arm represents a redundant kinematic structure with 7 DOFs which allows fine mobility in the operation space that corresponds to the human-arm range (Fig. 4). This robot mechanism is realized with 6 actuators for upper arm rotation in the shoulder joint, 4 actuators for rotation forearm in the elbow joint and 4 actuators for corresponding rotations in the wrist joint. Pronation and supination of the upper arm is enabled by one DC motor that rotates the entire spherical wrist with a "package" of five spindle drive actuators. The shoulder joint has appropriate amenability (compliance) realized by introducing passive elastic-damping elements (springs and dampers) into the structure (Fig. 5). They have a role to compensate gravitational torques and to allow proper compliance of the wrist when overloaded. These elements represent simple imitation of muscles in the system. At the same time, these elements act as antagonists that tend to make a recurrent movement of the wrist in flexion/tension and abduction/adduction. Abduction and adduction movements are achieved by activating corresponding pairs of spindle-drive actuators, where two motors are employed for abduction and

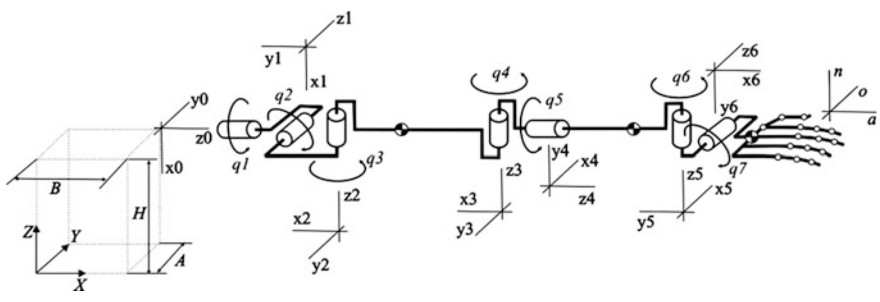

Fig. 4 Kinematic scheme of the robotic arm

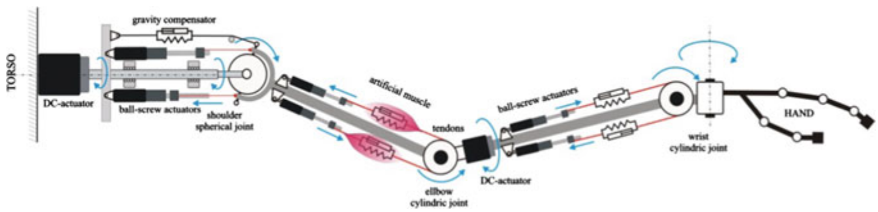

Fig. 5 High-level system description—principle of actuation, compliant elements, spherical joint in the shoulder

one (with the interplay of artificial muscle, Fig. 5) for adduction arm. Regarding to flexion and extension of arm movement, there are similarities with the previous case. In this paper it was assumed the same two types of linear spindle-drives, one for bending and one for elongation. Also, implementation of twist-actuators [24] is under consideration instead of spindle-drives or ball-screw actuators due to their fast response, compact dimension and power features.

In the elbow joint, the forearm pronation/supination and flexion/extension are possible. Pronation and supination are provided with a rotary DC motor, while bending and straightening is enabled by assistance of the pair of linear actuators: 2 motors for flexion and 1 motor for extension. In the robot forearm, the micro actuators with ball screw were arranged radially. The number of motors corresponds to the number of DOFs of the hand plus 2 motors introduced for flexion/extension and abduction/adduction of robot hand in the wrist joint. Motor types and their performances are determined by simulation of the hand model. The principle of actuation is simplistically depicted in a 2D diagram in Fig. 5. The CAD model of the proposed mechanical design is presented in Figs. 6 and 7.

Fig. 6 CAD model of the 7DOFs lightweight anthropomorphic arm with 20 DOFs bionic hand [25] integrated into the overall mechanical structure

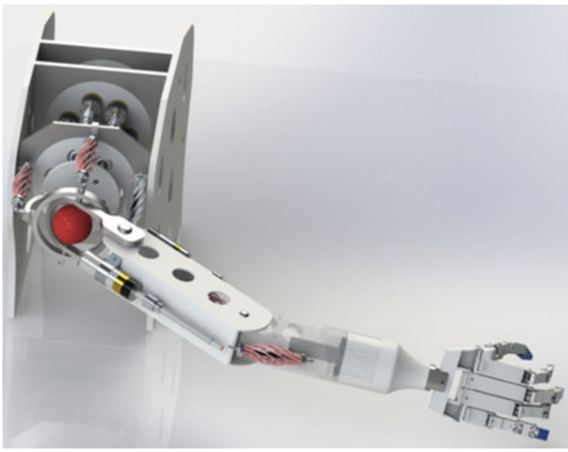

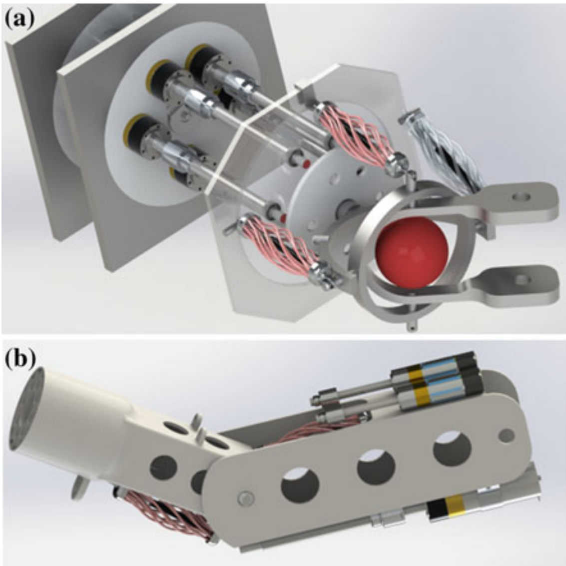

Fig. 7 Details of robot arm: **a** actuation of the spherical shoulder joint; **b** upper arm and forearm of robot mechanism

4 Control of Robot Arm

Control of over actuated, tendon-driven, 7 DOFs redundant, compliant robot arm with 20 DOFs multi-finger robotic hand [25] is a delicate task due to the system complexity and different requirements. Generally speaking, the arm with the hand represents together a coupled dynamical system. Robot arm has the role to take over the main load as well as to "carry on" the hand in the workspace. Robot hand is expected to ensure necessary precision (position and orientation) and desired contact forces and torques at the end-tip. Joints' rotations of robot arm are achieved by use of multiple linear actuators. The Faulhaber spindle drive linear motors of types BS22-1-5_DFF, 2232_BX4_CxD_DFF, 3268_BX4_DFF, BS32-2-0_DFF are chosen for power-driving. The advantage of the proposed over-actuated structure (Fig. 5) is:

- The payload of robot mechanism is distributed upon multiple actuators resulting in decreasing load (torque) per single actuator;
- In the case of failure of single motor, its' complementing one takes over the effort. The consequence is that robot task is accomplished even in conditions of performance degradation (low performance);
- Energy savings in actuators are achieved. Instead of single powerful motor, multiple powerful motors are utilized. In such a way, some of particular actuator can be switched off (disabled) without losing minimum of functionality.

Tension forces are transmitted from the linear actuators to the robot links by non-tensile tendons allowing rotations in the corresponding joints. In the

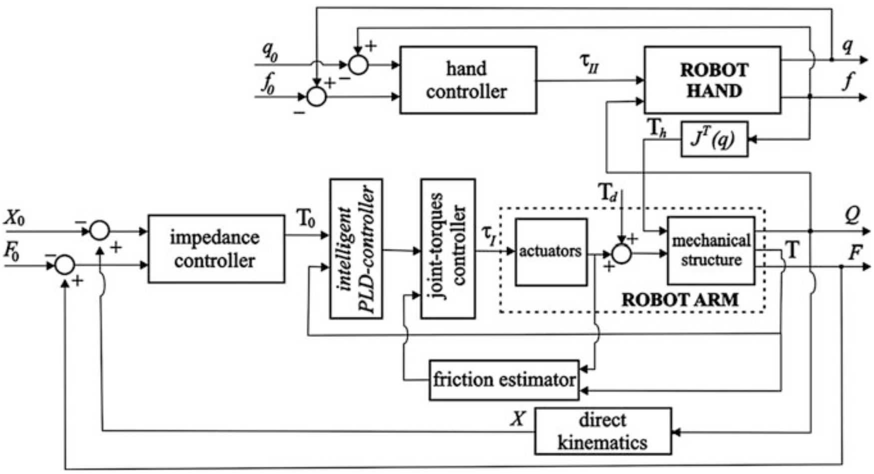

Fig. 8 Control-scheme of the robot arm with multi-finger hand

mechanical structure of robot-arm, there are certain elastic and damping elements included in the system [26], too. They give robot desired compliance. The compliance parameters are determined by simulation of robot model. In the same time, tendon introduces certain friction in the system. That additionally complicates the control task.

Elastic elements in the system are also used for straining tendons and preventing them of relaxation. That can cause potential delaying in the system. On the other hand, the passive pneumatic damper reduces or eliminates oscillations in the system due to presence of elasticity in the mechanical structure. The control block diagram of the robot arm with the multi-finger hand is shown in Fig. 8. It consists of robot arm controller and corresponding hand controller. They operate complementary each other. The controller has outer and inner loop (Fig. 8). In the outer loop, the impedance controller is used while the internal loop is in charge to control torques in robot joints. The entire control system is designed to operate in a "compliant" or in "stiff mode" depending on task type. Hand controller has two feedback loops: (i) position/velocity feedback loop in the joint coordinate space q and contact force feedback in the hand. The hand controller generates control torques τ_{II} in finger joints of the hand and corresponding tendon forces that rotate wrist. The *sliding mode control algorithm* is implemented within the hand controller.

Controller of the robot arm consists of the impedance controller and intelligent torque controller. Impedance controller includes two feedbacks: position/velocity feedback and force/torque feedback of the hand. Impedance controller calculates the control torques T_0 in the joints of hand that provide desired movement and desired impedance. Since the system is over-actuated, intelligent torque controller has to make appropriate distribution of control loads upon actuators that strengthen entire system.

Since the 7 DOFs robot mechanism has multiple actuators (over-actuated system), the intelligent controller determines load distribution in order to save energy and minimizes load of the actuators. The algorithm takes into account experimental experience with human muscles as well load distribution acquired from biological organism. The output variables from the torque controller are reference torques τ_I in the particular servo-actuators of the system. The joint torque controller uses torque feedbacks T from particular joints of hand. According to Fig. 8, the system states include joint coordinates of robot arm Q and contact forces F reduced to the center of mass of the hand.

The robot (arm and hand) dynamics is coupled. It is presented in the scheme (Fig. 8) by dashed lines. Torques of the hand are reduced to the center of mass and presented by the vector T_h. The intelligent torque controller takes into account the disturbance torques T_d. At the output, the joint torques controller generates new control signal τ_I that is result of compromises between desired movement and disturbance generated due to collisions with the environment.

5 Case Study

With aim to design optimal mechanical structure of robot arm (in sense to obtain a bio-mimetic structure of the mechanism), appropriate modeling and simulation of the 7DOFs over actuated LWR with appropriate linear actuators (as electro-mechanical model of biological muscle) and complementary elasto-damping elements in the mechanical structure was accomplished (see Figs. 4 and 5). Two characteristic cases were considered and simulated in the paper in order to determine joint torques and to identify actuator parameters. The first case study, regards to a typical abduction maneuver of the arm in the frontal plane (Fig. 3) with the maximal composite speed of 3 m/s. This arm movement is one of the most demanding manipulation maneuvers except the maneuver of carrying on payload being it requires fast movement in the field of gravity. The results of simulation of robot-arm dynamic model are given in the Figs. 9, 10, 11, 12 and 13. The end-tip trajectory of robot-arm is presented in Fig. 9. Corresponding composite speed and acceleration are given in Fig. 10. By simulating of robot-arm dynamic model, corresponding joint torques are calculated taking into account inertial effects, centrifugal and gravitational forces, friction in the system due to the tendon slipping over the small conductors added to the mechanical structure. The maximal torque regards to abduction of the arm in the shoulder joint. The graph of the abduction torque in the shoulder joint is presented in Fig. 11.

The joint torques about other axes are of less amplitudes than the abduction torque. Based on the calculated joint torques the tendon forces in the particular linear motors are determined. Consequently, maximal actuator force applied for shoulder abduction and adduction is approximately 200 N, actuator speed 0.10 m/s (Fig. 12) and motor stroke of 0.06 m (Fig. 13). The Faulhaber ball-screw actuators assumed from the producer’s catalogue fit well these system requirements.

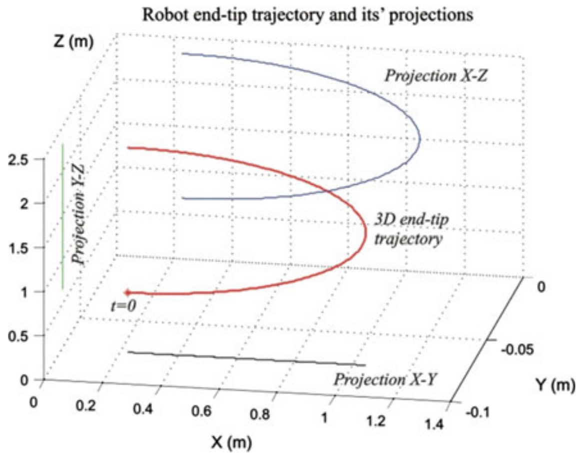

Fig. 9 End-tip trajectory for arm abduction in the frontal plane

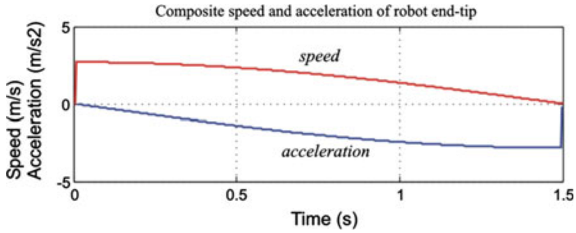

Fig. 10 Composite speed and acceleration of the robot-arm end-tip

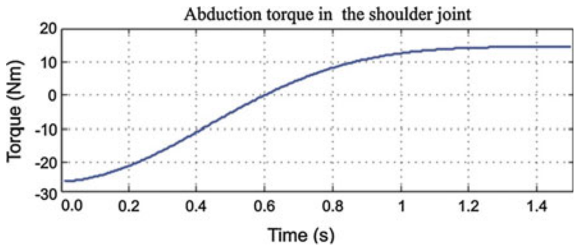

Fig. 11 Abduction torque in the shoulder joint (fast abduction)

The second case study regards to a slow payload carrying on to be done in the frontal plane that corresponds to an arm abduction maneuver (Fig. 14). The mass of 3 kg is carried on by robot arm. Corresponding joint torques are calculated from the dynamic model. Maximal torque in the shoulder joint is presented in Fig. 15. The

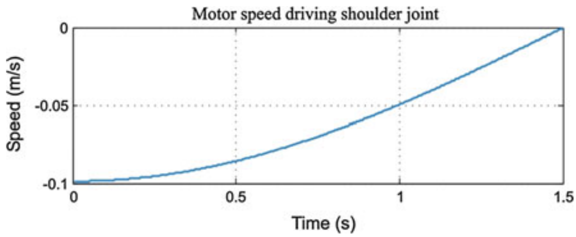

Fig. 12 Motor speed determined for the fast arm abduction in the shoulder joint

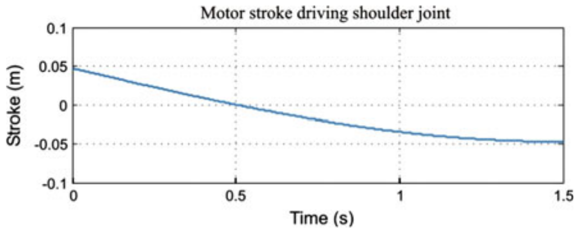

Fig. 13 Motor stroke calculated for the fast arm abduction in the shoulder joint

Fig. 14 Robot-arm end-tip trajectory for the case of carrying on payload in the frontal plane

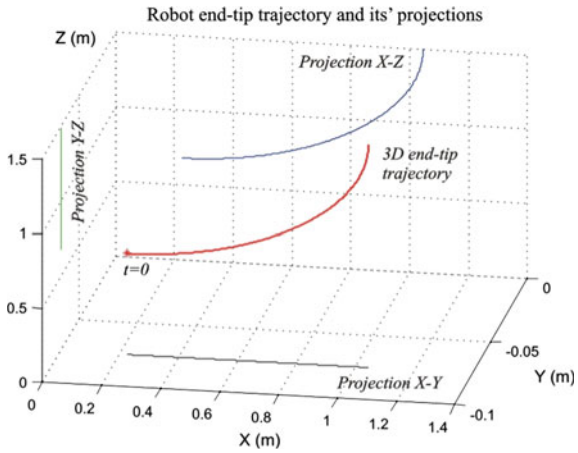

obtained torque in the shoulder joint does not overcome the abduction torque presented in Fig. 11. That assumes the assumed linear actuators satisfy both critical maneuvers—fast abduction as well payload carrying on in the same plane.

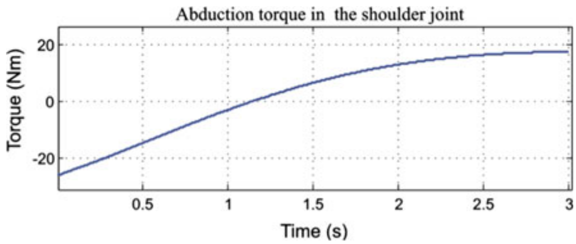

Fig. 15 Abduction torque in the shoulder joint for the payload of 3 kg brought into the position of the fully abducted robot-arm

6 Conclusion

Novel bio-inspired mechanical structure and intelligent control scheme of the lightweight robot arm with anthropomorphic characteristics was proposed in the paper. The designed bio-mimetic robot-arm satisfies criteria of anthropomorphism imposed in advance to achieve functionality and physical properties of human arm. The following conclusions can be derived: (i) There is no better design of artificial arm made by engineers than the nature has created through the evolution; (ii) Robot arm to be designed in the paper should not be required to achieve better accuracy than the human arm (up to 1.5 mm); (iii) Robot hand ensures high accuracy of the system (0.1 mm) but not the arm; (iv) Over actuated LWR with poly-articulated joints (shoulder, elbow, wrist) has significant advantage over the conventional mono-articulated systems; (v) Compliant structure is inevitable design concept of LWR to achieve anthropomorphic features; (vi) Mechanical structure with special spherical joint in the shoulder decreases the overall mass of the system but increase kinematical complexity; (vii) Over actuated structure of LWR saves energy due to the inherent capability of planning the payload distribution per actuators.

Acknowledgments Research in the paper was funded by the Serbian Ministry of Education, Science and Technology Development under the grants TR-35003 and III-44008. It is partially supported by the SNSF IP project IZ74Z0_137361/1 as well by Serbia-China bilateral project under the grant 451-03-02338/2012-14/12.

References

1. Siciliano B, Khatib O (eds) (2008) Springer handbook of robotics. Springer, Berlin. ISBN 978-3-540-23957-4
2. List of muscles of human body. http://en.wikipedia.org/wiki/List_of_muscles_of_the_human_body. Accessed Jan 2015
3. Muscle. http://en.wikipedia.org/wiki/Muscle. Accessed Jan 2015
4. Bischoff R, Kurth1 J, Schreiber G, Koeppe R, Albu-Schäffer A, Beyer A, Eiberger O, Haddadin S, Stemmer A, Grunwald2 G, Hirzinger G (2010) The KUKA-DLR lightweight robot arm: a new reference platform for robotics research and manufacturing. In: Robotics

(ISR), 2010 41st international symposium on and 2010 6th German conference on robotics (ROBOTIK)
5. Hirzinger G, Brunner B, Landzettel K, Sporer N, Butterfaß J, Schedl M (2003) Space robotics —DLR's telerobotic concepts, lightweight arms and articulated hands. Auton Robots 14(2–3):127–145
6. Ott Ch, Eiberger O, Friedl W, B¨auml B, Hillenbrand U, Borst Ch, Albu-Schaffer A, Brunner B, Hirschmuller H, Kielhofer S, Konietschke R, Suppa M, Wimb¨ock T, Zacharias F, Hirzinger G (2006) A humanoid two-arm system for dexterous manipulation. In: IEEE-RAS international conference on humanoid robots
7. Butterfaß J, Grebenstein M, Liu H, Hirzinger G (2001) DLR-Hand II: next generation of a dextrous robot hand. In: IEEE international conference on robotics and automation, pp 109–114
8. Hirzinger G, Albu-Schaeffer A (2015) Light-weight robots. http://www.scholarpedia.org/article/Light-weight_robots. Accessed Jan 2015
9. Payload fraction. http://en.wikipedia.org/wiki/Payload_fraction. Accessed Jan 2015
10. KUKA-robot. http://www.kuka-robotics.com/res/sps/e6c77545-903049b193f54d17c92173aa_Spez_KR_AGILUS_sixx_en.pdf. Accessed Jan 2015
11. DENSO-robot. http://www.densorobotics-europe.com/en/product/vs-6577g-b. Accessed Jan 2015
12. https://www.mhi.co.jp/technology/review/pdf/e405/e405298.pdf. Accessed Jan 2015
13. http://www.motoman.com/datasheets/SIA5F.pdf. Accessed Jan 2015
14. KUKA LBR iiwa 7R800 www.kuka-labs.com/en/pressevents/news/201304_LBR_iiwa_world_premiere.htm. Accessed Jan 2015
15. http://www.barrett.com/robot/products-arm.htm. Accessed Jan 2015
16. On line. http://www.schunk.com/schunk_files/attachments/LWA_datasheet_2012-03__EN.pdf
17. Meka Robotics' Humanoid Torso and Anthropomorphic Hands, Meka Robotics A2 Compliant Manipulator. http://www.hizook.com/blog/2009/10/18/meka-robotics-humanoid-torso-and-anthropomorphic-hands. Accessed Jan 2015
18. http://www.abb.com/cawp/abbzh254/8657f5e05ede6ac5c1257861002c8ed2.aspx. Accessed Jan 2015
19. Pratt Jerry, Krupp Ben, Morse Chris (2002) Series elastic actuators for high fidelity force control. Ind Robot J 29(3):234–241
20. Anthropomoprhism. http://www.newworldencyclopedia.org/entry/Anthro-pomorphism. Accessed Jan 2015
21. Universal joint. http://en.wikipedia.org/wiki/Universal_joint. Accessed Jan 2015
22. Serial manipulator. http://en.wikipedia.org/wiki/Serial_manipulator. Accessed Jan 2015
23. Dumitru V, Dumitru S (2011) Computer-aided modeling for a poly articulated robotic arm with spherical joints. In: Proceedings of the world congress on engineering, vol III WCE 2011, July 6–8, 2011, London, UK
24. Popov D, Gapanov I, Ryu JH (2013) Bidirectional elbow exoskeleton based on twisted-string actuators. In: Proceedings of 2013 IEEE/RSJ international conference on intelligent robots and systems (IROS), November 3–7, 2013, Tokyo, Japan, pp 5853–5858
25. Rodić A, Miloradović B, Popić S, Spasojević S, Karan B (2013) Development of modular compliant anthropomorphic robot hand. In: Pisla D, Bleuler H, Rodic A, Vaida C, Pisla A (eds) New trends in medical and service robots. theory and integrated applications, series: mechanisms and machine science. Springer Publishing House, vol 16, VIII, 238 p 167. ISBN 978-3-319-01591-0
26. Williamson P, Pratt D, Wright U (1995) Stiffness isn't everything proceedings of ISER '95, Stanford

Towards a Natural Interface for the Control of a Whole Arm Prosthesis

G. Gini, P. Belluco, F. Mutti, D. Rivela and A. Scannella

Abstract In the present study we illustrate a new concept for a user interface to control whole arm prosthesis. We extend the myo-electric control, taking into account the intended movement of the shoulder and integrating vision analysis to give a "visual control" to the user. While the control of the shoulder is partially obtained from pattern recognition of sEMG signals, the control of the elbow and wrist joints is only derived using the trajectory computed from the initial to the target position. We show results in simulation and discuss about future steps in developing the prosthesis.

Keywords Prosthesis control · sEMG signals · Classifiers · Kinect · User interface

1 Introduction

The interface between the patient and the prosthesis is critical to the success of the device. This is even truer for upper limbs prosthesis that can accomplish a large variety of tasks [5, 8, 16].

G. Gini (✉) · F. Mutti · D. Rivela · A. Scannella
DEIB, Politecnico di Milano, Milan, Italy
e-mail: giuseppina.gini@polimi.it

F. Mutti
e-mail: f.mutti@b10nix.com

D. Rivela
e-mail: diletta.rivela@mail.polimi.it

A. Scannella
e-mail: alessia.scannella@mail.polimi.it

P. Belluco
BIONIX, Milan, Italy
e-mail: p.belluco@b10nix.com

H. Bleuler et al. (eds.), *New Trends in Medical and Service Robots*,
Mechanisms and Machine Science 38, DOI 10.1007/978-3-319-23832-6_5

Today prosthetic solutions include aesthetical, functional passive, and actuated ones. While the first kind cannot make movements but only adapt to external forces, the functional ones offer a limited mobility that requires using other parts of the body to exert forces to actuate each dof. The fully actuated prostheses encounter both technical problems, due to the need of capturing the user intention, and psychological problems, due to the acceptability of the prosthesis. Often the user generates the command signal with myoelectric control [19, 25], but this method today applies only to a few dof. In the worst situation, a patient with an inter-scapular-thoracic amputation has lost all the seven degrees of freedom of the arm, and usually can control only elbow and wrist flexion, and hand closing [18]. Even though the controller requires extensive input from the user who usually moves one joint at a time and needs a long training time.

As reported in [4] up to now the most effective driving signals acquired from the patients have been based on the head motion. For instance the target to be reached by the hand is maintained on the axis, fixed to the head, perpendicular to the line connecting the eyes, while another head lateral movement drives the distance from the target to the face. A device including accelerometers and gyroscopes, positioned on the head, detects the head motion. This solution can be integrated with voice-activated movements.

We need to mention that, to deal with cognitive burden and user acceptance, an invasive surgical technique was conceived, called targeted muscle reinnervation (TMR) [15]; a residual muscle is enervated and then reinnervated with residual nerves of the amputated limb. After nerve growing, the EMG signals of the targeted muscle can be used to control a prosthetic device. However, classifying shoulder movements in TMR has generally been ignored to date.

Our goal here is to show a novel interface for the user of total upper limb prosthesis. It extends the EMG classification control to include other signals from the user. First we had to approach the novel task of classifying shoulder movements from sEMG signal, then to develop a vision system to find the target position. We are considering in particular grasping activities, the ones that are of primary importance for every day life.

In the past we developed control strategies for hand prosthesis [8, 17] and verified the real time performance of the EMG classifier [9]. In the present study we illustrate this new concept for a user interface in total upper limb prosthesis that extends the myo-electric control integrating vision analysis and trajectory computation: the sEMG signals indicate the shoulder movement to start, the visual analysis computes the target location on the object the user is locking at, and finally the trajectory to the grasping point is computed.

The paper is so organized. Section 2 presents an overview of the interface MyArm system (Fig. 1) we designed. Sections 3–5 give more details about the sub-modules that cooperate to obtain the controller. Section 6 summarizes the results and proposes possible future developments.

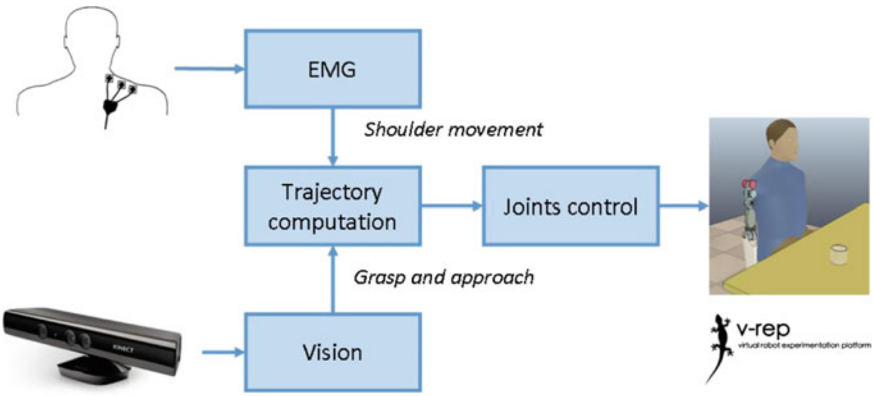

Fig. 1 The modules of MyArm: EMG, vision, trajectory generation and control

2 Design Principles of MyArm

The control system "MyArm" integrates different modules as in Fig. 1. Three modules give input to the joint controller: EMG classification, vision, and trajectory computation. The EMG module in MyArm adopts the pattern recognition-based control, in Fig. 2, that involves computing the subsequent stages here briefly described.

1. *Data segmentation* Each channel has to be segmented into a series of time windows, adjacent or overlapped. The window length has to satisfy real-time constraints that require the actuation delay must not be greater than 300. Smith [26] suggested that the optimum window length is between 150 and 250 ms; Phinyomark [20] highlighted that the best result in term of robustness is obtained with a length of 500 ms and an increment of 125 ms. The processing of myoelectric signals can be done including transients (i.e. at the contraction

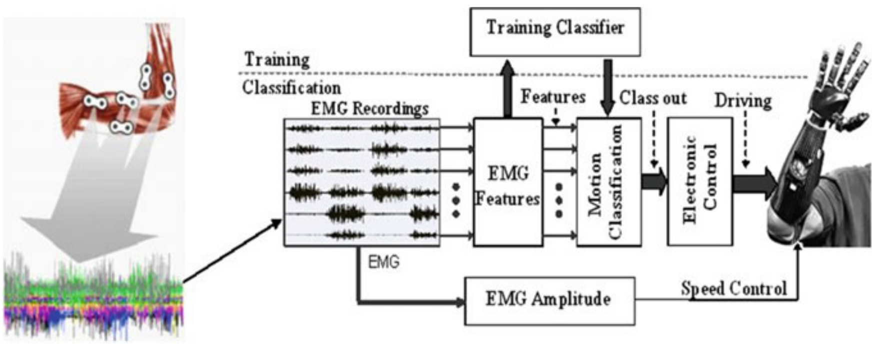

Fig. 2 The myoelectric based controller

onset) or at steady states only (i.e. during maintained contraction); Englehart [7] showed that steady state data are classified more accurately than transient data.

2. *Feature representation* This phase involves two stages: feature extraction and feature reduction. Generally, features belong to three main domains: time, frequency, and time-frequency [13]. The second stage is employed to reduce the dimensionality of the initial feature space, attempting to preserve the classification accuracy, while reducing the computational costs of the classifier [14]. Dimensionality reduction strategies may be either feature selection or feature projection, where a new feature subset is created combining the original features through a linear or non-linear mapping. Previous studies have shown that the projection approach leads to a higher discrimination ability compared to feature selection [12].
3. *Classification* The classifier receives as input the reduced feature set and it has to match the different patterns with the correct movement class [6].

Considering again Fig. 1, the vision system has to detect the object and compute the grasping point. It has to look at the scene, recognize the object the user is looking at, and compute the approach position to grasp it. The first choice was the hardware: given the fundamental need for a depth map, the only options were a stereo camera or a device for measuring the distance of every point. In 2010, Microsoft released an inexpensive sensor for the Xbox 360 gaming console, called Kinect, able to generate a point cloud combining a RGB camera and two IR depth sensors (using structured light scanning). Later on, PrimeSense introduced open source drivers, allowing new developers to use it for non-gaming contexts. In light of this, the Microsoft Kinect [11] was adopted. Moreover, several libraries concerning image analysis and 3D point clouds exist: while OpenCV is more based on two dimensional images, a novel open source project named Point Cloud Library (PCL) suited best our case. PCL is written in C++ and released under the BSD license. Thus, with little alterations, various algorithms needed for our goal were available in it. Our vision system makes use of the acquired points cloud, without the need of image analysis. After training on a number of objects, the system is able to compute the approach point to grasp objects [21, 24] of similar geometry and functionality.

After those points a trajectory for elbow and wrist can be computed and sent to the motor control. It is foreseen that a miniaturised kinect device will be mounted on special glasses able to compute the focus of attention of the user when looking at the object to take.

The entire MyArm system has been developed in the V_REP[1] frame. This open source environment provides specific algorithms for trajectory planning and obstacle avoidance, and can send the output both to a graphic simulator window and to the real robot. This framework will be valuable also for training the patient in using the prosthesis.

---

[1]v-rep by Coppelia Robotics. http://www.coppeliarobotics.com.

3 The EMG Module

Aim of this study was to experimentally verify whether a pattern recognition approach could be useful to classify a quite large number of shoulder movements. To this purpose we have implemented a number of classification algorithms and have compared the discrimination capabilities of different feature extraction methods. Then we have checked the possibility to reduce the number of muscles to be analyzed without losing classification accuracy.

In the last decades, the myoelectric prostheses control underwent a significant improvement after the introduction of sEMG pattern recognition strategies [13]. The pattern recognition control approach is founded on the assumption that patterns of sEMG signals from several muscles include information about the intentional movement of the amputated limb. The aim of this method is to match each sEMG pattern to one motion class among a multiplicity of preselected movements. Then the chosen movement is automatically performed in a pre-programmed mode by the prosthetic device.

Our EMG classifier has to detect shoulder movements. Unlike the conventional myoelectric control, our method exploits the contraction of several synergistic muscles related to the movement the amputee wishes to perform, and does not require that a single degree of freedom is independently controlled. In this way, a more intuitive and rapid control can be obtained.

Since there is no literature about classification of shoulder movements, we devised an experiment to collect and analyze sEMG data to verify the viability of our classifier.

The experimental data were collected from eight healthy subjects (four males and four females) aged 25.0 ± 1.8 years, informed about the experimental procedures. They performed a series of eight shoulder movements, chosen among the most common, that were repeated ten times each. Every movement included four sequential phases: resting, elevation, isometric holding, and return to the rest condition. All the movements have been executed with the arm fully extended. The planes considered are the usual frontal and sagittal planes, and the vertical plane rotated of 45° from the sagittal plane, as in Fig. 3. The eight movements are defined starting from the orthostatic position—with parallel feet at 12 cm distance, arms along the body with palms inside:

Fig. 3 Two of the movements: shoulder abduction in the *frontal plane*, and *top view* of shoulder elevation in a plane rotated 45° from the *sagittal plane*

- 4 flex/extensions in the sagittal plane to 45°, 90°, 110°, and −30°;
- 2 ab/adductions in the frontal plane to 45° and 90°;
- 2 elevations in the rotated plane to 45° and 90°.

We focused on these movements because usual prosthetic solutions for shoulder disarticulation can reasonably control only 2 degrees of freedom. For this reason humeral internal/external rotation was not considered.

Eight pairs of electrodes were placed over the following trunk muscles: clavicular and sternal heads of the pectoralis major, serratus anterior, trapezius descendent, trapezius transversalis, trapezius ascendent, infraspinatus, and latissimus dorsi. These muscles are indeed synergistic in the analyzed movements and they are superficial muscles preserved also after upper limb amputation. SEMG data were recorded by bipolar disposable electrodes (26 mm in diameter) connected to miniaturized, wireless probes for digital data collection. Each pair of electrodes was placed according to the guidelines provided by [2] with an interelectrode distance of 26 mm. SEMG signals were recorded at a sampling rate of 1.0 kHz and processed in Matlab.

Data analysis considered the only steady state phase (isometric hold) that is about 3 s. Six signal segmentation settings were tested, by combining different window sizes (L) and increments (I): (a) $L = 500$ ms, $I = 250$ ms, (b) $L = 500$ ms, $I = 125$ ms, (c) $L = 500$ ms, $I = 62$ ms, (d) $L = 250$ ms, $I = 250$ ms, (e) $L = 250$ ms, $I = 125$ ms, and (f) $L = 250$ ms, $I = 62$ ms. After a random shuffling of all acquired trials from the 8 subjects, data were split 60 % into a training dataset, and 40 % in a test dataset. The training set was used to train the classifier; the test set was employed to estimate the classification accuracy.

For each of the six segmentations tested, different feature sets were extracted and reduced using principal component analysis (PCA) to produce a new feature set by a linear projection of the original feature vector onto the eingenvector of the covariance matrix.

Classification was performed using linear discriminant analysis (LDA). This classifier was chosen due to its high performance in EMG signal classification, low computational cost, ease of implementation, high speed training and robustness, as reported in [12].

The performance of the classification system was defined in terms of classification error and was evaluated by considering three different sets of motion classes.

1. Nine motions as described above;
2. Five motions: shoulder extensions in the sagittal plane to 90° and −30°, shoulder abduction at 90°, shoulder elevation at 90° along the rotated plane, and rest;
3. Four motion classes: as before after removing shoulder elevation.

The feature set that gave the best results is the one proposed in [20], and includes sample entropy (SampEn), cepstral coefficients (CC) of the 4th order, root mean square (RMS), and WL. Its results on the test set are in Table 1. This best performance was obtained with $L = 500$ ms, $I = 62$ ms.

Table 1 The classification error for 4, 5, 9 classes

	Error (%)
4 classes	0.00
5 classes	2.61
9 classes	7.74

Table 2 The classification accuracy using 6 or 8 acquisition channels

	4 classes (%)	5 classes (%)	9 classes (%)
6 channels	99.98	96.11	88.31
8 channels	100	97.39	92.56

After observing that the classifier has very good accuracy, we investigated the effect of reducing the number of sEMG channels. With 6 channels, a small degradation in accuracy [10] is illustrated in Table 2.

To make the classifier answer available with a reduced number of electrodes, we can observe that a 4 classes classifier with 6 acquisition channels has still a very high accuracy. Moreover, to reduce the initial delay, we can consider using $L = 250$ ms, $I = 62$ ms, that we have found to produce a classification accuracy of 99.11 % for 4 classes. For more data and more details please refer to [22, 23].

4 The Vision Module

Picking up an item using an autonomous robot is a challenging and fairly novel task. It has been studied from a psychological, biological and engineering focus, without reaching satisfying results. Therefore, the ultimate aim is to provide the user (or the application) with the most suitable grasping points for the given item(s). It uses a training method were objects are shown to the system.

For each object we intend to generate only two grasping points—related to the centre of mass of the given cloud. These points are two because most of the artificial hands act like a gripper. The whole system presents a modern approach to a task that was never completely solved, adopting some state of the art algorithms and an inexpensive, effective and brand new hardware device.

The scenario where the system was designed and tested is that items are placed on a surface and they are not moving. At the same time, the camera, attached to the user head, is almost static too, and it faces them. The training and testing stages are performed without changing the pose of the camera with respect to the plane. Lighting conditions do not affect the outcome at all. Our vision module is based on a classifier to recognize the kind of object to grasp based purely on data collected from Kinect.

The main steps in analysing Kinect data both in training and testing are five: generate the point cloud, remove the table points, compute the nearest neighbours, cluster the cloud, and compute the barycentre and the grasping points. All the steps make use of an efficient representation based on k-d trees [3], a space-partitioning data structure for organizing points in a k-dimensional space. The classifier we built makes wide use of this structure that allows search, insert, and delete operations to have on average O (n log n) time complexity.

1. *Generate the point cloud* A point cloud is a set of unorganized, irregular points in 3D. To generate point cloud from depth image captured by the Kinect one may convert from (u, v, d)—the first two coordinates are the x/y position, while d is the distance provided by the IR sensor—to the point cloud, which represents points using the standard (x, y, z) coordinates.
2. *Remove the table* In order to identify the main objects placed in front of the Kinect, we have to cluster the scene, under the assumption that there is a plane (i.e. a table) where the items are placed on. Thus this table has to be removed from the scene, using the RANSAC (RANdom SAmple Consensus) method [27].
3. *Find neighbours* 3D feature estimation methodologies are needed. In general, PCL uses approximate methods to compute the nearest neighbours of a query point, using fast k-d tree queries. Once determined, the neighbouring points of a query point can be used to estimate a local feature representation that captures the geometry of the underlying sampled surface around the query point.
4. *Clustering* If we assume that the planar structure has been removed, clustering the remaining items is a necessary step to separate the individual object point clusters lying on the plane. We used the k-nearest neighbour algorithm (k-NN) [1], a method for classifying objects based on closest training examples in the feature space. k-NN is a type of instance-based learning, where the function is only approximated locally and all computation is deferred until classification. An object is classified by a majority vote of its neighbours, with the object being assigned to the class most common amongst its k nearest neighbours (k is a positive integer). If k equals 1, then the object is simply assigned to the class of its nearest neighbour. The FLANN library[2] has been used for clustering.
5. *Compute the grasping position* The final task is to estimate two points where the hand could firmly grasp and hold the item. Since the prosthetic hand we expect to use is a simple gripper, the approach of [19] suits our case. It requires to compute the item's centroid, which is the intersection of all straight lines that divide the object into two parts; then to compute the two grasping points P1 and P2, as in Fig. 4. Since we require the object to be held firmly, the centre of mass must lie on the straight line that connects P1 with P2 and the first of the two is the closest boundary point to the centroid. Issues arise when dealing with P2: since it lies on the line connecting P1 with the barycentre, it isn't part of the cloud and it wasn't visible to the camera, therefore it has to be estimated. Since we know the type and the orientation of the object, we define a parameter p that means "how far" P2 is with respect to the other two points. For most of the objects, given their symmetries, p should be equal to 1; however, the Kinect

[2] http://www.cs.ubc.ca/research/flann/.

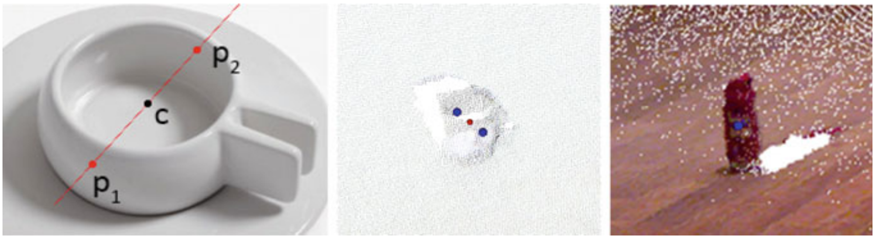

Fig. 4 Computing grasp in theory and on examples of the point cloud

usually sees a small portion of the object and the centroid is biased towards the visible points. As a consequence, P2 is a little farther than one would expect. In other cases such as when dealing with a cup, some points of its inner side are visible, therefore p = 1 works flawlessly.

The training phase consists of the following: place the object in front of the camera, compute its pose, rotate it and collect many poses, store in a k-d tree. All the computations are the same for either the training or the recognition phases. Given a set of training data, the nearest neighbour search returns a set of potential candidates with sorted distances to the query object. During testing we allow in the scene more than one object. Once they have been extracted as clusters, their nearest neighbours are computed. Lastly, the two grasping points are computed.

Classifiers have to be tested on a different test set to estimate the ability to generalize; we assess the goodness using accuracy [10]. An attempt to classify a new object placed in front of the Kinect can either yield a correct or a wrong prediction. The latter case can be subdivided into completely wrong classifications and those where the item was correctly identified, but not the pose.

A number of factors affect the outcome of the test, as the role of position and size of the objects, the number of items in the scene, possible overlapping, distance from the camera, number of different poses used in training, number of different items known to the system, and difference between the item used in training with the one used during testing. Consider that the Kinect sensor has a practical ranging limit of 0.6–3.5 m: the camera doesn't sense items closer, while farther ones are rendered with a poor number of points. Thin portions of objects are barely caught by the infrared grid and make the pose estimation extremely hard; for instance, the handle of a cup isn't recognized most of the times.

Ten items with 82 poses were used to train and test the system. The objects, in Fig. 5, include a cup with a handle, a deodorant spray can, a book, an alarm clock, a cardboard tube, an eyeglass case, a cube, an apple, a shoe, and a toilet paper roll. The parameter p has been computed using several empirical tests for every item. Results are in Table 3 for 4 distances and 15 tests per object per distance. Other trials considered also low overlapping and different number of objects in the scene without finding significant downgrade of the performance.

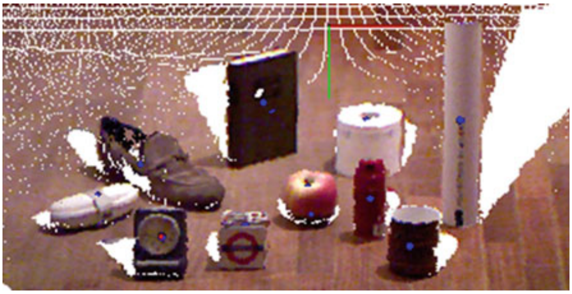

Fig. 5 The objects used for training

Table 3 Recognition statistics of the testing phase

Distance (m)	Recognition object (%)	Recognition pose (%)
0.6	100.0	100.0
1.1	100.0	93.3
1.6	100.0	86.6

5 Trajectory Generation Module

The trajectory generation considers the recognized shoulder movement and the grasp point to reach. Since there is a plane and possibly other point clouds recognized in the system, it has to compute a collision free trajectory to avoid the table and other objects.

The model of the prosthesis has been defined in the D-H notation, considering the mechanical system on the left of Fig. 5 that represents the prosthesis developed at Department of Mechanics in Politecnico di Milano [4]. There are 6 axes in the prosthesis: A for shoulder flexo-extension; B for the abduction of the shoulder; C for the axial rotation of the arm, obtained with a passive joint to adapt to external forces; D for the flexo extension of the lower arm; E for wrist prono-supination; F for wrist flexo-extension.

The direct kinematics is simply obtained after multiplication of the joints matrices and premultiplication of the matrix expressing the shoulder position with respect to Kinect. The inverse kinematics is computed in closed form using a geometric approach.

Trajectory computation requires two inputs: the EMG signal indicating the movement to do, and the point to reach computed from Kinect data. The trajectory computation generates the via points (at least approach and grasping) and sends them sequentially to the controller while monitoring the EMG input, that can change since the user may decide to terminate a task before the object is reached.

Considering the limitations in the wrist angles, 3 approaches to the grasp point are computed frontal, from top, from side. For each of them after setting the values for the wrist angles, we compute the wrist position and then the other joints values with the inverse kinematics.

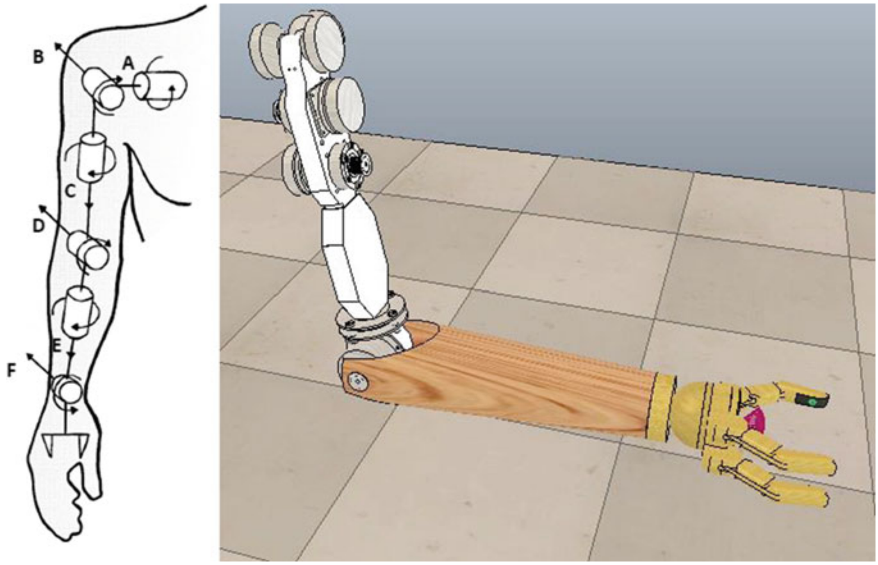

Fig. 6 The structure of the arm prosthesis including the hand, and its V-REP representation

All the computations are done in v-rep using the remote API (Application Programming Interface) approach that allows the user to control the simulation from remote hardware or software. In V-REP the model of the prosthesis is the one illustrated in Fig. 6 on the right. Since V-REP offers controllers and algorithms the implementation is straightforward.

6 Results and Conclusions

The system has been conceptually developed on the basis of a prototype prosthesis whose construction is under way at the Mechanical Department of Politecnico di Milano.

The overall system integration in v-rep has demonstrated the solution to be valuable in terms of precision of reaching. The error in Cartesian space is about 6 mm. Instead the time needed by the vision module is about 7 s, too much to integrate directly our vision solution in the controller.

As an important finding, the independence from the prosthesis is very high. The V-REP simulator solution offers an efficient way for the patient training without using the real prosthesis.

However implementing the real prosthesis has still some open issues: miniaturize the hardware, and better software solutions. Our system is a proof of concept that still needs engineering to become fully usable. Further activities are under way to adapt the architecture to the case of exoskeletons of the arm, where the role of the vision system can be reduced or even eliminated.

References

1. Altman NS (1992) An introduction to kernel and nearest-neighbor nonparametric regression. Am Stat 46(3):175–185
2. Barbero M, Merletti R, Rainoldi A (2012) Atlas of muscle innervation zones. Springer, Milan, Italy, pp 103–120
3. Bentley JL (1975) Multidimensional binary search trees used for associative searching. Commun ACM 18(9):509
4. Casolo F (2010) Elbow prosthesis for partial or total limb replacements. In: Casolo F (ed) Motion Control, Chapter 16. InTech (2010)
5. Corbett EA, Perreault EJ, Kuiken TA (2011) Comparison of electromyography and force as interfaces for prosthetic. J Rehabil Res Dev 48:629–642
6. Englehart K, Hudgins B (2003) A robust, real–time control scheme for multifunction myoelectric control. IEEE Trans Biomed Eng 50(7):848–854
7. Englehart KB, Hudgins B, Parker PA (2001) A wavelet-based continuous classification scheme for multifunction myoelectric control. IEEE Trans Biomed Eng 48(3):302–310
8. Gini G, Arvetti M, Somlai I, Folgheraiter M (2012) Acquisition and analysis of EMG signals to recognize multiple hand movements for prosthetic applications. Appl Bion Biomech 9:145–155
9. Gini G, Cavazzana L, Mutti F, Belluco P, Mauri A (2014) New results on classifying EMG signals for interfacing patients and mechanical devices. In: Rodic A, Pisla D, Bleuler H (eds) New trends in medical and service robots. Springer, vol 20 Mechanisms and Machines Sciences series (2014)
10. Han J, Kamber M, Pei J (2005) Data mining: concepts and techniques, Second Edition. Morgan Kaufmann, San Francisco
11. Han J, Shao L, Xu D, Shotton J (2013) Enhanced computer vision with microsoft kinect sensor: a review. IEEE Trans Cybernetics 43(5):1318–1334
12. Hargrove L, Losier Y, Lock BA, Englehart K, Hudgin B (2007) A real-time pattern recognition based myoelectric control usability study implemented in a virtual environment. In: Proceedings 29th annual international conference on IEEE EMBS. Lyon, France, pp 4842–4845 (2007)
13. Hudgins B, Parker P, Scott R (1993) A new strategy for multifunction myoelectric control. IEEE Trans Biomed Eng 40(1):82–94
14. Jain AJ, Duin RPW, Mao J (2000) Statistical pattern recognition: a review. IEEE Trans PAMI 22(1):4–37
15. Kuiken A, Li G, Lock BA, Lipschutz RD, Miller LA, Stubblefield KA, Englehart KB (2009) Targeted muscle reinnervation for real-time myoelectric control of multifunction artificial arms. JAMA 301(6):619–628
16. Lai JCK, Schoen MP, Perez Gracia A, Naidu DS, Leung SW (2007) Prosthetic devices: challenges and implications of robotic implants and biological interfaces. In: Proceedings of IMechE, vol 221, pp 173–183 (2007)
17. Lisi G, Cattaneo D, Belluco P, Gini G (2011) From the classification of EMG signals to the development of a new lower arm prosthesis. In: Proceedings of IFAC 18 world congress. Milan, pp. 6493–6498 (2011)
18. Miguelez JM, Miguelez, MD, Alley RD Amputations about the shoulder: prosthetic management, Chapter 21. American Academy of Orthopaedic Surgeons (online)

19. Parker P, Englehart K, Hudgins B (2006) Myoelectric signal processing for control of powered limb prostheses. J Electromyogr Kinesiol 16(6):541–548
20. Phinyomark A, Quaine F, Charbonnier S, Serviere C, Tarpin-Bernard F, Laurillau Y (2013) EMG feature evaluation for improving myoelectric pattern recognition robustness. Expert Syst Appl 40(12):4832–4840
21. Richtsfeld M, Vincze M (2008) Grasping of unknown objects from a table top. workshop on vision in action: efficient strategies for cognitive agents in complex environments. Marseille, France
22. Rivela D, Scannella A (2013) Classificazione del segnale sEMG tramite pattern recognition per il controllo del giunto della spalla di una protesi attiva di arto superiore, Master Thesis, Politecnico di Milano
23. Rusu RB, Cousins S (2011) 3D is here: point cloud library (PCL). In: Proceedings of IEEE ICRA
24. Saxena A, Driemeyer J, Ng AY (2008) Robotic grasping of novel objects using vision. Int J Robot Res 27(2):157–173
25. Shenoy PK, Miller J, Crawford B, Rao RPN (2008) Electromyographic control. IEEE Trans BME 55(3):1128–1135
26. Smith LH, Hargrove LJ, Lock BA, Kuiken TA (2011) Determining the optimal window length for pattern recognition-based myoelectric control: balancing the competing effects of classification error and controller delay. IEEE Trans Neural Syst Rehabil Eng 19(2):186–192
27. Yang MY, Forstner W (2010) Plane detection in point cloud data. University of Bonn

Design and Simulation of an Orthotic Device for Patients with Osteoarthritis

D. Tarnita, M. Catana, N. Dumitru and D.N. Tarnita

Abstract The first aim of this paper is the development of a virtual model of a new orthotic device, starting from an existent orthotic device, currently used in knee rehabilitation and from the virtual models developed for healthy knee joint and for the knee joint affected by osteoarthritis (OA) disease with *varus* inclination of 5°, 10°, 15°. The second aim consists in the obtaining of stress and displacements using numerical simulations for healthy knee joint, for knee joint affected by osteoarthritis (OA) and for orthotic device—OA knee assemblies. The Finite Element Method (FEM) is used to obtain the diagrams and the maximum values of von Mises stress and displacements for healthy knee, for the three studied cases of OA knee, orthotic devices-assemblies. These values are extracted and compared. Finally, an experimental study is provided in order to compare the range of motion and the amplitude of the flexion-extension knees of a five patients group with OA knees with and without orthosis, and to mark out the advantages of the proposed orthotic device.

Keywords Osteoarthritis · Human knee joint · 3D virtual model · Orthotic device · Numerical simulations · Finite element method

D. Tarnita (✉) · M. Catana · N. Dumitru
University of Craiova, Craiova, Romania
e-mail: tarnita.daniela@gmail.com

M. Catana
e-mail: marius_catana79@yahoo.com

N. Dumitru
e-mail: nicolae_dtru@yahoo.com

D.N. Tarnita
University of Medicine and Pharmacy, Craiova, Romania
e-mail: dan_tarnita@yahoo.com

H. Bleuler et al. (eds.), *New Trends in Medical and Service Robots*,
Mechanisms and Machine Science 38, DOI 10.1007/978-3-319-23832-6_6

1 Introduction

Virtual modeling of human knee joint has been addressed in several articles [1–9]. Virtual models were analyzed with FEM, after performing a finite element model with tetrahedral type [7–9], hexahedral, or using automatic meshing methods. The articles have used an algorithm for meshing with hexahedrons and bricks in order to analyze with a much better approximation for the tibio-femoral contact area [1, 3, 4]. Musculoskeletal disorders are the most frequent cause for long-lasting or chronic pain and for restrictions on mobility and physical performance [10]. They can lead, in the extreme case, to an increased morbidity. They affect hundreds of millions of people with important increases expected due to a doubling in the number of people over 50 years of age by 2020 [10].

Osteoarthritis (OA) is the most common joint disease that affects 30 % of adults over 50 years of age, two thirds of whom are women [10]; it is the fourth most frequent cause of health problems in women and the eighth—in men; about 40 % of all persons over the age of 70 are affected by knee osteoarthritis; about 80 % of persons with osteoarthritis suffer from limited mobility and about 25 % of them can no longer perform important basic activities of daily life [10].

The knee osteoarthritis is one of the major chronic diseases usually found in people of middle age and old age and also mainly causes various disabilities. It is associated with deterioration of the tibial and femoral cartilages and menisci, and it can be caused by various factors: misalignment, injury, genetics, and obesity. Knee osteoarthritis involves a degenerative process of cartilage in the knee joint leading to its loss [11]. Symptoms of OA are associated with altered load distributions across the knee, which cause an increase in the contact pressure on the tibio-femoral joints [12]. The most influential factor affecting load distributions across the knee is misalignment. Varus misalignment has been shown to increase OA progression in 70 % of persons with OA knee [11, 12]. In the absence of a cure for this disease, current therapies are used to reduce pain and improve joint using drugs which are associated with high rates of adverse events (gastrointestinal hemorrhage, heart attack) [13]. Many individuals with OA knee will finally require total knee replacement, a procedure that presents some inherent risks or morbidity. An alternative solution for OA treatment, non-pharmacologic and non-surgical, consists in use of an orthosis, which improves joint stability and joint mobility [13, 14].

The first aim of this paper is the development of a virtual model of a new orthotic device, starting from an existent orthotic device, used in knee rehabilitation, and from the virtual models developed for healthy knee joint and for the knee joint affected by osteoarthritis disease with inclination in *varus* by 5°, 10°, 15°. The second aim consists in the obtaining of stress and displacements using numerical simulations for healthy knee joint, for OA knee and for orthotic device—OA knee assemblies. FEM is used to obtain the diagrams and the maximum values of von Mises stress and displacements for healthy knee, for the three studied cases of OA knee, orthotic devices-assemblies. These values are extracted and compared.

Finally, an experimental study is provided in order to compare the range of motion and the amplitude of the flexion-extension knees of a five patients group with OA knees with and without orthosis.

2 Three Dimensional Modeling

The most important factor which affects load distributions across the knee is misalignment. Any shift from the collinear alignment, when the loading axis passes through the hip, knee and ankle, affects load distribution in knee. The distinct cases of progressive stages of OA knee differ by the progressive increase of damage on the tibial cartilage, on the menisci and on the femoral cartilage. The osteoarthritis gradually evolves with significant limitations of movement. Initially, pain occurs only under quadriceps muscle contraction and under increased mechanical stress (siting-to-standing transition, squats, prolonged walking on uneven ground). In the intermediate stage, the knee pain gets worse, it may occur at rest and it is accompanied by limitation of motion, quadriceps muscle atrophy and decrease of ligaments stability. In the final stage severe limits of knee flexion and muscle contracture are characteristic. In Fig. 1 the three stages of knee cartilages damage and evolution of the OA are presented.

2.1 3D Model of the Human Knee

To obtain the 3D geometric model of the healthy knee joint, CT images were processed using Space Claim and Design Modeler integrated applications which work under ANSYS software [16]. The computed tomography slice interval was set at 1.5 mm near the joint interface and 2.5 mm farther from the interface while providing enough data to create accurate computer-aided design models.

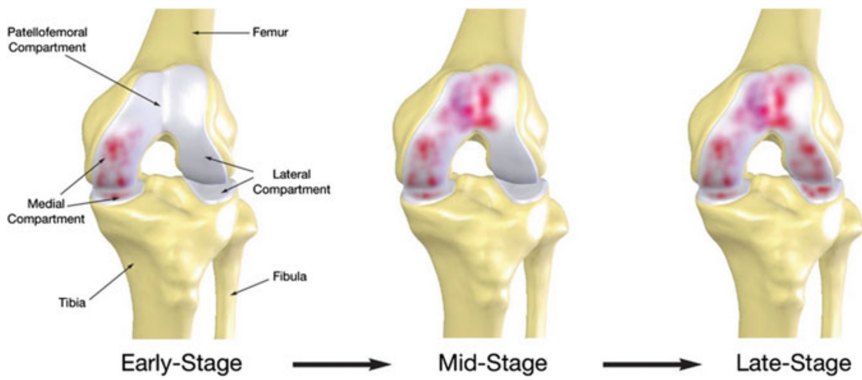

Fig. 1 The three stages of evolution of the OA [15]

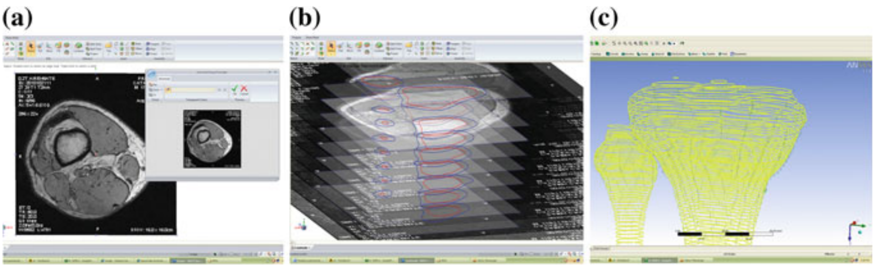

Fig. 2 **a** CT Images of the femur; **b** images imported in SpaceClaim; **c** contour lines imported in Design Modeler for tibia and peroneus

The CT files were imported in SpaceClaim as jpg files, where contour lines (inner and outer sections) were created (Fig. 2). The sections were first defined in SpaceClaim, and then they were imported one-by-one in DesignModeler parallel sketches. These operations are repeated for each tomographical image, and for each bone. The virtual biomechanical system of the human knee contains femur, tibia and fibula bones, medial and lateral ligaments, medial and lateral menisci, femoral and tibial cartilages [17]. Based on the modelled geometry of the bones, ligaments, cartilages and menisci were added (Fig. 3).

The knee joint alignment is measured by the angle formed by the intersection of the mechanical axes of the femur and the tibia In a varus knee, the axis passes medially from the knee center, resulting in an increase of contact pressure on medial tibio-femoral joint cartilage. The healthy joint is featured by an angle of 176° between the femoral axis and tibial axis, while for the joint affected by osteoarthritis

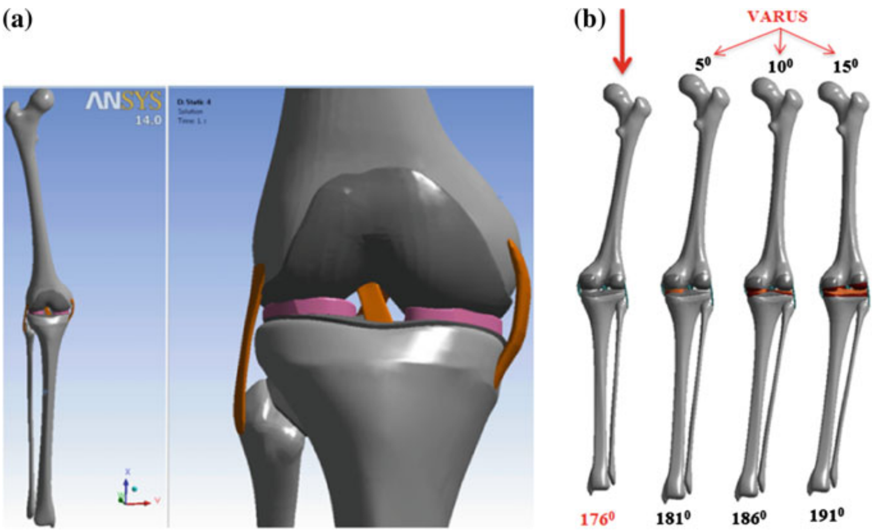

Fig. 3 **a** Virtual model of healthy knee joint. **b** Normal knee and three cases of varus inclination

from the medial compartment, the angle increases. We consider 3 cases of varus inclination: 5°, 10°, 15°, so the final angles between the femoral and tibial axes are:181°, 186°, 191° (Fig. 3b).

2.2 3D Model of the Initial Orthotic Device

Biomechanical studies have demonstrated that the varus misalignment of the knee can be corrected with application of an orthosis, which is an exoskeleton having two important objectives: knee stability improvement and gait rehabilitation. The virtual model of the initial orthotic device was developed starting from the real dimensions and shapes of a DonJoy type orthosis [18], currently used in joint stabilization and rehabilitation of knee movements. Based on technical drawings and using the real dimensions, the initial orthotic device was designed in ProEngineer, software which allows a high detailed modeling and an accurate technical approach [19]. Parametric sketches were designed based on solid models which have been defined through extrusion operations. The orthotic device is composed by both fixed elements (upper frame, lower frame, stabilizing mechanism with 2 gears) and mobile elements (upper rod and lower rod). The orthosis—knee joint assembly was developed by importing the virtual model of the orthotic device in the databases of osteoarthritic knee joint with inclination in *varus* of 5°, 10° and 15°, respectively. The components were placed in a global system XYZ. Proper positioning of the assembly components was done in Design Modeler pre-processor, under ANSYS Workbench 14.5 package. The virtual model of the initial orthotic device and the OA knee–orthotic device virtual assemblies for the three studied cases of varus inclination are presented in Fig. 4.

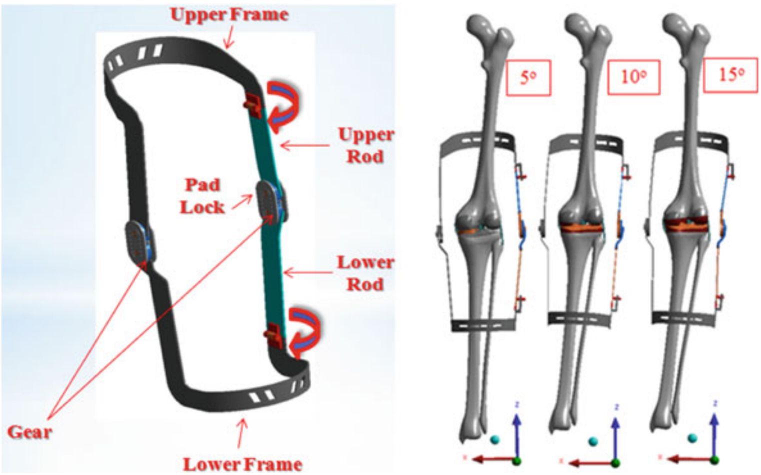

Fig. 4 Virtual model of initial orthosis and the three OA knee-initial orthosis virtual assemblies

2.3 3D Model of the Proposed Orthotic Device

Taking into account that the initial orthotic device is expensive and, also, it cannot be adapted to different degrees of osteoarthritis and to different human constitutional types, we have designed a new orthotic device. Our proposed orthotic device is less expensive and it implies modularity and a new solution of the misalignement correction system used to improve the joint stability and the rehabilitation of flexion-extension movements of the OA knee. The 3D model of the proposed orthotic device (Fig. 7) is designed in ProEngineer application, starting from drawing sketches.

The proposed orthotic device consists of the following components: upper frame (1) and lower frame (2); upper rod (3) and lower rod (4); the correction system (5) allows improving the alignment of the knee bones axis, due to the lateral mobility of its components. One of the orthosis sides has been made of moving elements that are attached to the upper and lower frames through a system of interlocking. The correction system consists of a circular plate lined with an elastic material that can be molded on the knee components without causing skin lesions when it creates pressure on the lateral or medial knee in order to correct the misalignement of the OA knee. The top and bottom sides of the circular piece are clamped with a chain ring each. The two chain rings are fixed to both rods, each provided with a screw which, by screwing or unscrewing, produces the chain elongation or shortening. They make the junction with the upper/lower frame by means of an upper/lower hinge joint. By shortening and lengthening movement, the knee is pushed to the normal axis. Lateral blocking and anchoring is done by the hexagonal screws positioned on the exterior side. The advantages of this proposed modular orthotic device versus the initial one are the simple design, the modularity, cost and reliability. In next section we'll compare, using numerical simulations, the results of both ortotic devices obtained to diminish the stress in OA knee. In Fig. 5 the virtual model of the proposed orthotic device—OA knee joint with the two phases: open device and closed device, are presented.

For geometric discretization into nodes and elements, we used Solid 186 and Solid 187 tetrahedron elements, which are defined by 20 nodes and, respectively by 10 nodes, having three degrees of freedom per node. The mesh structure of the both knee-orthosis assemblies is shown in Fig. 6. For the areas of interest the elements dimension is 1 mm and for the adjacent areas is up to 4 mm. Advanced discretization methods such as "Sweep", "HexDominant" and "Patch Conforming" were used. For each of ten studied cases: healthy knee (HK), the three cases of OA knee: Case 1:varus by 5°; Case 2:varus by 10°; Case 3:varus by 15°, for the three cases of initial orhosis-OA knee assembly (IO-OAK) and for the three cases of proposed orthosis–OA knee assembly (PO-OAK), the virtual model is discretized individually, the contact areas are readjusted and the analysis is run. In Table 1 the numbers of nodes and elements for knee joint and for orthosis corresponding to each studied case are presented.

The material properties are assigned to the different components of the assembly based on previously published data and they are found in Table 2.

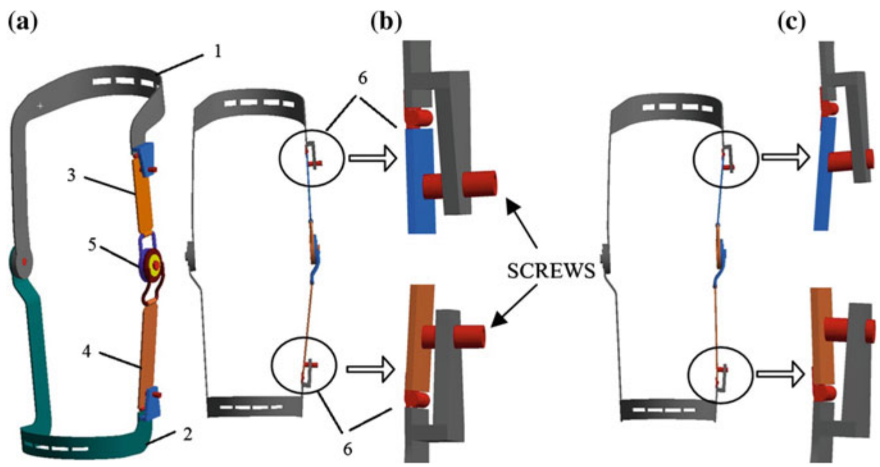

Fig. 5 **a** Virtual model of the proposed orthotic device—OA knee joint; **b** Device open, screws are not threaded; **c** Device closed, screws press on the *lower* and *upper* rods

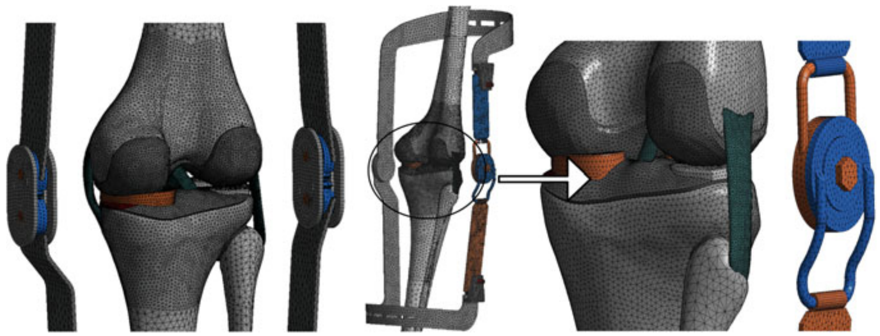

Fig. 6 Network of nodes and elements for IO-OAK and PO-OAK assemblies

Table 1 Nodes and elements network for the three OA knee-initial orthosis assemblies

Orthosis—knee joint assembly	Orthosis nodes	Joint nodes	Orthosis elements	Joint elements	Total nodes	Total elements
IO-OAK 5°	87.155	468.433	37.563	295.993	555.588	333.556
IO-OAK 10°	70.570	510.453	26.680	331.159	581.023	357.839
IO-OAK 15°	70.692	680.013	26.673	458.307	750.705	484.980
PO-OAK 5°	108.844	468.433	51.127	295.998	577.277	353.125
PO-OAK 10°	107.497	510.453	56.274	331.159	617.950	387.433
PO-OAK 15°	122.435	680.013	63.907	458.307	802.448	522.214

Table 2 Material properties [11, 12, 17]

Component	Cortical femur	Cortical tibia	Spongio bone	Cartilage	Meniscus	LCM LCL	LIP LIA	Alluminium alloy
Young's modul (MPa)	18,600	12,500	500	12	59	10	1	71,000
Poisson's ratio	0.3	0.3	0.3	0.475	0.49	0.49	0.49	0.33

3 Results

The numerical simulations and FEM analyses were processed for healthy knee joint, for the three cases of OA knee joint and for each case of OA knee joint-orthosis assemblies using AnsysWorkbench 14.5 software. The settings and the boundary conditions (Fig. 7) for finite element method analysis are presented bellow and can be also found in [17]:

- taking into account the big number of nodes and elements but, also, the presence of nonlinear contacts, for solving the analysis it is necessary to implement a "smaller steps" system;
- on the proximal head of the femur bone a body weight of 800 N force in the -Z axis direction is applied (Fig. 7a);
- on the same location, the "Remote Displacement" is applied; this setting allows Z offset and RotY around the femur, which allows movement of the hip (Fig. 7b);

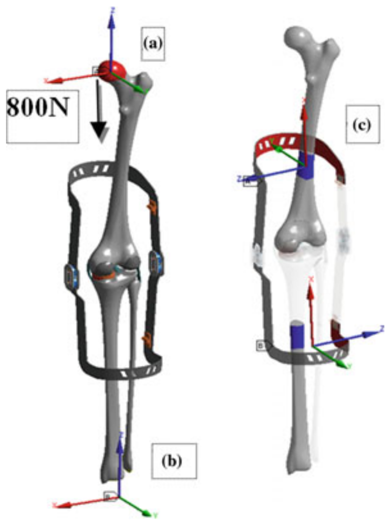

Fig. 7 Settings and boundary conditions

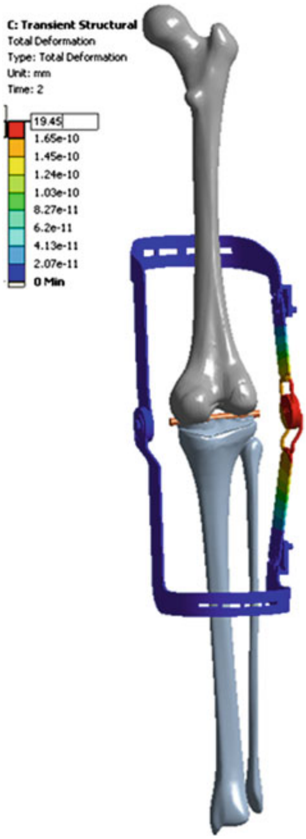

Fig. 8 Displacements for PO-OAK assembly

- the orthotic device fixation on the femur and on the tibia is done through a "Joint–Fixed" connection type (Fig. 7c);
- on the tibia distal head the "Remote Displacement" is applied; this setting allows RotY (movement of the ankle around the tibia) (Fig. 8).

Maximum stress and displacements for PO-OAK assembly are presented in Table 3.

Diagrams maps of von Mises stress and displacements developed on the proposed orthosis are presented in Fig. 9.

Table 3 Von Mises stress and displacements (TD—Total Displacement; DX, DY, DZ—Displacement on X, Y, Z axis) for assembly and for individual component of orthotic device

Type result	TD (mm)	DX (mm)	DY (mm)	DZ (mm)	Stress entire model (MPa)	Stress upper frame (MPa)	Stress lower frame (MPa)
Value	19.45	18.171	2.157	6.61	29.699	21.454	29.699

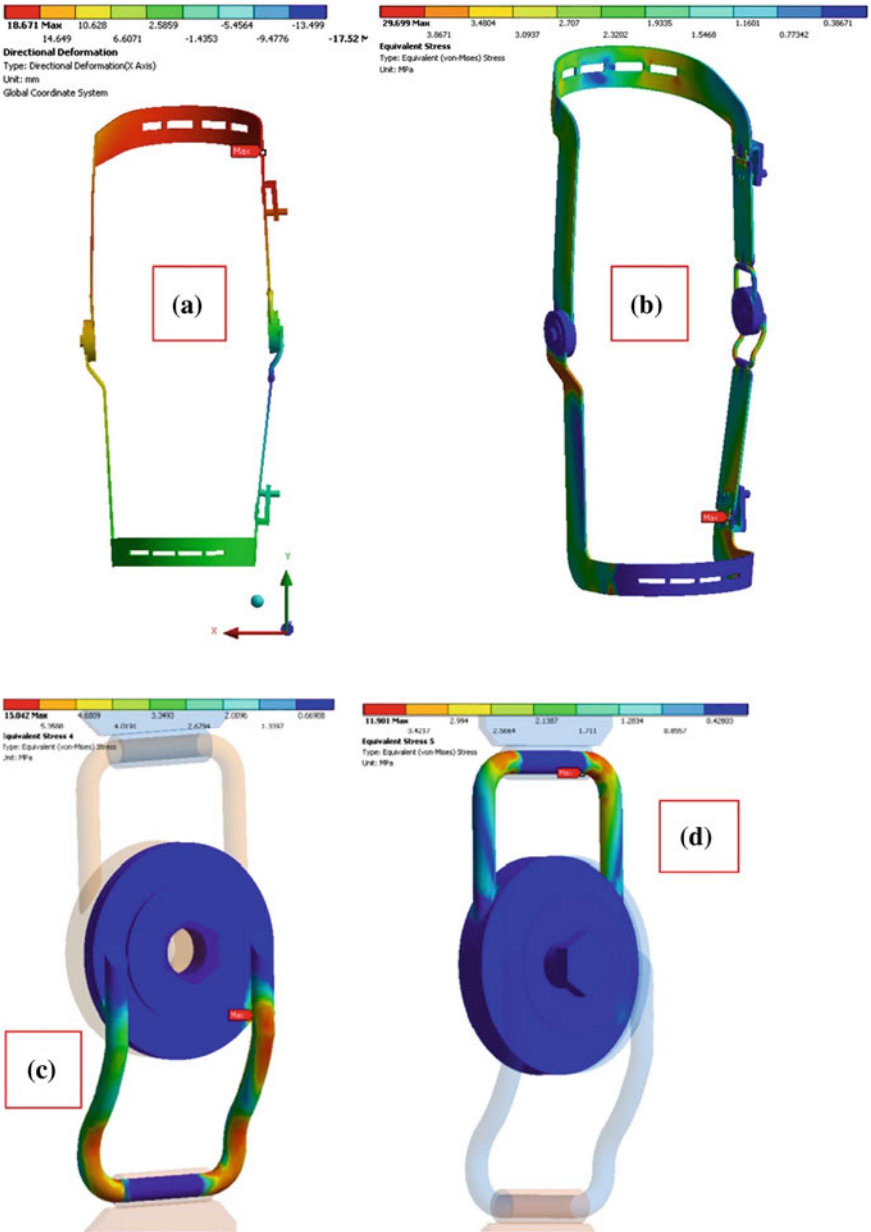

Fig. 9 Stress and displacements for proposed orthotic device: **a** displacement on x axis; **b** von Mises stress; **c**, **d** von Mises stress on both pieces of the misalignment correction system

The maximum von Mises stress (S) and the maximum displacements (D) obtained for FC, TC and M for the ten studied cases are presented in Table 4.

Analyzing the results obtained by numerical simulations, presented in Table 4, we can see an increase of the stress for OA knee joint versus the case of healthy knee joint for all components: femoral cartilage, tibial cartilage and menisci. The maximum values of von Mises stress in FC are bigger than in TC and in M. The OA knee is exposed to greater stress at the medial compartment of the articular cartilage of the tibia and femur. The maximum values of von Mises stress increase with 50 % in first OA case to approx. 120 % in third case in comparison with healthy knee. The results show that misalignment (varus variation) could damage the articular cartilage because they increase the stress magnitude, that progressively produce articular cartilage damage and it enhances the osteoarthritis phenomenon due to mechanical factors. The predictions are in general agreement with measurements reported in the literature. The results showed that the tibial cartilage presents the biggest stress in the OA analyzed cases [8, 9, 11]. Haut et al. [8] reported maximum stress values in the tibio-femoral contact area of 2.36 MPa in the lateral and 2.55 MPa in the medial side. Riegger-Krugh et al. [9] applied 1200 N of load and reported stress values of 2.5 MPa in the lateral side.

Applying the initial orthosis, in comparison with the OA knee, the maximum values decrease with about 12–15 %; applying the proposed orthosis, the values decrease with 15–20 %, which means the stress values for both cases are quite similar. The decrease of stress values proves an improvement in knee stability and rehabilitation.

The maps of stress values and displacements for FC, TC and M for case 2 (varus inclination of 10°) are presented in Fig. 10. Similar maps are obtained for healthy knee and for the other two OA cases.

Maps of stresses and displacements for FC, TC and M for proposed orthosis-OA knee assembly in varus inclination of 10° are presented in Figs. 11 and 12.

4 Experimental Tests

Experimental studies on the physical prototype of the proposed orthotic device (Fig. 13) represent a more appropriate approach to analyzing orthotics' performance during gait. The aim of this experimental study is to compare the range of motion and the amplitude of the flexion-extension knees of a five patients group with OA knees with and without orthosis. The study was approved by the Human Ethics Research Committee, University of Craiova, Romania. In Table 5 the mean values and standard deviations for anthropometric data of OA patients are presented.

The experimental test consisted of walking on treadmill at a speed of 3.6 km/h. For collecting the experimental data of the knee joint angle, we used a data acquisition system based on two electrogoniometers described in paper [20], one for each leg, for making possible to simultaneously read data during walking.

Table 4 The maximum von Mises stress values (MPa) and the maximum displacements (mm) obtained for femoral cartilage (FC), for tibial cartilage (TC) and for menisci (M)

Types of results	HK	OAK 5°	IO-OAK 5°	PO-OAK 5°	OAK 10°	IO-OAK 10°	PO-OAK 10°	OAK 15°	IO-OAK 15°	PO-OAK 15°
FC-S	2.41	3.42	2.98	2.67	4.01	3.43	3.12	5.34	4.68	3.98
TC-S	2.17	3.01	2.63	2.41	4.51	3.47	3.17	5.12	4.52	4.07
M-S	2.12	2.54	2.19	2.02	3.89	3.08	2.87	4.67	3.97	3.68
FC-D	7.17	1.61	1.21	1.05	2.70	2.25	2.12	4.23	3.36	3.12
TC-D	5.88	1.43	0.82	0.67	2.66	2.09	1.78	4.05	3.02	2.87
M-D	6.05	1.52	1.33	1.12	2.92	2.35	2.01	3.87	2.98	2.69

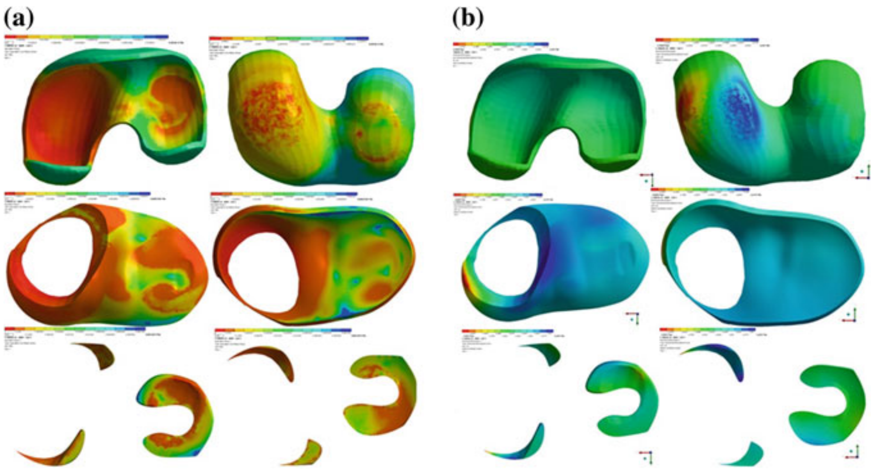

Fig. 10 The maps (*top* and *bottom* views) of **a** stress and **b** displacements for: FC (first line), TC (second line) and M (third line) for case 2 (varus 10°)

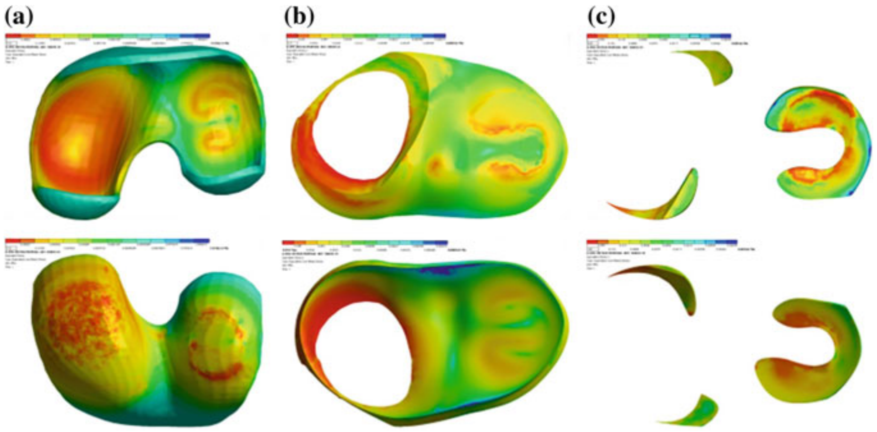

Fig. 11 Maps of stresses (*top* and *bottom* views) for PO-OAK: **a** FC-S; **b** TC-S; **c** M-S

The angular amplitudes of human knee flexion-extension during the gait performed on the treadmill were obtained for each healthy person from the report generated by the acquisition system based on electro-goniometer, as data files.

For more accurate results, considering the natural biological variability from one's individual step to another, but also from one individual to another, for each healthy subject were selected 8 consecutive cycles, which were normalized by interpolation with cubic Spline functions, using MATLAB environment, and reported on the abscissa at a scaled interval from 0 to 100 %. The average cycle was determined as being the data's arithmetical mean that correspond to the 8 cycles.

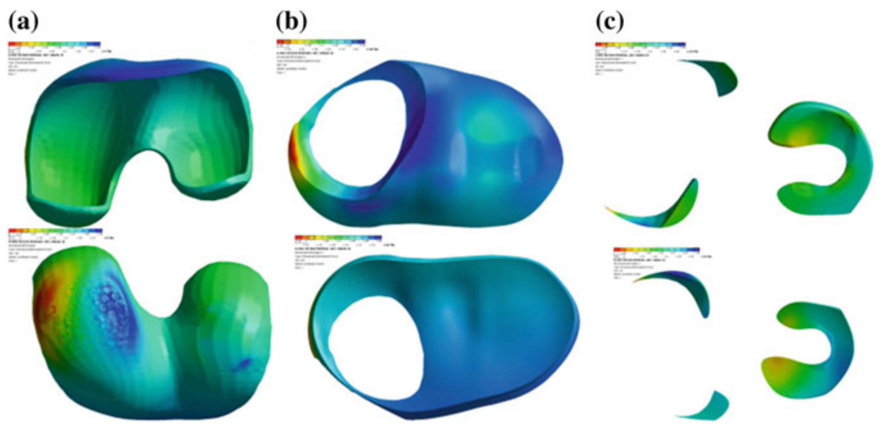

Fig. 12 Maps of displacements (*top* and *bottom* views) for PO-OAK: **a** FC-D; **b** TC-D; **c** M-D

Fig. 13 Virtual model an phisical prototype of the proposed orthotic device

Table 5 Mean values and standard deviations of anthropometric data for patients with OA

Subject	Age (years)	Weight (kg)	Height (cm)	Leg length (cm)	Hip–knee length (cm)	Knee–ankle length (cm)
Average	52.4	80.6	173.2	83.2	44.4	38.8
St. Dev.	4.04	15.71	10.26	11.58	6.66	5.36

In Fig. 14, there are being displayed the curves of the 8 cycles and the medium cycle corresponding to Subject No. 1 for different cases.

For each subject were drawn the curves of flexion-extension angles corresponding to each step, and also it has been determined and drawn the corresponding curve of the medium step.

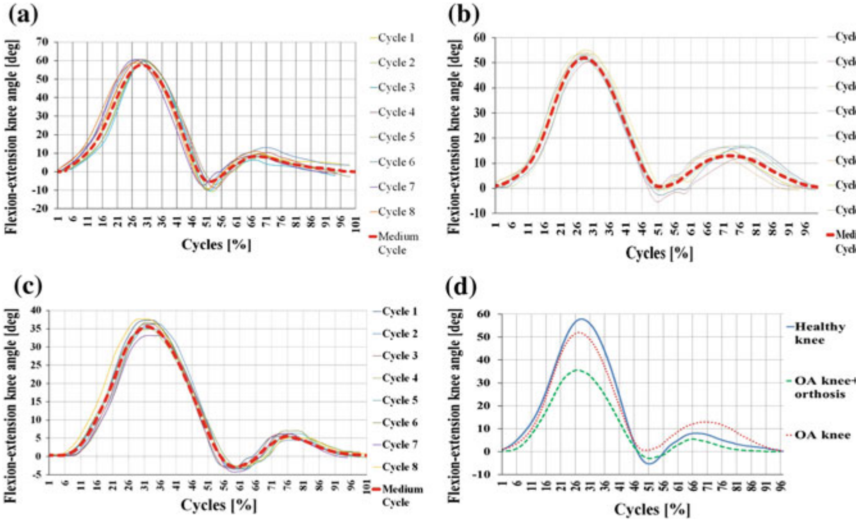

Fig. 14 The normalized cycles and the medium cycle for **a** healthy left knee; **b** OA knee **c** OA knee-proposed orthosis; **d** comparison of the medium cycles

5 Conclusions

The behavior of the virtual knee joint (healthy or affected, with or without orthosis or prosthesis) can give important informations which can be used in the fields of sport medicine, medicine sciences and biomedical robotics. The biomechanical behavior of human knee cartilages is important in order to understand the OA phenomenon due to mechanical factors, because it could be possible to find solutions to help people to diminish the OA effects using rehabilitation devices.

This paper presents advanced modeling and simulation methods, using the latest generation of CAD-CAE applications. For the geometric modeling of human knee joint, embedded applications as Design Modeler, SpaceClaim under Ansys Workbench software package had been used. For the geometric modeling of the orthotic devices, ProEngineer application there had been used.

A finite element model of the human knee helps surgeons and biomechanical researchers to develop improved implants and treatment method for patients suffering bone loss and diseases. The finite element analysis is a first step that provides results which can serve as guidelines for the final design, manufacturing and clinical testing of medical devices as orthoses or prostheses. The advantage of the numerical simulations used in medical and rehabilitation fields consists in the fact they can be done in advance without any invasive intervention and without any costs necessary to manufacture the medical devices before their final and optimized prototype.

Using Ansys simulation environment, the virtual knee and the knee joint–orthotic devices assemblies had been subjected to a FEM analysis. A comparison between the results obtained for healthy knee, for the three cases of OA knee (*varus* by 5°, 10°, 15°) and for IO-OAK assemblies and PO-OAK assemblies is presented. Understanding the stress of the knee joint is important because abnormal joint loading increases the risk of OA. Furthermore, these results could be used by an expert to determine preventive measures such as strength training or the use of orthotics to minimize the varus moment to reduce the load on the medial compartment of the knee.

In general, the results show that misalignment could damage the articular cartilage because they increase the stress magnitude, that progressively produce articular cartilage damage and it enhances the osteoarthritis phenomenon due to mechanical factors. The proposed orthotic device seeks to improve the quality of walking by stabilizing the joint, by rehabilitation of the knee movement and by minimizing the knee joint loads on femoral cartilage, tibial cartilage and on menisci. The obtained results show a good behavior of the proposed orthotic device which offers a good support of the body weight and an improving of knee stability, leading to the decrease of human knee stress by 25 %, which is significant in order to rehabilitate the OA patients. The results obtained in the present study using the virtual prototype are compared with the experimental and numerical results that have been obtained by other authors and are similar with them. Experimental tests show that the proposed orthotic device leads to an increase of the kinematical performances of the patient.

References

1. Fening DS (2005) The effects of meniscal sizing on the knee using finite element methods. College of Engineering and Technology of Ohio University, Athens
2. Bahraminasaba M (2011) Finite element analysis of the effect of shape memory alloy on the stress distribution and contact pressure in total knee replacement. Trends Biomater Artif Organs 25:3
3. Mohammad K (2011) A musculoskeletal model of a subject specific knee joint with menisci during the stance phase of a walk cycle, Dissertation in engineering and mathematics, University of Missouri-Kansas City
4. Kubicek M (2009) Stress strain analysis of knee joint. Eng Mech 16:5
5. Hartley YN (2009) The effect of the frontal plane tibiofemoral angle on the contact stress and strain at the knee joint, Mechanical Engineering Dissertations, Department of Mechanical and Industrial Engineering, Northeastern University
6. Harrysson OL (2007) Custom-designed orthopedic implants evaluated using finite element analysis of patient-specific computed tomography data: femoral-component case study, BMC Musculoskeletal Disorders
7. Vidal A (2008) Analysis, simulation and prediction of contact stresses in articular cartilage of knee joint, Department of Mechanical Engineering, Instituto Tecnologico de Celaya, Mexico, International Conference Ansys
8. Haut TL, Hull ML, Rashid MM, Jacobs CR (2002) A finite element model of the human knee joint for the study of tibio-femoral contact. J Biomech Eng 124:273–280
9. Riegger KC, Gerhart TN, Power WR, Hayes WC (1998) Tibiofemoral contact pressures in degenerative joint disease. Clin Orthop 348:233–245
10. http://www.bme.master.unibe.ch/unibe/medizin/bioeng/content/e818/e820/e1697/e2045/FAMusculoskeletal_eng.pdf

11. Yang N (2007) The effects of tibio-femural angle and body weight on the stress field in the knee joint. In: International mechanical engineering congress and exposition, Seattle
12. Chantarapanich N (2009) A finite element study of stress distributions in normal and osteoarthritic knee joints. J Med Assoc Thai 92
13. Kirkley A et al (1999) The effect of bracing on varus gonarthrosis. J B J S Am 81:539–548
14. Rubin G et al (1977) VAPC Prescription procedures for knee orthoses and knee-ankle-foot orthoses. Orthot Prosthet 31:9–25
15. http://www.jupitermed.com/osteoarthritis
16. www.ansys.com
17. Tarnita D, Catana M, Tarnita DN (2014) Contributions on the modeling and simulation of the human knee joint with applications to the robotic structures. In: New trends on medical and service robotics: challenges and solutions, pp 283–297. Springer Publishing House
18. www.djoglobal.com
19. www.proengineer.com
20. Tarnita D, Tarnita DN, Catana M (2013) Experimental measurement of flexion-extension move ment in normal and osteoarthritic human knee. Rom J Morphol Embry ol 54(2):309–313

Kinematic and Dynamic Study Contributions on Human Jaw System

N. Dumitru, C. Copilusi and M. Ciortan

Abstract This research addresses modeling the kinematic and dynamic response of the human jaw system, from an analytical, virtual and experimental viewpoint. Kinematic parameter variation laws have been identified which define the mandible motions on a human skull and a human subject through experimental measurements. A virtual human skull reconstruction it is presented, by using an original method and this was parameterized on a modular concept, based on the anatomy of a human subject. For this, equivalent mechanisms of the human jaw were elaborated and these represent a base frame for inverse kinematic modeling in an analytical way. This analysis has been validated with a numerical processing algorithm in order to identify the generalized coordinate variation laws. Human jaw muscle groups have been modeled as linear actuators. The aim of this research is to perform a dynamic analysis by using the finite element method, for stress and deformation distributions determination, on normal or critical motions cases. Mathematical and virtual models, created through a modular construction, easily permit us to evaluate in a dynamic mode different dental prostheses used in dentistry domain.

Keywords Mandible · Dynamic analysis · Kinematic model · Human skull · Virtual modeling

N. Dumitru (✉) · C. Copilusi · M. Ciortan
University of Craiova, Craiova, Romania
e-mail: nicolae_dtru@yahoo.com

C. Copilusi
e-mail: cristache03@yahoo.co.uk

M. Ciortan
e-mail: marinela_ciortan@yahoo.com

H. Bleuler et al. (eds.), *New Trends in Medical and Service Robots*,
Mechanisms and Machine Science 38, DOI 10.1007/978-3-319-23832-6_7

1 Introduction

The human jaw system study has been and still is, over time, one of the most important research themes for many researchers from large domains in the context of the medical environment [1]. This system is one of the most complex of the human body, due to its morphological components and functionality. Researchers such as [2] developed specific studies on this topic by establishing motion influence on the human speech process. Other researchers have made studies regarding kinematic models equivalent to the human jaw system by using different analytical or experimental methods [3–5]. Such analyses are useful e.g. in dentistry modeling and reconstruction areas, in order to determine mandible motion laws and some characteristic points trajectories, without considering the muscle system behavior. The muscle groups from the human jaw structure have a crucial role in mastication or speech processes and it cannot be neglected.

Thus, theoretical models of the human jaw system muscle groups were studied in [6, 7], and represent some starting points for this research. The kinematic analyses accomplished by these researchers were used on elaborating some mathematical models for human jaw dynamic behavior study [8–10].

Based on these models, a virtual reality simulation with specific finite element software has been developed [11].

The research aim is to identify the human jaw dynamic response on two major cases: motion laws variation depending on time for mandible kinematic parameters considering solid-rigid bodies, respectively, deformable bodies; stress, deformations and displacement diagrams determination, depending on time, by connecting the solid-rigid body motion with a deformable one, for any component from human jaw system.

For this aim, on first part a state of the art was performed in order to identify the problematic and objectives proposals. The input data used for this analysis are the mandible motion laws for main motions of the human jaw, during mastication, speech, etc. These laws can be determined through experimental tests on the second part of the research. The main interest for this is focused on mandible trajectories, by using equipment with high-speed recording cameras. Also these represent a template for kinematic model validation developed for inverse kinematic analysis, which will be performed in third part of the human jaw system research. Virtual simulations are performed in the fourth part. Also for this, a virtual model of a human skull will be developed based on CT-series, and will be used for a complex analysis performed on dynamic mode by applying some special parameterized modeling techniques, presented in the last part of the research. This research ends with final conclusions regarding the behavior modeling and virtual simulations on a dynamic mode in normal or critical conditions imposed to the analyzed muscle groups such as: temporal, masseters and pterygoid. Also by performing these analyses one can do a feasibility study to perform virtual tests on dental implants, for validating new concepts in dentistry domain.

2 Human Jaw Experimental Analysis

2.1 Geometrical Parameters Identification

Before starting the experimental analysis of a human jaw one it is needed to identify the mandible fundamental motions. These are: elevation, depression and protraction-retraction motions. These motions can be decomposed and studied in three reference plane: frontal, horizontal and sagittal plane. For this, the mandible can be considered as a spatial segment, with one marker "E" placed on the middle of the inter-incisive tooth, and this point represents the interest one for experimental studies.

On Fig. 1 it can be identified: TEM-temporal muscle; MAS-masseter muscle; PTL-lateral pterygoid muscle; PTM-median pterygoid muscle; Dr, St—left and right side of the mandible; XOY-transversal plane; ZOY-frontal plane; ZOX-sagittal plane. On this model the following parameters defines the mandible form and dimensions as a curved segment: A1, M1, N1, R, E, N2, M2, A2. These geometric parameters were evaluated by considering a human skull real model as: $(A_1A_2) = l_1 = 100.5$ mm; $(A_1M_1) = l_2 = 67$ mm; $(M_1N_1) = l_3 = 58$ mm; $(ES) = l_4 = 19$ mm; $\alpha = 27^\circ$; $\beta = 67^\circ$; $\gamma = 25^\circ$; r = 28 mm; $\delta = 81^\circ$; l5 = 86.5 mm.

2.2 Kinematic Parameters Identification

For the mandible motions, one it was used CONTEMPLAS equipment in the sight of variation laws determination. This equipment has two high-speed cameras for motion recording and Faculty of Mechanics—University of Craiova—Romania

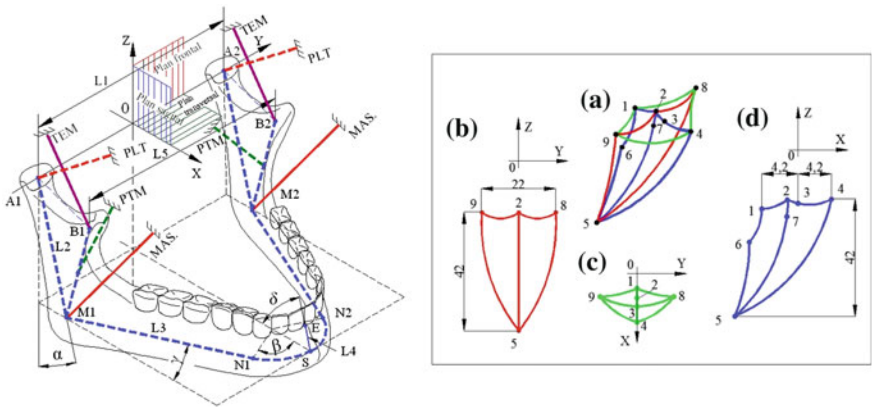

Fig. 1 Human mandible modeling as a spatial segment and the described theoretical curves during motions for point E (*a* spatial view; *b* frontal view; *c* bottom view, *d* lateral view)

owns this equipment in one of his laboratories. This equipment can record sequences with a speed of 350 frames/s. His integrated software can automatically track and recognize specific markers placed on the desired mobile system. These markers have reflective properties and represent the experimental analysis interest points. There were identified the mandible kinematic parameters variation depending on time (linear and angular positions) in case of a living human subject and also on a human skull dummy for three major cases: elevation, depression and protraction-retraction motions. This complex experimental analysis was developed for a time period of 10 s.

3 Human Mandible Inverse Kinematic Analysis

The human jaw mechanism is complex and it is almost impossible to obtain directly complete kinematic data from a real subject. Many researchers tried to realize some robotic models which can perform similar motions with the ones developed by humans during chewing processes. For elevation and depression motions there were used three different equivalent mechanisms. The input data for kinematic analysis were obtained on direct measurements over a real human skull. The muscles which actuate human mandible on the corresponding motions were replaced with linear actuators by taking into account the origins and insertion points. Each muscle has a crucial role on the human chewing process. The human mandible inverse kinematic analysis consists on evaluation of the kinematic parameters of the equivalent mechanism represented in Fig. 2. As an input data there are considered the positions, velocities and accelerations of the point T equivalent with point placed on the middle of the inter-incisive tooth. The kinematic model presented in Fig. 2 has three DOF and from a theoretical viewpoint this will be kinematically analyzed on sagittal plane. In case of direct kinematic analysis the variable parameters will be imposed on active joints B, E and H. Thus, these are used for links kinematic parameters determination. The link no 3 position is known, through point C

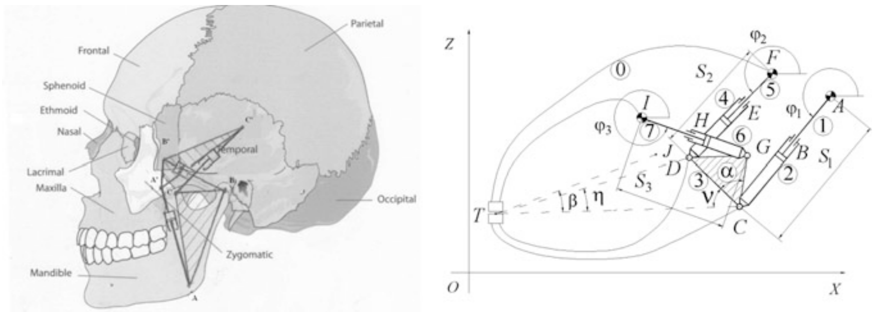

Fig. 2 Human mandible kinematic model for muscle linear actuation

position and φ_3 angle and from these variables, the position of point T can be determined.

For a direct kinematic analysis one it will impose variable parameters on active mechanism joints B, E and H. The aim of this is to determine the kinematic parameters of the mechanism links and especially point T. This can be possible by knowing the link no. 3 position, by C joint position and φ_3 angle.

In order to create a kinematic analysis algorithm by using a programming software, there are well known the following entry data: XA = 0.200 m; YA = 0.100 m; XF = 0.176 m; YF = 0.114 m; XI = 0.108 m; YI = 0.100 m; XT = 0.030 m; YT = 0.034 m; XJ = 0.140 m; YJ = 0.050 m; CD = 0.041 m; CG = 0.030 m; DG = 0.034 m; CT = 0.120 m; DT = 0.100 m; OM3 = 1 rad/s; EPS3 = 0 rad/s^2; Displacement = 0.2 m. For the mechanism inverse kinematic analysis from Fig. 2, the point T coordinates will be imposed, speed and accelerations projections on the XOY coordinate system, also the drive link no 3 position, angular speed and acceleration depending on coordinate fixed system.

For these data it will be considered the mandible elevation motion as an initial phase. Thus, the number of positions imposed for point "T" is "n = 21" and the step size is "incr = displacement/(n − 1)/2". The obtained results are presented on Figs. 3 and 4. On Fig. 3 are represented the φ_1, φ_2, φ_3 and φ_{TC} angle variations and on Fig. 4 there are represented the B, E and H translational joints variables.

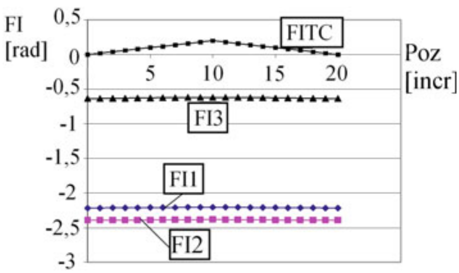

Fig. 3 φ_1, φ_2, φ_3 and φ_{TC} angle variations diagram

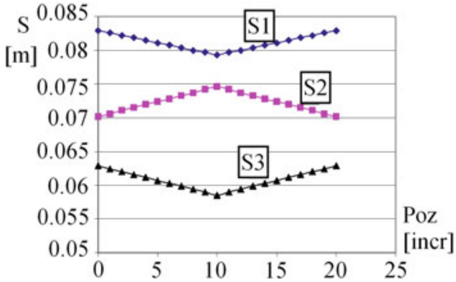

Fig. 4 B, E and H translational joints diagram

4 Human Jaw Geometric Modeling

In order to validate these kinematic results, a 3D virtual reality model of the human jaw has been built. Thus, it is necessary to obtain a simplified human jaw virtual model, based on a procedure which starts from CT-series. For this procedure it is necessary to use three main software: ImageJ, UltraEdit and CATIA. First step of the procedure represents the CT-series achievement based on a medical protocol. After, with ImageJ software aid, there are identified the voxels coordinate position on each CT-image and creating files with these in a **.cgo* format. Each voxel position was given by three numbers which represents numerical values on a 3D space. Last step of this procedure is represented by importing those files in CATIA/Quick Shape Reconstruction environment and by crossing specific modeling commands there are automatically generated 3D solids of the scanned human skull components.

5 Dynamic Analysis

The main objective for human jaw dynamic analysis is given by dynamic response identification for two major cases: kinematic parameters variation laws on time determination for mandible element, in two situations: solid-rigid body type motions, and deformable body type motion; distribution diagrams determination on time for stress, deformations and displacements by connecting the solid-rigid body type motion with a deformable body type, for any human jaw system components.

This complex dynamic analysis was also possible by applying special modeling techniques for whole parameterized mechanism, with implementing and virtual testing possibilities of some specific dentistry implants. Also for this analysis there were developed normal or critical analysis conditions, for obtaining the dynamic response in the proposed muscle group categories such as: masseter, temporal and pterygoid.

The proper method used for this analysis was the finite element method [12, 13] and for this the following essential steps were accomplished:

1. Importing the geometrical model and the input database definition for dynamic analysis with AnsysWorkbench.
2. Material properties according to [14] were defined as it follows: Longitudinal elasticity modulus: $1.5 \times 1010\ \text{N/m}^2$; Poisson ratio: 0.3; Density: $1300\ \text{kg/m}^3$.
3. Initial conditions and loads definition. The connection between human mandible and the rest of the skull was achieved in a first stage through 2DOF by defining the masseter and pterygoid muscles actuated based on the following motion laws:

   - For masseter muscle the acquired motion law was obtained experimentally and can be modeled through a polynomial function as:

$$
\begin{aligned}
M_{1^{\circ}rees} = & 53.2323116980194 + 9.35452417104385 \cdot t \\
& - 7.56606633739702 \cdot t^2 94 + 3.92744714101664 \cdot t^3 \\
& - 0.822936579737940 \cdot t^4 94 + 0.0733878803714015 \cdot t^5 \\
& - 0.00236916571951944 \cdot t^6
\end{aligned} \tag{1}
$$

- For pterygoid muscle the acquired motion law was obtained experimentally and can be modeled through a polynomial function as:

$$
\begin{aligned}
M_{2degrees} = & 56.9556461168417 - 1.96871495028217 \cdot t \\
& + 4.05428882061227 \cdot t^2 - 1.70468503612114 \cdot t^3 \\
& + 0.299520826167666 \cdot t^4 - 0.0244013429388200 \cdot t^5 \\
& - 0.000762463712591352 \cdot t^6
\end{aligned} \tag{2}
$$

These polynomial functions are plotted on diagrams on Figs. 5 and 6, by using a MAPLE computation algorithm. For stability control of the virtual model, the human skull will be fixed in space.

4. Contact definition between human skull virtual model components.
5. Masseter, temporal and pterygoid muscle groups modeling, which is assured with spring elements. For these, stiffness, damping factors and preload forces were defined in accordance with [1, 15].
6. Meshing the virtual model components with tetrahedral finite elements type and meshing network control on the critical zones with variable geometry (Fig. 7). This virtual model was conceived in a modular system with the possibility of teeth detaching for implants construction or prosthesis applications.
7. Dynamic response analysis of this system is possible by monitoring stress, displacements and deformations complex behavior for the elements which were considered as deformable ones.

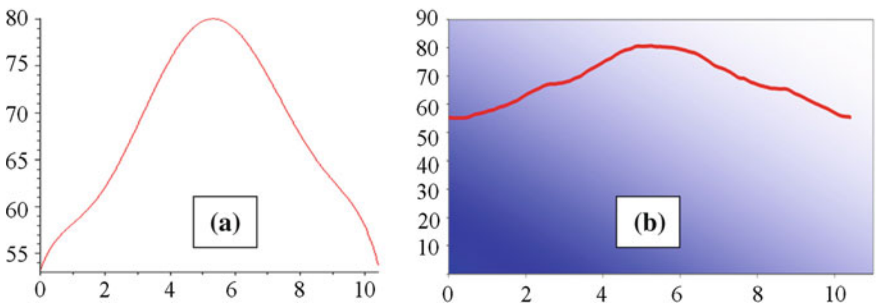

Fig. 5 Human mandible motion law (degrees) for actuating the masseter muscle versus time (seconds): **a** polynomial function with MAPLE algorithm; **b** experimental motion law obtained with CONTEMPLAS equipment

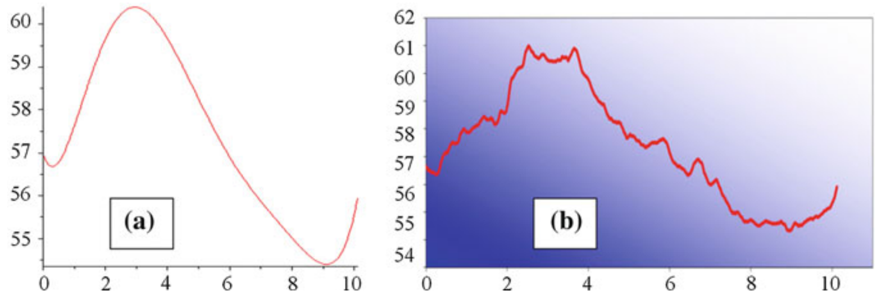

Fig. 6 Human mandible motion law (degrees) for actuating the pterygoid muscle versus time (seconds): **a** polynomial function with MAPLE algorithm; **b** experimental motion law obtained with CONTEMPLAS equipment

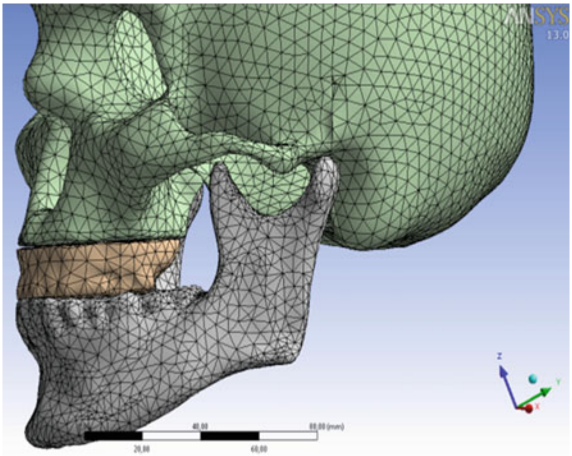

Fig. 7 Parameterized human skull mesh with tetrahedral finite elements type

Thus the dynamic analysis completion is performed in a coupled mode muscle—actuated joint by the possibility of dynamical characteristics of those muscle groups accordingly with [1, 15]. The dynamic models spatial configuration for chosen muscle pairs is shown in Fig. 8.

The mandible motion was experimentally analyzed on a 10 s time interval. The mandible dynamic response analysis was performed for different cases of temporal settings in case of angle variation motions of joints actuated by the pterygoid and masseter muscle groups. The mandible displacements, stress and deformation distributions have been determined for the following cases: virtual model actuated by

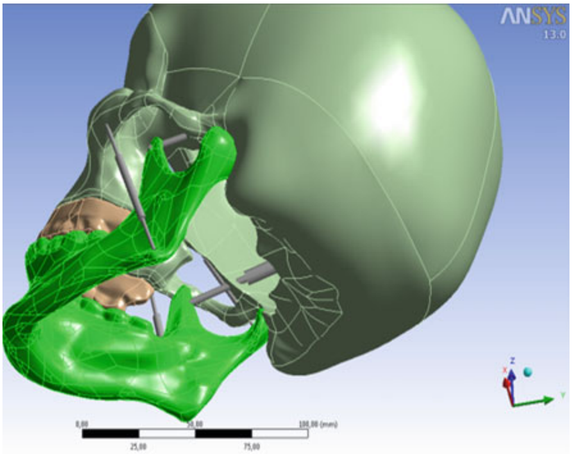

Fig. 8 Dynamic models spatial configuration for the analyzed muscle groups

actuation joints; motion analysis in a joined mode muscles-actuated joints for a complete dynamic model by considering also the damping; dynamic analysis considering the loads applied on molar teeth.

5.1 Dynamic Analysis in a Joined Mode Muscles-Actuated Joints with Dynamic Characteristics Definition of the Three Main Muscle Groups Accordingly with [11]

The dynamic models have been developed for the specified muscle categories (masseter, temporal and pterygoid), according with [1, 15]. So for these (Figs. 9 and 10), the input parameters on dynamic analysis consist in damping and stiffness factors on longitudinal direction, and also load force as it follows: masseter muscle dynamic model (k = 30 N/mm = 4.28 N_xs/m; F = 150 N); temporal muscle dynamic model (k = 6 N/mm = 2.14 N_xs/m; F = 150 N); pterygoid muscle dynamic model (k = 11 N/mm = 2.5 N_xs/m; F = 200 N).

5.2 Dynamic Analysis Considering the Loads Applied on Molar Teeth

For this case which this it is the most important one, a variable loading was considered on inferior molars. This it is conditioned by two situations: all inferior molars are loaded with a pressure which his distribution was appreciated as in

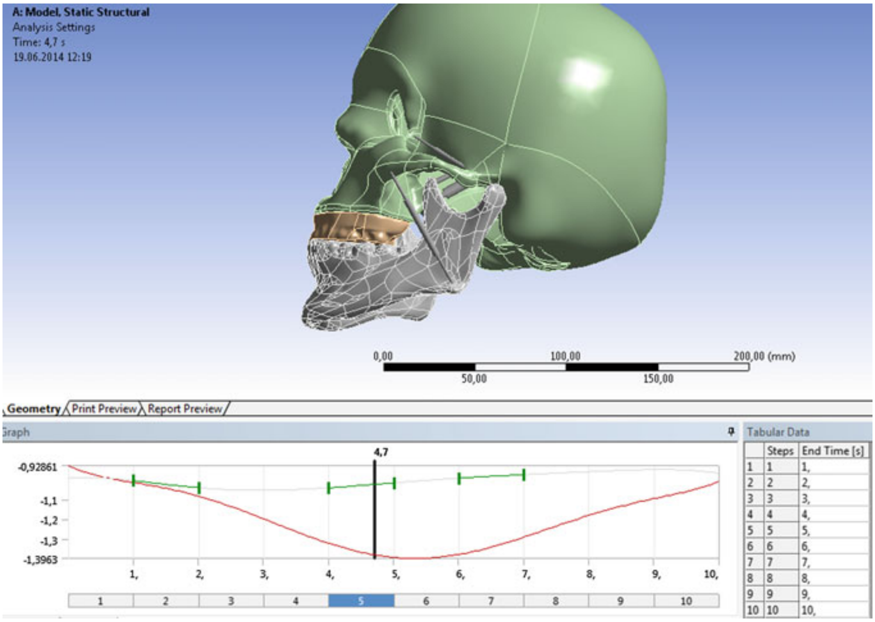

Fig. 9 Setting the dynamic analysis for a time interval of 10 s

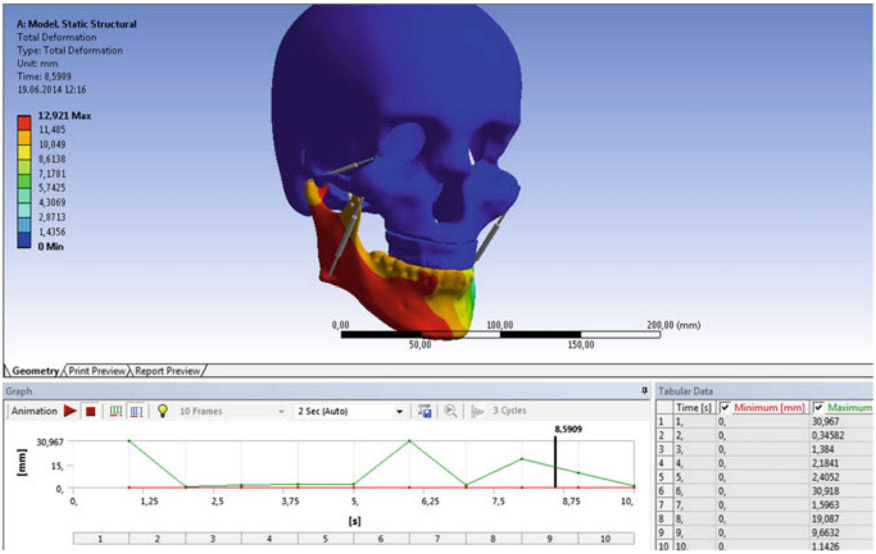

Fig. 10 Resultant displacements distribution (millimeters) according with lateral motion maximum amplitude

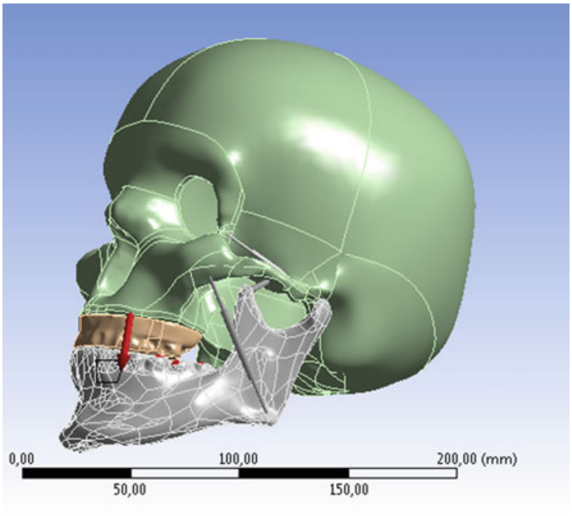

Fig. 11 Molar pressure distribution on mandible structure

Fig. 11 [16]; the main muscle groups (temporal, masseter and pterygoid) are modeled as springs with their main characteristics previously specified. After second case processing, the dynamic response is represented by resultant displacements, deformations and equivalent von Misses stress distributions. Ones are shown in Figs. 12 and 13.

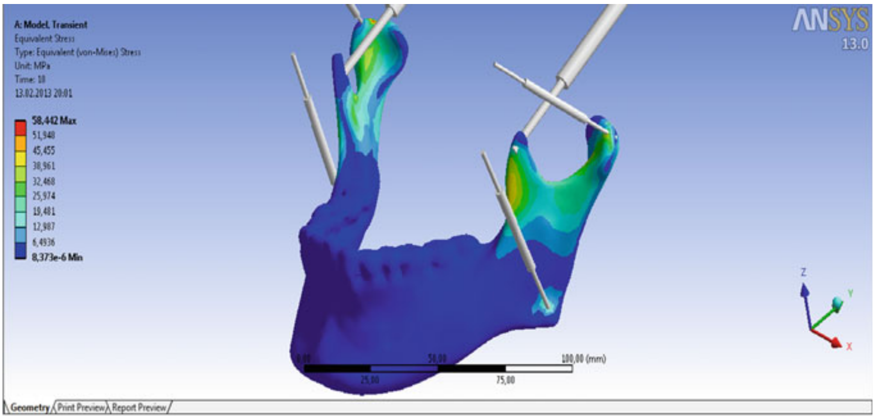

Fig. 12 Von Misses equivalent stress distribution (detail on mandible)

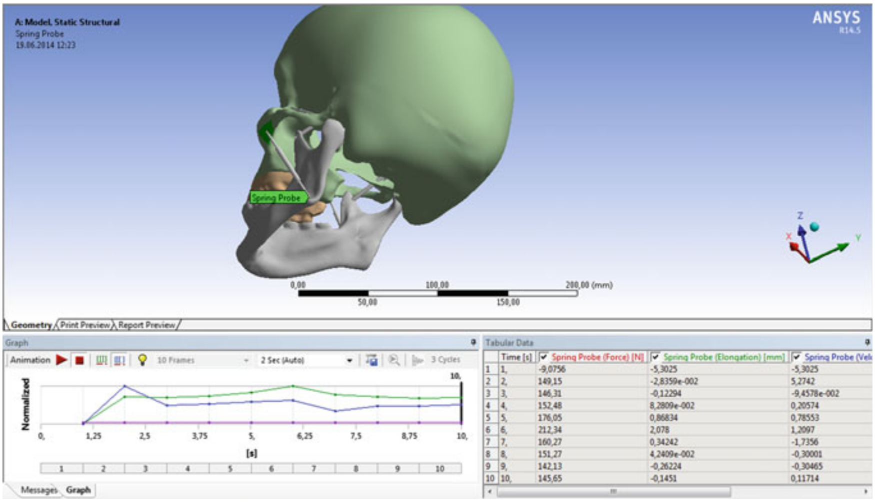

Fig. 13 Kinematic and dynamic parameters distribution for both muscle categories

6 Conclusions

The inverse kinematic analysis was performed by creating a proper equivalent human jaw mechanism system which has 3DOF and it simulates mandible motion in sagittal plane. On the kinematic model, linear actuators were introduced for mobility degrees modeling, in order to substitute the masseter, pterygoids and temporal muscle groups. The kinematic analysis simulation was accomplished by obtaining motion laws for two distinctive cases: motion for solid-rigid body type and deformable body type. Human jaw system dynamic analysis was performed for many mandible motion laws, which were actuated by the chosen muscle groups. Simulations for dynamic analysis were performed by connecting the solid-rigid body type motion with a deformable one. In addition, the mandible dynamic response was performed for different cases of angle variation laws temporal settings from the allocated joints of two muscle groups (masseter and pterygoid). It was considered a time interval for setup the virtual simulations in a dynamic mode. This was 10 s, and represents the same time considered on experimental tests.

The angle motion laws for the guide joints are defined from 0 to 10 s for masseter muscle equivalent model. For the joint actuated through pterygoid muscle, the response time interval was divided in a proper manner for a correct simulation of the chewing process. During this period, mandible was the mobile element, and the obtained results were stress, deformations and displacements for the following cases: actuated model only by drive joints; mandible motion analysis, actuated by muscle groups on a dynamic model without considering the damping coefficients; monitoring the displacements and deformations distribution for a muscle dynamic models defined on deformable elements; dynamic analysis on a coupled mode muscle-drive joints for a complete dynamic model with damping coefficients consideration; dynamic analysis for pressure distribution case when this is variable on teeth.

References

1. Gray H (1992) Anatomy of the human body. Lea & Febiger, Philadelphia
2. Paul L, Gribble M (1997) An examination of the degrees of freedom of human jaw motion in speech and mastication. J Speech, Lang Hearing Res 40:1341–1351
3. Chen X (1998) The instantaneous center of rotation during human jaw opening and its significance in interpreting the functional meaning of condylar translation. Am J Phys Anthropol 106:35–46
4. Yashiro K, Takagi M, Takada K (2003) Kinematic analysis of power-law relationship between jaw movement velocity and curvature. In: Proceedings of IEEE EMBS Asian-Pacific conference biomedical engineering. pp 276–277
5. Yatabe M, Zwijnenburg A, Megens CC, Naeije M (1997) Movements of the mandibular condyle kinematic center during jaw opening and closing. J Dent Res 714–719
6. Epstein M, Herzog W (1998) Theoretical models of skeletal muscle: biological and mathematical considerations. Wiley, Chichester
7. Goto TK, Langenbach GEJ, Hannam AG (2001) Length changes in the human masseter muscle after jaw movement. Anat Rec 262:293–300
8. Beek M, Koolstra JH, van Ruijven LJ, van Eijden TM (2000) Three-dimensional finite element analysis of the human temporomandibular joint disc. J Biomech 33:307–316
9. Hannam AG, Langenbach GEJ, Peck CC (1997) Computer simulation of jaw biomechanics. In: McNeill C (ed) Science and practice of occlusion. Chicago IL, Quintessence, pp 187–194
10. Koolstra JH, van Eijden TM (1997) Dynamics of the human masticatory muscles during a jaw open-close movement. J. Biomech 30:883–889
11. Koolstra JH, Van Eijden TM (2001) A method to predict muscle control in the kinematically and mechanically indeterminate human masticatory system. J. Biomech 34:1179–1188
12. Daryl L (2001) Logan: a first course in the finite element method
13. Dumitru N, Margine Al (2002) Bazele modelarii in ingineria mecanică. Editura Universitaria, Craiova
14. Koolstra JH, van Eijden TM (2005) Combined finite-element and rigid-body analysis of human jaw joint dynamics. J Biomech 38:12
15. Krebs M, Gallo LM, Airoldi RL et al (1994) Three-dimensional animation of the temporomandibular joint. Technol Health Care 2:193–207
16. Weijs WA, Hillen B (1984) Relationship between the physiological cross-section of the human jaw muscles and their cross-sectional area in computer tomograms. Acta Anat 118:129–138

A Robotic Platform for Lower Limb Optical Motion Tracking in Open Space

A. Ortlieb, J. Olivier, M. Bouri and H. Bleuler

Abstract Conventional human motion tracking techniques based on optical systems reports important limitations for mobile applications (e.g. small spatial covering, poor environment flexibility). The present paper addresses a novel approach for optical motion tracking in open space. The measurement unit is transferred from its stationary basis onto a robotic moving platform. The platform design and limitations are described in the first place. It follows a comparative analysis of the measurement data accuracy for the stationary and mobile system. Post-processing techniques to convert acquired motion from the platform coordinate system into the ground's absolute one are evaluated for the specific application of gait analysis.

Keywords Gait measurement · Lower limb · Optical motion tracking · Mobile robot · Mobile measurement system

1 Introduction

Human motion tracking is conceptually very old, however measurement systems appeared only during the late 19th century with the invention of photography. Pioneers in chronophotography, E. Muybridge and E.-J. Marey, allowed the first kinematic analyses of human and animal motion [1, 2]. The development of

A. Ortlieb (✉) · J. Olivier · M. Bouri · H. Bleuler
Ecole Polytechnique Fédérale de Lausanne (EPFL), Laboratory of Robotic Systems (LSRO), Lausanne, Switzerland
e-mail: amalric.ortlieb@epfl.ch

J. Olivier
e-mail: jeremy.olivier@epfl.ch

M. Bouri
e-mail: mohamed.bouri@epfl.ch

H. Bleuler
e-mail: hannes.bleuler@epfl.ch

H. Bleuler et al. (eds.), *New Trends in Medical and Service Robots*,
Mechanisms and Machine Science 38, DOI 10.1007/978-3-319-23832-6_8

technologies took a step further toward acquisition enhancement with cinephotography and, of main importance, data digitization which allows faster and systematic results extraction [3, 4]. Since these three last decades, optical tracking has evolved into different forms from marker-free to passive and active markers solutions. In parallel, non-optical tracking solutions such as IMU (inertial measurement unit) have been developed to propose fully portable solutions [5]. Their main advantages are their ability to cover an unrestricted spatial area, without possible occlusion and the price can be largely reduced in comparison to other technologies. However, optical measurement systems provide more complete data (full position versus only angular position for IMUs) and more robust data compared to IMUs that have drift issues.

Motion tracking has diverse applications in the fields of entertainment, sport, rehabilitation and engineering. This study focuses more on rehabilitation applications where optical tracking with passive markers is still most largely used for precise measurement in a confined environment. Conventional measurement installations are generally made of several camera units placed around a limited specific space [6].

Certain applications such as walking in different conditions or sports as running, skating, Nordic skiing, etc. requires at least a few meters for a relevant tracking. Experimental installations thus employ several cameras to cover a path of a certain length (e.g. 6 m [7], 8 m [8], 10 m [9]) or the activity is performed on a treadmill (e.g. [10, 11, 12 ,13]) with a larger collection of data. However, kinematics can be affected by the use of treadmills compared to over ground activities [14, 15].

The current study proposes the evaluation of a novel technique for optical motion tracking. The key characteristic of the setup being that the measurement unit is mounted on a robotic mobile platform which allows unrestricted spatial coverage. Previous work of Lafontaine and Lamontagne [16] has demonstrated the usability of a camera fastened to a moving rail cart for tracking ice skating performances.

The addressed mobile support is based on a wheeled cart designed for lower limb motion tracking during level-walking on smooth flat or inclined ground. Details about the optical measurement unit and the robotic platform are presented in the following chapter. The method, discussion on the validation and evaluation of the device is made regarding the platform motorization approach and the camera position sensing based on the data accuracy and robustness.

2 Materials and Methods

The material described here has been developed for gait analysis in the context of rehabilitation. The main specifications of this device are:

- Kinematic measurement of the absolute lower limbs positions: the 3-translations and 3-rotations measured with a frequency of over 30 sampling/walking cycle.
- Detection of the heel strike and toe-off events that delimit the stance phase.

The challenge of the proposed work is to develop a robotic platform with desired DOFs (degrees of freedom), i.e. motion in the horizontal plane, and high position sensing precision.

2.1 Optical Tracking

The optical measurement system has to satisfy harsh constraints regarding sensing precision, sampling rate, single or multiple units mounted on a small platform and low risks of occlusion. Technologies that fulfil the best requested specifications are based on active markers [17–19] with multiple linear cameras in one compact box. The Accutrack250® from Atracsys [18] is used in our developed installation with the system and configuration presented and evaluated previously [20]. The measurement setup composed of one 3-linear-camera unit and seven rigid markers is illustrated on Fig. 1.

The constructor claimed specifications of the system are a precision in position of 0.1 ‰ RMS error, a sample rate of 4000 LEDs/s (1 kHz for a single marker) and a maximum coverage of 3 m in depth for approximatively 2 m in width and 2 m in height at a distance of 1.5 m [18]. The principal advantage of the setup configuration is that it can track lower limbs from behind without occlusion with common range of motion with a single measurement unit.

In addition to the motion tracking, sensors to detect the rear and fore foot stance have been developed based on FSR technologies (Force Sensitive Resistor). Two sensing cells per foot are fasten under the heel and the fore foot and connected to the belonging foot marker to synchronize and transmit the data to the measurement unit. The stance information is converted from the FSR analogical signals into a single-digit value using a resistive threshold.

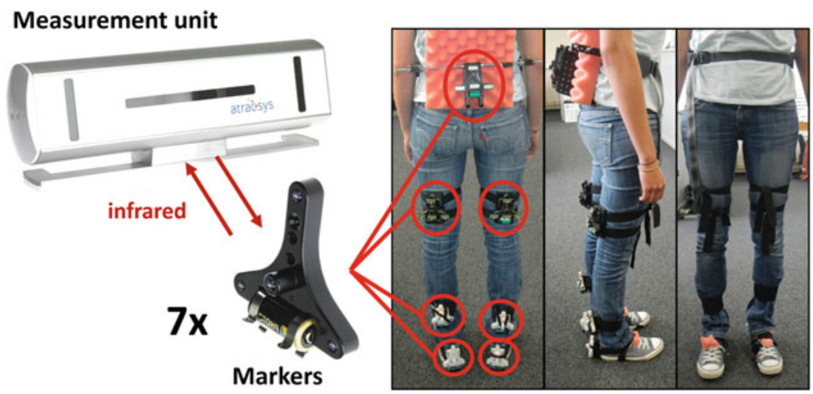

Fig. 1 System used for the motion tracking of the lower limbs composed of one measurement unit and seven markers on the limbs of interest (feet, shanks, thighs and trunk)

2.2 Mobile Robotic Platform

The concept of fastening an optical acquisition unit on a mobile basis is not new and has been used for a few decades in the fields of cinema, sport television or mobile robots for example. Systems moving over a rail are popular in such applications because of their motion stability. However, a rail structure constrains the setup to 1DOF (i.e. translation along the rail axis). In order to track walking freely over ground, a human-like 2DOF motion is adopted. A differential drive robot is thus used with a double DC motors actuation for both front wheels. Forward motion is performed by a synchronous rotation of wheels, while orientation is controlled through left and right wheels differential velocity. Two free wheels are added for the stability and support of the cart (free of rotation and orientation). A schematic representation of the platform can be observed on Fig. 2.

The optical measurement unit is positioned in front of the cart so that it simply needs to follow the walking subject at a regulated distance of roughly 1–2 m. Control of the mobile platform can be performed either autonomously through an embedded computer or manually with the help of someone while the system is turned to passive.

The front two wheels are large and flat iron casts with polymer cover that allow a high stiffness with smooth contact. DC motors and encoders are coupled with these two wheels to afford both actuation and position sensing of the platform. The relative position between the robot and the walking subject is measured through string potentiometers. The string pulley being constrained with a spring, it exerts a small pulling force on the subject (<2 N). The advantage of the string, however, is that there is a mechanical link between the subject and the robot. The subject is thus able to manually unclip the string fasten to his back as in case of emergency, which

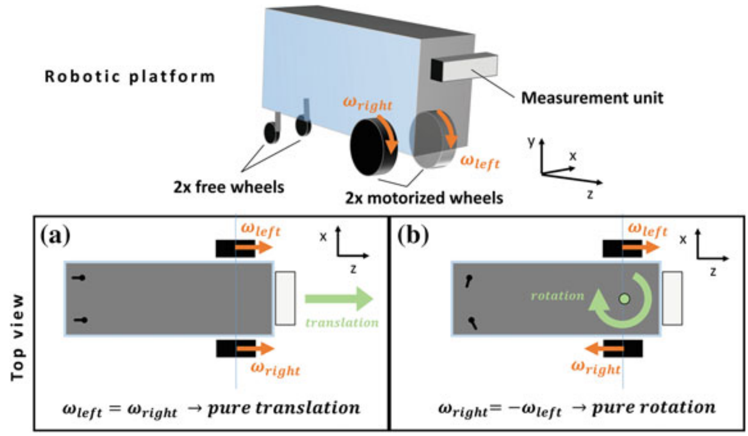

Fig. 2 Scheme of the basic elements of the mobile robotic platform with moving strategies composed of **a** forward/backward motion and **b** rotation in the x-z plane

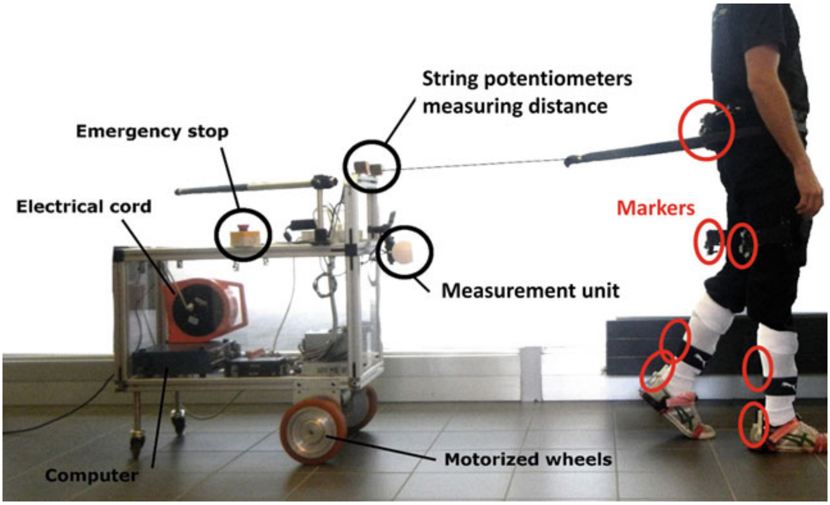

Fig. 3 Illustration of the robotic platform mobilizing the optical tracking system

will result in stopping the controller. Also in normal use, clipping/unclipping the string to the subject will turn on/off the controller which facilitates the setting up phases. The mobile platform can be seen on Fig. 3.

2.3 Control Strategy

The autonomous tracking approach necessitates the use of an embedded controller to orientate and move the cart forward/backward so that it aligns with the subject direction and stays at a defined distance from him. The other specifications for the controller are smooth and non-oscillating motion to afford a high stability of the measurement unit. The controller is implemented on a windows XP® computer using a real time extension (RTX from IntervalZero™) to ensure a constant 1 kHz sampling frequency. Motors are controlled in current/torque mode with a PD position-velocity controller implemented with feedback from the encoders mounted on the motors. The position set-points are functions of the relative position of the subject from the mobile platform. In order to provide informations for both backward/forward motion and change of direction, two string potentiometers are used. Their bases are mounted on the front of the cart at each corner and the strings' ends are bounded together so that it forms a triangle (see Fig. 4) which is clipped to the subject's back.

The difference in length between both strings provides a quasi-linear function of the relative angle between the subject and the platform orientation (for a restricted

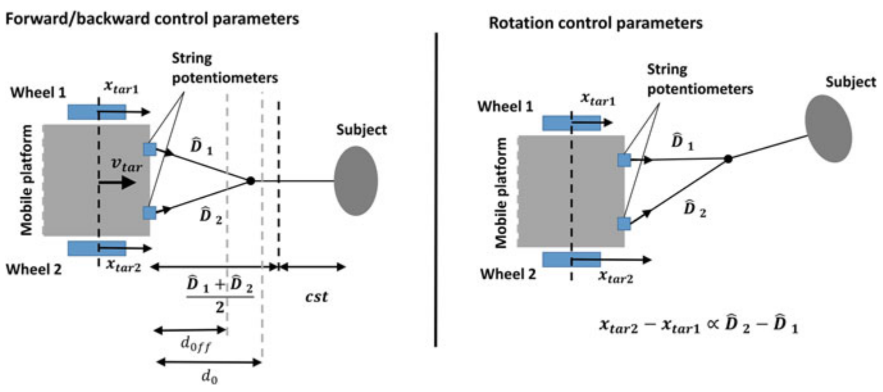

Fig. 4 Illustration of the mobile platform motion control parameters based on the subject relative position measured using two string potentiometers

angle range of ±45°). In complementarity, the mean of both string length allows to approximate the relative distance between the cart and the subject. The set-point of the controller are found in (1–3).

$$v_{tar} = c_v \cdot (\frac{\hat{D}_1 + \hat{D}_2}{2} - d_0) \quad (1)$$

$$x_{tar1} = \hat{x}_1 + v_{tar} \cdot \Delta t + c_\alpha \cdot (\hat{D}_1 - \hat{D}_2) \quad (2)$$

$$x_{tar2} = \hat{x}_2 + v_{tar} \cdot \Delta t - c_\alpha \cdot (\hat{D}_1 - \hat{D}_2) \quad (3)$$

Parameters are illustrated on Fig. 4. v_{tar} is the velocity set-point for both wheels, x_{tar1} and x_{tar2} are the position set-point for each wheels, $\hat{D}_1$ and $\hat{D}_2$ are the measured string potentiometer length, d_0 is a constant offset, c_v and c_a are positive coefficients, $\hat{x}_1$ and $\hat{x}_2$ are the wheels measured current position and Δt is the constant time step of 1 ms. To allow the platform to freeze as the string potentiometers are not clipped or unclipped from the subject, a sub-threshold condition (4) turns Eqs. (2) and (3) into (5).

$$if \quad \frac{\hat{D}_1 + \hat{D}_2}{2} < d_{off} \quad (4)$$

$$for \ i = 1, 2 \quad x_{tar\_i} = \hat{x}_i \quad (5)$$

where d_{off} is the sub-threshold value. A distinctive point of this controller is that the position set-points are dynamic (e.g. if the cart is manually moved it will stop at its new position and not come back to the previous position).

To provide a stable motion, filtering data is crucial, especially for the distance measurement between the platform and the subject's body, because the trunk has fast cyclic oscillations ($\sim$1 Hz) during walking. A simple average over the last 200 values has demonstrated good smoothing results for $\hat{D}_1$ and $\hat{D}_2$ with an acceptable delay (i.e. $\sim$100 ms) regarding the application.

3 Mobile to Ground Coordinates

The tracking unit being mobile, data acquired are dependent from the cart position and thus results need to be mapped into the ground coordinate frame to have an absolute positioning. The motion of the cart is assumed to be purely planar (any translation along the plane parallel to the ground (2DOFs) and rotation around the axis perpendicular to the ground (1DOF)). Geometry is simplified by stating that the mobile coordinate frame has 3DOFs which are translations along the x- and z-axes, plus one rotation around the y-axis (see Fig. 5 for the coordinate systems definition). The tracking system measures the data consisting in the vector $\hat{\vec{p}}$ and the matrix of rotation $\hat{R}_{p\_xyz}$ (Fig. 5). In order to determine the position in ground coordinate $\vec{p}'$, information about $\vec{s}'$ and matrix of rotation $R_{y'}$ are needed (i.e. the tracking unit position and orientation in the ground coordinate).

Two methods have been evaluated to determine the tracking unit position. The first technique used odometry, the rotation of the wheels measured by the encoders are used to define the cart position. The second approach, which is dependent from the application, consists of detecting one event or phase for which the motion is precisely known. In the case of walking, the foot still motion during stance can be detected from the angular velocity. The robot motion can then be easily extracted as the foot is fix in the ground coordinate. A drawback of this approach is that the combination of right and left mid-stance does not cover 100 % of a cycle, implying a short time of uncertainty on the motion.

The general equation for the calculation of $\vec{p}'$ and $R'_{p'\_xyz}$ which are the marker position and orientation expressed in the ground frame are given for both approaches in (6) and (7).

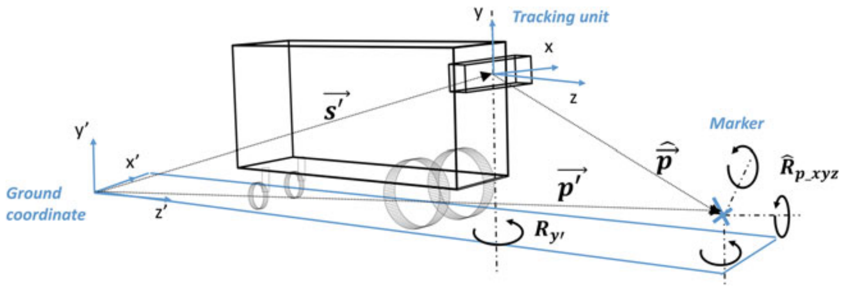

Fig. 5 Schema of the ground, the mobile platform and the marker and their coordinate frames

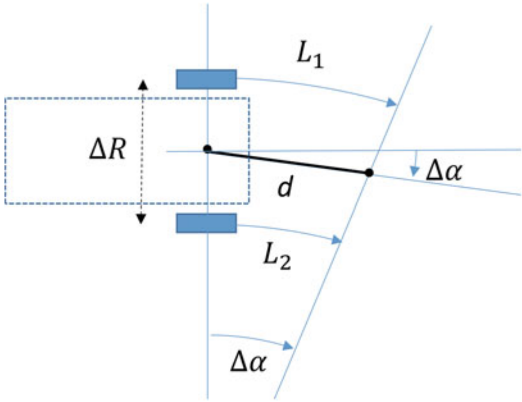

Fig. 6 Schema of the motion of the robotic platform and definition of the parameters

$$\vec{p}' = \vec{s}' + R_{y'} \cdot \hat{\vec{p}} \tag{6}$$

$$R'_{p'\_xyz} = R_{y'} \cdot \hat{R}_{p\_xyz} \tag{7}$$

For the first method, the position and orientation of the cart is incrementally calculated at each time step from each wheel displacement following Eqs. (8–11).

$$\Delta\alpha = \frac{\hat{L}_2 - \hat{L}_1}{\Delta R} \tag{8}$$

$$d = (\frac{2\hat{L}_1}{\Delta\alpha} + \Delta R) \cdot \sin(\frac{\Delta\alpha}{2}) \tag{9}$$

$$\alpha_i = \alpha_{i-1} + \Delta\alpha \tag{10}$$

$$\vec{s}_i = \vec{s}_{i-1} + R_{y'} \cdot d \cdot \vec{e}_z \tag{11}$$

where α is the angle defining the orientation of the robot ($R_{y'}$). $\hat{L}_1$ and $\hat{L}_2$ are both wheel displacements for a time step and ΔR is the constant distance between both wheels rotation axis. These parameters are geometrically represented on Fig. 6.

For the second approach, for the given marker, its position and orientation in the ground coordinate are constant over two time steps. Let's denote i and $i-1$ the two time steps of interest, the Eqs. (6) and (7) can be rearranged under conditions (12) and (13) to obtain (14) and (15).

$$\vec{p}'_i - \vec{p}'_{i-1} = 0 \tag{12}$$

$$R'_{p'\_xyz_i} \cdot R'^{-1}_{p'\_xyz_{i-1}} = I \tag{13}$$

$$\vec{s}'_i = \vec{s}'_{i-1} + R_{y'_{i-1}} \cdot \hat{\vec{p}}_{i-1} - R_{y'_i} \cdot \hat{\vec{p}}_i \tag{14}$$

$$R_{y'_i}^{-1} = \hat{R}_{p\_xyz_i} \cdot \hat{R}^{-1}_{p\_xyz_{i-1}} \cdot R_{y'_{i-1}} \tag{15}$$

where I is the identity matrix. Note that (15) should be calculated first in order to calculate (14). The material to solve both methods being presented, following results will highlight the practical differences between them.

4 Results

With the aim of validating the mobile measurement system, we propose a first comparison of the raw data collected by the tracking unit once in stationary mode with the subject walking on a treadmill and on the other hand with the mobile platform and on ground walking. Two observations are of main importance: the average acquisition frequency and the stability of the measurements. The latter is expressed in terms of standard deviation evaluated between the raw data and smoothen data, which indicates the noise affecting the data. To observe these parameters, tests on treadmill and over ground were performed at similar velocities. The fitting method employed is a smoothing spline function [21] with a p parameter of value 0.9999. Results are summarized in Table 1 for the stationary measurement at 2.5 km/h of walking on treadmill, in Table 2 for the corresponding mobile measurement over ground, in Table 3 for stationary measurement again but at 3.5 km/h and in Table 4 for mobile measurement approaching 3.5 km/h.

Table 1 Observation with the stationary measurement unit of walking on treadmill at 2.5 km/h

Limb	Position STD (mm)	Angle STD (°)	Average global acqu. freq. (Hz)	Time percentage of occlusion (%)
Right foot	1.1364	0.5844	87.19	6.40
Left thigh	0.7289	0.3792	Average acqu. freq. w/o occlusion (Hz)	Average occlusion duration (ms)
Trunk	0.3198	0.2830		
Average	0.7284	0.4156	91.44	39.9

Table 2 Observation with the mobile measurement unit of walking over ground at 2.5 km/h

Limb	Position STD (mm)	Angle STD (°)	Average global acqu. freq. (Hz)	Time percentage of occlusion (%)
Right foot	2.7148	2.1044	36.00	60.60
Left thigh	1.9721	0.3185	Average acqu. freq. w/o occlusion (Hz)	Average occlusion duration (ms)
Trunk	3.4936	0.1922		
Average	2.7269	0.8717	82.40	171.17

Table 3 Observation with the stationary measurement unit of walking on treadmill at 3.5 km/h

Limb	Position STD (mm)	Angle STD (°)	Average global acqu. freq. (Hz)	Time percentage of occlusion (%)
Right foot	1.9897	0.8812	71.64	20.56
Left thigh	1.1896	0.4389	Average acqu. freq. w/o occlusion (Hz)	Average occlusion duration (ms)
Trunk	0.4835	0.2881		
Average	1.2209	0.5361	84.16	51.39

Table 4 Observation with the mobile measurement unit of walking over ground at 3.5 km/h

Limb	Position STD (mm)	Angle STD (°)	Average global acqu. freq. (Hz)	Time percentage of occlusion (%)
Right foot	2.3921	0.7411	37.25	67.72
Left thigh	1.4716	0.5079	Average acqu. freq. w/o occlusion (Hz)	Average occlusion duration (ms)
Trunk	0.9302	0.2705		
Average	1.5980	0.5065	105.22	206.17

Observations are made for the right foot, the left thigh and the trunk. The standard deviation average over the three direction positions and over the three angular positions are presented to evaluate the measurements stability. Moreover four observations are drawn to investigate the temporal resolution:

- The average global acquisition frequency, which is the number of data collected over the time elapsed.
- The average acquisition frequency without occlusion, which is the number of data collected over the time elapsed without occlusions.
- The time percentage of occlusion, which is the sum of all occlusion duration divided by the total time elapsed.
- The average occlusion duration, which is the sum of all occlusion duration divided by the number of occlusions.

Note that, relatively to the theoretical measurement unit sampling frequency and experimental results, an occlusion is detected if the time elapsed between two acquisition (for the same marker) overpass a threshold of 30 ms.

The results presented in Tables 1, 2, 3 and 4 show that the average global acquisition frequency is 50 % smaller for the mobile system compared to the stationary one. However, the average acquisition frequency without acquisition is approximately constant among both procedures. In contrast, a distinctive difference in time of occlusion is recorded with an important percentage for the overground measurements compared to the one on treadmill.

For both position and angle, a correlation with the type of measurement or the walking speed is not obvious even if the mobile system appears to be noisier. Nevertheless standard deviation seems highly correlated to the limbs (distal limbs have bigger standard deviation). These observations will be discussed in the next section.

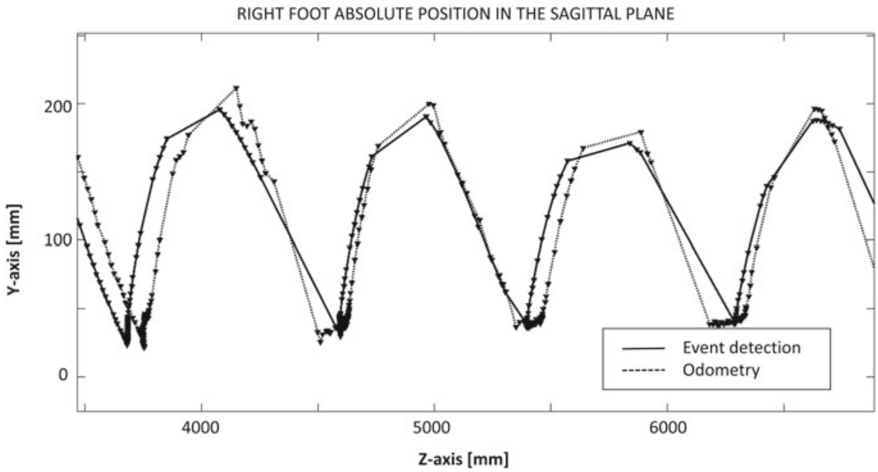

Fig. 7 Comparison of the absolute position of the right foot in the sagittal plane using two different post-processing methods: foot stance detection and odometry of the platform

Other observations are made to assess the quality of the methods to map the position data into the ground coordinate frame. Figure 7 illustrates a sampling over 4 cycles of the right foot position in the sagittal plane during walking with results of both methods. A divergence of up to 90 mm can be observed between the odometry and the stance reconstruction technique. Looking at bigger sampling, however, it is interesting to see that there is no cumulative increase of the error over the cycles. Figure 7 also highlights the fact that the error is generated around the stance phase (lower position in the y direction). Typically, the stance of the last cycle on Fig. 7 shows a translation in the z direction of more than 100 mm while the foot is in contact with the ground.

5 Discussion

The present study assessed the performances of an optical measurement tracking unit extended to open space environment based on a wheeled mobile platform. Results expressed in Tables 1, 2, 3 and 4 compared the static versus the mobile characteristics of the same measurement unit. They revealed that the sampling rate for the mobile system reached half of the performances of the static one. This difference can be attributed to a higher occlusion percentage of time as illustrated by the results. Occlusion, however, is more likely to be attributed to the subject's gait as the view angle does not change much from the stationary to the mobile setup. The average acquisition frequency without occlusion, which can be associated to the measurement unit sampling performances, demonstrated a constancy regardless of the mobility of the system. Globally, a percentage of occlusion of up to 60 % for a walking cycle frequency close to 1 Hz is tolerable but lower occlusion time as expected will increase the consistency of the data.

Position and angle measurements indicated that the mobile platform slightly affects the position measurement stability whereas the noise amplitude on the angle measurement were comparable. As demonstrated by the fact that more distal limbs have noisier data, the measurement unit is sensitive to the relative velocity of the markers. As the mobile device theoretically does not increase the relative velocity between the markers and the tracking unit, the small instability increase of the position measurement can be attributed to the ground irregularities that affected the mobile platform. The lower sampling frequency also could have played a role in the data irregularities. However, what can be highlighted here is the robustness of the angle measurement with a standard deviation close to 0.5° independently from the nature of the tracking.

Parallely, the reliability of the data reconstruction in the ground coordinate frame has been observed through two techniques, one based on the platform self-positioning and the other based on typical gait phase such as stance. The two approaches showed important variances for position but which are not so significant in term of velocity. Concerning the odometry approach, the robot controller communication sampling frequency is one of the issue that can explain some error and some solutions will be investigated. In the other hand, the phase detection approach is limited towards certain applications, thus both techniques can be implemented relatively to the context of the study.

The present study revealed the possibility of extending a tracking measurement unit toward open space applications on flat smooth ground. Such a system has a serious potential for clinical study where large set of data are needed and overground measurements are preferred. It can also compete to embedded measurement solutions for certain applications because of its robustness and completeness of kinematic information (i.e. limbs position and orientation).

Acknowledgments The study was supported by NCCR robotics, the National Center of Competence in Research (Switzerland), the ASRIM (Association Suisse Romande et Italienne contre les Myopathies) and the FSRMM (Fondation Suisse de Recherche sur les Maladies Musculaires).

References

1. Muybridge E (1887) Animal locomotion. An electro-photographic investigation of consecutive phases of animal movements (1872–1885). http://www.loc.gov/pictures/item/31004968/. Accessed 08 Nov 2014
2. Marey E-J (1873) La machine animale, locomotion terrestre et aérienne. G. Baillie, Paris
3. Whittle MW (1982) Calibration and performance of a 3-dimensional television system for kinematic analysis. J Biomech 15(3):185–196
4. Whittle MW (1996) Clinical gait analysis: a review. Hum Mov Sci 15(3):369–387
5. Zhou H, Hu H (2008) Human motion tracking for rehabilitation—a survey. Biomed Signal Process Control 3(1):1–18

6. Menache A (2004) Motion tracking system and method
7. DeVita P, Hortobagyi T (2000) Age causes a redistribution of joint torques and powers during gait. J Appl Physiol 88(5):1804–1811
8. Kirtley C, Whittle MW, Jefferson RJ (1985) Influence of walking speed on gait parameters. J Biomed Eng 7(4):282–288
9. Thomas M, McPherson M, Thayer R (1995) Offset skating characteristics of world cup level cross-country skiers. In: ISBS-conference proceedings archive, vol 1, no 1
10. Danion F, Varraine E, Bonnard M, Pailhous J (2003) Stride variability in human gait: the effect of stride frequency and stride length. Gait Posture 18(1):69–77
11. Thelen DG, Chumanov ES, Hoerth DM, Best TM, Swanson SC, Li L, Young M, Heiderscheit BC (2005) Hamstring muscle kinematics during treadmill sprinting. Med Sci Sports Exerc 37(1):108–114
12. Stoquart G, Detrembleur C, Lejeune T (2008) Effect of speed on kinematic, kinetic, electromyographic and energetic reference values during treadmill walking. Neurophysiologie Clinique/Clinical Neurophysiology 38(2):105–116
13. Nessler JA, Leone CJD, Gilliland S (2009) Nonlinear time series analysis of knee and ankle kinematics during side by side treadmill walking. Chaos Interdiscip J Nonlinear Sci 19 (2):026104
14. Alton F, Baldey L, Caplan S, Morrissey MC (1998) A kinematic comparison of overground and treadmill walking. Clin Biomech 13(6):434–440
15. Wank V, Frick U, Schmidtbleicher D (1998) Kinematics and electromyography of lower limb muscles in overground and treadmill running. Int J Sports Med 19(07):455–461
16. Dany Lafontaine ML (2010) 3-D kinematics using moving cameras. Part 1: development and validation of the mobile data acquisition system. Hum Kinet J. http://journals.humankinetics.com/jab-back-issues/jabvolume19issue4november/3dkinematicsusingmovingcameraspart1development-andvalidationofthemobiledataacquisitionsystem. Accessed 12 Nov 2014
17. Codamotion-Movement Analysis. http://www.codamotion.com/. Accessed 10 Nov 2014
18. Atracsys-accuTrack 250. http://atracsys.com/_products/accuTrack_compact.php. Accessed 14 Apr 2014
19. Measurement Sciences Products-Measurement Sciences. http://www.ndigital.com/msci/products/#optical-measurement. Accessed 10 Nov 2014
20. Ortlieb A, Olivier J, Bouri M, Bleuler H (2014) Evaluation of an active optical system for lower limb motion tracking. 3D AHM, Lausanne
21. Craven P, Wahba G (1978) Smoothing noisy data with spline functions. Numer Math 31 (4):377–403

Part II
Surgical Robotics

Virtual Planning of Needle Guidance for a Parallel Robot Used in Brachytherapy

B. Gherman, T. Girbacia, D. Cocorean, C. Vaida, S. Butnariu, N. Plitea, D. Talaba and D. Pisla

Abstract Brachytherapy (BT) is an innovative cancer treatment option that allows the delivery of high doses of radiation to specific areas of the body. BT has an important advantage: it doesn't irradiate unnecessarily healthy tissue, but focalizes mainly on the destruction of tumorous cells. The paper presents an innovative parallel robot designed for BT and a needle trajectory planning software. The algorithm designed for virtual planning of robotic needle insertion allows automatic or manual definition of the needles trajectory. A virtual reality environment has been modelled and simulations using a real needle trajectory have been conducted.

Keywords Parallel robot · Virtual reality · Brachytherapy · Trajectory planning

B. Gherman · D. Cocorean · C. Vaida · N. Plitea · D. Pisla (✉)
Technical University of Cluj-Napoca, Cluj-Napoca, Romania
e-mail: Doina.Pisla@mep.utcluj.ro

B. Gherman
e-mail: Bogdan.Gherman@mep.utcluj.ro

D. Cocorean
e-mail: Dragos.Cocorean@mep.utcluj.ro

C. Vaida
e-mail: Calin.Vaida@mep.utcluj.ro

N. Plitea
e-mail: Nicolae.Plitea@mep.utcluj.ro

T. Girbacia · S. Butnariu · D. Talaba
Transilvania University of Brasov, Brasov, Romania
e-mail: Teodora.Girbacia@unitbv.ro

S. Butnariu
e-mail: Butnariu@unitbv.ro

D. Talaba
e-mail: Talaba@unitbv.ro

H. Bleuler et al. (eds.), *New Trends in Medical and Service Robots*,
Mechanisms and Machine Science 38, DOI 10.1007/978-3-319-23832-6_9

1 Introduction

Cancer treatment contains numerous forms, according to the specific type of tumorous cells, interested organs or body areas, etc. Some of the most used cancer treatment methods involve chemotherapy, radiotherapy, surgery or combinations between them. These are all efficient ways of curing cancer, but in some cases, especially when the patient is very weak, the implied side effects may produce more damage than benefits. Brachytherapy (BT) is a relatively new approach in the fight against cancer using local radiation [6]. Thus, instead of irradiating a large area of the patient's body, using BT only the tumorous cells are irradiated. BT effectiveness has been demonstrated over the years, bringing good results, but it is conditioned by the following restriction: the BT needle must be precisely placed, since the radiation dose decreases abruptly from the base and an incorrect position leads to the damage of healthy tissue [17]. BT is commonly used as an effective treatment for cervical, prostate, breast, and skin cancer and can also be used to treat tumours in many other body sites [20, 21].

In [11] it has been shown that a robotic device enhances the needle placement precision beyond the natural human capabilities. In this sense, the positioning of the BT device becomes a challenging task where the use of a robotic device can extend the applications of this technique. In the pre-planning procedure, an important issue is the geometrically identification of the optimal trajectories, in order to avoid puncturing vital organs (bones, important blood vessels, internal organs, etc.).

Therefore, the new developed parallel robot offers a viable solution for the treatment of cancer patients considered inoperable or when their general status does not allow an aggressive treatment.

By far, robot-assisted BT seems to be a preferred technique for prostate cancer treatment. There are many studies [2, 20, 22] and medical centres which offer BT as a specific treatment for prostate cancer. H. Bassan et al. described in [1] the design of a 5-DOF (degrees of freedom) hybrid robotic system that performs 3D ultrasound guided percutaneous needle insertion surgery. Experiments using a prostate phantom were achieved by Fichtinger et al. in [5] and the results proved the technical viability of robot-assisted BT. Podder et al. in [15] presents the MIRAB robotic system for prostate BT. MIRAB, a 6-DOF robotic system, is capable of inserting and rotating 16 needles concurrently and depositing seeds autonomously according to the dosimetric plan. Bernardes et al. studied in [3] a robot-assisted approach for automatic steering of flexible bevelled needles in percutaneous procedures.

Virtual Reality is not only a tri-dimensional environment, but also a new instrument that offers solutions to the existing problems in medicine or other fields. Programming the trajectory of a robot for BT is a difficult task, due to the geometric and topologic complexity of the 3D model of the patient and to the multiple parameters of the BT procedure. In previous researches, VR technologies have been used just for learning BT procedure through haptic simulation [7–9] and to simulate the positioning of needles required for manual BT procedure [10, 18]. The novelty of this research consists in the use of Virtual Reality technology (VR) for defining preoperative trajectories for the proposed robotic system.

The paper is organised as follows: Sect. 2 presents the parallel robot for BT; Sect. 3 describes the virtual environment and algorithms for virtual planning of robotic needle insertion; Sect. 4 presents some simulations results in Siemens NX using a real needle trajectory; some conclusions and future work are presented in the last section.

2 The PARA-BRACHYROB Parallel Robot for Brachytherapy

The critical analysis of the latest achievements in robotic assisted BT has shown that the already developed structures are built for specific organs and moreover almost all are targeting the prostate [12]. In order to make possible a universal technique for cancer treatment on several organs of human body within BT, a new parallel robot has been developed.

The PARA-BRACHYROB parallel robot for BT has derived from the structure presented in [13, 14], by adding an additional, redundant 1-DOF mechanism represented by the q_6 active joint, dedicated for the needle insertion. The kinematic scheme of the robot is presented in Fig. 1. PARA-BRACHYROB is a cylindrical parallel robot having 5-DOF and two modules: the first one has 3-DOF and 3 active joints, namely: q_1, q_2, q_3 while the second one has 3-DOF and 2 active joints, namely: q_4, q_5. Each module works in cylindrical coordinates. Coordinates q_1, q_2

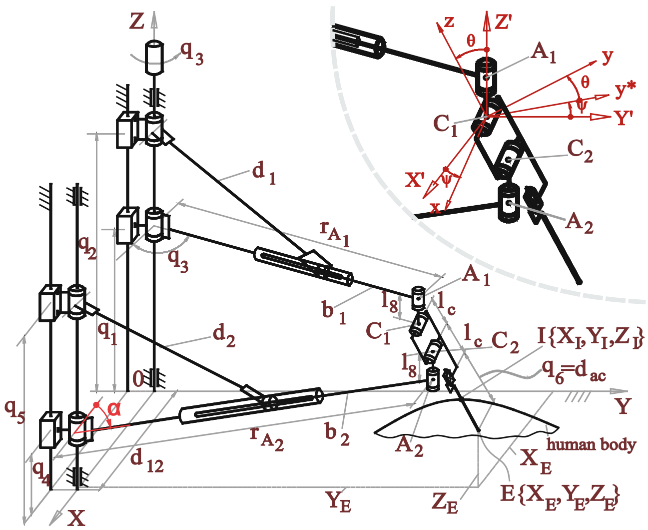

Fig. 1 The kinematic scheme of PARA-BRACHYROB parallel robot for brachytherapy

and q_4, q_5 represent prismatic joints along an axis parallel with OZ, while the third motion of each module is a rotation around the same axis. The first rotation joint, q_3 is an active joint, while the second rotation joint (for the second module) is a passive joint.

At the end points of the two modules, denoted with A_1 and A_2, a fixed coordinate system is introduced, namely OXYZ, with the Z axis along the active rotational axis of the first module. The two modules are interconnected with two passive Cardan joints. Both Cardan joints have the first rotation axis around the Z axis and the second one perpendicular on it. These two joints are connected through the element that guides the needle holder. This element includes the q_6 active joint, a prismatic actuator which allows the insertion of the BT needle between the insertion points into the patient's body end the target points, inside the tumour. During the needle insertion, all other five actuators are locked (fixed in position).

Having as input the geometric parameters as presented in Fig. 1: $d_1, b_1, l_1, d_2, b_2, l_2, l_c$, the closure equations of the PARA-BRACHYROB parallel robot for BT, used for the kinematics, can be defined as follows:

$$f_1 : Z_E + l_1 + (q_6 + 2 \cdot l_c) \cdot \cos(\theta) - q_1 = 0 \tag{1}$$

$$\begin{aligned} f_2 : X_E - (q_6 + 2 \cdot l_c) \cdot \sin(\theta) \cdot \cos(\psi) - \\ - \left[b_1 + \sqrt{d_1^2 - (q_2 - q_1)^2} \right] \cdot \cos(q_3) = 0 \end{aligned} \tag{2}$$

$$\begin{aligned} f_3 : Y_E - (q_6 + 2 \cdot l_c) \cdot \sin(\theta) \cdot \sin(\psi) - \\ - \left[b_1 + \sqrt{d_1^2 - (q_2 - q_1)^2} \right] \cdot \sin(q_3) = 0 \end{aligned} \tag{3}$$

$$f_4 : Z_E - l_2 + (q_6 + l_c) \cdot \cos(\theta) - q_4 = 0 \tag{4}$$

$$\begin{aligned} f_5 : & \, d_{12}^2 + X_E^2 + Y_E^2 + (q_6 + l_c)^2 \cdot \sin^2(\theta) - \\ & - 2 \cdot (q_6 + l_c) \cdot \sin(\theta) \cdot [(X_E - d_{12}) \cdot \cos(\psi) + Y_E \cdot \sin(\psi)] \\ & - 2 \cdot d_{12} \cdot X_E - b_2^2 - d_2^2 + (q_5 - q_4)^2 - 2 \cdot b_2 \cdot \sqrt{d_2^2 - (q_5 - q_4)^2} = 0 \end{aligned} \tag{5}$$

In the Eqs. (1–5), $E(X_E, Y_E, Z_E)$ represents the needle's tip coordinates, ψ and θ the needle's orientation (Euler angles, with ψ being the rotation around OZ axis and θ around the Ox axis—see Fig. 1). The active coordinate q_6 is considered as a constant parameter due to its redundancy (it is used only for needle insertion, while all other actuators are locked in place), thus leading to only five closure equations.

Based on the kinematic scheme defined in Fig. 1, computer modelled design (CAD model) of the PARA-BRACHYROB parallel robot was achieved (Fig. 2). It must be capable of manipulating the needle under CT-Scan guidance and the needle module must fit insider the CT-Scan gantry to enable real-time guidance and procedure monitoring.

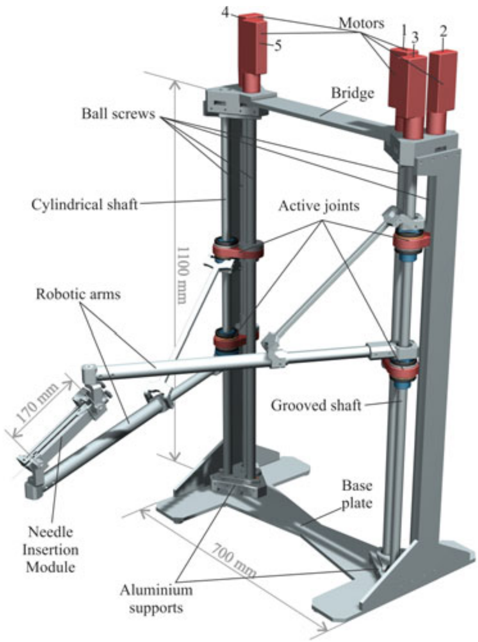

Fig. 2 The CAD model of PARA-BRACHYROB parallel robot for brachytherapy

The robotic structure sits on an aluminium plate frame supported by a baseplate which can be fixed to the CT table, with the main 5 active joints (motors) fixed to the top of the frame from where these are referenced (Fig. 2). The needle insertion modules motion will be obtained by rotating the ball screws or grooved shaft held by bearings connected to the fixed frame, necessary for a smooth motion at the active joints.

3 Needle Trajectory Definition for Brachytherapy

Compared to other pre-planning applications for robotic needle insertion presented in [4, 16], the novelty of the present approach is the possibility to generate automatically, using VR techniques, linear trajectories for the proposed robotic system that allows the avoidance of the proximity with high risk areas. In order to validate the generated trajectories for the needles we take into account as a simplifying hypothesis that all the bodies are considered to be perfectly rigid. The interaction between the needle and the human tissues is not simulated and it is a subject for further research activities. In the case of pre-planning for surgery, the main purpose is to achieve a virtual scene containing, on one hand, the necessary equipment in a real case intervention and, on the other hand, the 3D reconstructed model of the patient.

Virtual environment modeling The first step consists in modeling a 3D virtual environment, containing classical intervention equipment for surgery: surgical table, tables for medical instruments, surgical equipment, light sources, bed for patient transport, monitor, defibrillators, infusion support, infusion and medical equipment of specialized BT procedure: BT needle, guiding template (Fig. 3a). The next step was the integration of 3D anatomical models of two patients. Another virtual room was modelled and used to simulate the BT procedure in an imaging investigation setup consisting of: virtual room, CT—LigthSpeed 16 RT equipment and the patient (Fig. 3b).

Patient modelling The DICOM files, obtained after using computer tomography (CT), are used as input data for the 3D reconstruction of the patient's body. The segmentation technique (the separation and labelling of anatomical structures images and saving them in different layers) has been used when applications require the conversion of 2D slice type images into 3D models. Segmentation results are individual 3D surfaces with topological labels further saved as *.wrl* type file (VRML—Virtual Reality Modelling Language). A model obtained in this technique is shown in Fig. 4. Using the reconstructed 3D model of the patient, integrated in the virtual environment of an operating room, the BT procedure can be simulated, establishing the trajectory of the needles.

Algorithms for virtual planning of robotic needle insertion The interaction with the robotic system consists in the development of algorithms and implementation of software tools that allow the definition of linear trajectories for the robot which avoid the proximity with high risk areas. The algorithms for virtual planning of robotic needle insertion allow manual or automatic definition of the needles trajectory (Fig. 4) for every target point.

In order to determine the intersection between the linear trajectories of robot and the high risk areas a "ray-hit" collision detection algorithm was used. This algorithm allows the detection of the contact between a linear segment and the triangles of the virtual object mesh. On the linear segment, control points used for collision detection will be defined. The algorithm will provide the intersection point between

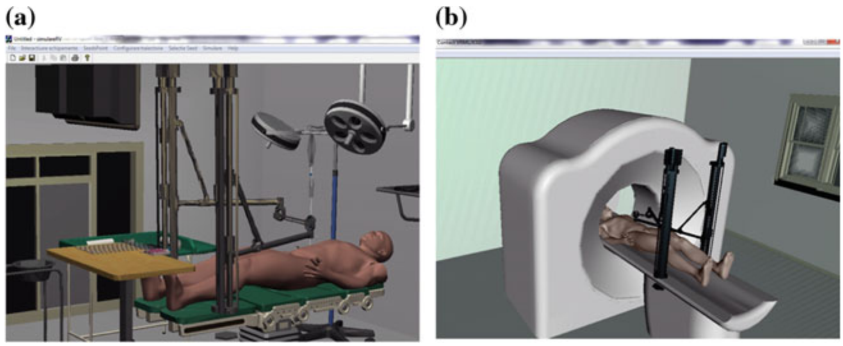

Fig. 3 Virtual environment modelling for the robotic brachytherapy pre-planning

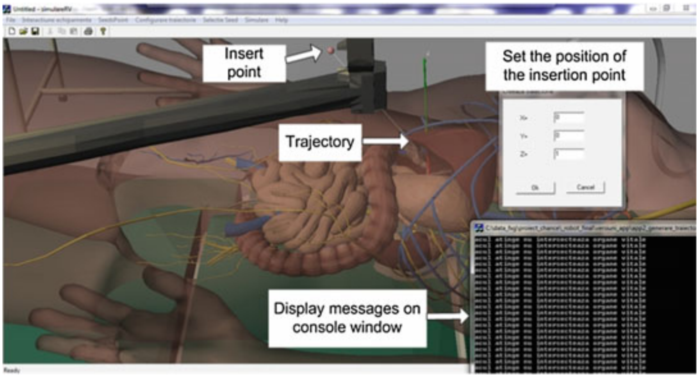

Fig. 4 Manual punctual pre-planning of a brachytherapy needle trajectory

a line corresponding to the BT needle mounted on the robot TCP and the intersected organs.

The main steps of the algorithm designed for manually defining the robot trajectories are:

- Interactive defining the insertion point/guiding template position using the GUI dialog window.
- Check the intersection between the linear trajectories of the needles and the patient's vital organs and display the results in the GUI console.
- Finally save the points that define the robot trajectories.

The main steps of the algorithm designed for automatic punctual generation of linear robot trajectories for each target point are:

- Step_1. Process the 3D model of the patient reconstructed from CT images.
- Step_2. Load the 3D model of the patient into the application.
- Step_3. Define the target area for treatment (tumour position).
- Step_4. Position the robot in the target area for treatment depending on the position of the tumour.
- Step_5. Load the points that define the workspace of the robot corresponding to the target area for treatment.
- Step_6. Successively calculate the intersection between each point of the workspace and each target point corresponding to the radioactive seeds. The result is a text file containing the robot trajectories and the anatomical component that the trajectories intersect (Fig. 5).
- Step_7. Finally, the resulting data is processed to extract the optimum trajectories.

The automated trajectory generation algorithm will process the 3D parametric data of the patient, determining the volumes that have to be avoided on the needle trajectory. These volumes consist of blood vessels, nerves, ganglions and other organs. The safety volume will be generated around the dangerous area with a

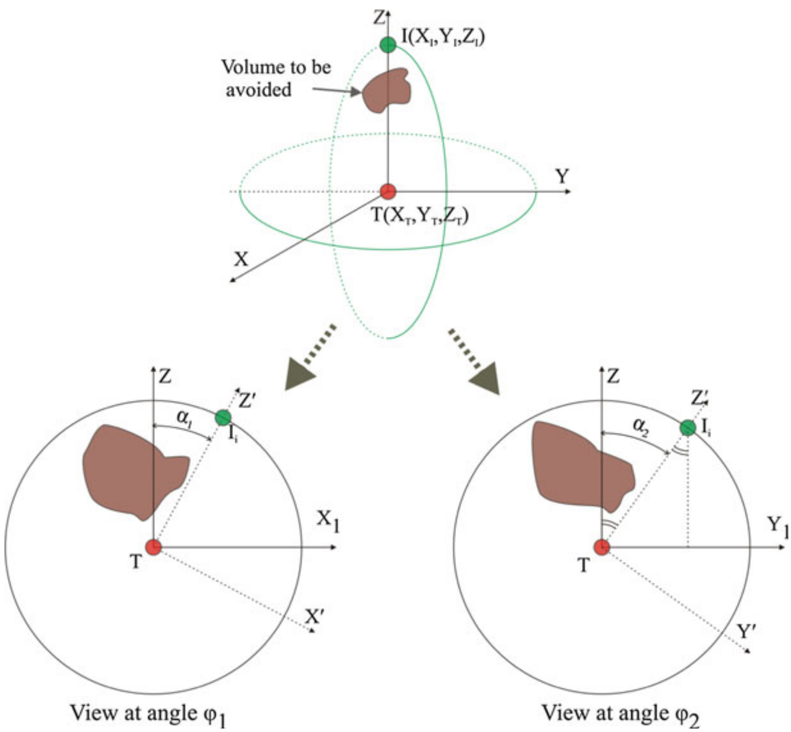

Fig. 5 Needle trajectory definition to avoid high-risk areas

safety margin of 5 up to 10 mm. The algorithm will try to determine the plane in which the first safe trajectory (having a minimum inclination α with respect to the initial trajectory—axis TZ in Fig. 5) is obtained. For that, the algorithm will generate successive cones with the apex in point T and the height TI, having a radius increment of 5 mm. When a new cone is generated, the algorithm will check for generatrices that do not intersect the restricted volume. When such a generatrix is found, it will be saved as the new safe needle trajectory for the target point T; otherwise the cone with larger radius will be generated.

VR software implementation The software system is composed of several software modules that allow the user to define robot trajectories in order to avoid the risk areas. The implemented software has a Single Document Interface structure and contains a display area of the virtual environment and a Graphical User Interface (GUI) area that contains a menu that allows sending of events to the virtual environment.

For the representation of 3D objects in the virtual environment the VRML language has been used. Editing VRML virtual environment was achieved through the application VRMLPad (www.parallelgraphics.com/products/vrmlpad/). The display of the 3D virtual environment was done through the BS Contact VRML player program (www.bitmanagement.de).

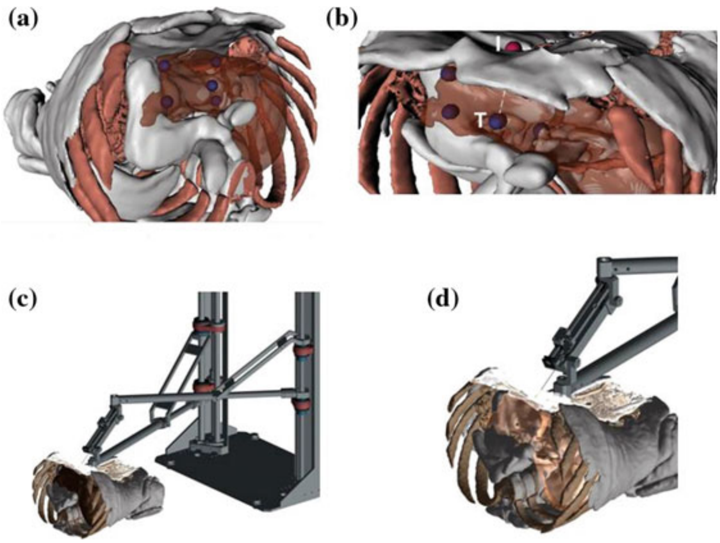

Fig. 6 Simulation of insertion of needle to the target using parallel robot designed for BT. **a** Five seed targets specified, **b** insert point and path planningfor one insertion, **c** robot at insertion point, **d** needle implanting at a target

4 Simulation Results in VR and Siemens NX Using a Real Needle Trajectory

In order to validate the chosen trajectory of the needles, a kinematic simulation using VR and the RecurDYN solver [19] from Siemens NX has been achieved, considering the following simplifying hypothesis:

- The gravity forces, the external and inertia forces have been neglected;
- The bodies are considered to be perfectly rigid.

The BT procedure has been simulated to demonstrate the virtual planning of needle guidance using parallel robot designed for BT. Figure 6 illustrates four steps of the procedure: (1) specification of target positions inside the liver using landmarks (Fig. 6a); (2) specified robot trajectory for one target point defined using the algorithm for automatic punctual generation of linear robot trajectories (Fig. 6b). The landmark illustrates the insertion point (I), while the dashed line illustrates the needle insertion trajectory; (3) movement of the robot up to the insertion point in the patient's body achieving in the same time the final orientation of the needle (Fig. 6c); the robot drives the needle to the target point, along the planned linear path (Fig. 6d).

The generated trajectory has been used as input into the RecurDYN software and the motion of the needle tip has been simulated. The considered test-case follows closely a real situation: the robot moves from the current arbitrary position, with

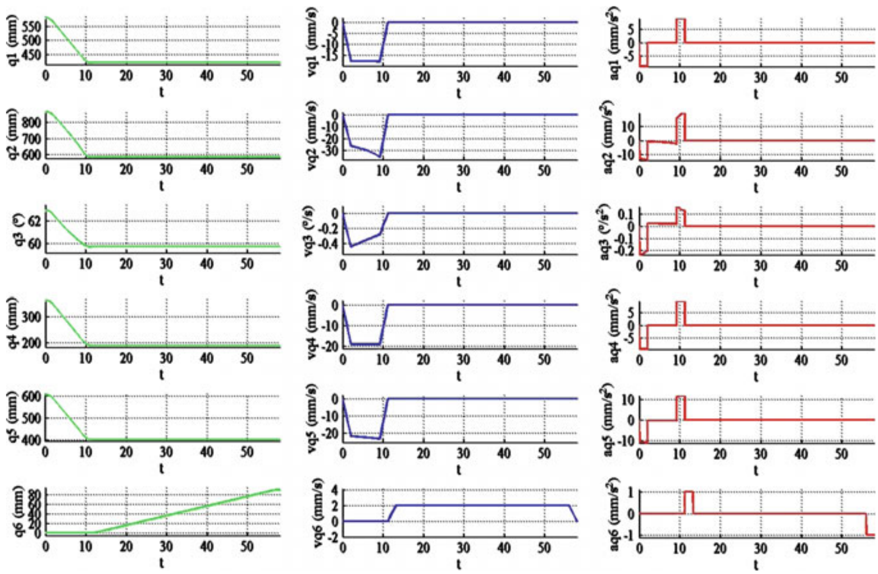

Fig. 7 The coordinates, velocities and accelerations variations for each active joint

respect to a fixed coordinate system, up to the insertion point in the patient's body, achieving in the same time the needle's final orientation, after which it will drive the needle to the target point, in the tumour along a linear path. The following values for the geometric parameters shown in Fig. 1 have been considered: $d_1 = 400\,\text{mm}$; $b_1 = 395\,\text{mm}$; $l_1 = 67\,\text{mm}$; $d_2 = 400\,\text{mm}$; $b_2 = 495\,\text{mm}$; $l_2 = 67\,\text{mm}; = 170\,\text{mm}$; $d_{ac} = -112.5\,\text{mm}$; $d_{12} = 615\,\text{mm}$.

The coordinates of the current position and orientation of the needle's tip, C, of the insertion point I and target point T (I and T being provided by the virtual needle trajectory planning software), are presented in (9).

$$\begin{cases} X_c = 307.5 \text{ mm}; \\ Y_c = 800 \text{ mm}; \\ Z_c = 400 \text{ mm}; \\ \psi_c = 90^\circ \\ \theta_c = 60^\circ \end{cases} \begin{cases} X_I = 333.23 \text{ mm}; \\ Y_I = 834.81 \text{ mm}; \\ Z_I = 221.02 \text{ mm}; \end{cases}, \begin{cases} X_T = 313.27 \text{ mm}; \\ Y_T = 905.34 \text{ mm}; \\ Z_T = 169.69 \text{ mm}; \end{cases} \quad (9)$$

The results, presented in Fig. 7, illustrate the active joints variation, namely position, velocity and acceleration. It is easily to observe how the decoupled motion is achieved: in the first part, until second 10, the robot is being positioned at the insertion point I (with the needle's final orientation) and, until the motion ends at second 20, the active joint q_6 drives the needle to the target point T along a linear path between I and T, with all other actuators being blocked.

5 Conclusions

The paper presents a novel algorithm for virtual planning of robotic needle insertion, based on the restrictions concerning the possibility of tissue penetration. This is capable of either generating automatically the needle linear trajectories or allowing the manual definition of the robot trajectories for needle insertion. A VR environment has been modelled using the CT-scan device and accessories, as well as the PARA-BRACHYROB parallel robot designed for BT, also presented in the paper. The robot has 5-DOF plus one prismatic redundant DOF used for the insertion of the needle up to the target point in the patient's tumour. The needle insertion algorithm has been tested using the NX-RecurDYN and simulations results have been presented.

Acknowledgments This paper was supported by the Post-Doctoral Programme POSDRU/159/1.5/S/137516, project co-funded from European Social Fund through the Human Resources Sectorial Operational Program 2007-2013, by the project no. 173/2012, code PN-II-PT-PCCA-2011-3.2-0414, entitled "Robotic assisted brachytherapy, an innovative approach of inoperable cancers—CHANCE" financed by UEFISCDI, and by the Scopes International Grant IZ74Z0_137361/1 entitled "Creative Alliance in Research and Education focused on Medical and Service Robotics CARE-Robotics".

References

1. Bassan H et al (2007) A novel manipulator for 3D ultrasound guided percutaneous needle insertion. In: Robotics and automation conference, pp 617–622
2. Baumann M et al (2011) Prosper: image and robot-guided prostate brachytherapy. Aquat Bot 32(2):63–65
3. Bernardes MC, Adorno BV, Poignet P, Borges GA (2013) Robot-assisted automatic insertion of steerable needles with closed-loop imaging feedback and intraoperative trajectory replanning. Mechatronics 23:630–645
4. Elgezua I, Kobayashi Y, Makatsu G, Fujie MG (2013) Survey on current state-of-the-art in needle insertion robots: open challenges for application in real surgery. Proc CIRP 5:94–99
5. Fichtinger G et al (2006) Robotically assisted prostate brachytherapy with transrectal ultrasound guidance. Phantom Exp Brachytherapy 5(1):14–26
6. Gerbaulet A, Pötter R, Mazeron J-J, Meertens H, Limbergen EV (2002) The GEC ESTRO handbook of brachytherapy. Eur Soc Therap Radiol Oncol. ISBN 978-90-804532-6-5
7. Goksel O, Sapchuk K, Salcudean SE (2011) Haptic simulator for prostate brachytherapy with simulated needle and probe interaction. Proc IEEE Conf Trans Haptics 4(3):188–198
8. Hao S, Iordachita II, Xiaoan Y, Cole GA, Fischer GS (2011) Reconfigurable MRI-guided robotic surgical manipulator: prostate brachytherapy and neurosurgery applications. Int Conf Med. Biol. Soc. pp 2111–2114

9. Hing JT, Brooks AD, Desai JP (2006) Reality-based needle insertion simulation for haptic feedback in prostate brachytherapy. Proc Int Conf Robot. Autom. 619–624
10. Jiang Y, Sankereacha R, Pignol J (2007) Software tool for breast cancer brachytherapy planning using VTK. In: Proceedings of 6th IEEE international conference on cognitive informatics, pp 381–384
11. Mateescu D (2010) Oncology patient guide-published in Romanian. Bennet Publishing House, Bucuresti. ISBN 978-973-87129-7-3
12. Pisla D et al (2014) Innovative approaches regarding robots for brachytherapy. New Trends Med Serv Robot Mech Mach Sci 20:63–78
13. Plitea N et al (2013) Parallel robot for brachytherapy with two kinematic guiding chains of the platform (the needle) type CYL-U. Patent pending, A/10006/2013
14. Plitea N et al (2014) Structural analysis and synthesis of parallel robots for brachytherapy. New Trends Med Serv Robot 16:191–204. http://link.springer.com/chapter/10.1007%2F978-3-319-01592-7_17
15. Podder T, Buzurovic I, Huang K, Yu Y (2010) MIRAB: an image-guided multichannel robot for prostate brachytherapy. Int J Radiat Oncol Biol Phys 78(3):S810
16. Polo A, Salembier C, Venselaar J, Hoskin P (2010) Review of intraoperative imaging and planning techniques in permanent seed prostate brachytherapy. Radiother Oncol 94:12–23
17. Salcudean SE, Prananta TD, Morris WJ, Spadinger I (2008) A robotic needle guide for prostate brachytherapy. Robot Autom 2975–2981
18. Schmidt-Ullrich PN, Todor DA, Cuttino LW, Arthur DW (2004) Virtual planning of multicatheter brachytherapy implants for accelerated partial breast irradiation. In: Proceedings of 26th international conference of engineering in medicine and biology society, vol 2, pp 3124–3127
19. Siemens NX, RecurDYN solver (2014). http://www.plm.automation.siemens.com/en_us/
20. Song DY et al (2011) Robotic needle guide for prostate brachytherapy. Clin Test Feasibility Perform Brachytherapy 10:57–63
21. Sparchez Z, Radu P, Zaharia T, Kacso G, Grigorescu I, Badea R (2010) Contrast enhanced ultrasound guidance: a new tool to improve accuracy in percutaneous biopsies. Med Ultrason 12(2):133–141
22. Strassmann G et al (2011) Advantage of robotic needle placement on a prostate model in HDR brachytherapy. Strahlenther Onkol 187(6):367–372
23. Trejos AL et al (2008) MIRA V: an integrated system for minimally invasive robot-assisted lung brachytherapy, In: International conferecne on robotics and automation, pp 2982–2987

Sensory Subtraction via Cutaneous Feedback in Robot-Assisted Surgery

Leonardo Meli, Claudio Pacchierotti and Domenico Prattichizzo

Abstract This paper presents a novel approach to force feedback in robot-assisted surgery. Haptic stimuli, consisting of kinesthetic and cutaneous components, are substituted with cutaneous feedback only. This new approach to sensory substitution is called *sensory subtraction*, as it subtracts the destabilizing kinesthetic part of the haptic interaction to leave only cutaneous cues. In order to evaluate the feasibility of the proposed technique, we carried out a bimanual teleoperation experiment, similar to the da Vinci Skills Simulator's Pegboard task. We compared the performance of our sensory subtraction approach with that of (1) complete haptic feedback and (2) auditory feedback in substitution of force feedback. Results assessed the proposed method as a viable solution to substitute haptic feedback in complex teleoperation scenarios. Moreover, this approach, as any other sensory substitution technique, allows to overcome any stability issue affecting the haptic loop.

Keywords Haptic interfaces · Telemedicine · Telerobotics · Surgery · Biomedical engineering · Tactile feedback

L. Meli (✉) · D. Prattichizzo
Department of Information Engineering and Mathematics,
University of Siena, Via Roma 56, 53100 Siena, Italy
e-mail: meli@dii.unisi.it

D. Prattichizzo
e-mail: prattichizzo@dii.unisi.it

L. Meli · C. Pacchierotti · D. Prattichizzo
Department of Advanced Robotics, Istituto Italiano Di Tecnologia,
Via Morego 30, 16163 Genoa, Italy
e-mail: claudio.pacchierotti@iit.it

H. Bleuler et al. (eds.), *New Trends in Medical and Service Robots*,
Mechanisms and Machine Science 38, DOI 10.1007/978-3-319-23832-6_10

1 Introduction

The widespread introduction of laparoscopic techniques during the last decade of the 20th century was one of the most prominent changes in modern surgical practice [1]. Many former open surgical procedures, e.g., cholecystectomy, colectomy, and nephrectomy, are now often performed as minimally invasive interventions. Minimally invasive procedures (MIPs) results in less infection, a quicker recovery time, and shorter hospital stays. Moreover, the recent introduction of robot-assisted surgical systems allows surgeons to improve their accuracy, dexterity, and reduce tremors [2].

In general, a surgical teleoperator consists of two mechanical systems of linkages, a master manipulator and a slave manipulator. These may be connected either mechanically, i.e., by cables or linkages, or actuating both master and slave and introducing a control layer via software. The slave robot is in charge of replicating the movements of the surgeon who, in turn, needs to observe the remote environment. There are many variations of this basic idea, considering the many different ways the surgeon can receive information from the operating theater. The da Vinci Surgical System, for example, let the surgeon see the remote environment through a stereoscopic video camera system. Another useful piece of information is haptic force feedback, that conveys to the surgeon information about the forces registered at the slave side. When motions and forces are exchanged between master and slave we refer to it as a bilateral force-reflecting teleoperation system [3]. However, despite clinical advantages, it is not common to find commercially available devices implementing haptic feedback. This is mainly due to the fact that haptic feedback may affect the stability of the teleoperation loop, leading to undesired oscillations of the system which can be unsafe for both the surgeon and the patient [4]. Despite stability issues, haptic stimuli play a fundamental role in enhancing the performance of teleoperation systems in terms of completion time of a given task [5, 6], accuracy [5, 7], peak [8, 9] and mean force [6, 9]. Therefore, guaranteeing stability while preserving transparency has always been a challenge.

In order to overcome these stability (and safety) issues, haptic feedback can be substituted with alternative feedback forms, such as visual or auditory cues [7, 10, 11]. This technique is known as *sensory substitution*. Although this technique is quite effective, the stimuli provided are often very different from the ones being substituted, and they may show worse performance than that achieved employing unaltered force feedback [4].

Cutaneous feedback has recently received great attention from researchers looking for an alternative to sensory substitution of force feedback; delivering ungrounded haptic cues to the surgeon's skin conveys rich information and does not affect the stability of the teleoperation system [4, 12, 13]. For example Prattichizzo et al. [4] found cutaneous feedback provided by a moving platform more effective than sensory substitution via visual feedback in a needle insertion task. King et al. [14] developed a modular pneumatic tactile feedback system to improve surgical performance of the da Vinci Surgical System. Another line of research focused on

Fig. 1 The da Vinci Skills Simulator contains a variety of scenarios (*right*) designed to give surgeons the opportunity to improve their proficiency with the da Vinci console controls (*left*)

vibrotactile feedback. The system created by McMahan et al. [12] for the Intuitive da Vinci robot lets the surgeon feel left and right instrument vibrations in real time; 114 surgeons and non-surgeons tested this system in dry-lab manipulation tasks and expressed a significant preference for the inclusion of vibrotactile cutaneous feedback [15]. Prattichizzo et al. [4] call this overall approach *sensory subtraction*, in contrast to *sensory substitution*, as it subtracts the destabilizing kinesthetic part of the haptic interaction to leave only cutaneous cues.

In this paper we extend the sensory subtraction idea to a challenging medical scenario. A teleoperation task, similar to the da Vinci Skills Simulator's Pegboard task (see Fig. 1), is proposed. Results were compared while providing different feedback conditions: (1) haptic feedback provided by a grounded haptic interface, (2) cutaneous tactile feedback provided by a couple of wearable cutaneous devices, and (3) auditory feedback in substitution of force feedback.

2 Fingertip Skin Deformation Devices

In this work we employed a novel wearable cutaneous device that consists of two platforms: one is located on the dorsal side of the distal phalanx, supporting three small DC motors, and the other is in contact with the volar surface of the fingertip (see Fig. 2). The motors shorten and lengthen three cables to move the platform

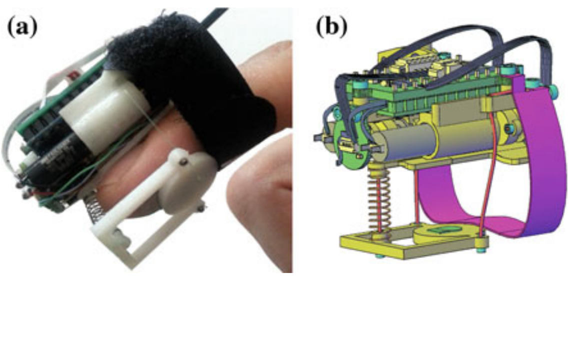

Fig. 2 The fingertip skin deformation device employed in sensory subtraction

toward the user's fingertip and re-angle it to simulate contacts with arbitrarily oriented surfaces. The actuators used for the device are three 0615S Falhauber motors, with planetary gear-heads having 16:1 reduction ratio. The maximum stall torque of the motor is 3.52 mNm. The relationship between the force to be provided and the inputs for the motors was estimated using the mathematical model of the fingertip presented in [16], which considered a linear relationship between resultant wrench at the fingertip and device's platform displacement. The device employed in this work can be also seen as a customized version of the cutaneous device used in [17]. With respect to [17], our device does not have the force sensor between the platform and the finger, and the two platforms have been redesigned to permit their use together with the Omega.7 haptic interfaces.

3 Peg Board Experiment

We evaluated the sensory subtraction idea in a bimanual peg board experiment. The experimental setup is shown in Fig. 3. The teleoperation system was composed of two Omega.7 haptic interfaces and four cutaneous devices on the master side, and a couple of virtual surgical pliers on the slave side. The operator was able to both move and rotate the pliers in the remote scenario and control their grip forces. The virtual environment consisted of four rings, two green and two red, and two pegs, one green and one red (see Fig. 3c). The rings weighted 30 g and had a minor radius of 3 cm, a major radius of 5 cm, and a height of 1 cm. The cylindrical pegs were fixed to the ground and had a radius of 2 cm and a height of 10 cm. A spring k_0 = 40 N/m was used to model the contact force between the proxies and the objects, according to the god-object model [18].

Seven participants (five males, two females, age range 20–30 years) took part in the experiment. Four of them had previous experience with haptic interfaces, but only two have previously used cutaneous devices. None of the participants reported any deficiencies in their visual or haptic perception abilities, and all of them were right-hand dominant. The task consisted of picking, one by one, the rings with one pair of pliers, passing them to the other pair, and placing them around the peg of the corresponding color. If the ring was placed in the wrong peg, the insertion was not

Fig. 3 Experimental setup. **a** General overview of the setup. **b** Detail of one hand wearing the cutaneous devices. **c** Virtual environment with surgical pliers

considered valid. The task started when the user grasped a ring for the very first time and ended when all the rings were placed around the pegs. A video of this experiment can be downloaded at http://goo.gl/TpQm65. Subjects were asked to complete the task as quickly as possible. A 10-min familiarization period was provided to participants to acquaint them with the experimental setup.

3.1 Force Feedback Techniques

Each participant performed nine trials of the aforementioned peg board task, with three randomized repetitions of each force feedback condition considered:

- haptic force feedback provided by the Omega.7 haptic interfaces (condition H),
- cutaneous force feedback provided by the cutaneous devices presented in Sect. 2 (condition C), i.e. our sensory subtraction approach,
- auditory feedback in substitution of force feedback, provided by changing the repetition frequency of a beep tone (condition A).

In all the considered conditions, the Omega.7 devices were in charge of controlling the movements of the surgical pliers by tracking position and orientation of the operator's hands. In conditions C and A the Omega.7 interfaces did not provide any force feedback. In condition A, the pair of pliers controlled by the operator's right hand produced a sound on the right earphone, and the other pair on the left one, making very easy for the operator to understand which tool was the one applying force.

3.2 Results

In order to evaluate the performance in each considered feedback condition, we recorded (1) the completion time needed to accomplish the task, (2) the forces generated by the contact between the pliers and the rings, and (3) the total displacement of the rings. Measuring the average of intensities of the contact forces is a widely-used approach to evaluate energy expenditure during the grasp [19]. Data resulting from different trials of the same feedback condition, performed by the same subject, were averaged before comparison with other modalities' data. Figure 4a shows the average time elapsed between the instant the user grasps the object for the very first time and when it completes the peg board task. Figure 4b reports the average grip forces generated by the two pairs of pliers and the rings along the direction of actuation of the Omega's gripper. Figure 4c shows the sum of the rings displacements, averaged over the subjects.

Means were analysed using a repeated measures ANOVA (completion time: $F(2, 12) = 61,908$, $p < 0.001$; contact forces: $F(2, 12) = 59,130$, $p < 0.001$; ring's displacement: $F(2, 12) = 37,671$, $p < 0.001$). Since the overall ANOVA result was

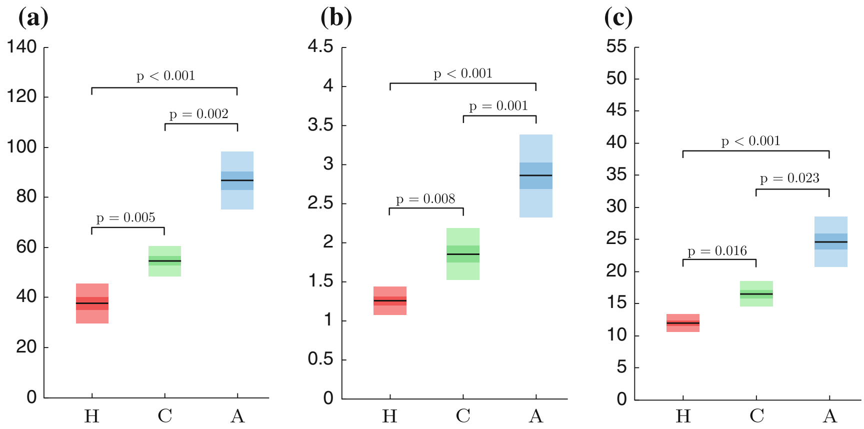

Fig. 4 Bimanual peg board experiment. Completion time, contact forces, and rings' displacement for the haptic (H), cutaneous (C) and auditive (A) conditions. Means are represented as black lines, while the lighter and darker color tones represent the SD and the SEM respectively. p-values of post hoc group comparisons are reported when a statistically significant difference is present (confidence interval of 95 %). **a** Completion time. **b** Contact forces. **c** Rings' displacement

statistically significant regarding all the conditions taken into account, the Bonferroni pairwise comparisons test was carried out on data. Data in all statistical tests were transformed, when necessary, to meet the statistical test initial assumptions [20]. The investigation revealed significant differences among all the conditions for all the considered metrics and the p-values about the different comparisons are reported in Fig. 4. Results show that our sensory subtraction approach (condition C) provides intermediate performance between haptic feedback provided by a grounded haptic interface (condition H) and sensory substitution via auditory feedback in terms of completion time, forces generated, and total displacement of the rings.

4 Peg Board Experiment with Communication Delay

A second experiment was then carried out. It considered the same task, carried out by the same seven subjects, with the same experimental setup and feedback modalities. However, this time we introduced a communication delay of 20 ms in the teleoperation loop. A video of this experiment, focusing on the unstable behaviour of the haptic modality, can be downloaded at http://goo.gl/5lbw04. In order to evaluate the performance of the considered feedback conditions, we collected the same data of the previous experiment, and we processed the data in the same way. Figure 5a shows the average task's completion time, Fig. 5b the average grip forces generated between the pliers and the rings and Fig. 5c the sum of the rings displacements averaged over the subjects.

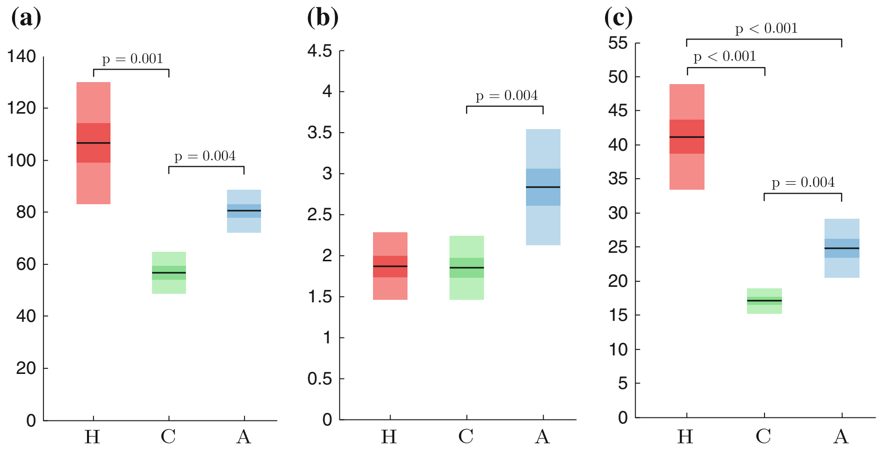

Fig. 5 Bimanual peg board experiment with communication delay of 20 ms between master and slave systems. Completion time, contact forces, and rings' displacement for the haptic (H), cutaneous (C) and auditive (A) conditions. Means are represented as black lines, while the lighter and darker color tones represent the SD and the SEM respectively. p-values of post hoc group comparisons are reported when a statistically significant difference is present (confidence interval of 95 %). **a** Completion time. **b** Contact forces. **c** Rings' displacement

Means were again analysed using a repeated measures ANOVA (completion time: $F(2, 12) = 61, 908$, $p < 0.001$; contact forces: $F(2, 12) = 59, 130$, $p < 0.001$; ring's displacement: $F(2, 12) = 37, 671$, $p < 0.001$). Since the overall ANOVA results were statistically different, a subsequent pairwise comparisons evaluations was performed on data. Data in all statistical tests were transformed, when necessary, to meet the statistical test initial assumptions [20]. The investigation revealed no significant difference between the haptic and auditory conditions (H and A) about the completion time, while only cutaneous and auditory conditions (C and A) resulted statistically significantly different about the contact forces. For what regards the rings' displacement the tests assessed statistically significant differences among all the three conditions. p-values about the multiple comparisons are reported in Fig. 5.

5 Discussion

We analyzed three feedback conditions in two different experiments. In the first experiment (no delay), subjects, while being provided with the haptic feedback (condition H), showed the best performance, as shown in Fig. 4. However, sensory subtraction (condition C) leads to significantly better results than using the auditory feedback (condition A).

In the second experiment, we introduced a communication delay of 20 ms between master and slave. Users showed a similar behavior with respect to the one registered in the first experiment when considering the sensory subtraction and substitution modalities (C and A), but they showed a high degradation of performance when haptic force feedback (H) was provided. Such an unstable behaviour is well-known in the literature and was here reported to point out the intrinsic stability of the sensory subtraction approach.

We can hence state that sensory subtraction is a viable approach to replace haptic feedback force in teleoperation, in particular in those scenarios where safety is a paramount and non-negotiable requirement, e.g., robotic surgery. It is also worth highlighting that our cutaneous-only approach is useful in *any* situation where it is possible to experience an unstable behavior. The stability of teleoperation systems with force reflection can be in fact significantly affected not only by communication latencies in the loop, but also by hard contacts, relaxed grasps, and reduced sampling rates [21].

6 Conclusions and Future Works

In this paper we exploited a novel force feedback approach for robot-assisted surgery, called *sensory subtraction*, which has been introduced in [4]. It consists of substituting haptic force with cutaneous stimuli only. However, in order to differentiate it from sensory substitution, we called it sensory subtraction, since haptic feedback provided by grounded interfaces can be considered as composed of cutaneous and kinesthetic components. Our approach can be then seen as the subtraction between the complete haptic interaction, cutaneous and kinesthetic, and its kinesthetic part.

A bimanual teleoperation task, similar to the *Peg Board* task proposed in the da Vinci Skills Simulator, has been used to evaluate the sensory subtraction performance. We also considered a complete haptic feedback modality, provided by a grounded haptic interface, and a popular sensory substitution technique, i.e., auditory feedback in substitution of force feedback. Our sensory subtraction approach performed better than sensory substitution, but, as expected, worse than the unaltered haptic feedback. However, while a small communication delay in the teleoperation force loop does not affect the sensory subtraction performance, it makes the system unstable in the presence of haptic feedback. Sensory subtraction can then be considered a viable solution when safety is paramount.

Although sensory subtraction seems a very promising approach, clinicians might not be positive about having four cutaneous devices on their fingertips during surgery. Moreover, sensing capabilities of human skin receptors upper bounds the force provided by this kind of cutaneous devices.

Work is in progress to design new cutaneous displays with better dynamic performance, in order to improve the subject's perception about the fingertip skin deformation. Moreover, similar experiments in a real scenario with a larger number of participants will be performed in the next future.

References

1. Ruurda JP, van Vroonhoven ThJMV, Broeders IAMJ (2002) Robot-assisted surgical systems: a new era in laparoscopic surgery. Ann R Coll Surg Engl 84(4):223
2. Nisky I, Hsieh MH, Okamura AM (2013) A framework for analysis of surgeon arm posture variability in robot-assisted surgery. In: Proceedings of IEEE international conference on robotics and automation, pp 245–251
3. Selha S, Dupont P, Howe RD, Torchiana DF (2002) Dexterity optimization by port placement in robot-assisted minimally invasive surgery. In: Intelligent systems and advanced manufacturing, pp 97–104
4. Prattichizzo D, Pacchierotti C, Rosati G (2012) Cutaneous force feedback as a sensory subtraction technique in haptics. IEEE Trans Haptics 5(4):289–300
5. Moody L, Baber C, Arvanitis TN, et al (2002) Objective surgical performance evaluation based on haptic feedback. In: Studies in health technology and informatics, pp 304–310
6. Pacchierotti C, Chinello F, Malvezzi M, Meli L, Prattichizzo D (2012) Two finger grasping simulation with cutaneous and kinesthetic force feedback. In: Haptics: perception, devices, mobility, and communication, pp 373–382
7. Pacchierotti C, Abayazid M, Misra S, Prattichizzo D (2014) Teleoperation of steerable flexible needles by combining kinesthetic and vibratory feedback. IEEE Trans Haptics 7(4):551–556
8. Hannaford B (1987) Task-level testing of the JPL-OMV smart end effector. In Proceedings of the workshop on space telerobotics, vol 2
9. Wagner CR, Stylopoulos N, Howe RD (2002) The role of force feedback in surgery: analysis of blunt dissection. In: Proceedings 10th symposium of haptic interfaces for virtual environment and teleoperator systems, pp 68–74
10. Massimino MJ (1995) Improved force perception through sensory substitution. Control Eng Pract 3(2):215–222
11. Okamura AM, Verner LN, Yamamoto T, Gwilliam JC, Griffiths PG (2011) Force feedback and sensory substitution for robot-assisted surgery. In Surgical, Robotics, pp 419–448
12. McMahan W, Gewirtz J, Standish D, Martin P, Kunkel JA, Lilavois M, Wedmid A, Lee DI, Kuchenbecker KJ (2011) Tool contact acceleration feedback for telerobotic surgery. IEEE Trans Haptics 4(3):210–220
13. Pacchierotti C, Tirmizi A, Bianchini G, Prattichizzo D (2013) Improving transparency in passive teleoperation by combining cutaneous and kinesthetic force feedback. In: Proceedings of IEEE/RSJ international conference on intelligent robots and systems (IROS), pp 4958–4963
14. King C-H, Culjat MO, Franco ML, Lewis CE, Dutson EP, Grundfest WS, Bisley JW (2009) Tactile feedback induces reduced grasping force in robot-assisted surgery. IEEE Trans Haptics 2(2):103–110
15. Koehn JK, Kuchenbecker, KJ Surgeons and non-surgeons prefer haptic feedback of instrument vibrations during robotic surgery. Accepted for publication in *Surgical Endoscopy*
16. Prattichizzo D, Chinello F, Pacchierotti C, Malvezzi M (2013) Towards wearability in fingertip haptics: a 3-dof wearable device for cutaneous force feedback. IEEE Trans Haptics 6 (4):506–516
17. Pacchierotti C, Tirmizi A, Prattichizzo D (2014) Improving transparency in teleoperation by means of cutaneous tactile force feedback. ACM Trans Appl Percept 11(1):4

18. Zilles CB, Salisbury JK (1995) A constraint-based god-object method for haptic display. In Proceedings of IEEE/RSJ international conference on intelligent robots and systems, vol 3, pp 146–151
19. Prattichizzo D, Trinkle J (2008) Chapter 28 on grasping. In: Siciliano B, Kathib O (eds), Handbook on robotics. Springer, Berlin, pp 671–700
20. Wallenstein S, Zucker CL, Fleiss JL (1980) Some statistical methods useful in circulation research. Circ Res 47(1):1–9
21. Hashtrudi-Zaad K, Salcudean SE (2002) Transparency in time-delayed systems and the effect of local force feedback for transparent teleoperation. IEEE Trans Robot Autom 18(1):108–114

Active Bending Electric Endoscope Using Shape Memory Alloy Wires

T. Kobayashi, T. Matsunaga and Y. Haga

Abstract The bending mechanism of a conventional endoscope operates by drawing wires from outside the human body. The shaft structure of endoscopes is relatively complex to avoid buckling by the tensile force of the wire. Therefore, it is difficult to make a conventional endoscope. In this study, an active bending electric endoscope was developed using SMA (shape memory alloy) wires. The SMA wires are driven by Joule heat generated by electric current. As a result, the shaft structure of the active bending mechanism is simplified compared to the conventional endoscope. The active bending mechanism using SMA wires simplifies inspection inside the human body. This device consists of a commercial CMOS imager, three LEDs and a shaft structure. It is capable of multidirectional bending with a curvature radius of approximately 40 mm at 300 mA. The active bending mechanism using SMA wires would be suitable for construction of a disposable endoscope.

Keywords SMA wire · Endoscope · Active bending mechanism · CMOS imager

1 Introduction

Endoscopy is widely practiced in modern medicine. The bending mechanism of a conventional endoscope operates involves drawing wires from outside the body [1]. The shaft structure of endoscopes is relatively complex to avoid buckling of the

T. Kobayashi (✉) · Y. Haga
Graduate School of Engineering, Tohoku University, Sendai, Japan
e-mail: takumi.kobayashi.s7@dc.tohoku.ac.jp

Y. Haga
e-mail: haga@bme.tohoku.ac.jp

T. Matsunaga
Micro System Integration Center, Tohoku University, Sendai, Japan
e-mail: matsunaga@bme.tohoku.ac.jp

Y. Haga
Graduate School of Biomedical Engineering, Tohoku University, Sendai, Japan

H. Bleuler et al. (eds.), *New Trends in Medical and Service Robots*,
Mechanisms and Machine Science 38, DOI 10.1007/978-3-319-23832-6_11

flexible shaft, and insertion is facilitated by the rigidity resulting from wire. Therefore, it is difficult to make a conventional endoscope disposable. To solve this problem, a number of active bending mechanisms using SMA (shape memory alloy) coils have been developed [2–4]. The SMA actuators contract owing to Joule heating when electric current is supplied to the SMA actuators. Therefore, the shaft structure of an active bending mechanism is simplified, compared to the conventional endoscope. On the other hand, compared with SMA coils, an SMA wire has the benefits of lower cost and precise control realized by feedback control utilizing electrical resistance of SMA wire. Unfortunately, the contraction length of an SMA wire is shorter than that of an SMA coil, resulting in a decreased bending angle of the multidirectional bending mechanism using the SMA wires. Although active bending mechanisms using SMA wires have been developed [5, 6], it is difficult to obtain a large bending angle, and heat dissipation is inhibited, because these devices utilize a multi-lumen tube.

In this study, a multidirectional bending mechanism using SMA wires with a large bending angle was developed. The actuation mechanism of the device can achieve a large bending angle through a technique, in which an SMA wire is held fixed and inactive SMA wires are released. An active bending electric endoscope using the multidirectional bending mechanism has also been developed [7]. Disposability is difficult to achieve because of the high cost of the CCD (charge coupled device) imager and that of the SMA coil. The actuation mechanism of our device is attached to a commercial CMOS (complementary metal oxide semiconductor) imager and three LEDs for endoscopic function. When the CMOS imager is reusable or inexpensive, the device can be realized as a disposable endoscope. As the active bending mechanism can be made disposable, sterilization and cleaning processes for the active bending mechanism are unnecessary.

2 Multidirectional Bending Mechanism

The active bending mechanism of the device proposed by the authors can realize a large bending angle by the following methods. As shown in Fig. 1, if the SMA wire is fixed at both ends, the wire tends to remain straight when it contracts, thus deflecting the bending mechanism. Straight mechanism construction deteriorates the bending angle. If the straight shape deformation of the SMA wire is prevented, the bending angle is improved, as shown by the calculation result in Fig. 1, allowing an arc shape to be achieved.

As shown in Fig. 2, there is a relationship between the bending angle and the distance from the center point to working point. If this distance decreases, the bending angle increases.

The structure of the bending mechanism is shown in Fig. 3. Straight-shape deformation is prevented by holding the SMA wire with a restraining coil. Another method of achieving a large bending angle is by releasing inactive SMA wires. As shown in Fig. 3, three SMA wires are positioned with a spacing of 120° around the

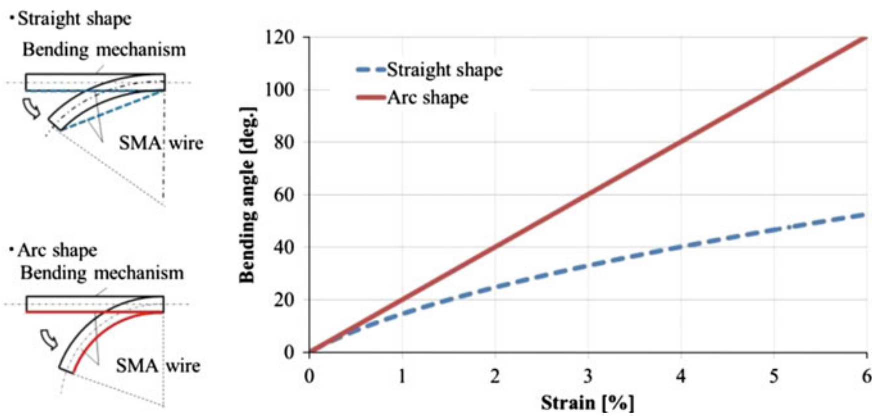

Fig. 1 Prevention of straight shape deformation

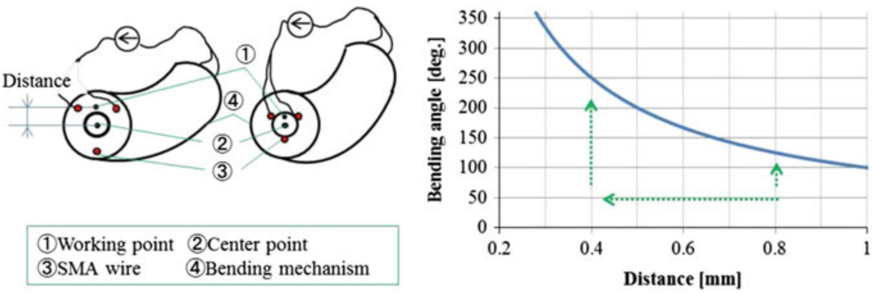

Fig. 2 Relationship between bending angle and distance

inner tube. When one or two SMA wires are actuated, they contract and bend the mechanism in a certain direction. The other inactive SMA wires shift inward without strain, as shown in Fig. 3, and prevent deterioration of the bending angle caused by inactive SMA wires.

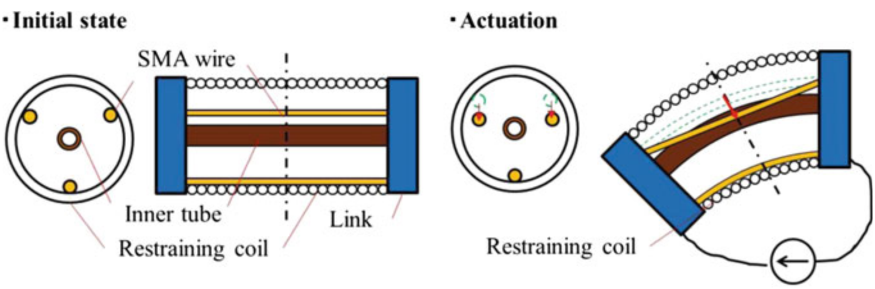

Fig. 3 Structure of multidirectional bending mechanism

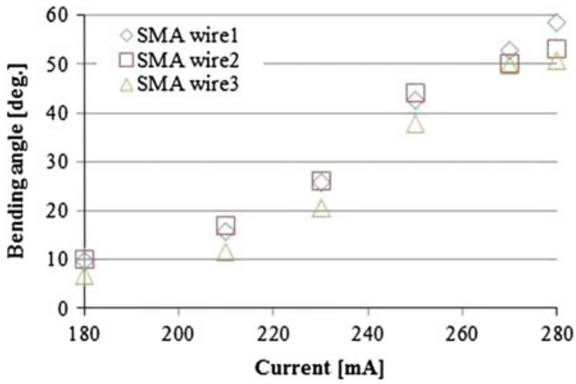

Fig. 4 Bending angle of the fabricated multidirectional bending mechanism as a function of current

The external diameter and length of the bending part of the fabricated multidirectional bending mechanism are 1.7 and 35 mm respectively. The bending angle is 59° (curvature radius 34 mm) at the driving current of 280 mA, as shown in Fig. 4.

3 Active Bending Electric Endoscope

An active bending electric endoscope using the multidirectional bending mechanism was fabricated as shown in Fig. 5. The endoscope consists of an imager component, a bending component and a shaft component. The imager component consists of a CMOS imager, three LEDs (1.6 × 0.8 × 0.68 mm, 556–723 mcd) on a link, a link for the light guide and a glass cover at the tip of the endoscope. The bending part consists of three SMA wires, a restraining coil made from stainless steel wire with a square cross section, and four links for positioning SMA wires. The imager component and the bending component are covered by an outer tube (silicone rubber tube, inner diameter 3.9 mm, outer diameter 4.1 mm). A silicone rubber tube (length is 2 m) is also utilized as the shaft. Four links are cut out from a paper phenolic plate using cutting tools. The three LEDs and the SMA wires are connected to lead wires.

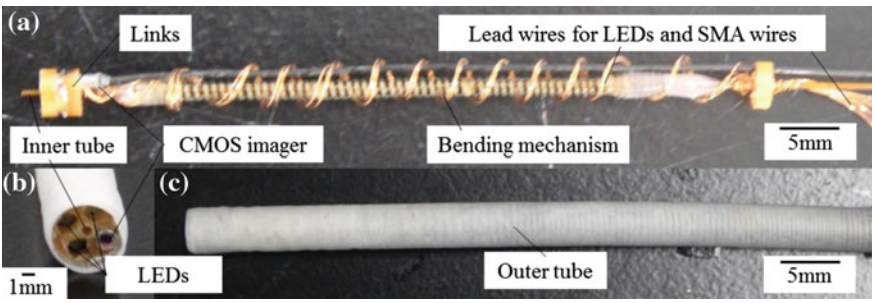

Fig. 5 Components of active bending electric endoscope

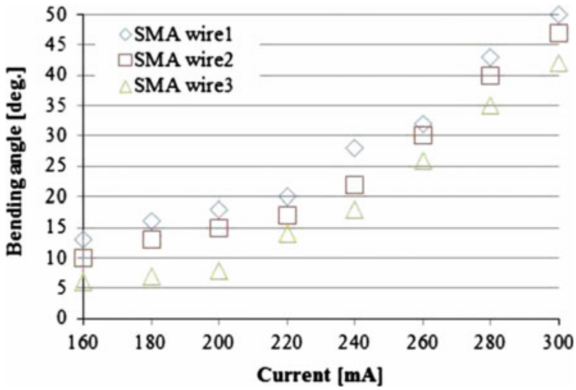

Fig. 6 Bending angle with actuation of one SMA wire

The external diameter and length of the bending part of the active bending electric endoscope are 4.3 and 35 mm, respectively. The CMOS imager (MEDIGUS 1.2 MM CAMERA, Medigus Co., diameter 1.2 mm, length 5 mm) is inserted into the bending device for endoscopic operation.

The bending mechanism of the fabricated active bending electric endoscope was evaluated. The bending angle of the active bending mechanism using one SMA wire actuation is shown in Fig. 6. The bending angle of the active bending mechanism was 50° (radius of curvature 40 mm) at 300 mA, as shown in Fig. 7. This bending angle was achieved in a few seconds. The bending angle of the active bending mechanism using two SMA wires for actuation is shown in Fig. 8. The bending angle was approximately 37° (radius of curvature 54 mm) at 220 mA, as shown in Fig. 9 and was also achieved in a few seconds.

The surface temperature of the bending mechanism was less than 41 °C, while the supplied current was 300 mA. The surface temperature of the device in the human body should be less than 41 °C to prevent protein denaturation. The surface temperature of the bending mechanism was tested in a thermostatic oven at 38 °C.

Fig. 7 Bending motion with actuation of one SMA wire

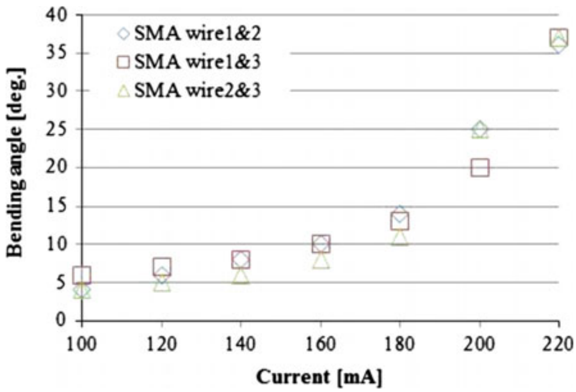

Fig. 8 Bending angle with actuation of two SMA wires

Fig. 9 Bending motion with actuation of two SMA wires

As a result, this device was found to be capable of bending and maintaining 43° deflection (radius of curvature 47 mm) for a long time inside the body.

The overall system with the active bending electric endoscope is shown in Fig. 10. It consists of a controller for the active bending mechanism, a CMOS imager connected to a video unit, and a monitor. The bending directions and angles are controlled by varying the ratio of the electric power among the three SMA wires [8]. This active bending electric endoscope was inserted into a model of a small intestine. Observation inside the model using the CMOS imager is shown in Figs. 11 and 12. This endoscope with the CMOS imager and LEDs can provide observation of circular folds (with the size of 2 mm) in the model.

4 Discussion

The three different bending directions have similar characteristics, as shown in Figs. 6 and 8. The distance between the center point of the device and the working point of the SMA wires, which depends on the number of SMA wires, is inversely

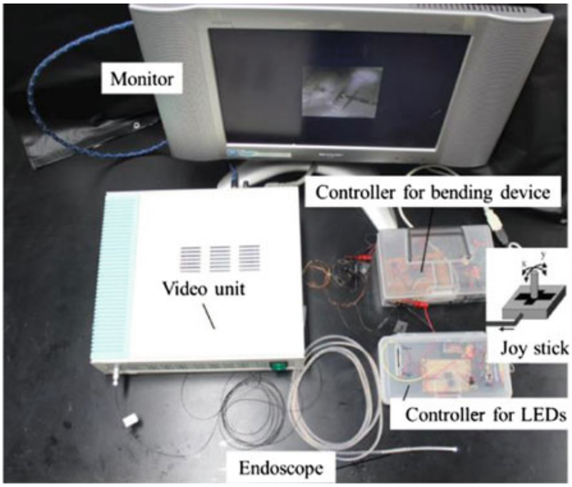

Fig. 10 Total system of the active bending electric endoscope

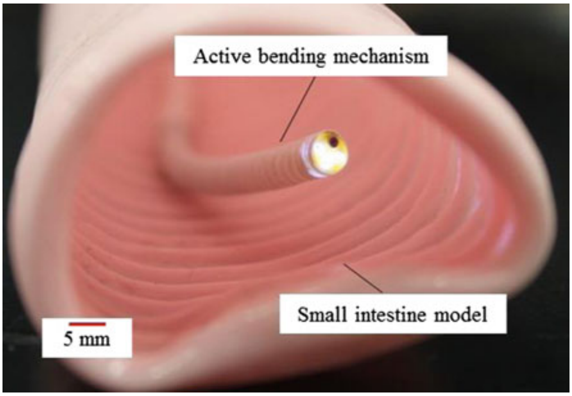

Fig. 11 A active bending electric endoscope in the small intestine model

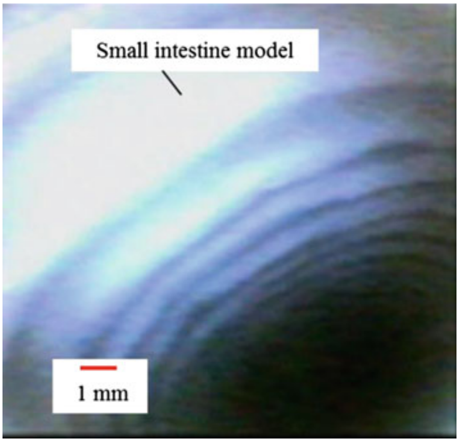

Fig. 12 Obtained image of inside of small intestine model using the CMOS imager

proportional to the bending angle. Therefore, the bending angle of the bending mechanism using two SMA wires for actuation is larger than the bending angle of one SMA wire for actuation under 220 mA.

The surface temperature of the SMA actuator increased to 70 °C under the maximum SMA actuator contraction. The bending angle of the active bending mechanism using SMA coils developed by Makishi et al. (Outer diameter 3.9 mm, bending length 35 mm) was 70° (radius of curvature 29 mm) with the surface temperature under 41 °C in the atmosphere [7]. In a later work, the bending angle of the active bending mechanism using SMA wires developed by Takizawa et al. (Outer diameter 1.5 mm, bending length 20 mm) was 90° (radius of curvature 13 mm) with the surface temperature higher than 60 °C [9]. As they evaluated their device in the atmosphere, their devices were not suitable for usage in the human body, because it seemed that the bending angle of their devices decreased with the surface temperature under 41 °C in a thermostatic oven at 38 °C. On the other hand, the device proposed here has an air space between the SMA wires and the surface of the device. The bending angle of this device is 43° (radius of curvature 47 mm) for a long time inside the human body with the surface temperature of the device under 41 °C.

As mentioned above, the bending angle of the active bending mechanism using one SMA wire actuation achieves 50° in a few seconds, whereas that of the mechanism using two SMA wires achieves 37° in a few seconds. When the presented device demands fast bending, feedback control utilizing electric resistance of the SMA wires would be effective. The device using a feedback control would be able to quickly bend in response to an optimized feedback control system. Additionally, the feedback control utilizing electric resistance of the SMA wire would be effective for precise control that is not influenced by thermal disturbance.

The SMA wire in the active bending mechanism was characterized by elongation and contraction reciprocated through more than about one billion cycles [10]. This capability can make it possible for use in a disposable endoscope.

The active bending electric endoscope can make observations inside a small intestine model using the CMOS imager and LEDs. This endoscope realized observation of circular folds (with size of 2 mm) in the model. This active bending electric endoscope is expected to be useful for inspecting stenosed lesions of the small intestine, which require prompt treatment. The illumination intensity of the LEDs should be improved for navigating the endoscope from the cardia to the pylorus of the stomach. If the CMOS imager is relatively inexpensive, the active bending electric endoscope can be disposable. On the other hand, when the CMOS imager has to be reused, the addition of a tube acting as a CMOS imager channel would be effective.

5 Conclusions

In this study, the actuation mechanism of the proposed device was able to achieve a large bending angle through a technique, in which an SMA wire was held fixed and the inactive SMA wires were released. This active bending electric endoscope was developed using a multidirectional bending mechanism for inspecting the digestive tract. The bending angle of the multidirectional bending mechanism was 59° (curvature radius 34 mm), whereas that of the active bending electric endoscope was 50° (curvature radius 34 mm). Additionally, the device can bend and maintain a 43° angle (radius of curvature 47 mm) for a long time inside the body. For future work, we plan to measure other characteristics of this device (e.g., patient tolerance and deflection force when in contact with the inner tissues) to make it a complementary tool in medical applications.

The active bending electric endoscope can observe inside a small intestine model using a CMOS imager and LEDs. This device does not have a CMOS imager channel. Therefore, it is difficult to reuse the CMOS imager. On the other hand, the proposed device with a tube acting as a CMOS imager channel can be disposable. As the active bending mechanism can be realized disposable, sterilization and cleaning processes for the active bending mechanism are unnecessary. In the future work, we will attempt to perform drug delivery using the working channel. Feedback control utilizing electric resistance of the SMA wires will be added for precise and high-speed control.

References

1. Ueda Y (2005) Endo-scope systems. J Reliab Eng Assoc Japan 22(4):280–287 (in Japanese)
2. Ikuta K, Tsukamoto M, Hirose S (1987) Development of shape memory alloy actuator. Characteristics measurements of the alloy and development of an active endoscope: Characteristics measurements of the alloy and development of and active endoscope. Rob Soc Japan 5(2):87–101 (in Japanese)
3. Haga Y, Esashi M (2000) Small diameter active catheter using shape memory alloy coils. IEEE J Trans Sens Micromach 120(11):509–514
4. Mineta T, Mitsui T, Watanabe Y, Kobayashi S, Haga Y, Esashi M (2001) Batch fabricated flat meandering shape memory alloy actuator for active catheter. Sens Actuators A 88:112–120
5. Ohta R (2001) Results of R&D on catheter-type micromachine. In: Proceedings of 2001 international symposium on micromechatronics and human science, pp 5–12
6. Fukuda T, Guo S, Arai F, Kosuge K, Negoro M (1994) A study on active catheter system: 1st report, structure, experimental results and characteristic evaluation of multiunits using SMA active catheter with multi D. O. F. Trans JSME 60(573):1727–1734 (in Japanese)
7. Makishi W, Ikeda M, Esashi M, Matsunaga T, Haga Y (2011) Development of active bending electric endoscope using shape memory alloy for disposable and thin endoscope. Trans Inst Electr Eng Japan 131(3):102–110 (in Japanese)
8. Makishi W, Matsunaga T, Esashi M, Haga Y (2007) Active bending electric endoscope using shape memory alloy coil actuators. Trans Inst Electr Eng Japan 127(2):75–81 (in Japanese)
9. Takizawa H, Tosaka H, Ohta R, Kaneko S, Ueda Y (1999) Development of a Microfine active bending catheter equipped with MIF tactile sensors. In: Proceedings of IEEE MEMS'99, pp 412–417
10. Homma D, Uemura S, Nakazawa F (2007) Functional anisotropic shape memory alloy fiber and differential servo actuator. In: Proceedings of the international conference on shape memory and superelastic technologies, pp 463–472

Kinematic Analysis of Instruments for Minimally Invasive Robotic Surgery: Generalization of the Reference Task

B. Deutschmann, R. Konietschke and C. Ott

Abstract In minimally invasive robotic surgery, actuated instruments are used that provide additional degrees of freedom (DoF) inside the human body. Kinematic limitations due to the instrument could endanger the secure execution of a surgical task. Numerous design alternatives are proposed in the literature whereas little work is done that evaluates the performance of these instruments in an objective way. This paper presents recent extensions towards a method from Deutschmann et al. (IEEE conference on intelligent robots and systems, 2013 [1]) to evaluate alternative designs of instrument kinematics with respect to their ability to perform surgical tasks. These extensions include further analysis of the task "suturing", one of the key tasks in robotic surgery, to extract the main components and generalize it with respect to the arbitrariness in which way this task occurs during a minimally invasive intervention. The paper concludes with more recent evaluation results and gives recommendations for instruments and their kinematic structure.

Keywords Medical robotics · Robotic telesurgery · Kinematics · Workspace analysis · Laparoscopic suturing

1 Introduction

In robot guided minimally invasive interventions, the possibility of in situ manipulation without workspace limitations and a secure execution of the surgical task are amongst the main demands of the surgeons. In this context "intracorporeal suturing" is considered as the fundamental task [2]. Commonly, the robotic system on the outside of the patient is responsible for the positioning of the tool center point (TCP). In contrast, the robotized instrument with its wrist like joints at the tip,

B. Deutschmann (✉) · R. Konietschke · C. Ott
Institute of Robotics and Mechatronics, German Aerospace Center (DLR), Wessling, Germany
e-mail: bastian.deutschmann@dlr.de

H. Bleuler et al. (eds.), *New Trends in Medical and Service Robots*, Mechanisms and Machine Science 38, DOI 10.1007/978-3-319-23832-6_12

acting inside the patient, is mainly responsible for the orientation of the TCP. Suturing requires a great amount of maneuverability and flexibility from the instrument wrist-like joints [3]. Limitations of this wrist kinematics would endanger the severe procedure of placing a suture.

Numerous design proposals of instrument kinematics for minimally invasive surgery can be found in the literature [4–8]. A performance evaluation of these proposals regarding surgical tasks is not stated. However, a method that incorporates an evaluation of performance based on a relevant task would be exceptionally useful prior to building prototypes to reduce the cost and save time. Furthermore, the importance of kinematic design parameters, e.g. the joint sequence or the range of motion of a joint, can be identified to guide mechanical designers.

In minimally invasive surgery, the relative position of the entry port with respect to the area of interest, i.e. the setup, is patient specific. However, this setup greatly influences the performance of an instrument regarding a desired task, e.g. placing a suture. Therefore, an evaluation method that is independent of this setup would be of main concern.

Related publications are for example the work of Çavuşoğlu et al. [9], which evaluated two instrument kinematics with respect to their ability to perform a surgical knot. Or Sallé et al. [10] which evaluated arbitrary axis arrangements for a redundant instrument to be able to perform a complete anastomosis for coronary artery bypass. Both methods incorporate quantitative criteria to account for e.g. the manipulability while performing the task. For a detailed state of the art see [1].

According to [11], a method that evaluates the performance of a manipulator needs to clearly specify the task and the tool separately in order to determine the respective influence on the overall performance. The task specific evaluation method published in [1] incorporates this clear specification and is used as a basis for the current work. The focus of the paper at hand is the development of a more generalized task description by

1. a more detailed examination of the suturing task including a classification into the two subtasks of "stitching" and "knot tying"
2. a uniform sampling method for the rotation group *SO(3)* to characterize the task probabilistically [11].

The generalization provides a task that includes motions mainly affecting the instruments capabilities which contributes to a precise evaluation process. The aforementioned feature and the method's independence on the setup is the main benefit and uniqueness of the method compared with other evaluation methods [9, 10]. The paper concludes with recommendations for the kinematic designs of instruments with respect to the task of suturing.

The paper is structured by four sections. In Sect. 2, the proposed method will be surveyed whereas Sect. 3 assesses the key component, the task description, in a more detailed way. Section 4 presents three examples and Sect. 5 revises benefits and limitations of the method and gives perspectives for future developments.

2 Method

The proposed method aims at evaluating the performance of kinematic design alternatives of instruments for minimally invasive surgery with respect to a given task, prior to building them. The course of the method is presented in Fig. 1, left. Following [11], the "tool" and the "task" need to be clearly specified as a primary step. Here, "tool" is referred to as "set of design alternatives". Subsequently, kinematic simulations are performed yielding the joint angles of the instrument, necessary to execute the task. Based on these joint angles, the predefined success ratio "SUR" and Shaft Distance "d_{IB}" criteria are applied to evaluate the performance. The "SUR" value accounts for the amount of successfully performed tasks and it ranges from 0 to 100 %. The "d_{IB}" value accounts for the consumed space during task execution and is only bounded from below. High values for "SUR" and low values for "d_{IB}" are desirable. Except for the task set presented in Sect. 3, the mentioned parts of the method are already published in [1]. However, parameters used to characterize the instruments and to configure the simulation are briefly recalled in the following.

An instrument is considered as a manipulator with 6DoF attached to the trocar i.e. the entry point to the patient, see Fig. 1 right. Here, the reference frame $\boldsymbol{T}_{Tr}$ for all other assigned frames is located, with x-axis pointing along the shaft of the instrument. At the trocar, 3DoF are located with joint angles q_1, q_2, d_3, see Fig. 1 right. These joint angles are independent of the instrument that is attached to it and are introduced to abstract the robot outside the patient. The instrument itself possesses 3DoF which are realized by a roll axis along the shaft, q_{Roll}, followed by an arbitrary sequence of pitch and yaw axes, RoM_{Pitch} and RoM_{Yaw}. To omit redundancy, a linear relationship between subsequent pitch and subsequent yaw is implemented. Each instrument possesses a tool center point TCP ${}^{Tr}\boldsymbol{T}_{TCP}$, i.e. a

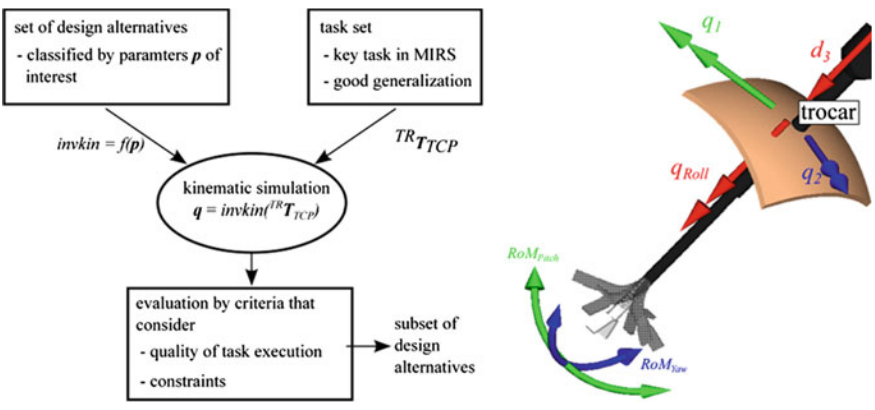

Fig. 1 *Left* Course of the evaluation method. *Right* Abstraction of a minimally invasive instrument with trocar and six resulting DoF's (Image adopted from [14])

frame at which for example a needle is grasped. Parameters, which are used to characterize instruments within the present method, are

1. The range of motion of the instrument: $RoM = \pm(q_{Roll,lim}, q_{Pitch,lim,i}, q_{Yaw,lim,i})$
2. The total number of pitch and yaw joints (N_{Pitch}, N_{Yaw})
3. The joint sequence, i.e. the order of the pitch and yaw joints
4. The total kinematic length l_{kin} i.e. the distance from the intersection of the first two axes (roll ∩ pitch/yaw), ending at the TCP.

Another important parameter is the initial length of the shaft, i.e. the initial distance of the trocar towards the instruments TCP frame ${}^{Tr}\boldsymbol{T}_{TCP}$, denoted as ${}^{Tr}\boldsymbol{t}_{TCP}$. For more details, see [1].

3 Generalization of Tasks

As stated by Sheridan [11], the choice and specification of the tool and the task are considered to be the crucial points in every evaluation method. Since the "tools", i.e. the instruments, are already specified, a generalized specification of the task is presented in the following. According to [11], the description of a task utilized for performance evaluation should contain (1) a probabilistic characterization of the initial and final configuration pose of the manipulator and (2) the description at all possible task trajectories, i.e. the steps in between initial and final configuration. With respect to these two points, the overall task of "intracorporeal suturing" will be specified as

1. An initial pose of the needle with respect to a pose of the incision line
2. An ascending "stitching" and "knot tying" trajectory including the final pose, after the knot is tight.

In the following paragraphs, these specifications are explained in more detail. The acquisition of the "intracorporeal suturing" trajectory was done with a camera system, which tracked the TCP pose of a needle holder (NH) while performing "intracorporeal suture" in an open surgery test bed. Five expert surgeons and one trainee were asked to do this. For details, see [1]. This acquisition yielded a trajectory of the TCP of the NH with respect to the cameras reference frame. For the further developments of the task, it is necessary to represent this trajectory with respect to the pose of the incision line (IL), yielding

$$ {}^{IL}\boldsymbol{T}_{TCP}(t_n) = \left({}^{REF}\boldsymbol{T}_{IL}\right)^{-1} \cdot {}^{REF}\boldsymbol{T}_{TCP}(t_n) \quad (1) $$

${}^{REF}\boldsymbol{T}_{IL}$ represents the pose of the IL calibrated before the tracking experiment. To further specify the task "intracorporeal suturing", this trajectory will be decomposed into two parts which are dependent and independent of location of the IL, see Sect. 3.1. To achieve the suggested probabilistic characterization of the task, a uniform sampling of the pose of IL is done which is explained in Sect. 3.2.

3.1 Task Decomposition

According to [12], "intracorporeal suturing" can be decomposed into two major subtasks, which are "stitching" and "knot tying".

"Stitching" is the motion of the needle through the two flaps of the incision and consists of seven consecutive steps [12]: (1) Positioning the needle (2) Grasping the tissue (3) Pulling the needle through (4) Re-positioning the needle (5) Re-grasping the tissue (6) Re-pulling the needle through (7) Pulling suture through. Obviously, this subtask can be considered as a close interaction with the incision line (IL) and surrounding tissue. Therefore, a first hypothesis is set up which is substantiated afterwards.

Hypothesis 1: "stitching" is dependent on the pose of the IL For the task "stitching", several guidelines exist that can be found in basic surgical skill literature [13]. First of all, a complete suture should provide a level surface with a symmetric, small amount of eversion of the edges. The sides of the wound should be well aligned, so that redundant tissue does not develop at the end of the IL and cause vertical or horizontal misalignment. Consequently, the virtual connection between the penetration into and out of the tissue should be perpendicular to the line of incision.

To further investigate this dependency of the "stitching" task, we performed an experiment with the daVinci© surgical system at the department of urology, university of Leipzig where 4 experienced surgeons were asked to perform an "intracorporeal suture" on a standardized test-bed [14]. The IL was rotated in steps of 30°, starting from 0° and ending at 120°, to investigate whether the "stitching" motion adapts to the changed line of incision.

In Fig. 2, motion details of a "stitching" motion with respect to 5 different orientation of the IL (green) are presented as image sequence of 3 images in 5 columns. First of all, it can be confirmed, that the assumption of the right angularity of the "stitching" motion with respect to the IL is correct. Needle (first and second row) and suture string (third row) can be observed to be perpendicular throughout every investigated angle of the IL. Furthermore, the axis along the branches of the needle holder is by observation parallel during the "stitching" of both wound sides. Both observations confirm Hypothesis 1.

The second subtask, "knot tying", is the motion of forming a loop and tightening the knot and consists of four consecutive steps [12]: (1) Positioning the needle and suture (2) Forming loops (3) Pulling short tail through loops (4) Pulling knot tight. The steps 1–3 are considered here to be free movements since there is no interaction with the line of incision and surrounding tissue. They are performed based on the surgeons experience and are adjusted to existing constraints in the workspace. Therefore, the following, second hypothesis is set up and substantiated afterwards.

Hypothesis 2: "knot tying" is independent on the orientation of the IL Forming a proper knot in surgery is considered as a crucial and complex task, however the pure motion necessary to form the loops and tighten the knot is considered to

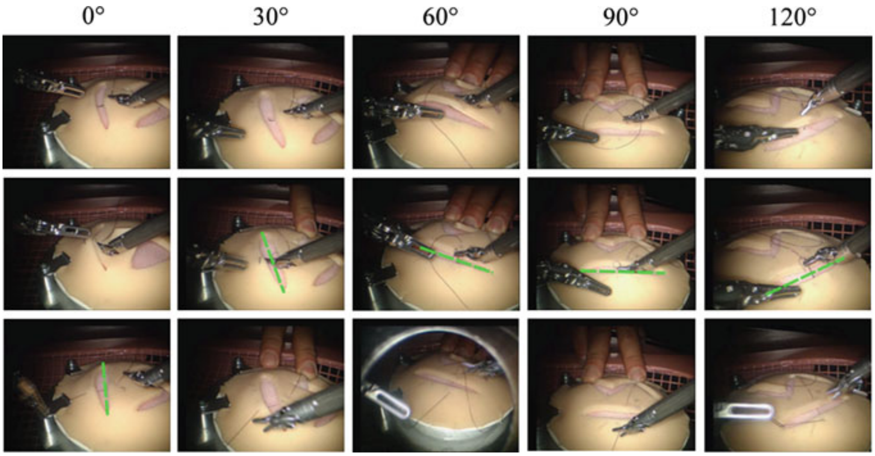

Fig. 2 Orientation of the needle holder/needle during the subtask "stitching" of the task suturing w.r.t the orientation of the incision line (*green*). Images are shown exemplarily from one surgeon

require less then 6DoF but at least 3DoF [15]. Except from step 4 "pull the knot tight", the motion is not in direct contact with the tissue and therefore the space in which the motion takes place can be chosen freely within the confined space of a minimally invasive intervention. For this, Hypothesis 2 holds. To substantiate this, again observations from the experiments with the daVinci© surgical system at the department of urology, university of Leipzig are presented. In Fig. 3, motion details of a "knot tying" motion with respect to 5 different orientations of the IL (5 columns) are presented as an image sequence of 3 images. Although images of the

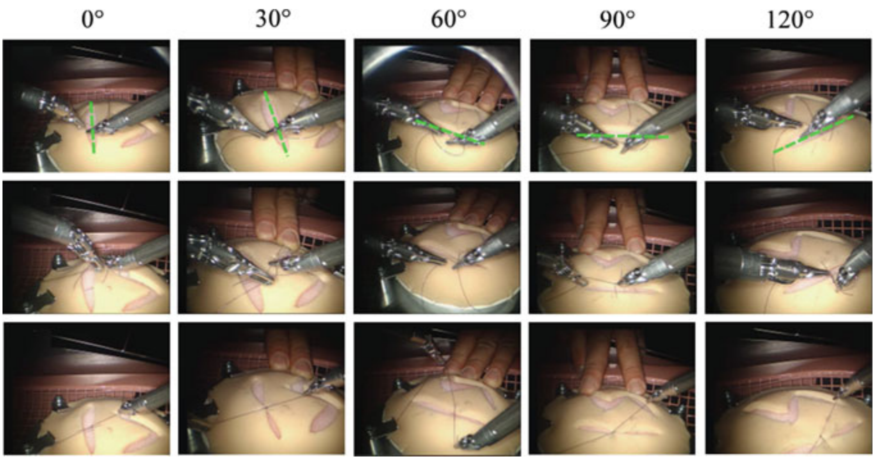

Fig. 3 Orientation of the NH/needle during the subtask "knot tying" w.r.t. the orientation of the incision *line* (*green*). Images are shown exemplarily from one surgeon

respective steps vary, no correlation between the orientation of the IL and the orientation of the needle holder can be observed.

As a summary of the paragraph, "intracorporeal suturing" can be decomposed in two subtasks, the "stitching" motion, which is rather complex and dependent on the orientation of the IL, and the subtask "knot tying", a motion which is performed without having contact to the tissue and therefore needs less DoF. Moreover, it is independent on the orientation of the IL.

3.2 Sampling of the Line of Incision

An instrument has to enable the task "intracorporeal suturing" in a diversity of orientations in a minimally invasive intervention. To account for this diversity, the initial orientation of the IL ${}^{Tr}\boldsymbol{R}_{IL,init} \in SO(3)$ is sampled uniformly by using a method proposed in [16]. This method ensures a deterministic equivolumetric sampling of *SO(3)*, the space of 3 dimensional rotations. It is based on a multiresolution grid on sequences of Cartesian products, e.g. the Cartesian product of S^1 and S^2 creating the space *SO(3)*. The resulting grid of the space $S^1 \otimes S^2$ has N_p points, [16]. To generate the aforementioned uniform deterministic sequence over *SO(3)*, the open source C++ library by Jain [17] is used. The output grid is parameterized using unit quaternions *(x, y, z, w)*. Thus, the initial orientation of the IL at each grid point *i* is rotated

$$
\begin{aligned}
{}^{Tr}\boldsymbol{R}_{IL,i} &= {}^{Tr}\boldsymbol{R}_{IL,init} \cdot {}^{IL,init}\boldsymbol{R}(x_i, y_i, z_i, w_i) \quad i = 1 \cdots N_p \\
{}^{Tr}\boldsymbol{R}_{IL,i} &= \begin{bmatrix} {}^{Tr}\boldsymbol{R}_{IL,i} & {}^{Tr}\boldsymbol{t}_{IL} \\ \underline{0}^T & 1 \end{bmatrix}
\end{aligned} \tag{2}
$$

whereas ${}^{Tr}\boldsymbol{R}_i(x_i, y_i, z_i, w_i) \in SO(3)$ is one grid point of the sample set in *SO(3)* and ${}^{Tr}\boldsymbol{t}_{IL}$ is the initial distance vector, starting at the global reference frame at the trocar and ending at the initial suture line, see Sect. 2. The creation of this uniform grid of initial IL orientation is illustrated in Fig. 4.

3.3 Overall Task—Summary

The overall task for the proposed evaluation method is presented in a general manner, the initial pose is characterized probabilistically and the trajectory embodies a key task for the surgical field generalized for the evaluation of instruments. The task constitutes of the following elements. A suturing trajectory ${}^{IL}\boldsymbol{T}_{TCP} \in R^{4x4}$, see Eq. (1), is performed at N_p different initial orientation of the IL ${}^{Tr}\boldsymbol{T}_{IL,i} \in R^{4x4}$, see Eq. (2) and Fig. 4. The overall trajectory for the *i*th grid point is described as

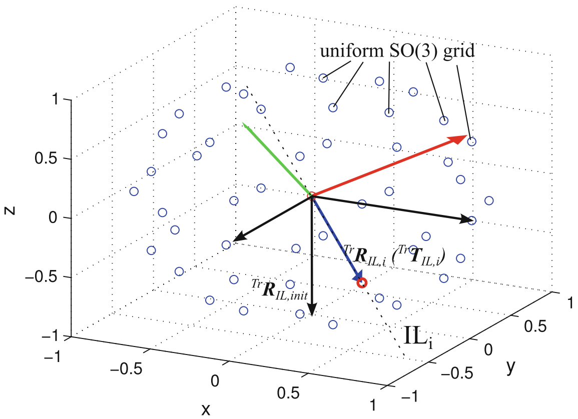

Fig. 4 Creation uniform grid of ILs. The orientation of the initial incision line $^{Tr}\boldsymbol{R}_{IL,init}$ (black) is sampled with a the uniform grid of the *SO(3)* of size N_p created around the origin of $^{Tr}\boldsymbol{R}_{IL,ini}$. A resulting incision line IL_i with frame $^{Tr}\boldsymbol{R}_{IL,i}$ (*colored*) is illustrated as an example

$$^{Tr}\boldsymbol{T}_{TCP.i}(t_n) = {}^{TR}\boldsymbol{T}_{IL,i} \cdot {}^{IL}\boldsymbol{T}_{TCP}(t_n) \tag{3}$$

This TCP trajectory serves as an input for the kinematic simulation, see Fig. 1 left, which needs to be executed for the evaluation process. The relevant component of the task "intracorporeal suturing" is identified to be "stitching" which results from the observations stated in Sect. 3.1. The suturing trajectory $^{IL}\boldsymbol{T}_{TCP} \in R^{4x4}$, see Eq. (1), however contains the "stitching" and the "knot tying" motion. Aside from other factors, the influence of both trajectories, i.e. "stitching" and "stitching" + "knot tying" = "intracorporeal suturing", will be presented in the next section.

4 Results

In the following section, four different use cases will be presented. First of all, it is examined, whether a full "suturing" trajectory or only the "stitching" partition is used for the evaluation. It will be shown, that the application of only the "stitching" motion is sufficient. Afterwards, a comparison of different alternatives from the literature will be shown. The subsequent example contains a sampling over different *RoM*'s for the roll axis of different alternatives to highlight its contribution to the *SUR* value i.e. how successful the task "stitching" is performed with respect to different orientations of the IL.

Example 1: The first example examines different task trajectories and their influence on the evaluation criteria *SUR*- and d_{IB} value. The task trajectories in focus are (1) complete "intracorporeal suture" composed of "stitching" and "knot tying" and (2) the "stitching" trajectory solitary. The results of this comparison are

Table 1 Influence of the task trajectory on the *SUR* value from different instruments

Design	"Stitching" + "Knot tying" mean (*SUR*) ± std (%)	"Stitching" mean (*SUR*) ± std (%)
Madhani [5]	28.8 ± 8.2	36.2 ± 6.5
Berkelmann [6]	26.5 ± 7.6	33.1 ± 6.9
Cooper [7]	26.23 ± 7.5	36.4 ± 4.5
Harada [8]	29.7 ± 8.4	35.8 ± 6.6

presented in Table 1. As mentioned earlier, for the complete suture, the initial orientation of the "knot tying" motion is sampled as well, since the initial orientation of the "stitching" motion is sampled (see Sect. 3.2 Sampling of the line of incision). However, it is stated that the "knot tying" motion is independent of the line of incision and therefore needs not necessarily to be sampled. Thus, the results for the *SUR* values attained with the "suturing" motion illustrate a kind of worst case scenario. The results contain mean-values and standard deviation for the *SUR* value for different instrument designs from literature (number of joints, joint sequence and kinematic length are known from the respective publication) sampled over different *RoM*s for the roll (±180° to ±360°) pitch and yaw (±70° to ±100°) axes. From Table 1, it can be observed that the "stitching" part of the suturing trajectory exhibits the main contribution to the evaluation results since the *SUR* values attained for the different reference trajectories "stitching" and "suturing" do not vary by more than the respective standard deviation. The decrease of the *SUR* values when performing a complete "*suturing*" motion can be addressed to the aforementioned assumed "worst case". In conclusion, the reference trajectory "stitching" was chosen for the following examples.

Example 2: In Table 2, a comparison of five instrument designs from the relevant literature is shown. As mentioned earlier, the reference trajectory is a "stitching" motion. By observation, these findings can be stated:

1. As kinematic length increases, the shaft distance criterion increases as well, e.g. l_{kin} = 20 mm yields approx. d_{IB} of 8 mm whereas l_{kin} = 10 mm yields approx. d_{IB} of 5 mm
2. The low *SUR* 6.4 % design [4] is due to the small range of the pitch and yaw joints with ±45° each, whereas the other alternatives realize ±90°.

Table 2 Comparison of 5 instrument alternatives evaluated with the proposed method

Design	RoM (°)	$N_{pitch,yaw}$	Type	l_{kin} (mm)	SUR (%)	d_{IB} (mm)
Madhani [5]	±(270, 90, 90)	(1, 1)	RPY	10	39.5	5.0 ± 0.8
Berkelmann [6]	±(180, 90, 90)	(4, 4)	RPYPYPYPY	20	26.6	8.1 ± 2.4
Seibold [4]	±(180, 45, 45)	(1, 1)	RPY	30	6.4	15.0 ± 0.5
Cooper [7]	±(270, 90, 90)	(2, 2)	RPYYP	20	38.3	8.2 ± 2.5
Harada [8]	±(180, 90, 90)	(2, 2)	RPYPY	10	25.1	5.2 ± 1.3

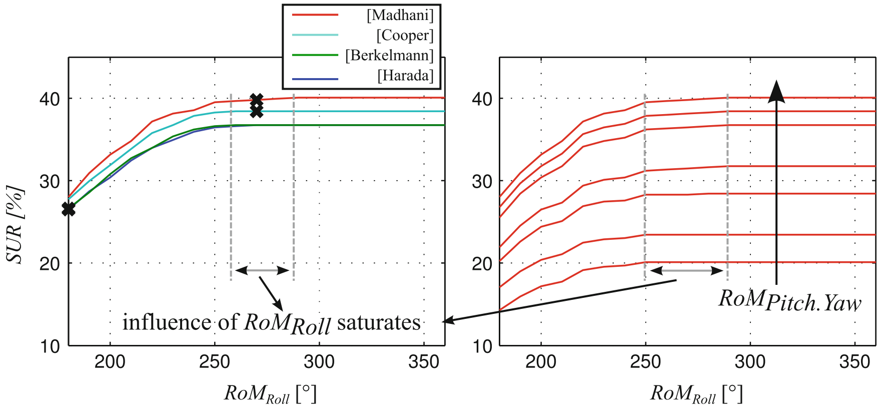

Fig. 5 Influence of the RoM of the roll joint regarding different instrument designs (*left*) and varying RoM for the pitch and yaw axis of the design from Madhani [5] (*right*)

3. The superiority of designs [5, 7] are due to the high *RoM* in the roll axis of ±270°, whereas the others only realize ±180°.

Example 3: Point 3 from Example 2 motivated us to further investigate the potential influence of the roll axis, especially if we consider the case of a multi turn roll axis, i.e. a roll axis without limits. Therefore, four designs with the same *RoM* for the pitch and yaw joints are considered [5–8] (see Fig. 5, left). Furthermore, the design from Madhani [5] is investigated were the *RoM* of the pitch and yaw joints is varied from ±70° to ±100°, (see Fig. 5, right). By observation, we can conclude that the influence of the roll axis onto the *SUR* value saturates in between ±255° and ±290°. This saturating characteristic is

1. independent of the evaluated instrument kinematic and
2. independent of the *RoM* of the pitch an yaw joints

5 Conclusion

The paper at hand presented extensions and new results for the method published in [1] to evaluate alternative instrument kinematics w.r.t. their ability to perform a surgical task. The extensions included a more generalized representation of the reference task “intracorporeal suturing” by decomposition it into two subtasks, “stitching” and “knot tying”. As “stitching” was identified to be the more complex motion and is also strongly dependent on the orientation of the incision line, it is the subtask representing the main challenge for an instrument and therefore it was proposed to be sufficient to use only this subtask in the evaluation method. The approach could be confirmed by the results presented in Sect. 4, Example 1.

The method incorporates criteria that reflect the performance of an instrument alternative with respect to the developed task and the consumed space while executing it. With these criteria, mechanical designers are able to compare new or known instrument kinematics quantitatively in order to develop them task specifically, see Sect. 4 Example 2. Notably, the setup independence and the task generalization including specific motions that mainly affects the instruments capabilities contributes to a precise evaluation process and is the benefit of this method compared to others, e.g. [9, 10].

The method and its derived conclusions can be generalized to all instrument designs incorporating a roll axis as their first axis followed by an arbitrary sequence of pitch and yaw axis. This type of instrument is the most common design see e.g. [4–8]. To incorporate instruments with one or more intermediate roll axes, e.g. the instrument from [10], the instrument classification parameters as well as the kinematic simulation algorithm needs to be adapted which will be in focus of future work on this topic.

As conclusion we recommend for instrument designers to carefully design the range of motion of the roll axis, which should be ±270° for the tasks examined in this paper. As the performance saturates at ±270°, the general assumption that a greater range of motion yields a higher performance could be reconsidered.

Acknowledgments The authors would like to thank all surgeons for participating in the experiments, which are Prof. Rau, Dr. Authenrieth, Dr. Maurer, Dr. Do and PD Dr. Weikert.

References

1. Deutschmann B, Konietschke R, Albu-Schäffer A (2013) Task-specific evaluation of kinematic designs for instruments in minimally invasive robotic surgery. In: IEEE conference on intelligent robots and systems, pp 3590–3597
2. Derossis AM, Fried GM, Abrahamowicz M, Sigman HH, Barkun JS, Meakins JL (1998) Development of a model for training and evaluation of laparoscopic skills. Am J Surg 175 (6):482–487
3. Moorthy K, Munz Y, Dosis A, Hernandez J, Martin S, Bello F, Rockall T, Darzi A (2004) Dexterity enhancement with robotic surgery. Surg Endosc 18(5):790–795
4. Seibold US (2013) An advanced force feedback tool design for minimally invasive robotic surgery. TUM München
5. Madhani J (1998) Articulated surgical instrument for performing minimally invasive surgery with enhanced dexterity and sensitivity, US5792135
6. Berkelman P, Ma J (2009) A compact modular teleoperated robotic system for laparoscopic surgery. Int J Rob Res 28(9):1198–1215
7. Cooper T (2003) Surgical toll having positively postiionable tendon-actuated multi-disk wrist joint.pdf, US2003036748A1
8. Harada K, Tsubouchi K (2005) Micro manipulators for intrauterine fetal surgery in an open MRI. IEEE Conf Robot Autom, 2–7

9. Cavusoglu MC, Villanueva I, Tendick F (2001) Workspace analysis of robotic manipulators for a teleoperated suturing task. In: Conference on intelligent robots and systems,. 4:2234–2239
10. Salle D, Bidaud P (2004) An optimal kinematic design for a highly dextrous MIS instrument. In: Advances in robot kinematics, Springer, 399–408
11. Sheridan T (1976) Evaluation of tools and tasks: reflections on the problem of specifying robot/manipulator performance, pp 27–38
12. Cao C, MacKenzie C, Payandeh S (1996) Task and motion analyses in endoscopic surgery
13. Murakami C, Odland P (1993) Techniques suturing simple and knot tying. In: Basic surgical concepts and procedures, pp 178–188
14. Chamberlain (2014) Suture Skills POD. (Online) Available: http://www.thecgroup.com/product/robotic/skills/suture-skills-pod
15. Kang H (2002) Robotic knot tying in minimally invasive surgeries. In: IEEE conference on intelligent robots and systems, pp 1421–1426
16. Yershova A, Jain S, Lavalle SM, Mitchell JC (2010) Generating Uniform Incremental Grids on SO(3) Using the Hopf Fibration. Int J Rob Res 29(7):801–812
17. Jain S (2009) Library for uniform deterministic sequences/sets of samples over 2-sphere and SO(3)

Third Arm Manipulation for Surgical Applications: An Experimental Study

E. Abdi, M. Bouri, S. Himidan, E. Burdet and H. Bleuler

Abstract Surgeons need assistance in most types of surgery. This necessary teamwork is costly and can be a source of error and inefficiency due to communication problems such as a lack of coherence among the surgeon's and assistants' actions. A robotic arm under the surgeon's full control improves his/her dexterity and simplifies the teamwork. While the hardware of such an arm is readily available, the most efficient way to use it remains an open question. This chapter presents our experimental setup and paradigm for studying the control of a third arm for the surgeon. This study mainly focuses on the embodiment mechanism of the third arm, the intuitiveness of the control strategy and the appropriate level of complexity of the tasks.

Keywords Third arm · Telemanipulator · Embodiment · Virtual reality · Robotic surgery

1 Introduction

Teamwork is essential in almost every type of surgery as surgeons need assistance for various activities during an operation. However it can be a source of error and inefficiency especially if the assistant is novice or unfamiliar with the surgeon [1]. Each surgeon has his/her unique commanding method; also each assistant may execute the commands with a variable degree of accuracy and precision. Our vision is that some of the drawbacks of teamwork could be reduced if the surgeon could

E. Abdi (✉) · M. Bouri · H. Bleuler
École Polytechnique Fédérale de Lausanne (EPFL), Lausanne, Switzerland
e-mail: elahe.abdi@epfl.ch

S. Himidan
University of Toronto, Toronto, Canada

E. Burdet
Imperial College of Science, Technology and Medicine, London, UK

H. Bleuler et al. (eds.), *New Trends in Medical and Service Robots*,
Mechanisms and Machine Science 38, DOI 10.1007/978-3-319-23832-6_13

work with a third robotic arm under his/her own full control. This could decrease errors arising from miscommunication among the surgical team, and the surgeon would be more autonomous and dexterous. In addition, this could help define new surgical techniques and operational tasks, which are impossible to realize with only two hands.

A supernumerary arm may especially be useful when surgeons have to perform tiresome, repeated and long tasks during the surgery. In the majority of cases they need one or more assistants to hold the surgical instruments, hand them the required tools and assist in performing difficult tasks that are not possible to be done single handed.

Direct observation of microsurgery, laparoscopic surgery and open surgery reveals some essential situations in which the surgeon requires direct assistance. The authors have identified some examples of these situations. In microsurgery, due to the small dimensions of the nerves and vessels it is important to keep them fixed during suturing under the microscope. An assistant does this task. Holding the structures in the correct position to be sutured may last for a long time as the suturing task in this kind of surgery is very delicate and precise. Also in order to perform the anastomosis of an artery, the surgeon needs to change instrument throughout the process. An instrument with blunt tip is inserted into the vessel and a tweezers holds the thread during suturing. A surgeon equipped with three functional hands may not need to change instruments during the process. Furthermore, a robotic third arm would not have any problem remaining at a fixed position, in contrast to a human assistant suffering from tremor and fatigue. Microsurgery is usually a lengthy procedure and although the surgeon sits during the surgery, the long periods of concentration and the repetitive tasks of suturing and holding the tissues are quite exhausting. On the other hand, in laparoscopic surgery three instruments are needed for suturing, two of which are actively involved in the process while the third one is used to support the thread and make the stitch more stable. The third instrument should just be placed and held in the right position with no need for movement of its jaws. A third robotic arm thus could significantly increase the independence of the surgeon. In open surgery, a third arm may be useful for holding a suction tube to clear blood or retract organs that block the work site. However, generally in this kind of surgery, an advanced third arm with improved manipulation capacity seems desirable.

Robotic instruments are already present in the modern surgical theater. Teleoperated surgery (also called «Robotic Surgery») is rapidly gaining popularity among surgeons and patients alike for a variety of reasons. It allows minimal invasiveness without the drawback of very difficult, counter-intuitive manipulation. It provides a more comfortable working setup for the surgeon as he/she can sit during the operation. Also a robotic instrument compared to a human can be more precise, more dexterous and steadier. The decisive factor is the intuitiveness of complex manipulation in a restricted workspace and in a minimally invasive setting. This factor stands out dramatically when comparing current teleoperated surgical robotics with "conventional" mini-invasive surgery tools. Robotic surgery thus opens up the potential for new surgical techniques and wider capabilities. Research in cognitive neuroscience indicates that crucial advantage in intuitive handling of complex bi-manual, multi-degree-of-freedom manipulation is due to the efficient embodiment of the tool [2]. In other words, this means that the human sensory-motor system accepts quickly and naturally a bimanual tool as extension of the operator's hands.

In 1998, Botvinick and Cohen [3] demonstrated the possibility of inducing the perceptual illusion of owning a rubber hand. This demonstrated the plasticity of the brain's perception of the body. In their famous "rubber hand illusion", they placed the real arm of the subject behind a screen and put a rubber hand in his sight. After 10 min of simultaneous stroking of the two hands, the subjects had the illusion of feeling the stroke on the rubber hand. From research in cognitive neurosciences [4, 5] and from other examples (e.g. musicians) it is known that the human brain has the capacity of embodiment of supernumerary members. This applies to both the rubber limbs as well as the virtual limbs.

This is precisely the research topic of this contribution, namely natural intuitive control of a third artificial (robotic) supernumerary arm [6] that the user would control as a natural arm. The next section is devoted to explaining the strategy for controlling the third arm, and then the experimental setup used for the study is described in detail, followed by the experimental paradigm. Finally some initial results and conclusions are presented.

2 Review of the Third Arm Control Strategies

Ideally the surgeon would have direct control over all the devices involved in any surgery. During the past years there have been a number of attempts to provide robotic assistants for the surgeon, especially to hold the camera during laparoscopic surgery. Three approaches for controlling the robot have been developed. The existing robots are motion controlled e.g. EndoAssist [7], voice activated e.g. AESOP (Automated Endoscope System for Optimal Positioning) [8], or simply commanded by a joystick e.g. LapMan [9].

EndoAssist was first introduced in a paper in the year 1982 [10]. In EndoAssist the movement of the camera is directed by the surgeon's head movements. This is accomplished using a head mounted infra-red emitter and a sensor which detects the motion of the emitter (Fig. 1). A foot clutch is used to avoid any unnecessary movement of the camera. A study was performed to compare the EndoAssist with a human camera holder. The results showed no significant difference in complication rates or total operative times between the two methods.

AESOP was first released in 1994 in USA (Fig. 2). The control commands with the voice of the operating surgeon are stored in a card and can be used during the surgery. The robot has 7 DOF and can be controlled either by a voice, hand or foot actuated controller [11]. Kavoussi and Moore [12] compared the accuracy of AESOP with a human assistant in holding the endoscope during urological laparoscopic surgery. They assessed the operative time, erroneous camera motions,

Fig. 1 EndoAssist: The arrow shows the camera driver [7]

Fig. 2 AESOP robot [19]

complications and outcome. The robotic arm holds the camera in a steadier manner with less inadvertent movements. They concluded that a robotic camera holder is more effective and accurate compared to a human assistant.

According to Wagner et al. [13] AESOP and EndoAssist have the same surgical performance. EndoAssist responds accurately and enables the surgeon to have the exact desired view. On the other hand, it is bulky, cannot be mounted on the table and its activation and inactivation is dependent on a pedal. The surgeon has to push

Fig. 3 LapMan and LapStick (www.medsys.be/surgical-robots)

a pedal to start or stop the tracking of his/her own head movements; otherwise the camera will respond to every single movement of the surgeon's head, which is not desirable.

The LapMan endoscope holder robot developed in 2004 is controlled by a joystick (LapStick) clipped onto a laparoscopic surgical instrument under the surgeon's index finger (Fig. 3) [14]. It allows the surgeon to operate in conditions of restricted surgical assistance.

Also in 2004, Kwon et al. [15] proposed a combination of the two main control methods used for the camera holding robots. Their robot named KaLAR, may be controlled either by voice commands, or by tracking the surgical instrument which has already been marked. According to their research, in order to reduce the required voice commands for controlling the robot, it should have more information about what is going on during surgery. For example, change of surgical instruments and insertion and extraction of the instruments may be used as indicators of transition phases.

A more recent camera holder robot is the LER (light endoscope robot) developed in 2007 [16]. It is a voice controlled robot which can be placed on the patient's skin and is lighter and smaller than the older similar robots. Finally, there is the commercialized ViKY [17] also released in the year 2007, originated from the TIMC-IMAG laboratory [16] and manufactured by Endocontrol company. It can be entirely sterilized and can be directly mounted on the operating table. It has 3 DOF and can be controlled either by voice commands or a multidirectional footswitch. In the next version they will attempt to improve the control method based on visual servoing using instrument tracking [17]. Their preliminary results are encouraging. They also hope to have a relatively independent camera holder so that the surgeon can focus more on the operation.

Although these robots are found to be useful, they require the surgeon to divide his/her attention between the operation and control of the robot. Moreover, most of these robots simply hold and direct the camera in laparoscopic surgery. Our contribution aims at more general use of the third hand requiring more complex control.

3 Development of a Third Arm Control Experiment

One of the main goals of this study is to develop a control strategy which is easy, natural and intuitive for controlling a third robotic arm. The control interface should be non-invasive with minimum distraction for the surgeon, as the operation demands maximum level of attention of the surgeon.

One strategy to control the robotic arm would consist of using the foot. We already use our feet in different tasks like driving, playing musical instruments such as organs or percussion, pottery, etc. Interestingly enough, the use of the foot in these applications is not a distraction for the user. It is also proven in the case of arm amputees that people can even write or draw with their feet, indicating the high level of control and precision that can be achieved with the foot through practice. This strategy is non-invasive and does not require high-tech systems. One of the main shortcomings of the foot is that normally, with little practice, it cannot reach the same level of precision as of the hands, especially in multi-degrees-of-freedom tasks such as complex manipulation. However this problem may be addressed by using an appropriate foot interface. Here we design experiments to investigate how such an interface could be used together with the hands. In particular we study the faculty to simultaneously control three virtual hands: Two corresponding to our natural hands and the third one commanded by an appropriate foot device.

3.1 Experimental Setup

The details of the interface used in experimental studies are explained in this section. As a first step, the studies are realized in virtual reality. A series of computer games are designed in which the player has to use three virtual hands to succeed in the game. It is reported in the literature that a first person view of the fake or virtual body is essential in the illusion of ownership [18]. In addition, a realistic skin tone and body shape are important factors in the embodiment [5, 18]. These results motivated us to produce a realistic view of the hand in virtual reality. Also, it is desirable to reproduce the finger movements of the two real hands in virtual reality. It provides the possibility of using hand gestures for commanding. Tracking finger movements has two main benefits: first, the virtual hands will look more realistic as they mimic the exact movements of the real hands; second, it would be possible to use finger movements as command signals in the games.

Different kinds of software and hardware have been developed for detecting the finger motions, however not all of them have the desired level of accuracy and rendering speed. In the present experimental setup Microsoft XBOX 360 Kinect© depth cameras are used for tracking the movements of the limbs. However, at the time of development of the setup (Fall 2013) there was no inherent SDK for this type of camera for detecting the finger motions. Thus, we have used the Nimble VR Company SDK which is free for academic use. They have chosen a set of most

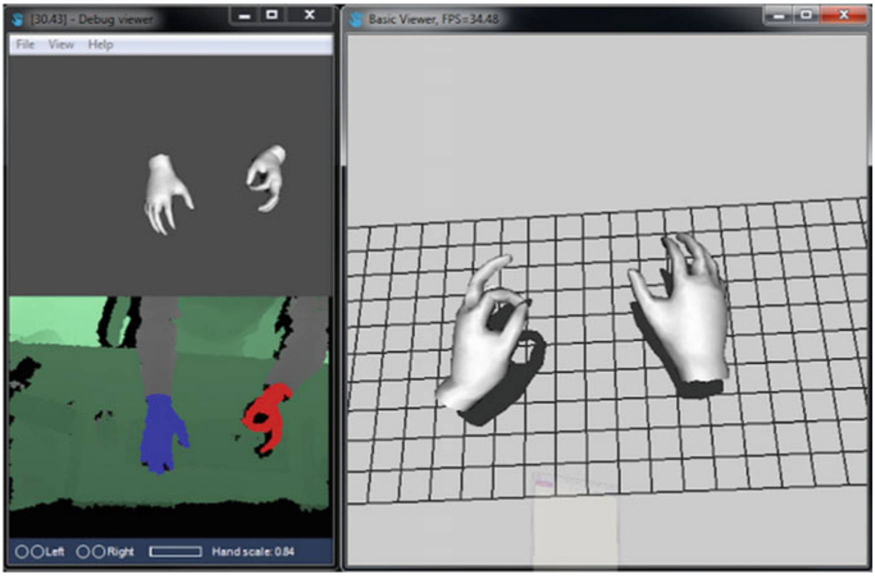

Fig. 4 *Left up* the model produced by the Nimble VR SDK, *left down* hands tracked by the camera, *right* virtual hands used in a program (nimblevr.com)

popular hand gestures and defined them in their library. Consequently, it can recognize a limited number of hand gestures (8 gestures as of Fall 2013). Figure 4 shows a screenshot of the virtual hands produced by the Nimble VR's SDK on the basis of the real hands tracked by the Kinect camera.

The Nimble VR's SDK is designed to run on a PC with the following minimum specifications: Intel Core i7 2.3 GHz or above, 8 GB of RAM and Windows 7 64-bit or Mac OS X 10.8.2.

We have used two XBOX 360 Kinect cameras; one for tracking the movements of the subject's two real hands and another one for tracking the movements of the feet. Each SDK can support one camera. This indicates that two SDKs should run on two different threads in parallel to render the two normal hands and the third hand in virtual reality. Each PC can support only one SDK at a time so in order to have both SDKs functioning simultaneously; each should run on one PC. Consequently, a network of two PCs is necessary for the whole setup to function appropriately in real-time.

A set of computer games is prepared in which three virtual hands are used simultaneously to complete the game. Two of the virtual hands mimic the movements of the two real hands and the third one is actually the foot modeled as a hand. Three games are designed, each aimed at a specific research question.

The first game studies the possibility of controlling the third hand by foot. In this case study, the subject has to move the three hands to touch three rectangles on the screen simultaneously as fast as possible. The second game is aimed towards

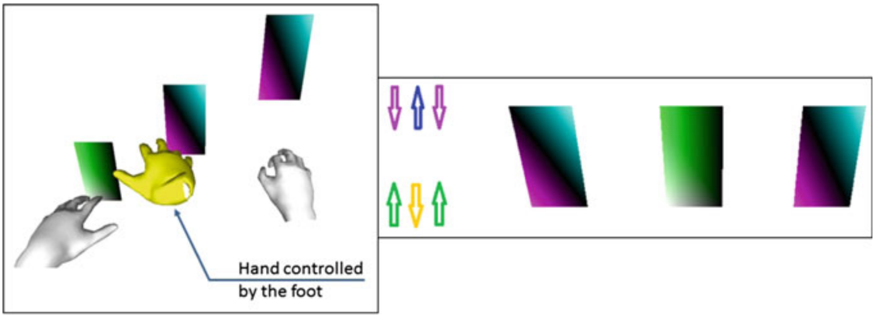

Fig. 5 *Left* three virtual hands and three targets in the first game. *Right rectangles* and *arrows* indicating the right direction of motion for each rectangle

studying the possibility of moving the real hands and the virtual hand independently in different directions. The user moves three rectangles in the direction of the arrows on the screen. The simultaneous movements of the three rectangles in the right directions should last for 3 s (Fig. 5). Once a successful movement is detected, the directions of the arrows change 180°. Each set of arrows appears on the screen twice. In the last game, aimed to study the feasibility of simultaneous usage of three hands for performing more complicated tasks, the user should catch three falling objects before they reach the ground. The falling speed of the objects increases as one improves in the game. All the subjects play the games in the same order from the first one to the last one. The first game is the easiest one and the last game is the hardest. Each game is played twice. The first time the subject gets familiar with the rules and the second time he/she can concentrate on having a better performance.

At the end of each game, participants fill in a questionnaire about the intuitiveness of the control strategy, the complexity of the task and its mental and physical burdens. The time spent for each game and the success rate are recorded.

4 Results

This experimental setup has been tested with thirteen participants. Their answers to the questionnaires and their actual performance are the assessment factors for the system.

Initial results show that people improved in controlling the third hand as they practice more. This indicates that the task can be successfully carried out but requires some practice. Time required to complete the task is one indicator of improvement in the game. Figure 6 shows the average time for all the subjects for completing the second game. In this game the subjects have to move the rectangles in the direction of the indicator arrows on the screen. The subjects play the whole game twice. The required time for completing the game reduces from the first to the second trial.

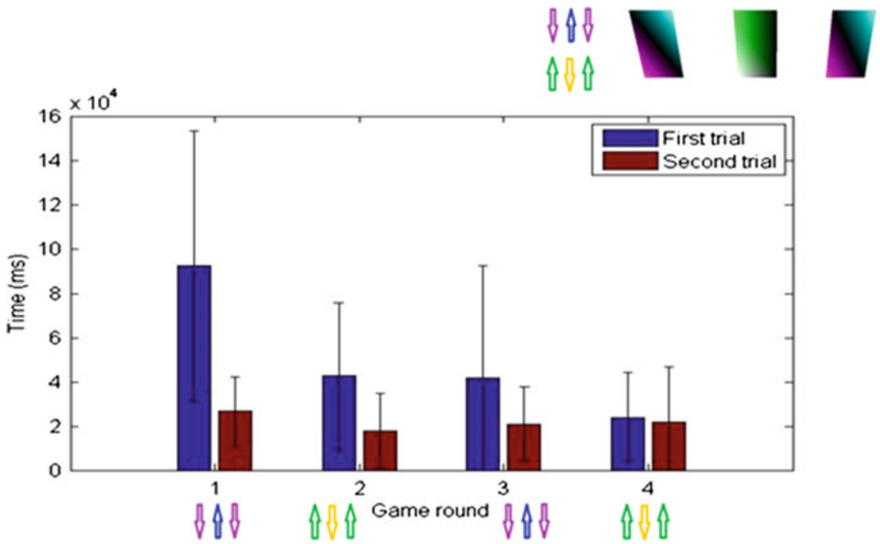

Fig. 6 Average performance time for all the subjects in the second game for the first and the second trials

Responses to the questionnaire show that in general, most participants do not find the experiment tiring mentally nor physically. This is seen positively but may be also attributed to the fact that the total time required for the experiment is not so long as it lasts for about 15–20 min only.

The participants reported finding the third game more helpful in mastering the control of the third hand. In this game, the player has to catch the objects before they reach the ground. There are two possible reasons for this. First, this game is always the last one played. This means that people have practiced during the previous games and they have become familiar with using the system. Second, during this game people have to move their feet more than in the other games.

5 Conclusions

The need for communication in the operating room between individuals can be a source of error and inefficiency. Currently the surgeon must rely on assistants for a large number of tasks. If the assistant does not have sufficient experience, this can be unnerving for the surgeon and dangerous for the patient. A third robotic arm under the surgeon's full control would decrease his/her dependency on assistants.

This contribution described our initial research on the possibility of controlling a third hand simultaneously with the two real hands. The most important issues to address are related to the appropriate control strategy and the embodiment of the third arm. The foot is a good candidate for controlling the third arm as we already use our feet for driving, playing musical instruments, etc., and it has proven to be quite reliable and capable for many tasks. An experimental setup was developed in which the user interacts in a virtual reality scenario using three virtual hands. Two of the virtual hands mimic the motions of the real hands and the third one is controlled by one foot. Two Microsoft Kinect cameras are used for tracking the movements of the two real hands and the foot. The possibility of the simultaneous use of three hands, the process of embodiment of the third arm and the appropriate level of complexity of the tasks are evaluated.

Initial results presented in this study showed that after some practice, the subjects improve dramatically and they feel more at ease. In addition, for most of the subjects using the foot for controlling the third arm is not mentally or physically tiring. The next steps will involve adding force feedback to the system as well as controlling a real robot using a more sophisticated foot interface and the limit of complexity of operations that can be conducted in this way.

Acknowledgments E. Burdet was funded in part by the EU-H2020 ICT-644727 COGIMON grant.

References

1. Nurok M, Sundt TM, Frankel A (2011) Teamwork and communication in the operating room: relationship to discrete outcomes and research challenges. Anesthesiol Clin 29(1):1–11
2. Clark A (2007) Re-inventing ourselves: the plasticity of embodiment, sensing, and mind. J Med Philos 32(3):263–282
3. Botvinick M, Cohen J (1998) Rubber hands 'feel' touch that eyes see. Nature 391(6669):756
4. Sengul A, van Michiel E, Rognini G, Aspell JE, Bleuler H, Blanke O (2012) Extending the body to virtual tools using a robotic surgical interface: evidence from the crossmodal congruency task. PLoS ONE 7(12)
5. Shokur SI, Peter L, Bleuler H, Miguel N (2011) Social interaction probed by reaching to face images: rhesus monkeys consider a textured monkey avatar as a conspecific. In: Society for neuroscience. Washington DC, USA
6. Llorens-Bonilla B, Parietti F, Asada HH (2012) Demonstration-based control of supernumerary robotic limbs. In: 2012 IEEE/RSJ international conference on intelligent robots and systems (IROS)
7. Rane A et al (2007) Initial experience with the endoassist (R) camera holding robot in laparoscopic urological surgery. Eur Urol Suppl 6(2):186
8. Unger SW, Unger HM, Bass RT (1994) AESOP robotic arm. Surg Endosc 8(9):1131
9. Polet R, Donnez J (2004) Gynecologic laparoscopic surgery with a palm-controlled laparoscope holder. J Am Assoc Gynecol Laparoscopists 11(1):73–78
10. Dagan J, Bat L (1982) Endoassist, a mechanical device to support an endoscope. Gastrointest Endosc 28(2):97–98
11. Bozovic V (2008) Medical robotics, vol 1. I-Tech Education and Publishing, p 536
12. Kavoussi LR, Moore RG (1995) Comparison of robotic versus human laparoscopic camera control 154:2134. J Urol (1997), 158(4):1530–1530

13. Wagner AA et al (2006) Comparison of surgical performance during laparoscopic radical prostatectomy of two robotic camera holders, EndoAssist and AESOP: a pilot study. Urology 68(1):70–74
14. Polet R, Donnez J (2008) Using a laparoscope manipulator (LAPMAN) in laparoscopic gynecological surgery. Surg Technol Int 17:187–191
15. Kwon DS, Ko SY, Kim J (2008) Intelligent laparoscopic assistant robot through surgery task model: how to give intelligence to medical robots. In: Bozovic V (ed) Medical robotics, I-Tech Education and Publishing. ISBN: 978-3-902613-18-9
16. Long JA et al (2007) Development of miniaturized light endoscope-holder robot for laparoscopic surgery. J Endourol 21(8):911–914
17. Voros S et al (2010) ViKY robotic scope holder: initial clinical experience and preliminary results using instrument tracking. IEEE/ASME Trans Mechatron 15(6):879–886
18. Maselli A, Slater M (2013) The building blocks of the full body ownership illusion. Frontiers Human Neurosci 7:83
19. Mettler L, Ibrahim M, Jonat W (1998) One year of experience working with the aid of a robotic assistant (the voice-controlled optic holder AESOP) in gynaecological endoscopic surgery. Hum Reprod 13(10):2748–2750

Robotic Surgical Approach in Limited Access Anatomical Areas

N. Crisan, Iulia Pop and I. Coman

Abstract The implementation of robotic surgery in the urological practice was extremely fast due to the advantages offered by this technology, advantages that outweigh the difficulties of the surgical techniques. Some of the challenges of the urological surgeries are the result of the limited access areas. Moreover, the surgery of the male pelvis (which is very narrow) is very difficult because the surgical gestures that are of great importance for the functional outcomes of the patient (urinary incontinence, erectile dysfunction) are performed in a limited access area. Also, the surgery of the retroperitoneum implies access in a narrow space in order to perform plastic or reconstructive interventions that involve the great abdominal blood vessels. Our aim was to evaluate the robotic surgical approach when performing urologic surgeries in limited access areas like the pelvis (radical prostatectomy, radical cystectomy) and the retroperitoneum (partial nephrectomy, radical nephrectomy, pyeloplasty). From a technical point of view, we evaluated the positioning of the trocars, the alignment between the trocars for the camera and for the instruments, the positioning of the trocar for the assistant surgeon, the conflicts between the robotic arms or between the robotic arms and the assistant surgeon's instruments. The technical aspects were reported to the perioperative and postoperative parameters in order to evaluate the way in which the technical difficulties influence the surgical technique. For the retroperitoneal approach, we used 5 trocars with a particular type of positioning, developed at the Robotic Surgery Center in Cluj-Napoca. The final aspect of the positioning of the robotic trocars is triangular shaped, which offers a generous movement space for them, but also for the assistant surgeon. There were no conflicts between the robotic arms and none of surgeries

N. Crisan (✉) · I. Coman
University of Medicine and Pharmacy "Iuliu Hatieganu" and Urology Department,
Clinical Municipal Hospital, Cluj-Napoca, Romania
e-mail: drnicolaecrisan@gmail.com

I. Coman
e-mail: jcoman@yahoo.com

I. Pop
Urology Department, Clinical Municipal Hospital, Cluj-Napoca, Romania
e-mail: dr.iuliapop@gmail.com

H. Bleuler et al. (eds.), *New Trends in Medical and Service Robots*,
Mechanisms and Machine Science 38, DOI 10.1007/978-3-319-23832-6_14

required conversion. The hospital stay varied depending on the complexity of the procedure. The robotic surgery has well-known technical advantages, but it also shows improvement for the access in limited areas, like the male pelvis and the retroperitoneum. Using the robotic approach and a well studied trocar positioning, the surgeon is able to perform very complex maneuvers without difficulties due to the limited access and without altering the perioperative and postoperative outcomes.

Keywords Robotic surgery · Robotic approach · Robotic cystectomy · Robotic pediatric surgery

1 Introduction

The implementation of robotic surgery in the urological practice was extremely fast due to the advantages offered by this technology, advantages that outweigh the difficulties of the surgical techniques. For example, robotic radical prostatectomy is considered the gold standard treatment for organ confined prostate cancer in countries where this technology is available [5]; furthermore, in 2008, robotic partial nephrectomy, of all the surgical techniques, had the most important development worldwide [12].

Some of the challenges of the urological surgeries are the result of the limited access areas or of the complexity of the procedures that require a large operating field. The surgery of the male pelvis (which is very narrow) is very difficult because the surgical gestures that are of great importance for the functional outcomes of the patient (continence, potency) are performed in limited access areas [13]. Also, the surgery of the retroperitoneum implies access in a narrow space in order to perform plastic or reconstructive procedures that involve the great abdominal blood vessels [10]. The most difficult cases regarding the robotic access are the pediatric ones. Robotic radical cystectomy with intracorporeal ileal neobladder is a complex procedure, that implies access both to the pelvis—where the urinary bladder is located, and to the abdomen—where the ileon is located. For this surgery, the operating field is very large, so there is a risk that the robotic instruments might not be long enough to offer full access to the anatomical structures.

2 Factors that Raise Technical Challenges for the Robotic Approach

The causes for the limitations of the robotic approach are determined by two types of variables: the characteristics of the patient and the characteristics of the robot.

2.1 The Characteristics of the Patient

The characteristics of the patient show a wide variation, which demands that the surgeon adapts the positioning of the trocars and the surgical technique. The main limitation comes from the skeletal system, because in order to avoid conflicts it is mandatory that between the bony extremities and the robotic trocars there is a distance of more than 2 cm. The bony extremities that delineate the operating field are: the pubis, the anterosuperior iliac spines, the iliac crest and the ribs. So, for the positioning of the trocars, the surgeon must take into consideration the following characteristics of the patient:

- The height of the patient—tall patients have a longer distance between the pelvic diaphragm and the ileon. This aspect has two implications: on one hand, the robotic instruments will have limited access to the two extreme points of the surgical field (the pelvic diaphragm and the ileon); on the other hand, the bowel loop will be brought down with difficulty to the urethra for the anastomosis, when ileal neobladder is performed
- The abdominal circumference—which is determined by the obesity degree of the patient
- The distance between the pubis and the umbilicus—allows the appreciation of the required depth of the approach. This characteristic is essential for ensuring the access of robotic instruments in the pelvis
- The distance between the antero-superior iliac spines—according to the opening degree of the pelvis, the robotic trocars will be positioned closer—with risk of conflict, or more distanced—avoiding the conflicts
- The distance between the costal margin and the iliac crest is essential for the retroperitoneal approach, where the small access space for the robot may lead to conflicts between the robotic arms.

For the positioning of the trocars, the surgeon uses some anatomical landmarks: the pubis, umbilicus, anterosuperior iliac spines, costal margin, the 12th rib, iliac crest and paravertebral muscles (Fig. 1).

The characteristics of the male pelvis can be evaluated pre-operatively by magnetic resonance imaging (MRI). Endorectal coil MRI has been increasingly used during the last 10 years. One of its main purposes is to diagnose, characterize and stage prostate cancer, but this imaging method can also help the surgeon in the pre-operative planning, by offering information about the male pelvis and the workspace that it affords. As the male pelvis is usually very narrow and the prostate is situated very deep in the pelvic cavity, the access and the exposure are critical during robotic radical prostatectomy (removal of the prostate and seminal vesicles with curative intention for prostate cancer). All the main surgical gestures that are of great importance for the oncological and functional outcomes of the patient are dependent on the space afforded by the deep pelvis [8].

The difficulty of the surgery is characterized using the operative time, estimated blood loss and surgical margin status. Even though many studies stated that obese

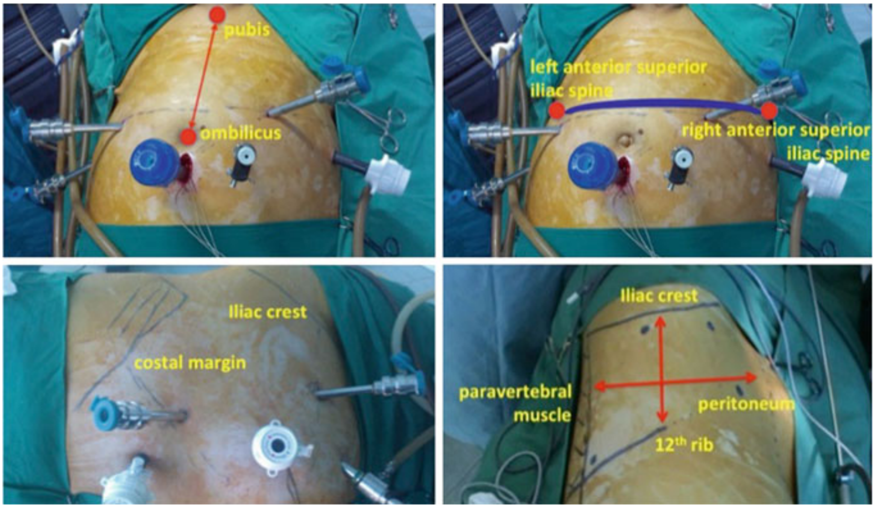

Fig. 1 Anatomical landmarks: pubis and umbilicus (*up left*), anterosuperior iliac spines (*up right*), costal margin and iliac crest (*down left*), 12th rib, iliac crest and paravertebral muscles (*down right*)

and overweight patients have more difficult surgeries, it is important to be aware that even nonobese patients may present a challenge for robotic surgery if certain anatomic features are unfavourable [8].

The main pelvic parameters evaluated by MRI which can assess the potential working space for the robotic instruments are:

- the anteroposterior inlet (from the sacral promontory to the most superior margin of the pubic symphysis)
- the pelvic depth (from the sacral promontory to the most inferior point of the pubic symphysis)
- the anteroposterior distance at midpelvis (from the inferior margin of the pubic symphysis to the sacrococcygeal junction)
- the pelvic outlet (from the inferior aspect of the pubic symphysis to the tip of the coccyx)
- the interspinous distance
- the intertuberous distance
- the pelvic cavity index (PCI = pelvic inlet × interspinous distance/pelvic depth).

The authors noticed that patients with prostate volume (PV) below 35 mL and PV-to-PCI ratio below 6 had lower blood loss and shorter operative time (robotic radical prostatectomy) in comparison with the patients with prostate volume above 35 mL and PV-to-PCI ratio above 6. Also, a longer operative time was correlated with an increased prostatic transverse diameter. Small PCI was correlated with positive surgical margins (residual cancer after surgery) and, most important, with their localisation at the apex of the prostate [6]. In another study, Matikainen et al. confirmed that apical positive surgical margins are more frequent in surgically challenging pelvises. They showed that the presence of apical positive surgical margins correlates with a greater apical prostate depth (AD—the craniocaudal distance from the most proximal margin of the pubic symphysis to the level of the distal margin of the prostatic apex), but with lower pelvic dimension index (interspinous distance/AD), bony width index (bony width measured at the mid-femoral head level/AD) and soft-tissue width index (the narrowest distance between the levator muscles/AD) [9].

In other words, operating a large prostate within a small pelvis will be more challenging than a small prostate in a large pelvis [8].

By measuring all these parameters that characterize the prostate and the male pelvis, the pre-operative MRI evaluation can alert the surgeon about the difficulty of the intervention, so he can adapt the positioning of the trocars in order to ensure the proper instrument mobility and exposure of the anatomical structures, as well as to avoid the conflicts between the robotic arms and maintain the oncological and functional outcomes.

2.2 The Characteristics of the Robot

The characteristics of the robot that influence the surgical approach are:

- The length of the instruments—when the surgical field is large (for example, for the robotic radical cystectomy with intracorporeal ileal neobladder the surgeon needs access both to the pelvis, where the bladder is located, and to the abdomen, where the ileon is) there is a risk that the instruments cannot reach the extreme anatomical points: inferior—pelvic diaphragm, superior—small bowel. Also, for the radical nephroureterectomy with perimeatic cystectomy the surgeon needs a wide working space, from the superior pole of the kidney (superior abdomen) to the urinary bladder (pelvis) (Fig. 2)
- The positioning of the trocars—the robotic trocars must be positioned at least 8 cm apart and at a distance of more than 2 cm from any bony extremity
- The positioning of the robotic cart towards the patient is important in order to avoid conflicts between the robotic arms when the surgeon performs actions at the extremities of the operating field, and also in order to allow the camera to visualize the entire operating field. The robotic cart can be positioned from the head, feet or back of the patient (Fig. 3).

Depending on these characteristics of the robot there are access limitations for the instruments: depth or laterality limitations. Moreover, there can be access limitations for the camera with the impossibility of proper visualization of the complete operating field.

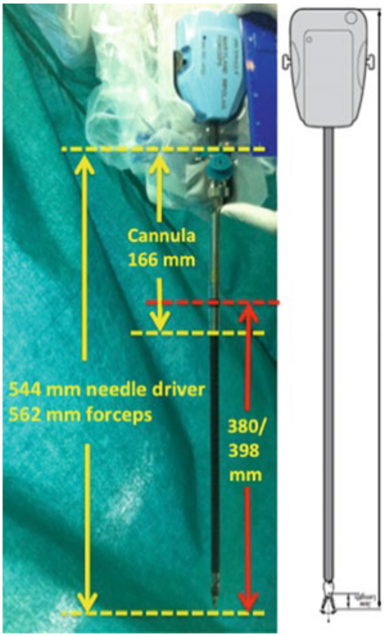

Fig. 2 Work-effective length of the robotic instruments

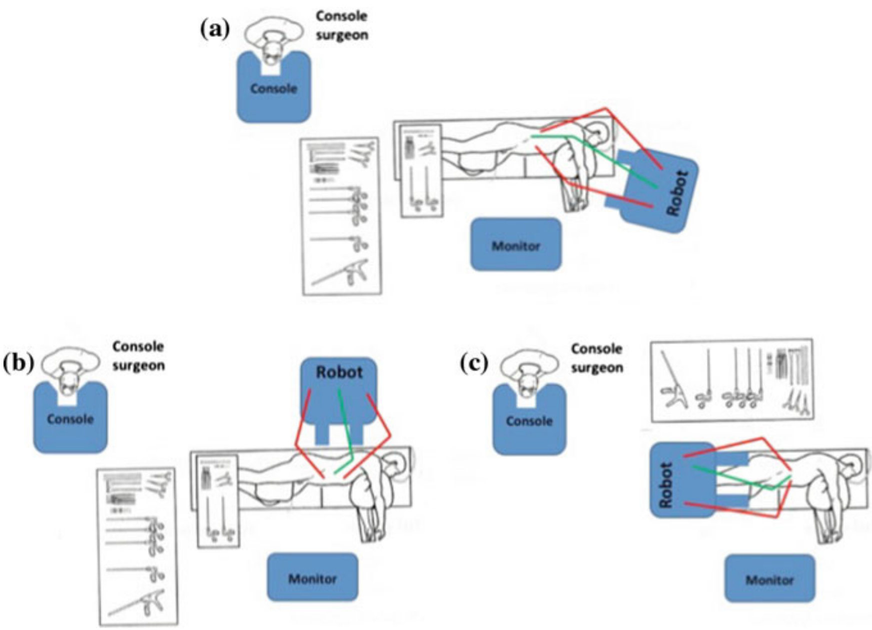

Fig. 3 The positioning of the robotic cart towards the patient

3 Robotic Surgical Approach for Different Types of Procedures

The aim of our study was to evaluate the robotic surgical approach when performing urologic surgeries in limited access areas like the pelvis (radical prostatectomy, radical cystectomy), the retroperitoneum (partial nephrectomy, radical nephrectomy, pyeloplasty), or complex procedures (radical nephroureterectomy with perimeatic cystectomy, radical cystectomy with ileal neobladder).

3.1 Robotic Surgery in the Pelvis—Radical Prostatectomy and Radical Cystectomy with Intracorporeal Ileal Neobladder

An important advantage of robotic surgery is access in small volume spaces. The smallest volume in which surgical gestures can be performed is a 60 mm side cube. Still, in order to avoid the complications or technical difficulties (conflicts between the robotic arms) the minimal recommended work volume should be similar to a 130 mm side cube [13].

Typically, the positioning of the trocars for the robotic approach of the pelvis (for radical prostatectomy) is performed as follows:

- The trocar for the robotic camera immediately cranial to the umbilicus
- The trocars for the robotic arms are positioned at 8–9 cm from the trocar for the camera, on the transverse line passing 2 cm below the navel. The trocar for the 3rd robotic arm is positioned at 8–9 cm from the left robotic trocar and four fingers cranial to the left anterosuperior iliac spine.

This positioning of the trocars allows the access inferiorly to the pelvic diaphragm, but also superior, during lymphadenectomy, up to the crossover of the ureter with the iliac vessels. Thus, using this positioning of the trocars, there are no limitations of access to the extreme points of the surgical field (lower and upper) during radical prostatectomy.

The mean operative time of robotic radical prostatectomy was 190 min (120–318 min). By respecting the positioning of the trocars stated before, there were no conflicts between the robotic arms and the oncological and functional outcomes at 6 months post-operatively were comparable with the ones published by other centers: 93.9 % of the patients had undetectable PSA levels, 88.9 % were continent (<1 pad/day) and 47.9 % had spontaneous erections. The medium blood loss was 250 ml and the mean hospital stay was 7 days.

Another robotic surgical procedure in the pelvis that implies technical issues for the robotic instruments is the radical cystectomy with lymphadenectomy and intracorporeal ileal neobladder.

3.1.1 Technical Difficulties for Robotic Radical Cystectomy with Intracoporeal Ileal Neobladder

Compared with radical prostatectomy, radical cystectomy involves extra time for the ileal neobladder, and for this surgical step the trocars need to be positioned more cranial in order to allow access to the bowel. Furthermore, due to the wide operating field, extended from the pelvic diaphragm to the lower ileum, there are technical difficulties related to limited access and the positioning of the trocars is essential. A caudal positioning of the trocars will not allow access to the bowel and thus will compromise the neobladder. A too cranial positioning of the trocars will not allow access to the apex of the prostate and the urethra and will compromise the anastomosis between the urethra and neobladder [2].

3.1.2 Technical Recommendations for Robotic Radical Cystectomy with Intracorporeal Ileal Neobladder

By respecting the patient's characteristics and analyzing the robotic access to all anatomic levels, the surgeon uses an arrangement of the trocars similar to that described above for radical prostatectomy, but positioning all trocars 2–3 cm cranially. Depending on the patient's height, the instruments can be positioned up to 5 cm cranial to the umbilicus, while keeping a distance between the pubis and the trocar for the robotic camera of no more than 24 cm [11]. Also, the 30° robotic camera is also used and allows efficient visualization of the bowel (Fig. 4).

3.2 Robotic Radical Nephroureterectomy with Perimeatic Cystectomy

Robotic radical nephroureterectomy with perimeatic cystectomy is a procedure that raises technical issues regarding the access because it implies a large operating field, extended from the upper abdomen (upper renal pole) to the pelvis (bladder). The positioning of the trocars and robot cannot be used both for the kidney and bladder steps of the surgery. In this situation, the surgeon can reposition the cart with the robotic arms to facilitate access to the bladder and sometimes even reposition the robotic trocars. Another possibility to facilitate access of the robot in the pelvis is introducing the robotic trocar for the 2nd arm through the trocar for the assistant (Fig. 5) [6, 15].

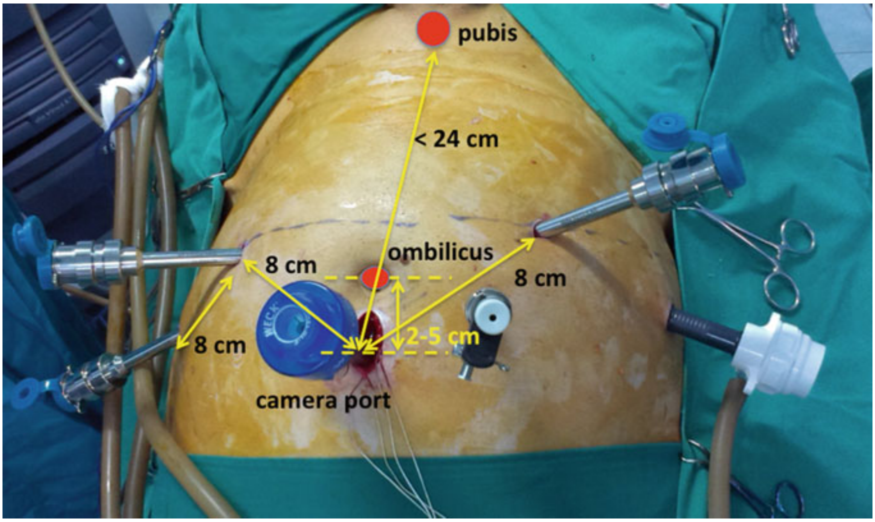

Fig. 4 The positioning of the trocars for the robotic radical cystectomy with intracorporeal ileal neobladder

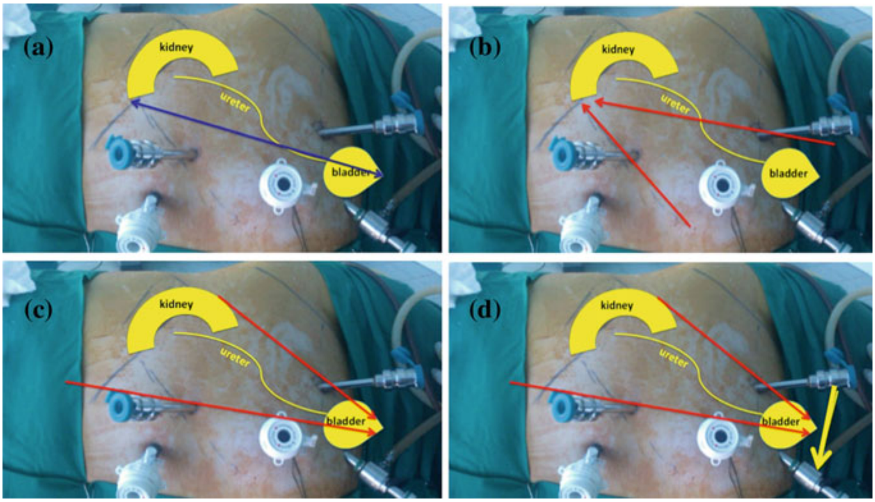

Fig. 5 The approach and positioning of the trocars for the radical nephroureterectomy with perimeatic cystectomy. **a** The two target organs for robotic approach (kidney and urinary bladder); **b** the use of the trocars for facilitating the access to the kidney; **c** the use of the trocars for facilitating the access to the urinary bladder; **d** introducing of the robotic arm through the trocar for the assistant surgeon in order to facilitate the access to the pelvis

3.3 The Robotic Retroperitoneal Approach

The robotic retroperitoneal approach is used by a small number of surgeons because of the reduced access space that exposes to a risk of conflict, either between robotic arms, or between robotic arms and the assistant surgeon instruments. The access space is limited inferiorly by the iliac crest, posteriorly by the spine and paravertebral muscles and superiorly by the 12th rib. Nevertheless, this type of surgical approach has some advantages: quick and direct access on the ureter and renal artery, easy access to posterior valve kidney tumors and easy management in case of complications. There are two variables that can facilitate this access: the arrangement of the trocars and the positioning of the robot.

In order to gain a wider working space and avoid conflicts between the robotic arms, the surgeon can use a triangular disposition of trocars, developed at the Robotic Surgery Center in Cluj-Napoca [3]. The first trocar is positioned in the costomuscular angle (for the first robotic arm); the second trocar at 8 cm from the first, above the iliac crest (for the robotic camera); the third trocar at 8 cm from the 2nd, on the line that prolongs the 12th rib. The trocars for the assistant surgeon are positioned between the camera and the arm 1, and 2 respectively (Fig. 6). The robot is positioned slightly anterior and above the patient's head [3, 4]. The final aspect of the positioning of the robotic trocars is triangular shaped, which offers a generous movement space for them, but also for the assistant surgeon. The mean time for this type of approach was 35 min. There were no conflicts between the robotic arms and none of surgeries required conversion. The blood loss was minimal (85 ml). The hospital stay varied depending on the complexity of the procedure.

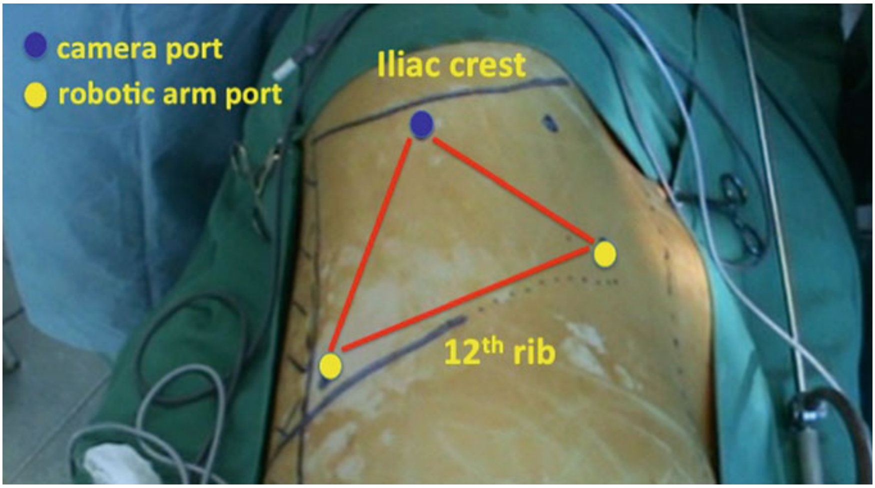

Fig. 6 The positioning of the trocars for the robotic retroperitoneal approach

3.4 Robotic Surgery in Pediatric Urology

One of the reasons that robotic surgery was developed was to allow access and precise gestures in small and difficult to reach areas. Pediatric urologic conditions imply both extirpative and reconstructive techniques, which can be translated from adults with some technical refinements.

The specific features of robotic surgery in children are:

- The smaller size of the children presents a more reduced working space in comparison with the adults—while an adult pneumoperitoneum provides approximately 5–6 L working space, a 1-year-old boy will present a 1 L intra-abdominal space [7]
- There is a limited area on the abdominal wall to place the trocars, so there is a greater risk of conflicts between the robotic arms or the trocars. A difference of a few millimetres can affect the safety of the operation, making the location and placement of trocars critical in children [14]
- The thinness of the abdominal wall makes the maintenance of the pneumoperitoneum difficult during instrument exchange [1]
- The higher compliance of the abdominal wall of the children makes trocar placement more difficult because it provides less resistance, thus increasing the risk of injuring the intra-abdominal structures [14].

In order to overcome these challenges, many features have been developed for robotic urologic surgery. The producers tried to limit the size of the trocars, so at the present moment, complete instrumentation is available in 2, 3, 5 and 10 mm formats. But the port size is in direct relation with the rigidity of the instruments. While the 5 and 10 mm instruments are effectively rigid, the 3 and 2 mm instruments flex to varying degrees based on manufacturer, length and instrument type, thus providing a surrogate of the tactile feedback. Moreover, the 2 mm instruments need acclimation to their flexibility, while the 3 mm ones can be used immediately by the surgeon [14].

The recommended intra-abdominal pressure for children is between 8 mmHg (0–2 years) and 15 mmHg (>10 years). An increase in the pressure to 20 mmHg will ease the trocar insertion by increasing the resistance of the abdominal wall to deformation. Also, it is advised that the trocars are placed in a more “curved” triangular position in order to maximize exposure and ergonomics [14].

3.5 Adjustments of the New Robotic Systems in Order to Overcome the Technical Difficulties

Recently, the Xi robotic surgical system was launched, meeting exactly these technical challenges during surgery (Fig. 7). Thus, this system has the following changes:

Fig. 7 The adjustments of the da Vinci Xi system

- The robotic instruments are longer
- The robotic camera can be positioned on either arm
- The robotic arms are positioned on a rotating system which allows 180° rotation.

4 Conclusions

The robotic surgery has well-known technical advantages, but, also it shows improvement for the access in limited areas, like the male pelvis, the retroperitoneum and children. The positioning of the robotic trocars must be adjusted and personalized depending on the anatomical characteristics of the patient and on the type of surgery. Using the robotic approach and a well studied trocar positioning, the surgeon is able to perform very complex maneuvres without difficulties due to the limited access (conflicts between the robotic arms or conversion to open surgery) or operating field and without altering the perioperative and postoperative outcomes.

Acknowledgments This paper was realized within the Partnership Programme in priority domains—PN-II, which runs with the financial support of MEN-UEFISCDI, Project no. 247/2014.

References

1. Casale P (2008) Robotic pediatric urology. Exp Rev Med Dev 5:59–64
2. Chan ES, Yee CH, Lo KL, Chan CK, Hou SM, Ng CF (2013) Side-docking technique for robot-assisted urologic pelvic surgery. Urology 82(6):1300–1303
3. Crisan N, Neiculescu C, Matei DV, Coman I (2013) Robotic retroperitoneal approach: a new technique for the upper urinary tract and adrenal gland. Int J Med Robot 9(4):492–496
4. Ghani KR1, Porter J, Menon M, Rogers C (2014) Robotic retroperitoneal partial nephrectomy: a step-by-step guide. BJU Int doi:10.1111/bju.12709 [Epub ahead of print]
5. Giri S, Sarkar DK (2012) Current status of robotic surgery. Indian J Surg 74(3):242–247
6. Hemal AK, Stansel I, Babbar P, Patel M (2011) Robotic-assisted nephroureterectomy and bladder cuff excision without intraoperative repositioning. Urology 78(2):357–364
7. Kutikov A, Fossett LK, Ramchandani P et al (2006) Incidence of benign pathologic findings at partial nephrectomy for solitary renal mass presumed to be renal cell carcinoma on preoperative imaging. Urology 68:737–740
8. Mason BM, Hakimi AA, Faleck D, Chernyak V, Rozenblitt A, Ghavamian R (2010) The role of preoperative endo-rectal coil magnetic resonance imaging in predicting surgical difficulty for robotic prostatectomy. Urology 76(5):1130–1135
9. Matikainen MP, von Bodman CJ, Secin FP, Yunis LH, Vora K, Guillonneau B et al (2010) The depth of the prostatic apex is an independent predictor of positive apical margins at radical prostatectomy. BJU Int 106(5):622–626
10. Patel M, Porter J (2013) Robotic retroperitoneal surgery: a contemporary review. Curr Opin Urol 23(1):51–56
11. Pruthi RS, Nix J, McRackan D, Hickerson A, Nielsen ME, Raynor M et al (2010) Robotic-assisted laparoscopic intracorporeal urinary diversion. Eur Urol 57(6):1013–1021
12. Reyes JM, Smaldone MC, Uzzo RG, Viterbo R (2012) Current status of robot-assisted partial nephrectomy. Curr Urol Rep 13(1):24–37
13. Thakre AA, Bailly Y, Sun LW, Van Meer F, Yeung CK (2008) Is smaller workspace a limitation for robot performance in laparoscopy? J Urol 179(3):1138–1142
14. Tomaszewski JJ, Casella DP, Turner RM 2nd, Casale P, Ost MC (2012) Pediatric laparoscopic and robot-assisted laparoscopic surgery: technical considerations. J Endourol 26(6):602–613
15. Zargar H, Krishnan J, Autorino R, Akca O, Brandao LF, Laydner H et al (2014) Robotic nephroureterectomy: a simplified approach requiring no patient repositioning or robot redocking. Eur Urol pii S0302-2838(14)00189-4

Part III
Educational and Service Robotics

Ranger, An Example of Integration of Robotics into the Home Ecosystem

Francesco Mondada, Julia Fink, Séverin Lemaignan, David Mansolino, Florian Wille and Karmen Franinović

Abstract This paper presents the concept and a case study of a *robject*, a robotic entity embedded in an everyday object. Robjects use the affordance of the original object to ensure an efficient interaction and a high acceptance. The example of the *ranger robot* shows how this approach can be applied to a domestic environment. We explore the integration of a robot (*robject*) into a family household, by regarding the home as a ecosystem, which consists of people, things, activities, and interactions. Our evaluation study of the *ranger robot* in families validates this holistic approach and shows the impact of this type of design in respect to the complexity of the robotic system.

Keywords Holistic approach · Ecosystem · Cooperation with humans · Domestic service robots · Robject · Ranger robot

1 Introduction

Since years, predictions say service robotics will massively enter in every home [1]. In Europe, a large survey made in 2012 shows a general public perception which is still not very open to home service robotics. Robots are perceived as a good tool

F. Mondada (✉) · S. Lemaignan
Laboratoire de Systèmes Robotiques (LSRO), Ecole Polytechnique Fédérale de Lausanne (EPFL), Lausanne, Switzerland
e-mail: francesco.mondada@epfl.ch

J. Fink · S. Lemaignan
Computer-Human Interaction in Learning and Instruction Laboratory (CHILI), Ecole Polytechnique Fédérale de Lausanne (EPFL), Lausanne, Switzerland

D. Mansolino
Distributed Intelligent Systems and Algorithms Laboratory (DISAL), Ecole Polytechnique Fédérale de Lausanne (EPFL), Lausanne, Switzerland

F. Wille · K. Franinović
Embodied Interaction Lab, Zurich University of the Arts, Zurich, Switzerland

H. Bleuler et al. (eds.), *New Trends in Medical and Service Robots*,
Mechanisms and Machine Science 38, DOI 10.1007/978-3-319-23832-6_15

mainly for dangerous tasks [2]. In the same survey, a majority of people thinks robots should be banned from typical home service scenarios that include children, elderly or disabled care. Only 13 % of the European citizen think robots should be applied in priority to "domestic use, such as cleaning". Also among researchers it has not been clear what a robot exactly should do in homes [3]. Pantofaru et al. [3] explored the role of robots in home organization (tidying, storing), and found that robots could have a potentially high impact on this. Similarly, Bell et al. [4] suggest that robots could be used in tidying up scenarios in the domestic environment.

Although only few such systems have entered the consumer market, several researchers took advantage of these few success and studied the acceptance of robotics technology by the users. Bauwens et al. [5] showed that the main factors impacting the adoption of robotics at home are, from the most to the less important:

1. The practical utility
2. The integration into the home ecosystem (physical space, users, habits)
3. The economic utility

Most of the service robots developed in research consider only a subset of these criteria, approaching single disciplines such as HRI, mechatronics or robotic functionality.

In this paper we present a holistic approach and an example of mechatronic implementation looking for a balance between functionality, cost and integration into the ecosystem. We believe that a holistic and interdisciplinary approach can improve acceptance and bring robotics in homes in a faster and more meaningful way. Our approach consists in integrating robotics technology into daily objects, making them what we call *robjects*. Robjects can easily blend into the home ecosystem because of the embodiment in an object that is already integrated into the ecosystem and has a clear function in it. Robjects also aim at a close synergy with the users, replacing high technological requirements with better human-robot interaction for collaboration. These principles have already been applied to some successful systems in industry, as illustrated in Sect. 2. Section 3 presents an example of robject and the first results of user tests.

2 State of the Art

In homes, research aims at adding intelligence into home automation, for instance to implement user activity recognition [6] and integrate service robots [7]. In most cases this technology, which is still very heavy, targets assistive living for elderly. A set of European research projects work exactly on this issue: Robot-ERA [8] is developing several service robots for indoor and outdoor use, integrated in smart houses and providing a set of services for older people, Giraffe+ [9] integrates a telepresence robot into a smart home where the sensor network allows context recognition and interpretation of collected data, ACCOMPANY [10] develops a robotic companion integrated into an intelligent environment, providing services to elderly users to enable independent living at home, MOBISERV [11] aims at studying innovative technology to support independent living of older adults at home or in specialized institutions, CompanionAble [12] has worked on the synergy between robotics and ambient intelligence technologies enabling a care-giver's assistive environment and HOBBIT [13] develops a socially assistive robot that helps elderly at home. All these projects involve robots that have a human-like presence in the environment. Few projects such as RUBICON [14] have a more general approach and study a more generic network of sensors and actuators, without a predefined application of assisted living in mind. Finally only very few consider the interaction with children. The MOnarCH project [15] is studying the interaction with children in hospitals with a smaller robot, still having a human-like shape. Their study on interaction is probably one of the closest to our project.

The integration of designers in research projects to study interaction aspects and gather information on new approaches is very recent in the field. A good experiment has been carried out in the University of Hertfordshire Robot House, where artists lived full-time with various robots in a smart home environment [16]. This approach gives many insights on interactions aspects, as we saw in our project.

Although most of the service robots developed in research lab do not meet market requirements or address only part of the requirements, few managed to become successful products. Among them we can find the Kiva systems [17] or the Baxter robot [18], both systems focusing on cooperation with humans, functional shapes, low cost and high added value functionalities. This situation confirms what Takayama et al. [19] found: "people would feel more positively toward robots doing occupations *with* people rather than *in place* of people". Transposing this approach to homes for a use with children, we developed a robot to help tidying-up the children's room, which has been considered as an interesting task by previous studies [3, 4].

3 The Ranger Robot

The *ranger* robot (see Fig. 1) is based on a common object that can be found in every children room: a wooden storage box for toys. This object has been transformed into what we call a *robject*, i.e. an object augmented with robotic features. This transformation has been carried out by an interdisciplinary team including mechatronic engineers, interaction designers, ethnographers and roboticists. The goal of this *augmentation* or *robotization* of the object is to improve the functionalities (using competences in robotics and mechatronics) by building on the top of an existing interaction and affordance (using competences in interaction design) and create a new form of robot that can be accepted in an existing ecosystem (using competences in ethnography).

The resulting *ranger* robot has a body based on the original wooden box but is equipped with wheels, mechanical eyes, inertial sensors, distance sensors, ground sensors, a bumper, an inside balance, capacitive external touch sensors, LED panels

Fig. 1 A set of ranger robots in a room. Their home is under the bed, where they sleep recharging their battery. *Photo* Alain Herzog

behind the wooden surface, sound, eyeglasses, a detachable pacifier and a range-and-bearing (R&B) system to detect other rangers, the battery charger and a beacon to know where the play zone is (see Fig. 2 for most details and Fig. 1 for a global view). Its body is shaped to support a very specific interaction aimed at encouraging the children to tidy up their room. Instead of maximizing the robotics functionalities for this type of application, the optimization is made at a higher level, taking into account the capabilities of the children, the ecosystem and the possible interaction. Therefore, we made the choice to not equip the *ranger* with arms, for instance, because this adds complexity and cost that can be avoided using

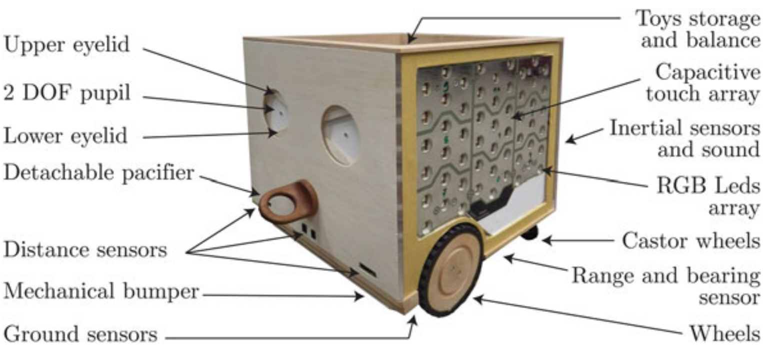

Fig. 2 The ranger robot main components and their locations. The eyeglasses have been removed for the purpose of the illustration

the right form of interaction. The new *robject* is supposed to remain helping and interacting with the children instead of becoming a tool that does a task on its own. Finally, by keeping a role close to the original storage box, the *ranger* increases its acceptance by the children and their parents.

The internal architecture of the robot is illustrated in Fig. 3. The *ranger* has four processors. The main one is a full embedded computer running Linux and providing the main wireless connectivity, data storage and sound management. Three micro-controllers, connected using a CAN bus, manage the real-time part of the robot, including power, sensors and actuators. The ASEBA framework [20] is used to control the whole system and makes the link with ROS controllers. Slam and navigation are implemented using ROS.

The shape of the ranger has been designed to keep a neutral wooden surface that can become a projection surface from inside. The 186 RGB LEDs that can project light on this surface can create a large set of animated patterns. The eyes are fully mechanical, without any screen, creating a coherent image of physical device. The eyelids allow to give more expression and close the eyes when inactive. The eyeglasses of different colors allow a protection of the mechanics of the eyes and at the same time allow a distinction among the several rangers holding several types of toys, for instance. The pacifier is also made of wood but includes a magnet to be placed in the "mouth" of the rangers. For some experiments we add a RGBD Primesense sensor connected by USB to the Linux board and helping in navigation and obstacle detection.

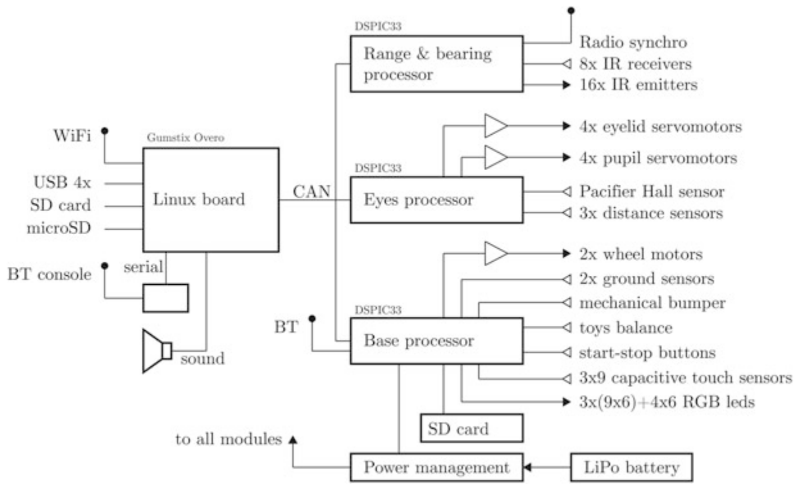

Fig. 3 The structure of the electronics of the ranger robot. Four processors manage the functionalities and can be expanded using the USB ports of the Linux board

3.1 Ranger Use Scenario

The use scenario is based on a room equipped with a bed under which several rangers can be stored (see Fig. 1). Under the bed we placed, for each ranger, a recharging station equipped with a R&B beacon. This is the home of the rangers where they sleep, with closed eyes, most of the time. Their behavior is defined by a state machine. Figure 4 shows a simplified version of the state machine controlling the ranger behavior.

The children have a controller object (called "collector") where they can place up to three pacifiers. This collector of pacifiers can be seen on the bottom, center, of Fig. 1. The collector is equipped with a beacon. To play with their toys, the children identify which ranger holds them. Each ranger has a different color of glasses. The child can wake up the right ranger by taking away the pacifier from its mouth. The child then puts the pacifiers in the collector placed where the children want to play. The ranger will wake up and navigate toward the collector beacon. Once the child wants to send back the ranger home, he can simply put again the pacifiers in its "mouth" and the ranger will go back home to sleep (and recharge). The ranger can also decide to go back home if it sees that the battery level is too low. A set of behaviors is used to keep the child engaged. The child is motivated to tidy up and fill ranger by the robots' expressions showing signs of hunger and sadness when not being "fed"—while displaying happiness as a rewarding behavior if toys are being placed inside ranger.

3.2 Validation

We tested the ranger concept in 14 families in a first short-term study [21]. One ranger prototype was placed in the room of the children while a researcher was discussing with the family in another room. The family was then asked to go in the room of the children and discover the ranger (Fig. 5). The ranger was remotely controlled from a third room through a hidden camera, following a predefined

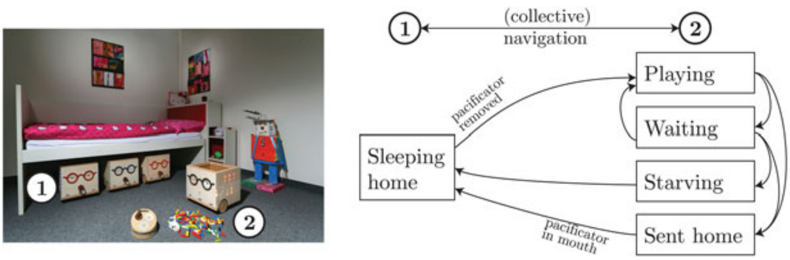

Fig. 4 The behavior of the ranger is based on two positions: under the bed (home) and on the playing site. At home the ranger can be charged and the playing site is marked by a beacon where the children place the pacifiers

Fig. 5 An image taken during user tests in families

scenario describing the behavior, following a Wizard-of-Oz methodology [22]. In half of the families we adopted a reactive behavior, with the ranger waiting for actions of the children before reacting. In the other half we adopted a proactive behavior, with the ranger proactively moving and looking for objects on the ground.

These tests have shown a very high acceptance, as illustrated by the detailed results presented in [21]. Moreover we observed that marginally significantly more toys were put and removed in the reactive scenario compared to the proactive one. This demonstrates that the robot can achieve good performances even with a minimalist behavior.

The next step consists in making tests with users in a configuration similar to the one presented in Fig. 1 and for a long period, to see to what extent users engage in using the ranger after novelty effects have worn off.

4 Conclusion

We presented the concept and design of the ranger robot, a robotic storage box that can interact with children to motivate them to tidy-up their room. This concept is very similar to the one adopted by several successful industrial robotics systems that have shown the path of a smart integration of human and robotic activities, limiting the requirements for the robotic technology and improving performances thanks to a good human-robot cooperation. Following this design approach, we can design robots that fit with the factors identified by Bauwens et al. [5]: practical utility, integration in the ecosystem and economic utility. The validation in families has shown that *ranger* achieves high acceptance rates and a good utility in short-time experiments. In parallel, this test shows that good performances can be achieved with a minimal behavior, helping to reach the economic utility. These results are achieved because of the embodiment into a daily-life object, ensuring an optimal affordance and integration into the home ecosystem. This example illustrates the potential of the *robjects* concept but also shows that this concept requires a holistic approach that integrates interaction design, robotics and mechatronics design.

Acknowledgments This work was supported by the Swiss National Center of Competence in Research "Robotics".

References

1. Gates B (2007) A robot in every home. Sci Am 296:58–65
2. Eurobarometer (2012) Public attitudes towards robots, Technical Report March, 2012
3. Pantofaru C, Takayama L, Foote T, Soto B (2012) Exploring the role of robots in home organization. In: Proceedings of the seventh annual ACM/IEEE international conference on Human-Robot Interaction—HRI'12, p 327
4. Bell G, Blythe M, Sengers P (2005) Making by making strange: defamiliarization and the design of domestic technologies. ACM Trans Comput Hum Interact 12:149–173
5. Bauwens V, Fink J (2012) Will your household adopt your new robot? Interactions 19:60
6. Duque I, Dautenhahn K, Koay KL, Willcock I, Christianson B (2013) Knowledge-driven user activity recognition for a smart house. Development and validation of a generic and low-cost, resource-efficient system. In: The sixth international conference on advances in computer-human interactions, ACHI, pp 141–146
7. Cavallo F, Aquilano M, Bonaccorsi M, Limosani R, Manzi A, Carrozza MC, Dario P (2013) On the design, development and experimentation of the ASTRO assistive robot integrated in smart environments. In: IEEE international conference on robotics and automation (ICRA), vol 2, pp 4310–4315, May 2013
8. Aquilano M, Carrozza MC, Dario P (2012) Robot-Era project (FP7-ICT-2011.5.4): from the end-users perspective to robotics. Preliminary findings. In: Proceedings of the AAL—ambient assisted living forum. Eindhoven, The Netherlands
9. Coradeschi S, Cesta A, Cortellessa G, Coraci L, Gonzalez J, Karlsson L, Furfari F, Loutfi A, Orlandini A, Palumbo F, Pecora F, von Rump S, Štimec A, Ullberg J, Östlund B (2013) Giraffplus: combining social interaction and long term monitoring for promoting independent living. In: Proceedings of human system interaction (HSI), pp 578–585. IEEE, June 2013
10. Amirabdollahian F, op den Akker R, Bedaf S, Bormann R, Draper H, Evers V, Gelderblom G, Gutierrez Ruiz C, Hewson D, Hu N, Iacono I, Koay K, Krose B, Marti P, Michel H, Prevot-Huille H, Reiser U, Saunders J, Sorell T, Dautenhahn K (2013) Accompany: acceptable robotics companions for ageing years—multidimensional aspects of human-system interactions. In: The 6th international conference on human system interaction (HSI), pp 570–577, June 2013
11. Nani M, Caleb-solly P, Dogramadgi S, Fear C, Heuvel HVD (2010) MOBISERV: an integrated intelligent home environment for the provision of health, nutrition and mobility services to the elderly. In: 4th companion robotics workshop in brussels
12. Gross HM, Schroeter C, Mueller S, Volkhardt M, Einhorn E, Bley A, Martin C, Langner T, Merten M (2011) Progress in developing a socially assistive mobile home robot companion for the elderly with mild cognitive impairment. In: IEEE international conference on intelligent robots and systems, pp 2430–2437

13. Fischinger D, Einramhof P, Wohlkinger W, Papoutsakis K, Mayer P, Panek P, Koertner T, Hofmann S, Argyros A, Vincze M et al (2013) Hobbit-the mutual care robot. In: Workshop-Proceedings of ASROB
14. Bacciu D, Barsocchi P, Chessa S, Gallicchio C, Micheli A (2013) An experimental characterization of reservoir computing in ambient assisted living applications. Neural Comput Appl 24:1451–1464
15. Sequeira J, Lima P, Saffiotti A, Gonzalez-Pacheco V, Salichs M (2013) MOnarCH: Multi-robot cognitive systems operating in hospitals. In: ICRA 2013 workshop on many robot systems
16. Lehmann H, Walters M, Dumitriu A, May A, Koay K, Saez-Pons J, Syrdal D, Wood L, Saunders J, Burke N, Duque-Garcia I, Christianson B, Dautenhahn K (2013) Artists as HRI pioneers: a creative approach to developing novel interactions for living with robots. In: Herrmann G, Pearson M, Lenz A, Bremner P, Spiers A, Leonards U (eds) Social robotics vol 8239. Lecture Notes in Computer Science, pp 402–411. Springer International Publishing, Berlin
17. Wurman P, D'Andrea R, Mountz M (2008) Coordinating hundreds of cooperative, autonomous vehicles in warehouses. AI Mag 29(1):9–20
18. Fitzgerald C (ed) (2013) Developing baxter. In: IEEE international conference on technologies for practical robot applications (TePRA), pp 1–6
19. Takayama L, Ju W, Nass C (2008) Beyond dirty, dangerous and dull: what everyday people think robots should do. In: Proceedings of the 3rd ACM/IEEE international conference on Human robot interaction, pp 25–32
20. Magnenat S, Rtornaz P, Bonani M, Longchamp V, Mondada F (2011) ASEBA: a modular architecture for event-based control of complex robots. IEEE/ASME Trans Mechatron 16 (2):321–329
21. Fink J, Lemaignan S, Dillenbourg P, Rétornaz P, Vaussard F, Berthoud A, Mondada F, Wille F, Franinovic K (2014) Which robot behavior can motivate children to tidy up their toys ? Design and evaluation of ranger. In: Proceedings of the 2014 ACM/IEEE international conference on Human-robot interaction, pp 439–446
22. Green P, Wei-Haas L (1985) The rapid development of user interfaces: experience with the wizard of oz method. In: Proceedings of the human factors and ergonomics society annual meeting, vol 29, pp 470–474. Sage Publications

Human-like Robot MARKO in the Rehabilitation of Children with Cerebral Palsy

B. Borovac, M. Gnjatović, S. Savić, M. Raković and M. Nikolić

Abstract Actual research in the field of robot-supported therapy is dominantly oriented on systems for clinical neurorehabilitation of motor disorders and therapy of difficulties related to autism. However, very little attention is dedicated to the functional development of the therapeutic robot, which would be capable of participating, actively and intelligently, in a verbal dialogue of natural language with a patient and therapist. In this paper an approach is presented for incorporating the human-like robot MARKO in the physical therapy for children with cerebral palsy (CP). The mechanical design of the robot MARKO is briefly described and its context aware cognitive system which connects modules for sensorimotor system, speech recognition, speech synthesis and robot vision is presented. The robot is conceived as a child's playmate, able to manage three-party natural language conversation with a child and a therapist involved. Traditional CP physical therapies are usually repetitive, lengthy and tedious which results in a patient's lack of interest and disengagement with the therapy. On the other hand, treatment progress and the improvement of the neural functionality are directly proportional to the amount of time spent exercising. The idea is to use the robot to assist doctors in habilitation/rehabilitation of children, with a basic therapeutical role to motivate the children to practice therapy harder and longer. To achieve this, the robot must fulfill several requirements: it must have hardware design which provides sufficient capabilities for demonstration of gross and fine motor skills exercises, it must have appropriate character design to be able to establish affective attachment of the child,

B. Borovac (✉) · M. Gnjatović · S. Savić · M. Raković · M. Nikolić
Faculty of Technical Sciences, University of Novi Sad, Trg D. Obradovica 6,
21000 Novi Sad, Serbia
e-mail: borovac@uns.ac.rs

S. Savić
e-mail: savics@uns.ac.rs

M. Raković
e-mail: rakovicm@uns.ac.rs

M. Nikolić
e-mail: milutinn@uns.ac.rs

H. Bleuler et al. (eds.), *New Trends in Medical and Service Robots*,
Mechanisms and Machine Science 38, DOI 10.1007/978-3-319-23832-6_16

and it must be able to communicate with children verbally (speech recognition and synthesis), and non-verbally (facial expressions, gestures).

Keywords Assistive robot · Cerebral palsy · Social robot · Adaptive behavior · Context awareness

1 Introduction

The applications of rehabilitation and assistive robotics are spreading every day. Actual research in the field of robot-supported therapy is significantly oriented on systems for clinical neurorehabilitation of motor disorders and therapy of difficulties related to autism. Some representative applications in the field of rehabilitation and assistive robotics are “TWENDY-ONE” [1], a robot assistant for the elderly population and “Bandit” [2], an assistive robot for post-stroke rehabilitation. In [3, 4] research has been conducted for the application of social robots in therapy of children with autism but only recently some results of robot application in cerebral palsy therapy have been published [5, 6]. In [5] the humanoid robot “KineTron” is presented, which acts like a coach to encourage the patient during cerebral palsy therapy. It has nine predefined movement scenarios combined with voice and music. A more advanced solution is the robot “Ursus” that acts as a child’s playmate in a game scenario that combines a real robot and virtual reality. Showing calmly the correct movements with its arms, talking about interesting child-centered matters, playing music and projecting pictures, videos and augmented reality (AR) games on an external screen, are some of the many resources that Ursus pulls out to capture the child’s attention and interest [6].

The clinical descriptive term “cerebral palsy” relates to permanent developmental disorders that occurred early in human biological development or in early childhood. These developmental disorders primarily refer to conditions of abnormal gross and fine motor functioning that can lead to secondary problems with behavior and participation in society [7]. It is important for the patient’s benefit to start with the therapy as early as possible. Medical treatments include tedious and repetitive exercises, so children quickly lose their interest. Since their progress directly depends on time spent exercising it is important to find a way to keep the children’s attention occupied and keep them motivated. This is why the MARKO robot is perceived as an assistant in habilitation/rehabilitation of children, by motivating them to spend more time exercising. Three main applications of MARKO in the therapy are participation in gross motor skills exercises (which involves free space motion), fine motor skills exercises (which involves constrained motion and object manipulation) and speech exercises.

The main idea is to engage a child with a robot, as its friendly and intelligent playmate, and to create an interesting game-like atmosphere as opposed to a difficult and tedious medical treatment. In order to establish the affective bond between a child and the robot, the design of the robot head and face was specially analyzed [8]. In early childhood, humans can perceive the direction of attention of others and reliably follow gaze [9]. This fact emphasizes the significance of the robot's eyes mechanism design, which has an important role in facial expressions and showing the direction of attention. Social interaction relies primarily on vision, touch, and proprioception using the mouth, face, hands, and eyes [9]. Therefore, in order to make the robot socially acceptable and to provide an affective attachment with a child, the robot must have all these elements. It also has to be adapted to some conventions of social interaction and must have suitable hardware design which enables facial expressions as well as emotions and intentions recognition. Intention and emotions are conveyed by elaborate and specific movements, gestures, and sounds [9]. Thus the robot has to possess appropriate mechanisms to recognize those.

One of the innovative aspects of MARKO, compared to most of the similar realized robotic systems, is its ability to participate in a verbal dialogue of natural language with a patient and a therapist. MARKO will be able to participate in rehabilitation scenarios that are not totally prepared in advance and then just repeated. Due to its cognitive system, dialogue management system, and speech recognition and synthesis system [10] MARKO will be able to realize any exercising scenario provided by a therapist through a proper set of voice commands, so the rehabilitation can be customized and adapted to each child's needs, abilities and preferences. The dialogue management system is based on the attention state model which integrates neurocognitive understanding of the focus of attention in computational and corpora linguistics [11, 12]. The context of interaction and a dialogue strategy can be easily changed or adapted, by a therapist themself, to a new therapy scenario or the special needs of a current patient, which is another major innovation in the field [12]. In the therapy scenario with MARKO, children will be using relative spatial perspective which is most natural for them [12]. This is an advantage compared to therapies with games in virtual augmented reality where children are using intrinsic spatial perspective, since their character is projected in the virtual reality of the game. Because of its friendly appearance, bilateral voice interaction and facial expressions, Marko the robot makes an impression of an intelligent playmate. The child's interest in exercising is thus maintained which hopefully will lead to better therapy results.

2 Therapy Scenarios

Three domains are considered for robot application in the therapy of children with cerebral palsy. They are participation in gross motor skills exercises, fine motor skills exercises and speech exercises. The first and the second application are discussed in this paper. The advantage of using the robot in therapy is the opportunity to use its technical resources (stereovision, speech recognition…) to monitor the current state of the child and their progress during the treatment. For example, it is possible to measure the patient's joint ranges during his/her performance of exercises or to record the speech sessions. It also becomes possible to create the database for each patient from the measured data. This would allow the therapist to analyze and monitor the patient's progress, and to make adaptations and customizations of the therapy for each patient.

A partial set of gross motor skill exercises is illustrated in Fig. 1. In order to perform these exercises the robot has to be anthropomorphic, with a similar kinematic structure as humans. Therapy of motor skill disorders in children is long-term and tiresome and the aim is to help the patient to develop as many motor skills as possible or to learn how to compensate for the lack of them. Regarding the gross motor skills exercises, each exercise is first demonstrated to the patient by the therapist. During that demonstration the robot should recognize the exercise, using its vision system, in order to be prepared to repeat it. The therapist first asks the patient to repeat the exercise. If the child is not able to reproduce the demonstrated movement, because of fatigue or some other reason, the therapist asks the robot to perform the exercise to stimulate the patient. The robot should also say something encouraging to the child.

Sometimes children that undergo therapy do not have a proper knowledge and understanding of spatial relations. They may not understand the terms in front, behind, above, etc…, and likewise perhaps cannot show where their head or abdomen is. Therefore, during the therapy they also learn and acquire knowledge of spatial relations. One of the common exercises in conventional therapy is the exercise when children perform gross motor skills exercises in front of the mirror. A similar therapy scenario which includes the robot is illustrated in Fig. 2.

In this scenario the patient and the robot stand face to face. The robot demonstrates the exercise specified by the therapist, and the child should repeat it. The idea is to use the Kinect sensor to track a patient's skeleton movements [13] and to store the data in the database. This would allow the therapist to monitor the patient's progress in therapy.

Therapy for fine motor skills includes manipulation of objects of different geometrical forms and colors. The therapist, patient and robot sit at the table and participate in three-party natural language conversation. The therapist gives an

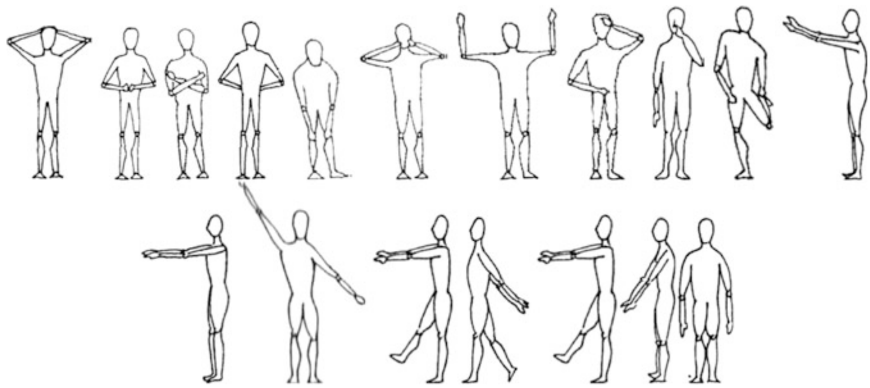

Fig. 1 Schematic drawing of gross motor skills exercises

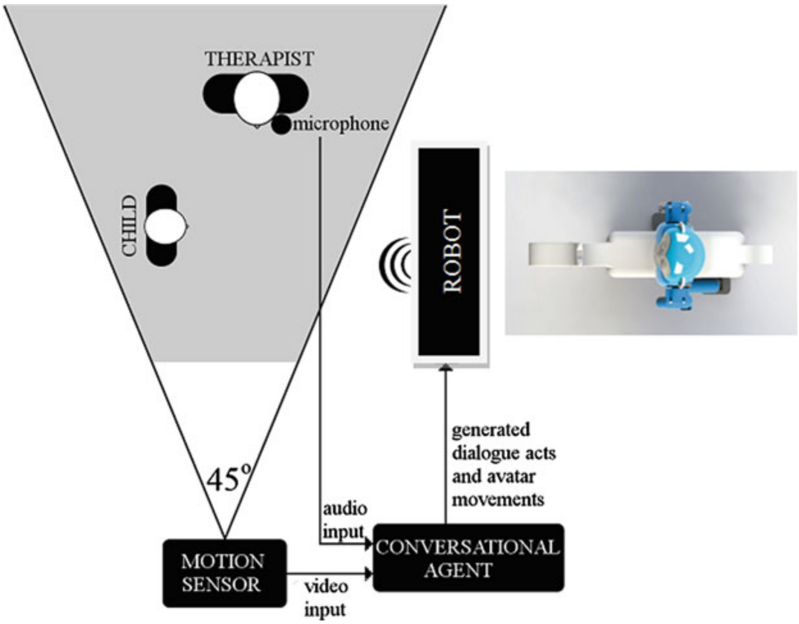

Fig. 2 Sketch of the system for gross motor skills therapy

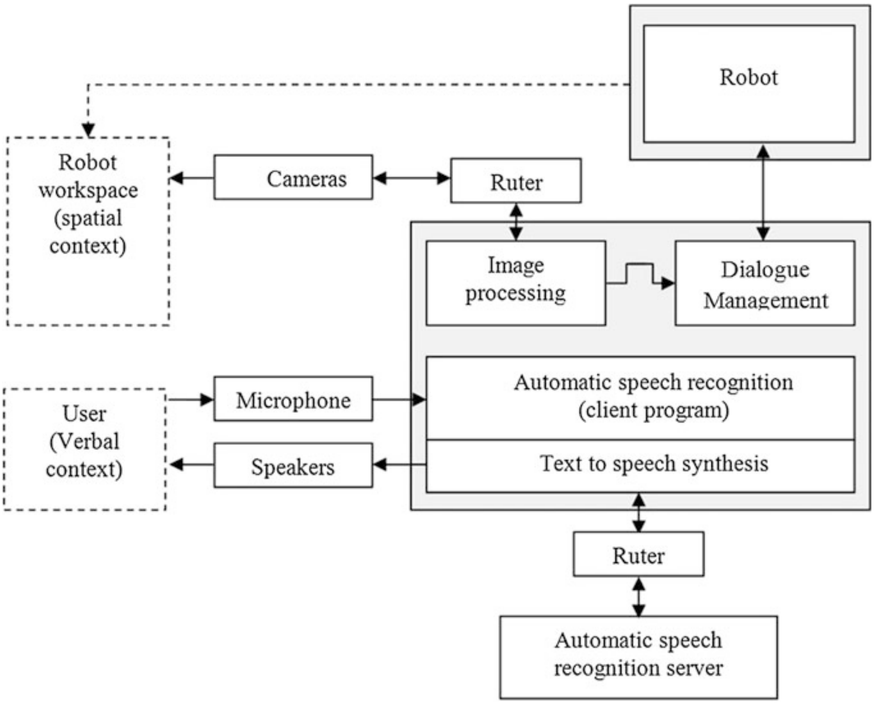

Fig. 3 Principle scheme of the system for fine motor skills therapy

instruction to the child to pick up the object of a certain color and shape and to put it on a specific place on the table. If the child is not able to perform the task or does it in a wrong way, then the therapist gives the robot voice command to perform the same task and show it to the child. If the child performs the task successfully, the robot would say something nice to commend them. If the child failed to perform the task, the robot should say something nice and encouraging anyway. The block diagram of the whole robotic system used in fine motor skills therapy is given in Fig. 3. This system has been experimentally verified with an industrial robot [14].

As represented in Fig. 3, during the interaction users and the robotic system share the common language context, which refers to the verbal dialogue and spatial context, as well as to their non-verbal actions (for example changes of position of the objects in space). Based on the analysis of the verbal and spatial context, the cognitive system makes the decision regarding the interpretation of the dialogues and non-verbal actions of the user, and the generation of dialogue acts and non-verbal actions of the robot.

3 Cognitive System

So far, very little attention has been dedicated to the functional development of therapeutic robots, which could be capable of participating, actively and intelligently, in a verbal dialogue of natural language with a patient and a therapist. The robot presented in this paper is conceived as a human-like cognitive agent intended to participate in the physical therapy of children with cerebral palsy along with the ability to manage a three-party natural language conversation with the patient and the therapist. Considering the fundamental role of language in social interactions and in establishing an individual's identity, it is assumed that this therapy approach will significantly help the child to establish social connections within the therapy environment and keep motivation afloat during therapy.

The presented cognitive system, based on the attention state model (focus tree), implements the functionality of adaptive dialogue management and natural language processing [11, 12]. Functional requests for the cognitive system include analytical and generative aspects of robot dialogue acts. Analytical aspects primarily refer to the need to train the cognitive system to interpret user commands of different syntax structures. During the therapy it is not recommended and sometimes even not possible to force the user to adapt his/her voice commands to the syntax rules that are determined by the system designer. Instead, the users should be enabled to the greatest possible extent, to express themselves spontaneously. Therefore, the cognitive system that is designed within this project can interpret the user voice commands of different syntax constructions (including incomplete commands, context-dependent commands, and incorrectly formulated commands), as well as commands that linguistically encode different spatial perspectives (for example: the difference between the therapist's left and the robot's left). Sometimes, if needed the system takes the initiative in the interaction and guides the user to complete the started command or to resolve the ambiguity.

Generative aspects primarily refer to the need of making the cognitive system capable of dynamically adapting its dialogue strategy to the current context of interaction (which includes a number of parameters such as: user commands, states in the space, focus of attention, child's emotional state, history of interaction…). Therefore, the cognitive system considers these parameters each time during the interaction when it should interpret a user's command, generate dialogue act or decide which command to forward to the robot system. The rules for decision making are called dialogue strategy. An additional level of adaptability is achieved by enabling the therapist to independently redefine the dialogue strategy and context of interaction.

The request to include a therapist in the system design process is not surprising, since the therapist has the knowledge specific for the considered domain of clinical rehabilitation, and can provide the insight into the significant aspects of therapy interaction (including clinically relevant changes of the child's emotional states and appropriate therapeutic interventions). However, post-implementation changes and adaptations are inevitable. Some of the basic reasons are:

- Therapy includes performance of different exercises (fine motor skills, gross motor skills, speech exercises) which force the system to participate in different dialogue domains.
- Children, suffering from cerebral palsy, differ significantly so there is a need for individual adaptation of system dialogue strategy, even within the same therapeutic exercise.
- Therapy of children with cerebral palsy is a long-term process, and it is most likely that the children will change their abilities and affinities. The system dialogue behavior should adapt to these changes.
- Presence of the robot system may cause intensive emotional reactions in children (from affective connection with the system to aversion towards it). These reactions are hard to predict in the system design phase.

On the other hand, if in usual practice the therapist needs the technical support for each system adaptation, this makes it inefficient, time consuming and therefore unacceptable for therapy. Hence, the software platform has been developed which provides the therapist the capability to design and test the dialogue behavior of the robot system by himself/herself (i.e. dialogue strategies and context of interaction) [12].

4 Mechanical Design and Control Architecture

Robot MARKO is designed as a humanoid with two legs, two arms, torso and a head. It will be placed on a horse-like mobile platform with a differential drive for motion in its environment. Robot anthropomorphic structure is determined by its intended application. The CAD model of the robot with its hardware modules is shown in Fig. 4. The robot will have a central cognitive system which will integrate a dialogue management system (with speech recognition and synthesis), stereo vision and a sensorimotor system. Having such a system the robot will be able to detect presence of any person (patient or therapist) and respond in a most natural way.

Robot MARKO has 33 DOFs without hands and a mobile platform. Most of the robot's arm and leg joints are actuated with Dunkermotoren BG series brushless DC motors with an integrated incremental 19 bit single turn and 12 bit multi turn absolute encoders. It has a pair of cameras in its eyes which will be used only to detect a child's position (with a stereo vision) and to provide switching to a compliant control mode at the right moment. Microsoft Kinect will be used for motion planning to provide position and orientation of objects in the surrounding environment during object manipulation. Voice commands will be detected with a microphone array placed on the robot. Microphone array will be also used to detect the direction of the sound input. It will enable the robot to detect the position of the person who is speaking and to turn its head and eyes towards that person. This will

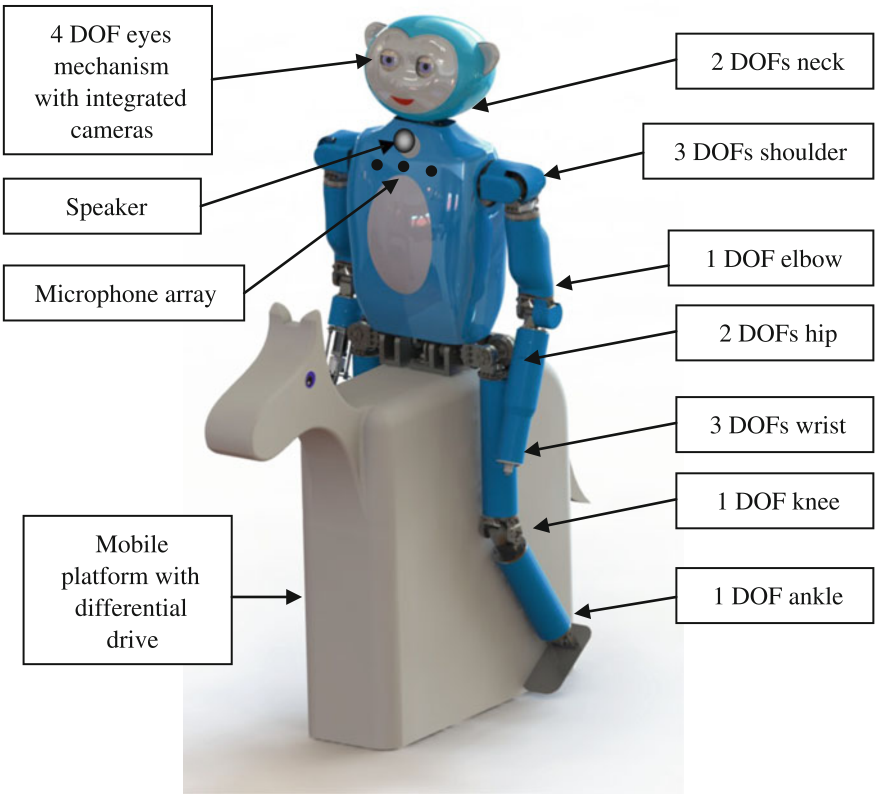

Fig. 4 CAD model of MARKO concept

help the robot to focus its attention on the subject and will contribute to the natural appearance of human-robot interaction.

The Robot head is an extremely important part of the whole system because from the user's point of view, the robot expresses emotions through facial expressions and it is the main mechanism for verbal and non-verbal communication. The Robot neck has 2 DOFs and it is designed as a differential mechanism with bevel gears. It can perform flexion/extension movements (yes gesture) and rotation around vertical axis (no gesture). These two movements are very important for non-verbal interaction and for expressing opinions and attitudes. This mechanism also allows the robot to establish and keep eye contact with the interlocutor and to draw attention on the object in focus, which contributes significantly to the anthropomorphic and natural appearance of robot behavior. Eyes mechanism has 4 DOFs. Each eye can move upward/downward and to the left and right. Also upper and lower eyelids are independently actuated. Eyes blinking occurs randomly every 2–10 s, similar to humans. The Robot's face is manufactured on a 3D printer. The color for the robot MARKO as well as its round shape and heart-shaped face were adopted according to the results of tests, performed by psychologists [8] in order to analyze children's preferences for the robot appearance. The CAD model of the robot neck with its eyes mechanism and manufactured head are shown in Fig. 5.

An initial assumption during the robot design phase was that the robot should dominantly express positive emotions in order to encourage and motivate the patient. Therefore, the default inherent appearance, which determined the shape of the mouth, presents the emotional state of happiness. The Robot mouth and ears are not actuated. They are made of transparent plastic on a 3D printer and are illuminated from the inside with RGB LEDs. There are several LEDs in the mouth whose lightning pattern should simulate the impression of talking.

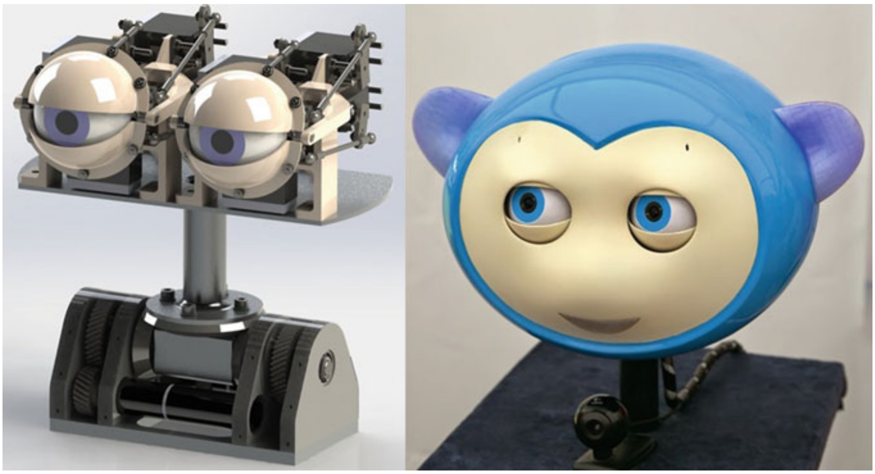

Fig. 5 CAD model of neck and eyes mechanism (*left*); realization of robot head (*right*)

A kinematic structure with 7 DOFs closely approximating human arms has been adopted for robot arm design. Joint ranges, link dimensions and masses are designed to match human arm parameters to the maximum extent possible [15]. In Fig. 6 the realized robot arms and CAD model of arm and leg are shown.

The shoulder joint is approximated with three rotational joints whose axes of rotation intersect at one point. Actuators for the first two DOFs are placed inside the robot torso to reduce the masses and moments of inertia of the movable arm parts. The elbow joint has 1 DOF and the wrist joint has 3 DOFs whose axes of rotation intersect at one point. The Robot torso will have only one DOF for flexion/extension. This joint will increase the workspace of robot arms.

The Robot legs have 4 DOFs. The Hip joint has 2 DOFs and can perform flexion/extension and lateral flexion/extension movements. There is 1 DOF in the knee joint and 1 DOF in the ankle joint. The legs have a simplified design. A plastic mask will be designed which will cover the carbon tubes and joint mechanisms and provide the final appearance of robot legs. Since the robot is set on a mobile platform, legs are not designed for biped walking and they are not even in contact with the ground. They are only intended to be used for performing gross motor skills exercises.

Hardware design should represent a base for implementation of safe and compliant motion control of robot arms. The control architecture is hierarchical and will be composed of a central unit and distributed motion control units. The central unit is conceived as the above described high level cognitive based controller which integrates all the subsystems including a vision subsystem, audio subsystem, communication subsystem and peripheral motion controllers whereas the peripheral

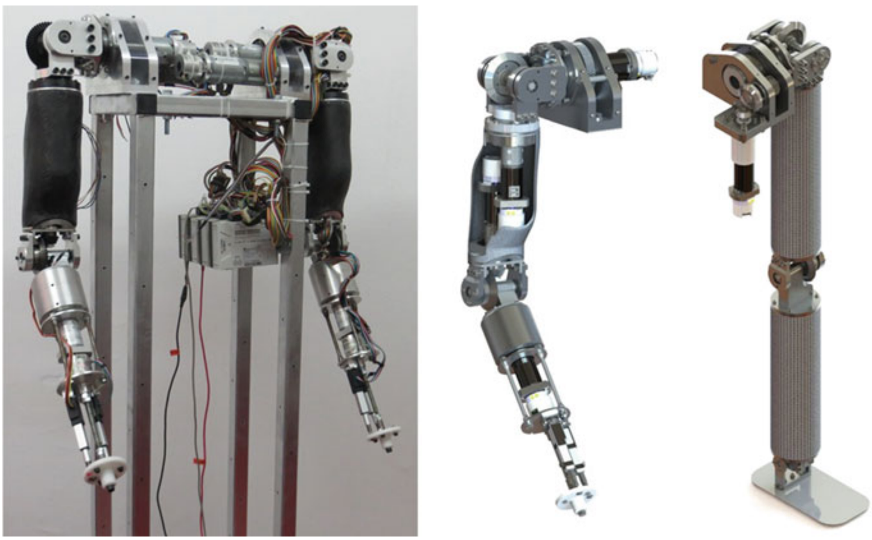

Fig. 6 Realization of robot arms (*left*); CAD model of arm (*middle*); CAD model of leg (*right*)

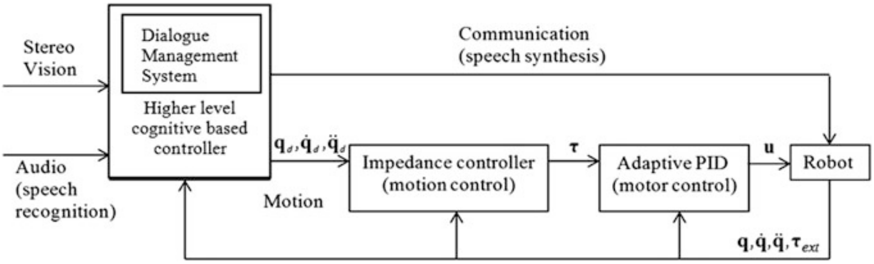

Fig. 7 Control architecture composed of motion, motor and cognitive controllers, which connects modules for sensorimotor system, speech recognition, speech synthesis and robot vision

motion controllers are responsible for low level motion control. The control architecture is shown in Fig. 7.

The joint motion controllers are distributed such that each arm will have three and each leg will have two microcontroller boards, i.e. peripheral motion control units. A block diagram of the control hardware is shown in Fig. 7. The peripheral motion control unit is designed to control either two brushless DC motors or one brushless DC motor and two brushed DC motors (in the case of wrist joint only). Each peripheral unit is equipped with one ARM® Cortex™-M4-based MCU and each controller is responsible for the position, velocity and current measurement of two joints as well as for interfacing with two three-phase half bridge inverters for driving two brushless DC motors. The communication between peripheral units and the central unit is realized through 10 MBit/s UART communication allowing the fast transition of control. This hardware configuration is designed to be powerful enough for the integration of the real-time synchronized control of 7 DOFs in each arm.

5 Conclusion

This paper proposes a novel approach for the incorporation of a human-like robot in the physical therapy of children with cerebral palsy. Robot MARKO is conceived as a social playmate with a basic therapeutical role to motivate the children to persist in the long and tedious therapy. Considering the fundamental role of language in social interactions as well as in establishing an individual's identity, therapeutic robot MARKO was designed to be capable of participating, actively and intelligently, in a multi-party dialogue in natural language. It is assumed that this ability of the robot to communicate with the patient in natural language will significantly help establish the affective connection between the robot and a patient. The robot's mechanical design is mainly determined by a set of exercises and tasks that the robot should be able to perform. A hardware design is presented which provides sufficient capabilities for the robot to participate in the gross and fine motor skills exercises, as well as to socially interact with humans through verbal and non-verbal communication. The importance of the robot head design is emphasized since facial expressions are the foundation for emotional expression. The robot's character appearance is also significant for the establishment of affective connection. Future work will include testing of the robotic system and the proposed therapy approach in real clinical settings.

Acknowledgments This work was funded by the Ministry of education and science of the Republic of Serbia under contract III44008 and by Provincial secretariat for science and technological development under contract 114-451-2116/2011. The authors would like to thank the company Dunkermotoren for its support and equipment donation.

References

1. Iwata H, Sugano S (2009) Design of human symbiotic robot TWENDY-ONE. In: Proceedings of IEEE international conference on robotics and automation. IEEE, Kobe, pp 580–586
2. Wade E, Parnandi A, Mead R, Matarić M (2011) Socially assistive robotics for guiding motor task practice. PALADYN J Behav Robot 2(4):218–227
3. Malik NA, Shamsuddin S, Yussof H, Miskam MA, Hamid AC (2013) Feasibility of using a humanoid robot to elicit communicational response in children with mild autism. In: Proceedings of IOP conference series: materials science and engineering, vol 53, Conference 1
4. Ranatunga I, Rajruangrabin J, Popa DO, Makedon F (2011) Enhanced therapeutic interactivity using social robot Zeno. In: Proceedings of PETRA'11. 4th international conference on pervasive technologies related to assistive environments, Crete, Greece, No. 57, 25–27 May 2011
5. Kozyavkin V, Kachmar O, Ablikova I (2014) Humanoid social robots in the rehabilitation of children with cerebral palsy. Research workshop "ICTs for improving patient rehabilitation research techniques", Oldenburg, Germany
6. Calderita LV, Bustos P, Suárez Mejías C, Ferrer González B, Bandera A (2013) Rehabilitation for children while playing with a robotic assistant in a serious game. In: Proceedings of NEUROTECHNIX 2013, Vilamoura, Portugal
7. Rosenbaum P, Paneth N, Leviton A, Goldstein M, Bax M, Damiano D, Dan B, Jacobsson B (2007) A report: the definition and classification of cerebral palsy. Dev Med Child Neurol Suppl 109:8–14
8. Oros M, Nikolić M, Borovac B, Jerković I (2014) Children's preference of appearance and parents' attitudes towards assistive robots. IEEE-RAS International Conference on Humanoid Robots (14; Madrid; 2014) Str. pp 360–365. ISBN 978-1-4799-7173-2/14
9. Vernon D, von Hofsten K, Fadiga L (2011) A roadmap for cognitive development in humanoid robots, series: cognitive systems monographs, vol 11. Springer, Berlin
10. Delic V, Pekar D, Obradovic R, Jakovljevic N, Miskovic D (2007) A review of AlfaNum continuous automatic speech recognition system. In: Proceedings of XII international conference "speech and computer" (SPECOM'2007), Moscow, Russia, pp 15–18
11. Gnjatović M (2007) Adaptive dialogue management in human-machine interaction. Verlag Dr Hut, Berlin
12. Gnjatović M (2014) Therapist-centered design of a robot's dialogue behavior. Cogn Comput. Springer US. doi:10.1007/s12559-014-9272-1. Accessed 5 May 2014. ISSN: 1866-9964
13. Karan B, Golubović S, Gnjatović M (2014) Markerless vision-based skeleton tracking in therapy of gross motor skill disorders in children. In: New trends on medical and service robotics: challenges and solutions. Springer monograph series mechanisms and machine

science, vol 20, pp 99–93. Proceedings of the 2nd international workshop new trends on medical and service robotics, MESROB 2013

14. Tasevski T, Nikolić M, Mišković D (2013) Integration of an industrial robot with the system for image and voice recognition. Serbian J Electr Eng 10(1):219–230
15. Savić S, Raković M, Borovac B (2013) Mechanical design and control algorithm for the arm of humanoid robot MARKO. In: Proceedings of 6th PSU-UNS international conference on engineering and technology ICET 2013, Novi Sad, Serbia

Give Children Toys Robots to Educate and/or NeuroReeducate: The Example of PEKOPPA

I. Giannopulu and T. Watanabe

Abstract Using an InterActor toy robot named PEKOPPA in a "speaker-listener" situation, we have compared the verbal and the emotional expressions of neurotypical and autistic children aged 6–7 years. The speaker was always a child (neurotypical or autistic); the listener was a human or the toy robot which reacts to speech expression by nodding only. The results appear to indicate that minimalistic artificial environments could be considered as the root of neuronal organization and reorganization with the potential to improve brain activity. They would support the embrainment of cognitive verbal and nonverbal emotional information processing.

Keywords Neurotypical child · Autism · Robot · Play · Emotion · Embrainment

1 Introduction

Development is the result of a complex process with at least three foci: one in the central nervous system, one in the mind and one in the child's dynamic interactions with the natural vs. artificial environment, that is, robots [1]. Verbal and nonverbal cognition as well as emotion develop at the interface between neural processes. Toys have a central role. Toys seem provide an interesting account of "how" physical objects are able to act as support for the symbolic play of children. With development, symbolic play with action grows into language. Note that children access language because of their capacity to construct coherent multimodal interactions which are based on the links between the symbolized toys [1]. This is of great interest, particularly when considering that nonverbal multimodal behavior is

I. Giannopulu (✉)
IHU-a-ICM Prisme-Pierre and Marie Curie University, Paris, France
e-mail: igiannopulu@psycho-prat.fr

T. Watanabe
Okayama Prefectural University, Soja, Japan
e-mail: watanabe@cse.oka-pu.ac.jp

H. Bleuler et al. (eds.), *New Trends in Medical and Service Robots*,
Mechanisms and Machine Science 38, DOI 10.1007/978-3-319-23832-6_17

probably at the origin of what is arguably one of the trademarks of human cognition: the capacity to generate thoughts and concepts for ourselves and for the others which can be verbally expressed with the aim to communicate.

With that in mind, imagine a scenery of communication between two people, one speaking the other listening. The speaker is elaborating a multivariable equation. They are trying to conceptualize within their brain and encode according to rules of semantics and syntax, and then externalize into spoken form. Speech engenders an avalanche of neuronal responses in the listener. The listener is computing and trying to solve the proposed equation displaying various verbal and nonverbal reactions in response to the utterances of the speaker. Verbal reaction necessitates the elaboration of coherent (grammatical and syntactically) sentence. Nonverbal reaction takes the form of head nods and/or various kinds of facial expressions. Intimately connected with the utterances of the speaker, these responses signify that the utterance is being accepted, understood, integrated [2]. Successful communication requires that both speaker and listener accurately interpret (via verbal and nonverbal emotional processes) the meaning of each other referential statement.

Neurotypical developing listener and speaker are able to consider verbal, nonverbal (i.e., head nods), emotional (i.e., facial expressions) conventions and rules as well as each other referential statement. Using a modeling approach, recent neuroimaging studies have reported that both speech comprehension and speech expression activate a bilateral fronto-temporo-parietal network in the brain, fully characterized by the dynamic interaction among all the components (production and reception of speech but also for cognitive nonverbal emotional processes) [3]. Failure of the exterior superior temporal sulcus [4], of the interior temporal lobe, amygdala included [5], of the connectivity between temporal regions [6] as well as of the inferior prefrontal cortex [7] i.e., the mirror neurone system, is accepted as an explanation for atypical neurodevelopment, such as autism [8, 9]. The atypical neural architecture causes impairment in social interaction, in communications skills and interests and reduces the ability of mentalizing, i.e., represent the referential statement of other people [9].

Imagine now that in the aforementioned situation of "speaker and listener", the speaker is an autistic child trying to elaborate a multivariable equation. Complex in nature, the elaboration of this equation becomes more complex notably when the listener is a human, who is characterized by a high degree of variability on verbal and nonverbal reactions, (i.e., unpredictable reactions) [10]. Adding the fact that the child is impaired in interpreting the referential statement of other people [9], listener's verbal and nonverbal contributions are not always scrutinized.

Different studies have shown that animate robots using different stimulations encourage interaction in autistic children [11]. Despite these studies, only marginal attention has been paid to the comparison of neurotypical and autistic children in human-human and human-robot interaction. In the context of an interdisciplinary study (cognitive neuroscience, psychiatry and engineering) using a "speaker-listener" situation, we have compared the verbal and nonverbal emotional expressions of neurotypical and autistic children aged 6 years. The speaker was always a child (neurotypical or autistic); the listener was a human or an InterActor robot, i.e., a toy robot which reacts to speech expression by nodding only. Given the fact that the InterActor robot is characterized by a low degree of variability in reactions (i.e., predictable reactions) and the human by a high degree of variability in reactions (i.e., unpredictable reactions), our general hypothesis is that verbal and emotional expressions of autistic children could be better facilitated by the InterActor Robot than by the human.

2 Methods

2.1 Participants

Two groups of children, one "neurotypical" and one "autistic" participated in the study. Twenty neurotypical children (10 boys and 10 girls) composed the "neurotypical group"; twenty children (14 boys and 6 girls) composed the "autistic group". The developmental age of typical children ranged from 6 to 7 years old (mean 6.1 years; sd 7 months). The developmental age of autistic children ranged from 6 to 7 years old (mean 6 years; sd 8 months) [12]. The mean age of autistic children when first words appeared was 28 months (sd 7 months). The autistic children were diagnosed according to the DSM IV-TR criteria of autism [13]. The Childhood Autism Rating Scale-CARS [14] has been administrated by an experienced psychiatrist. The scores varied from 31 to 35 points signifying that the autistic population was composed of middle autistic children. They were all verbal. All autistic children were attending typical school classes with typical educational arrangements. The study was approved by the local ethics committee and was in accordance with the Helsinki convention. Anonymity was guaranteed.

2.2 Robot

An InterActor robot, i.e., a small toy robot called "Pekoppa", was used as a listener [15]. Pekoppa is shaped like a bilobed plant and its leaves and stem make a nodding response based on speech input and supports the sharing of mutual embodiment in communication (Fig. 1). It uses a material called BioMetal made of a shape-memory alloy as its driving force. The timing of nodding is predicted using a hierarchy model consisting of two stages: macro and micro (Fig. 2). The macro stage estimates whether a nodding response exists or not in a duration unit, which consists of a talkspurt episode T(i) and the following silence episode S(i) with a hangover value of 4/30 s. The estimator Mu(i) is a moving-average (MA) model, expressed as the weighted sum of unit speech activity R(i) in (1) and (2). When Mu (i) exceeds a threshold value, nodding M(i) also becomes an MA model, estimated as the weighted sum of the binary speech signal V(i) in (3). Pekoppa demonstrates

Fig. 1 Pekoppa robot

Fig. 2 Listener's interaction model

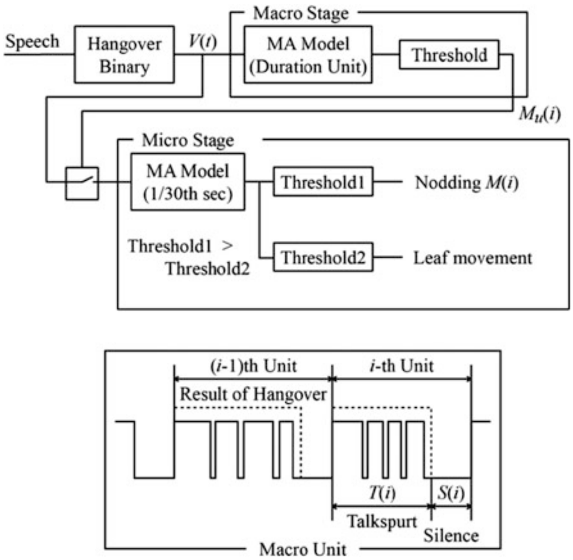

three degrees of movements: big and small nods and a slight twitch of the leaves by controlling the threshold values of the nodding prediction. The threshold of the leaf movement is set lower than that of the nodding prediction.

$$M_u(i) = \sum_{j=1}^{J} a(j)R(i-j) + u(i) \tag{1}$$

$$R(i) = \frac{T(i)}{T(i) + S(i)} \tag{2}$$

$a(j)$ linear prediction coefficient
$T(i)$ talkspurt duration in the i-th duration unit

$S(i)$ silence duration in the i-th duration unit
$u(i)$ noise

$$M(i) = \sum_{k=1}^{K} b(j)V(i-j) + w(i) \quad (3)$$

$b(j)$ linear prediction coefficient
$V(i)$ voice
$w(i)$ noise

2.3 Procedure

For both groups, the study took place in a room which was familiar to the children. We defined three conditions: the first one was called "rest condition", the second was named "with human" (i.e., child-adult) and the third one was called "with robot" (i.e., child-Pekoppa). The second and third conditions were counterbalanced across the children. The duration of the "rest condition" was 1 min; the second and third conditions each lasted approximately 7 min. The inter-condition interval was approximately about 30 s. For each child, the whole experimental session lasted 15 min (Fig. 3).

In order to neutralize a possible "human impact" on children's behavior, the experimenter was the same person for each child in each condition and group. At the beginning of each session, the experimenter presented the robot to the child explaining that the robot nods whenever the child speaks. Then, the experimenter hid the robot. The session was run as follows: during the "rest condition", the heart

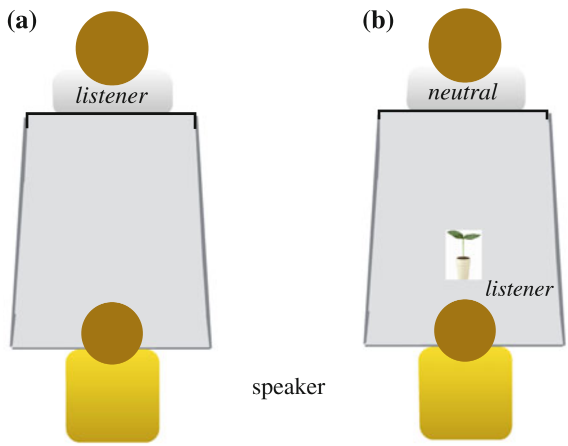

Fig. 3 Listener-Speaker situation

rate of each child was measured in silence. During the “Human InterActor” condition, the child was invited to discuss with the experimenter. The experimenter initiated discussion and after listened to the child acting as the speaker. The heart rate, as well as the frequency of words and verbs expressed by each child was measured. During the “robot InterActor” condition, Pekoppa was set to nod movements; the experimenter gave the robot to the child inviting the child to use it. The robot was the listener, the child was the speaker and the experiment remained silent and discreet. The heart rate and the frequency of words and verbs expressed by the child were recorded once again.

2.4 Analysis

The analysis was based on (a) the heart rate[1] (b) the number of words and verbs expressed by each child. The data analysis was performed with SPSS Statistics 17.0.

3 Results

The distribution of heart rate and words in both age groups approximates a parametric shape. With such distributions, the mean was been chosen as central index for comparisons. We performed statistic of comparisons using the t-student test, the ANOVA’s test and the chi-square test to examine differences in heart rate, number of words and intensity of emotional feeling between the two experimental conditions (“with human” and “with Robot” i.e., Pekoppa), for neurotypical and autistic children. The obtained results were very similar. We present the results of chi-square test (χ^2 test) which can be used as a substitute for t and ANOVA tests [16].

Figure 4 represents the mean heart rate of neurotypical and autistic children both at inter-individual and intra-individual levels.

At the intra-individual level, the statistical analysis showed that relative to the “rest condition”, the mean heart rate of neurotypical children was higher when the children were in contact with the InterActor robot ($\chi^2 = 6.68$, $p < 0.01$) than when they were in contact with the human ($\chi^2 = 4.09$, $p < 0.05$). However, the mean heart rate of neurotypical children didn’t differ significantly when they interacted with the human or with the InterActor robot ($\chi^2 = 2.83$, $p > 0.05$). Similarly, relative to the “rest condition”, the mean heart rate of autistic children was higher when they

[1]Heart rate is measured in beat per minute (bpm) using a frequency counter ring placed on the index finger of each child. The experiment noted the HR of each child every 5 s. The physiological heart rate limits correspond to 95 bpm (±30) at the age of 6–7 years.

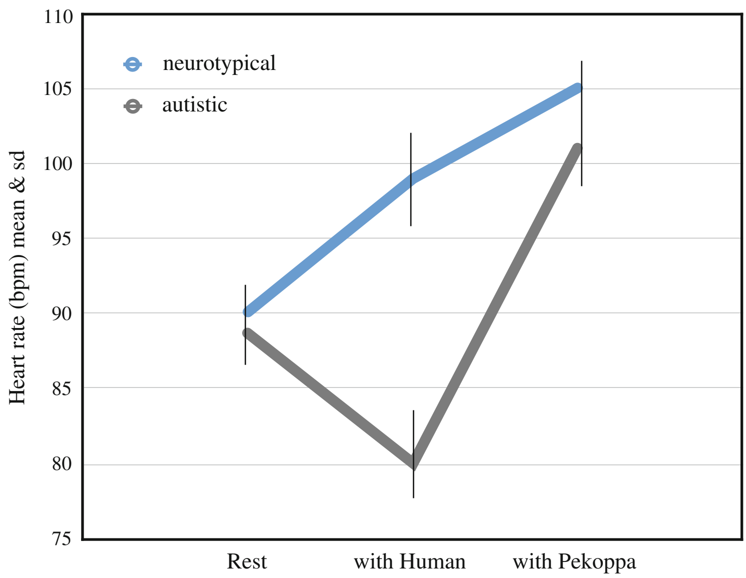

Fig. 4 Mean heart rate

interacted with the InterActor robot (χ^2 = 7.01, p < 0.01) than when they interacted with the human (χ^2 = 5.01, p < 0.05). Finally, the mean heart rate of autistic children was higher when they were with the InterActor robot than when they were with the human (χ^2 = 7.84, p < 0.01).

At the inter-individual level, the mean heart rate of neurotypical and autistic children was similar (χ^2 = 2.06, p > 0.10) in the "rest condition". However, compared to the heart rate of neurotypical children, the mean heart rate of autistic children was lower when they interact with the human (χ^2 = 8.68, p < 0.005). The mean heart rate of autistic children didn't differ from that of neurotypical children when the InterActor was the robot (χ^2 = 2.85, p > 0.05).

Two independent judges unfamiliar with the aim of the study completed the analysis of the number of words for each child in each experimental condition ("human InterActor" and "robot InterActor"). Both performed the analyses of audio sequences. Inter-judge reliability was assessed using intra-class coefficients to make the comparison between them. The inter-judge reliability was good (Cohen's kappa = 0.82).

At the inter-individual level, as shown in Fig. 5, the mean number of words (nouns and verbs) was low in the "with human" condition for autistic children (χ^2 = 4.86, p < 0.05) and in the "with robot" condition for neurotypical children (χ^2 = 5.98, p < 0.025). The mean number of words expressed by autistic children in the "with robot" condition didn't differ from the mean number of words expressed by neurotypical children in the "with human" condition (χ^2 = 1.34, p > 0.10). At the intra-individual level, the mean number of words was higher when the autistic

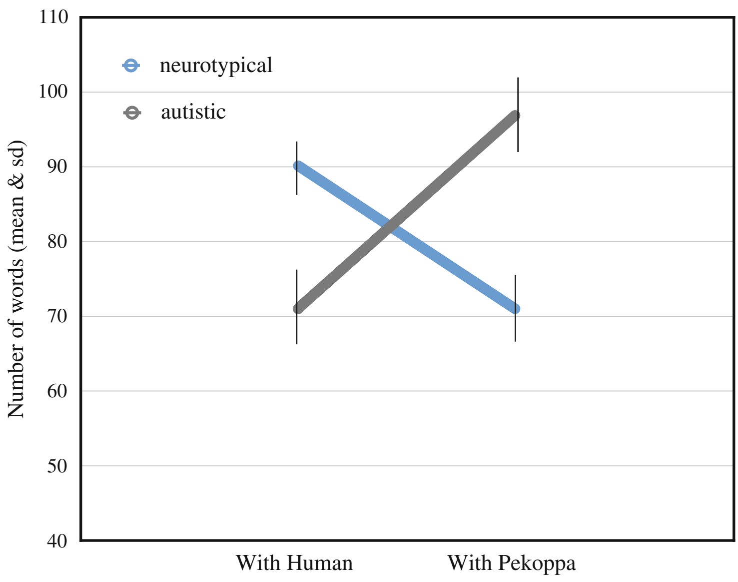

Fig. 5 Number of words (nouns and verbs)

children had the robot as interlocutor than when the interlocutor was a human (χ^2 = 5.97, $p < 0.025$). The quasi opposite configuration was observed for the neurotypical children (χ^2 = 4.78, $p < 0.05$).

4 Discussion

The present study aims at analyzing the embrainment of verbal and emotional expressions in neurotypical and autistic children aged 6–7 years. Our approach centered on the effects of a human or an InterActor robot in the context of a "speaker-listener" situation: the speaker was always the child; the listener was a human or an InterActor robot. To this end physiological data (i.e., heart rate), as well as behavioral data (i.e., number of nouns and verbs) were considered. The results showed that (1) the heart rate of autistic children is low when the listener was a human and increased nearer to levels of neurotypical children when the listener was the InterActor robot; (2) the number of words expressed by the autistic children was higher when the interlocutor was the robot.

Fundamentally, the results are consistent with our hypothesis according to which the predictability, i.e., the simplicity, of the InterActor robot would facilitate the emotional and verbal expressions of autistic children. Our results showed significant differences of heart rate depending on whether the listener was a human or a robot. When the listener was a human, the children showed a low heart rate; when the listener was an InterActor robot, their heart rate increased. Such a result cannot be attributed to an order effect as the order of “human-human” and “human-robot” conditions have been counterbalanced. On the contrary, it can be understood as an effect of the InterActor robot on autistic children’s mental state. This interpretation is also supported by the fact that when the autistic children had the InterActor robot as listener, their heart rate didn’t differ from the heart rate of neurotypical children in the same condition. It is also interesting to note that the heart rate of the neurotypical children didn’t differ when the listener was a human or a InterActor robot. Such difference reveals that an InterActor robot would improve autistic children behavior. This inference is reinforced by the fact that the physiological data we recorded reflects the modifications of orthosympathetic and parasympathetic autonomous nervous system which is dynamically (and bidirectionally) connected to the central nervous system [17]. Physiologically, the lower regulation of heart rate (in “with human” condition) reflects poorer action of the myelinated vagus nerve [18] which in turn would would signify poor neural activity in temporal cortex (amygdala included), in cingulate cortex and in prefrontal cortex [19]. This neural architecture is hypo-activated in children with autism [8, 9], causing impairment in cognitive verbal, nonverbal and emotional behavior [4–6, 9]. Such hypo-activation would explain autistic children’s behavior when the listener is the human. Contrary to research suggesting that autistic children show disruptions in autonomic responses to environmental (human) stressors [20], our findings indicate no disruptions in autonomic responses and that these responses don’t exceed the physiological limits. Apparently, when the listener is the InterActor robot, the heart rate of children with autism increases indicating a “mobilisation” of a given mental state. Such “mobilisation” would provide support for the social engagement of autistic children. Namely, by making the autistic children available to engage emotionally (and verbally), the InterActor robot seems to modify their neural activity: the children enjoyed participating. It is noteworthy that they also verbalized such pleasurable sentiments at the end of the experiment. Essentially, the present results are consistant with our previous assumptions that toy robots would improve autistic children brain functioning [11].

The above considerations could account for the number of words (nouns and verbs) expressed by the children. Even if the autistic children were verbal, the present finding indicated that when the listener was an InterActor robot, the number of words expressed by the autistic children was higher than the number of words they express when the listener was a human. Interestingly, such verbal behavior doesn’t differ from that of neurotypical children when these latter had a human as listener. Once again, the use of the InterActor robot would afford autistic children to express themselves as neurotypical children do with humans. This data is consistent with previous studies which have demonstrated that verbal expression can be facilitated by the active (but discreet) presence of a robot [11].

5 Conclusion

It can be concluded that minimalistic artificial environments could be considered as the root of neuronal organization and reorganization with the potential to improve brain activity in order to support the embrainment of cognitive verbal and emotional information processing.

Acknowledgments We thank all the participants and their parents, The Major, the Pedagogical Inspector, the Director and the team of the principal elementary school of the first district of Paris, the National Department of Education and Research. The research is supported by the Franco-Japanese Foundation of Paris.

References

1. Giannopulu I (2013) Multimodal interactions in typically and atypically developing children: natural vs. artificial environments. Cogn Process 14:323–331
2. Bavelas JB, Coates L, Johnson T (2002) Listener responses as a collaborative process: the role of gaze. J Commun 52:566–580
3. Dick AS, Solodkin A, Small SL (2010) Neural development of networks for audiovisual speech comprehension. Brain Lang 114:101–114
4. Pelphrey KA, Caster EJ (2008) Charting the typical and atypical development of the social brain. Dev Psychopathol 20:1081–1102
5. Corbett BA, Carmean V, Ravizza S, Wendelken C, Henry ML, Carter C, Rivera SM (2009) A functional and structural study of emotion and face processing in children with autism. Psychiatry Res 30:196–205
6. Frith U, Frith CD (2003) Development and neurophysiology of mentalizing. Philos Trans Royal Soc B Biol Sci 358:459–473
7. Brothers L (1990) The social brain: a project for integrating primate behaviour and neurophysiology in a new domain. Concepts Neurosci 1:27–51
8. Iacoboni M, Mazziotta JC (2007) Mirror neuron system: basic findings and clinical applications. Ann Neurol 3:213–218
9. Baron-Cohen S (1995) Mindblindness. MIT Press, Cambridge
10. Pierno AC, Mari M, Lusher D, Castiello U (2008) Robotic movement elicits visuomotor priming in children with autism. Neuropsychologia 46:448–454
11. Giannopulu I (2013) Multimodal cognitive nonverbal and verbal interactions: the neurorehabilitation of autistic children via mobile toy robots. IARIA Intl J Adv Life Sci 5:214–222
12. Kaufman AS, Kaufman NL (2008) K-ABC-II. La batterie pour l'examen psychologique de l'enfant-deuxième édition. Pearson-Paris ECPA, Paris
13. DSM-IV-TR (2003) Manuel diagnostique et statistique des troubles mentaux. Paris, Editions Masson
14. Schopler E, De Reichler RJ, Vellis RF, Daly K (1980) Toward objective classification of childhood autism: childhood Autism Rating Scale (CARS). JADD 10:91–103
15. Watanabe T (2011) Human-entrained embodied interaction and communication technology. Emotion Eng 161–177
16. Gravetter FJ, Wallnau LB (2000) Statistics for the behavioral sciences, 5th edn. Wadsworth Thomson Learning, Belmont
17. Giannopulu I, Montreynaud V, Watanabe T (2014) Neurotypical and autistic children aged 6 to 7 years in a speaker-listener situation with a human or a minimalist interactor robot. In:

The 23rd IEEE international symposium on robot and human interactive communication. IEEE RO-MAN, pp 942–948
18. Manta S (2012) Effets Neurophysiologiques de la stimulation du nerf vague: Implication dans le traitement de la dépression résistante et optimisation des paramètres de stimulation. Thèse de Doctorat, Université de Montréal, Canada
19. Porges SW, Furman SA (2011) The early development of the autonomic nervous system provides a neural platform for social behavior: a polyvagal perspective. Infant Child Dev 20(1):106–118
20. Toichi M, Kamio Y (2003) Paradoxal autonomic response to mental tasks in autism. J Autism Dev Disord 33:417–426

Automatic Segmentation of Therapeutic Exercises Motion Data with a Predictive Event Approach

S. Spasojevic, R. Ventura, J. Santos-Victor, V. Potkonjak and A. Rodić

Abstract We propose a novel approach for detecting events in data sequences, based on a predictive method using Gaussian processes. We have applied this approach for detecting relevant events in the therapeutic exercise sequences, wherein obtained results in addition to a suitable classifier, can be used directly for gesture segmentation. During exercise performing, motion data in the sense of 3D position of characteristic skeleton joints for each frame are acquired using a RGBD camera. Trajectories of joints relevant for the upper-body therapeutic exercises of Parkinson's patients are modelled as Gaussian processes. Our event detection procedure using an adaptive Gaussian process predictor has been shown to outperform a first derivative based approach.

Keywords Gesture segmentation · Predictive event approach · Gaussian processes · Physical rehabilitation · RGBD camera

S. Spasojevic (✉) · V. Potkonjak
Faculty of Electrical Engineering and Mihailo Pupin Institute, University of Belgrade, Belgrade, Serbia
e-mail: sofija.spasojevic@pupin.rs

V. Potkonjak
e-mail: potkonjak@yahoo.com

S. Spasojevic · A. Rodić
Mihailo Pupin Institute, University of Belgrade, Belgrade, Serbia
e-mail: aleksandar.rodic@pupin.rs

S. Spasojevic · R. Ventura · J. Santos-Victor
Institute for Systems and Robotics, Instituto Superior Técnico, University of Lisbon, Lisbon, Portugal
e-mail: rodrigo.ventura@isr.tecnico.ulisboa.pt

J. Santos-Victor
e-mail: jasv@isr.tecnico.ulisboa.pt

H. Bleuler et al. (eds.), *New Trends in Medical and Service Robots*,
Mechanisms and Machine Science 38, DOI 10.1007/978-3-319-23832-6_18

1 Introduction

Recent research in medical and service robotics has shown growing application of various robotic systems into the medical practice. Such systems have been mainly developed as a support for the traditional physical rehabilitation therapy and treatment, since the conventional techniques rely on the clinical assessment tools [1]. Robotic prostheses have been designed for the assistance during movements performing at patients with the reduced mobility. Other systems have been developed for the purposes of monitoring and evaluating patient's performance during different rehabilitation tasks. The advantages of their usage are the superiority of quantitative system outputs comparing to the subjective evaluations of therapists [1] and enhancement of patient's motivation. Our method can be potentially integrated into one such system for movement examination and characterization, since the main goal of our approach is to enhance the efficiency of motion data analysis in patients with neurological disorders. In addition, the Kinect device that has been used in our study for the movement data acquisition can be attached to the rehabilitation robot, which would increase patient's motivation through the interaction with the robot, and on the other side, motion data can be collected and analyzed in real time.

This paper presents a predictive event approach for automatic segmentation of therapeutic exercise sequences. When dealing with analysis of rehabilitation exercises, it is often required to pre-process the collected data. In order to examine the movements and to carry out the relevant measurements and determine the parameters of interest, each movement must be segmented from a given sequence and analyzed separately.

In general, gesture recognition tasks require gesture acquisition followed by the central step of segmentation, which can have a huge impact on the classification rate of the gesture recognition system. Gesture segmentation and recognition systems have significant applications in many different fields such as virtual and augmented reality [2], industrial process control [3], physical rehabilitation [4], human-robot interaction [5], computer games [6] etc. Due to this, gesture segmentation is an active research topic and challenging scientific problem, fairly present in the latest research.

The predictive event approach is based on a principle of detecting an event when sensor data depart significantly from an adaptive model-based predictor. We have used portable, low-cost Kinect device with marker-free based technique. During exercise execution, the skeleton is continuously detected and 3D positions of characteristic human joints are collected for each frame (Fig. 1). From the original data set, which consists of all collected joints motion data, we have extracted the ones from interest for upper body movement therapeutic exercises (hand and elbow joint). Trajectories of selected joints are modelled as Gaussian processes. Based on this data set, a Gaussian process based predictor is adapted and used to detect significant changes in the exercise sequences. The results over the formed dataset are compared with commonly used technique and illustrate the superiority of our approach.

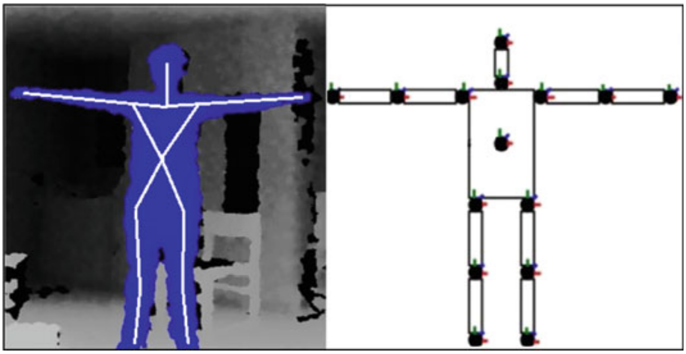

Fig. 1 Skeleton tracking (*left*) and collected joints (*right*)

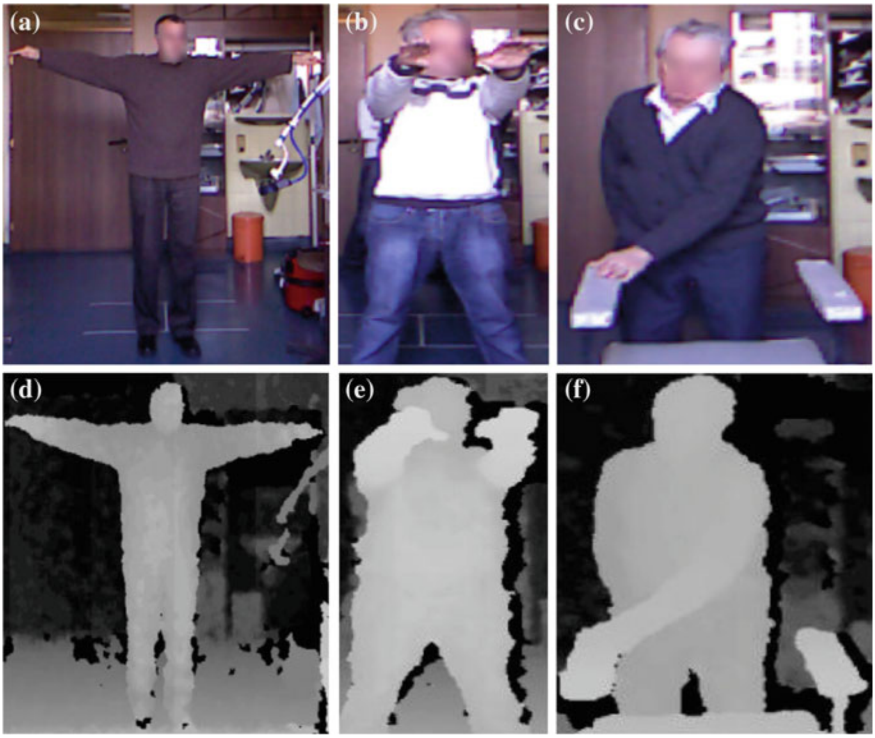

Fig. 2 Exercises acquisition using Kinect—RGB (**a**, **b**, **c**) and depth (**d**, **e**, **f**) stream

2 Related Work

Frequently used methods for gesture segmentation are based on the Dynamic Programming (DP) [7, 8], Dynamic Time Warping (DTW) [9, 10] and Hidden Markov Models (HMM) [11–14].

A technique based on the simple sliding window combined with simple moving average filter is used in [15]. The author defines the content of each gesture in the following form: starting static posture, dynamic gesture part and ending static posture. In addition, to obtain a more robust segmentation, the author observes also the length of each analyzed sequence to eliminate the appearance of the static part into dynamic part of the gesture.

In [16] the authors developed an algorithm for segmentation of dance sequences. This algorithm, called Hierarchical Activity Segmentation, is based on the division of the human body onto hierarchically dependent structures. They take into account relevant motion parameters for body segments (segmental force, kinetic energy and momentum) that characterize motion in the levels of defined hierarchy. In [17] the authors took a dynamical system approach for dynamic system identification, however, that approach did not account for sensor noise.

Previously, a prediction-based approach to event segmentation was taken, based on an adaptive dynamical system approach [18, 19]. In this paper, we study a different approach employing a probabilistic model (Gaussian processes) as a machine learning method [20] that provides information about both, value and uncertainty. This method has shown good properties related to complexity model, processing time and remarkable results in comparison with commonly used method.

3 Experimental Group and Algorithm

Participants in this study are patients with Parkinson's disease. Data collected using Kinect device on sampling frequency of 27 Hz consist of 3D position of characteristic skeleton joints, along with RGB and depth video sequences (Fig. 2). Acquired exercises are instructed by the therapist and give the insight of patient's upper body functionality. In total, three different exercises (Fig. 2) for eight patients are collected. Each exercise is repeated at least seven times. In case of exercises performed by the hands (Fig. 2) only trajectories of the elbow and hand joint are relevant for the further processing. All coordinates are normalized with respect to the torso and filtered using a low pass filter of second order with cutoff frequency of 2 Hz due to measurement noise.

Trajectories of elbow and hand joint positions are modelled as Gaussian processes and three predictive Gaussian prediction model (each model for one coordinate) are formed. Number of hyper-parameters which define the meaning and covariance functions of Gaussian process depends on the form of input and output training set samples. Let n be the number of frames in the exercise sequence and

x_i value of x-coordinate in *i*th frame. Training input set (Eq. 1) consists of samples that are organized as *k* dimensional vectors:

$$X = ([x_1 \ldots x_k];\ [x_2 \ldots x_{k+1}];\ \ldots;\ [x_{n-(k-1)} \ldots x_n]) \tag{1}$$

Training output set (Eq. 2) contains from following scalar samples of appropriate training input vector sample:

$$X_* = (x_{k+1};\ x_{k+2}; \ldots; x_n) \tag{2}$$

This procedure is repeated analogously in the case of the input and output training set for y coordinate, Y and Y*. Given this data set, corresponding mean functions of Gaussian models have per *k*, and covariance functions per two free parameters, which are determined in the process of hyper-parameters optimization.

Predictive models are defined using input and output training and input testing set, obtained hyper-parameters and selection of appropriate inference method. Models are formed for x and y trajectories of hand joints, since the exercises are performed in x–y plane. The values of the z-coordinate in this case did not give any contribution to the final result; therefore they are not taken into account.

Errors of prediction in the form of the difference between real (x, y) and predicted values ($\hat{x}$, $\hat{y}$) are calculated at each step. Since the Gaussian process based predictor predicts both, mean and variance, in order to obtain a normalized distance metric, Mahalanobis distance (3) is also calculated at each step. Using this metric, the method becomes more sensitive to small errors caused by highly uncertain data points.

$$MD = \sqrt{\begin{bmatrix} x - \hat{x} & y - \hat{y} \end{bmatrix} \begin{bmatrix} \sigma_x & 0 \\ 0 & \sigma_y \end{bmatrix}^{-1} \begin{bmatrix} x - \hat{x} \\ y - \hat{y} \end{bmatrix}} \tag{3}$$

Where σ_x and σ_y are predictive variances for first and second Gaussian predictive model, respectively.

4 Results

We observed changes of the Mahalanobis distance through exercise sequence. When the Mahalanobis distance increases significantly for several successive time steps and then drops again, boundary points of that segment are marked as events. Mahalanobis distance for one sequence of exercises is shown on the Fig. 3. Peaks that have the greatest values represent points in the sequence where the values of x and y hand coordinate suddenly increase or decrease. More precisely, positions where Mahalanobis distance has greater value than a determined threshold (Fig. 3) are marked as events. As the threshold varies, positions and numbers of events are

Fig. 3 Mahalanobis distance with event detection

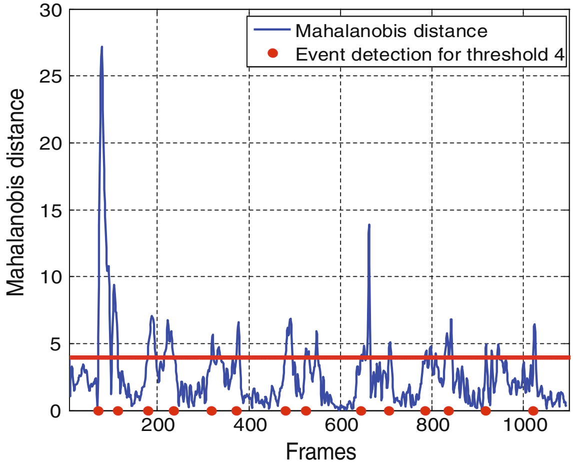

Fig. 4 True and predicted values with detected events

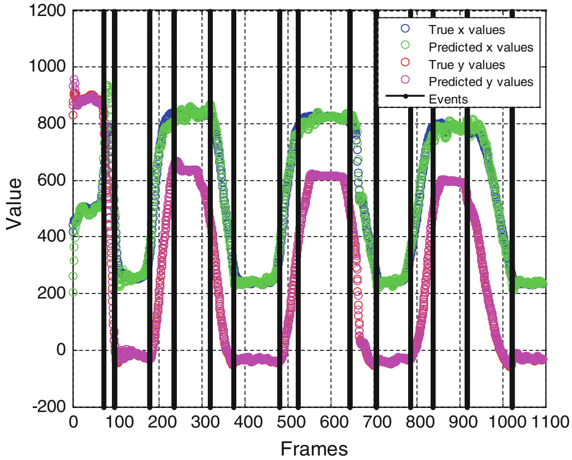

changing and this is the only parameter that is necessary to adjust. The hand trajectory of true and predicted x and y coordinates of hand joint together with detected events for k = 5 (1, 2) are shown on Fig. 4.

Figure 3 shows that detected events correspond to the characteristic points in the sequence where the values of x or y coordinate of hand joint start or stop to change significantly. In order to classify all events between the ones with meaningful information, for example real beginnings and ends of individual exercises, classification technique based on the Hidden Markov Model (HMM) will be applied.

The approach described in this paper is compared with standard technique for detecting characteristic or extreme points in the sequence—technique of the first derivative. Comparison of these two methods (Fig. 5) is based on the combined sensitivity and specificity criteria (4–6), commonly used statistical tool for

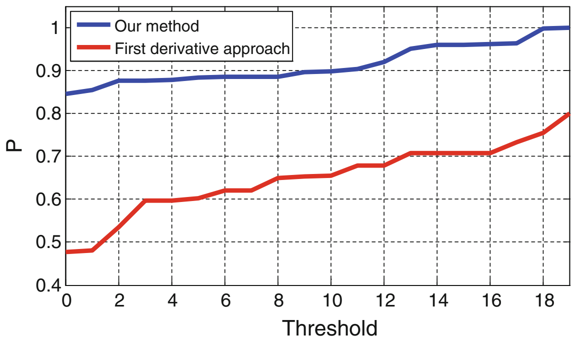

Fig. 5 A comparison of our method and first derivative approach based on sensitivity and specificity criteria

measuring classifier performance [21]. Value P (y-axis on Fig. 5) is calculated using relations (4–6) for different values of the threshold in the case of five exercise sequences.

$$P = \sqrt{sens \cdot spec} \tag{4}$$

$$sens = \frac{TP}{TP + FN} \tag{5}$$

$$spec = \frac{TN}{TN + FP} \tag{6}$$

In relations (Eqs. 5 and 6), TP denotes the number of true positives, FN the number of false negatives, TN the number of true negatives and FP the number of false positives. According to the form of (4–6) it can be seen that greater values of sensitivity and specificity indicate better performances of the approach, hence Fig. 5 clearly illustrate the superiority and advantage of our approach.

5 Conclusion and Future Work

We have presented one approach for therapeutic exercise segmentation based on a predictive Gaussian model and event detection principle. This approach has shown excellent results in the sense of correct detection of significant changes during therapeutic exercise performing and advantage in comparison with commonly used technique of the first derivative.

Next extension of this work will be oriented to the integration of this approach with HMM in order of meaningful event classification. Future work will be focused on the improvement of this method and generalization in case of larger and more diverse gesture sequences and implementation in real time environments.

Acknowledgments This work was partially funded by bilateral project COLBAR, between Instituto Superior Técnico, Lisbon, Portugal and Mihailo Pupin Institute, Belgrade, Serbia, FCT [PEst-OE/EEI/LA0009/2013], III44008, TR35003 and SNSF IP SCOPES, IZ74Z0_137361/1.

References

1. Goetz C, Tilley B, Shaftman S et al (2008) Movement disorder society-sponsored revision of the unified parkinson's disease rating scale (MDS-UPDRS): scale presentation and clinimetric testing results. Mov Disord 22:2129–2170
2. Cruz-Neira C, Sandin D, DeFanti T et al (1992) The cave: audio visual experience automatic virtual environment. Commun ACM 35(6):64–72
3. Starner T, Leibe B, Minnen D et al (2003) The perceptive workbench: computervision-based gesture tracking, object tracking, and 3d reconstruction of augmented desks. Mach Vis Appl 14(1):59–71
4. Gama A, Chaves T, Figueiredo L et al (2012) Guidance and movement correction based on therapeutics movements for motor rehabilitation support systems. In: 14th symposium on virtual and augmented reality, pp 191–200
5. Lee S (2006) Automatic gesture recognition for intelligent human-robot interaction. In: Proceedings of 7th international conference on automatic face and gesture recognition, pp 645–650
6. Park H, Jung D, Kim H (2006) Vision-based game interface using Human Gesture. In: Advances in image and video technology, pp 662–671
7. Alon J, Athitsos V, Sclaroff S (2005) Accurate and efficient gesture spotting via pruning and subgesture reasoning. In: Proceedings of IEEE ICCV workshop on human computer interaction, pp 189–198
8. Oka R (1998) Spotting method for classification of real world data. Comput J 41(8):559–565
9. Darrell T, Essa I, Pentland A (1996) Task-specific gesture analysis in real-time using interpolated views. Pattern Anal Mach Intell 18(12):1236–1242
10. Kruskall J, Liberman M (1983) The symmetric time warping algorithm: From continuous to discrete. In: Time warps, string edits and macromolecules. pp 125–162
11. Morguet P, Lang M (1998) Spotting dynamic hand gestures in video image sequences using hidden Markov models. In: Proceedings of IEEE international conference on image processing. pp 193–197
12. Starner T, Weaver J, Pentland A (1998) Real-time American Sign Language recognition using a desk and wearable computer based video. Pattern Anal Mach Intell 20(12):1371–1375
13. Chen F, Fu C, Huang C (2003) Hand gesture recognition using a real-time tracking method and Hidden Markov Models. Image Video Comput 21(8):745–758
14. Wilson A, Bobick A (1999) Parametric hidden Markov models for gesture recognition. Pattern Anal Mach Intell 21(9):884–900
15. Kwon DY (2008) A design framework for 3D spatial gesture interfaces. PhD, ETH, Switzerland
16. Kahol K, Tripathi P, Panchanathan S (2004) Automated gesture segmentation from dance sequences. In: Proceeings of IEEE 6th international conference on automatic face and gesture recognition, pp 883–888
17. Kocian J, Girard A, Banko B et al (2005) Dynamic system identification with Gaussian processes. Math Comput Model Dyn Syst 11(4):411–424
18. Nery Bruno, Ventura Rodrigo (2011) A dynamical systems approach to online event segmentation in cognitive robotics. Paladyn. J Behav Robot 2(1):18–24

19. Nery Bruno, Ventura Rodrigo (2013) On the scalability and convergence of simultaneous parameter identification and synchronization of dynamical systems. Complex Syst 22(3):203–219
20. Rasmussen C, Williams C (2006) Gaussian processes for machine learning. The MIT Press, Cambridge
21. Sokolova M, Lapalme G (2009) A systematic analysis of performance measures for classification tasks. Inf Process Manage 45(4):427–437

Arm Motions of a Humanoid Inspired by Human Motion

Marija Tomić, C. Vassallo, C. Chevallereau, Aleksandar Rodić and Veljko Potkonjak

Abstract New generations of humanoid robots are becoming more faithful copies of the human body. From the human point of view, besides the human's look, the interest of humanoid robot can be in the more natural communication and interaction with human. Humanoid is also well adapted to environment dedicated to human, home or company. With morphology close to human one, it can be expected that the humanoid can replace the human in its task, but also that it can acquire human skills. Our objective is to generate anthropometric motion of humanoid robot inspired by human motion in everyday human activities. This can be done by imitation process, but in this context, each task has to be learned independently. Thus our approach consists in the search of the criterion used by human to achieve a task since the joint motion for achieving the same task is not unique. We will consider motions of the upper-body of the robots in which each arm has 7 degrees of freedom. Criteria that be explored are the minimization of the joint displacement, minimization of the kinetic energy and the proximity to ergonomic configuration. A study at the kinematic level based on generalized pseudo

M. Tomić (✉)
School of Electrical Engineering, Serbia, IMP, Belgrade, Serbia, and IRCCyN, Ecole Centrale de Nantes, Nantes, France
e-mail: marija.tomic@pupin.rs

C. Vassallo
CNRS; LAAS; Université de Toulouse; UPS, INSA, INP, ISAE; LAAS, F-31077 Toulouse, France
e-mail: christian.vassallo@laas.fr

C. Chevallereau
IRCCyN, Ecole Centrale de Nantes, Nantes, France
e-mail: christine.chevallereau@irccyn.ec-nantes.fr

A. Rodić
Robotics Laboratory IMP, Belgrade, Serbia
e-mail: aleksandar.rodic@pupin.rs

V. Potkonjak
School of Electrical Engineering, University of Belgrade, Belgrade, Serbia
e-mail: potkonjak@yahoo.com

H. Bleuler et al. (eds.), *New Trends in Medical and Service Robots*,
Mechanisms and Machine Science 38, DOI 10.1007/978-3-319-23832-6_19

inverse of the Jacobian matrix is implemented. The joint motions obtained by minimization of the criterion are compared to the human motion adapted to the kinematic of the humanoid. The choice of the criterion optimized by the human is the one that corresponds to the smallest difference on joint configuration during all motion. Four different types of motion are considered.

Keywords Human motion · Inverse kinematics algorithm · Capture motion system · Humanoids

1 Introduction

New generations of humanoid robots are becoming more faithful copies of the human body. With morphology close to human one, it can be expected that the humanoid can replace the human in its task, but also that it can acquire the human skills. Our objective is to generate anthropometric motion of humanoid robot inspired by human motion in the everyday human activities. A human movement is a coordinated gesticulation resulting from simultaneous muscle contractions generated by an electric nervous signal. The understanding and modeling of human movement and motion are based on observation. Motion observation evolves with the evolution of the available technologies for observation [16]. Nowadays the motion capture technologies are based on acoustic, magnetic, mechanical, inertial and optical systems. One of the most common systems is marker-based motion capture system. The information from the markers can be useful to obtain the kinematic characteristics of human. The algorithms for automatically estimating a structure and geometrical parameters of a subject's skeletal from optical motion capture data are presented in [2, 8]. The parameters are modeled as the generalized coordinates of virtual mechanical joints. In other papers, the specific parameters obtained from the recorded data are used to mimic human motion like swivel angel of elbow [19] and elbow elevation angle [7]. Some other approaches are used for imitation human motion. Cartesian control approach in which a set of control points on the humanoid is selected and the robot is virtually connected to the measured marker points via translational springs are presented in [12].

Generally, the arms of a human or humanoid are viewed as a structure for moving the hands. It is often assumed that the human/humanoid task is to follow prescribed trajectory of the hands. But, even including position and orientation of each hand, this task can be achieved on a different way due to joint redundancy. Human body has many degrees of freedom (DoF), and classical kinematic representation of each arm involves 7 DoF. The redundancy is increased with the possibility of displacement of the trunk. In robot control, the redundancy is generally solved at the kinematic level using inverse kinematic (IK) algorithm by minimization of criterion or by definition of several tasks with different priority level [10]. The numerical approach for solving IK algorithm for redundant robots gives one solution from the set of infinite solutions. There are several methods for solving numerical IK problems for redundant robots. Whitney [20] proposed to use the Moore-Penrose pseudoinverse of the Jacobian matrix. This solution generates the minimum norm of joint velocities. The main disadvantage of this method is that it produces discontinuity in joint velocities near the singularities [4]. Park [13] proposed the weighted pseudoinverse algorithm. This algorithm can be used for minimization of the kinetic energy. The optimization criteria can also be the joint limit avoidance, obstacle avoidance, mathematical singularity avoidance, dexterity, energy minimizing and other criteria [3, 11, 18]. Including these optimization criteria in the null space of Jacobian, the IK algorithm finds a joint configuration which satisfies the end-effector task and minimizes the chosen criterion.

Our objective is to characterize human skill via the definition of the criterion that is minimized. The natural candidate criteria are the minimization of joint displacement, the minimization of kinetic energy and the proximity to ergonomic configuration. To define this criterion, we will compare the results in joint space obtained with various criteria for given task with respect to the human motion. Since a humanoid robot with a limited number of joints cannot reproduce human motions, a first step in our research is to define human-like motion using imitation or conversion technique. This motion will be referred as imitation motion in the following.

We proposed a nonlinear optimization algorithm for human to humanoid motion conversion. This approach is based on the definition of Virtual Markers attached on the segment of the scaled model of the robot. During the movements, the joint motions of the humanoid model are calculated such that the position and orientation evolutions of Virtual Markers match the Real Markers evolution attached to the actor.

The obtained joint motions from the imitation algorithm are also used to define the desired position and orientation of robot wrists and as a reference to characterize human-like behavior. Following the position and orientation of wrists are the tasks of inverse kinematics algorithms. To achieve these tasks several inverse kinematics algorithms with different criterions are used. From the point of view of the proximity of humanoid and imitation motion in joint space, a comparative analysis of the results obtained with the various criteria is done in order to conclude which criterion induces human-like motion.

The structure of the paper is the following. In Sect. 2 the human motion and used capture motion system will be presented. In Sect. 3, the humanoid and the conversion algorithms which define the imitation motion of the humanoid are explained. In Sect. 4 the Cartesian task is defined and several inverse kinematic solutions are proposed. In Sect. 5, the obtained results are discussed. Lastly, the article ends with some concluding remarks and perspectives in Sect. 6.

2 Studied Human Motion and Capture Motion System

2.1 Studied Human Motions

This study is dedicated to dual arm motions. The problem of balance is not explored and we will assume that the waist of the human is fixed. For the arms, we consider motion without contact with the environment like hello motion and motion with contact with the environment like rotation of wheels and valves where the motions of arms are synchronized.

Using capture motion system the four different motions of one actor are recorded. The motions are:

- Hello motion (see Fig. 1a)
- Rotate of horizontal wheel (see Fig. 1b)
- Rotation of vertical wheel (see Fig. 1c)
- Rotation of two valves placed in horizontal plane (see Fig. 1d)

2.2 Motion Capture System

The system consists of a hybrid suit of 17 targets with 6 DoF relative to the feet, shins, thighs, shoulders, upper-arms, forearms, hands, head, hip, back and torso (see Fig. 1). A set of 8 infra-red (IR) cameras is used. The ART software acquires the 2D information of each IR camera and provides the transformation matrices relative to the different local frames attached to the body parts [1]. The outputs of the

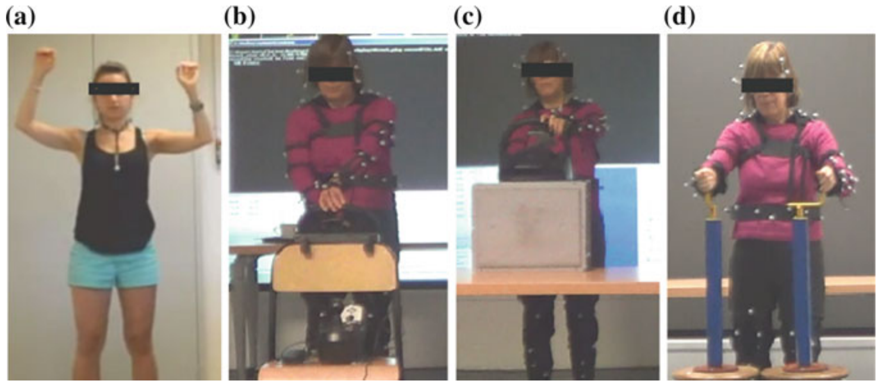

Fig. 1 Recorded motion of human by capture motion system: **a** Hello motion, **b** Rotation of horizontal wheel, **c** Rotation of vertical wheel and **d** Rotation of two valves

measurement system are the position and orientation of the markers frames attached on the limbs and the frames on actor's joints. Each joint is assumed to be a spherical joint and its position is defined based on the intersections of marker frames.

3 Human to Humanoid Motion Conversion

The problems of human to humanoid motion conversion arise because of differences between the actor and the robot. A human has 206 bones linked by different types of joints (immovable, cartilaginous, semi-mobile, hinged, ball and socket joints) and human body joints tend to be not stiff. The human motion is ensured by around 640 skeletal muscles. On the other hand the humanoid robot has rigid serial kinematic chains with rigid joints equipped with limited number of sensors [9].With a humanoid robot with enough number of joints and kinematic and dynamic property not too far from those of a human, the imitation of human movements can be achieved. A classical kinematic representation of each human arm and leg involves 7 DoF and 6 DoF respectively. Thus humanoid robots for dual arm manipulation often include 7 DoF per arm as the ROMEO robot used in this study. Conversion from human to humanoid motion begins with the record of human movement using a motion capture system. Based on a robot model and measurements from the capture motion system the conversion algorithm can be defined. General structure of conversion human to humanoid motion is shown on Fig. 2.

When the objective of the imitation is to define joint motion for the humanoid, an intermediate model should be introduced as the joint arrangement of the robot and the body size of the human in order to have motions that are the closest to those

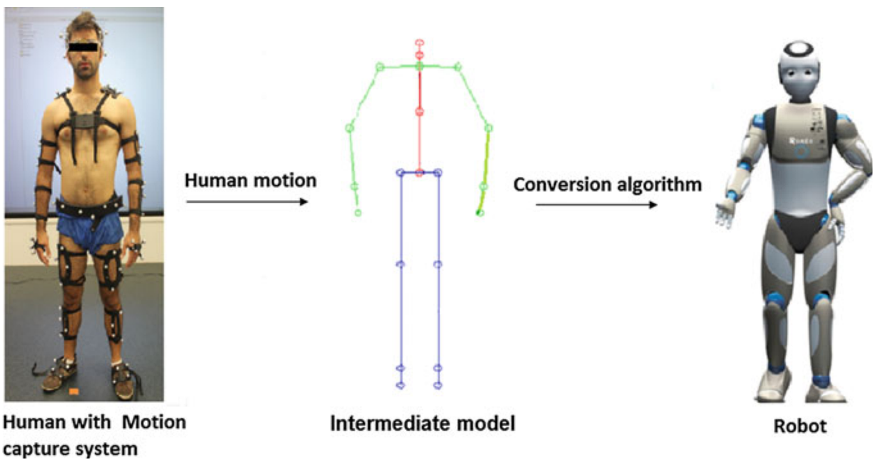

Fig. 2 Human to humanoid motion

from the human [14]. The final results in imitation process are joints motion of the humanoid obtain using the measurements from the capture motion system.

3.1 Robot ROMEO

Humanoid robot ROMEO is developed by Aldebaran Company (see Fig. 3a). It is 1.4 m tall and has 37 DoF, including, 7 DoF for each arm, 6 DoF for each leg, 2 DoF for each eye, 1 DoF for each foot, and 3 DoF for the backbone.

The kinematic model of upper part of robot ROMEO which is used in simulation of human movements is shown of Fig. 3b. It contains 25 DoF: 7 in trunk, 2 in neck and 2 in head and 7 in each arm. The first 6 DoF in trunk represent the moving of legs where first 3 are translation and second 3 rotation joints.

3.2 Algorithms of Conversion Based on Virtual Markers

The basic idea is to define some Virtual Markers on the humanoid robot such that during movements their position and orientation evolution match one of the Real Markers equipped by the actor.

The dimensions of segments of the intermediate model robot are scaled on human dimension. Scaling a robot to the dimension of a human is based on the calculation of the dimension of human from data of joints recorded with Capture motion system. The frames attached to the joints of the actor motion (in ART

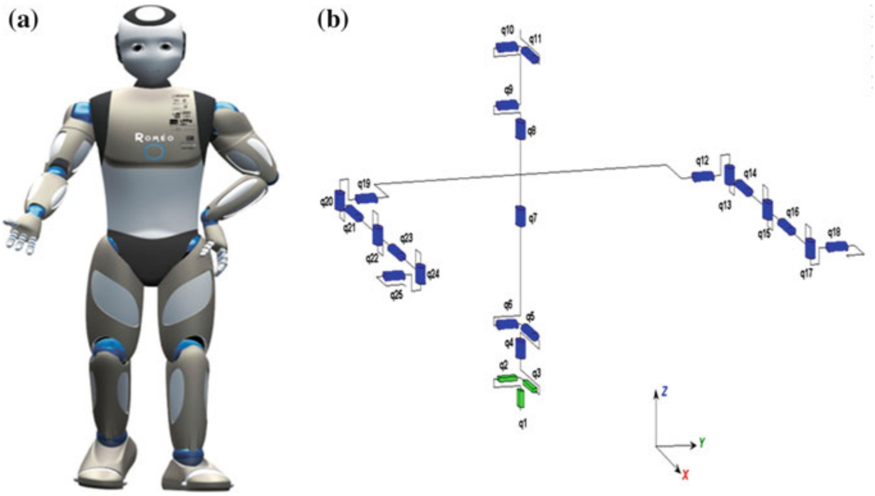

Fig. 3 **a** Robot ROMEO [5]; **b** Kinematic model of robot ROMEO

system) are different from the frames attached to the joints of the robot model, but their positions are coincident. The dimensions of human's segments are calculated as the mean Euclidian distance between two adjacent joints from recorded data. The dimension of similar segments for both sides of the body are calculated as mean value of segment from left and right side (e.g. dimension for upper arm is mean value of dimension of right upper arm and left upper arm). On this way the intermediate model is scaled to the dimension of human and it is possible to match the motion of Real Marker with Virtual Marker.

In order to achieve good tracking of Real Markers with Virtual Markers it is necessary to attach the Virtual Markers to the intermediate model, by defining a fixed transformation matrix between the Virtual Marker frame and the closest proximal frame attached to the joint. This is done by identification of the Virtual Marker frame and the Real Marker frame in an initial configuration of the robot. Starting from a prescribed configuration of the human, the initial closest configuration of the intermediate model is calculated based on the recorded position of the frame attached to the joint and required angle of the wrist. The initial configuration is kept constant during several sampling periods in order to limit error due to noise. Initialization process is presented with more details in [17].

Using these transformation matrices between frame attached to the joint and Virtual Marker frame, it is possible to calculate the joint configuration of the intermediate humanoid model in order to match the calculated configuration of the Virtual Marker frame and the Real Marker frame measurements. The *MatLab* optimization function *fmincon* (see [15]) is used in imitation process for calculation of the generalized coordinates of robot's joints $q_{imitation}(t)$ for recorded motion of actor in each sample. The criteria function is minimization of the difference in position and orientation between Real and Virtual Markers. The error in position is calculated as Euclidian distance between the positions of Real Markers P_{rm} and Virtual Markers P_{vm}. The error in orientation is calculated as difference between quaternion representation of orientation of frame attached to Real Marker R_{rm} and quaternion representation of orientation of frame attached to Virtual Marker R_{vm}. Since orientation measurements are less precise than position measurements, the error in orientation is multiplied by weighted factor α less than 1 and the orientation of the proximal markers frames are not included but replaced by the error in position of the frame attached to the joint, the orientation of the distal marker frame has to be included. Due to large differences in kinematic model between human and humanoid, the criterion cannot be zero, and the choice of the weighted factor α affects the results. The general criteria function of optimization algorithm is (1):

$$\min \begin{pmatrix} \sum_{i=1}^{M_p} \|P_{rm_i}(t) - P_{vm_i}(t)\|_2 + \alpha \sum_{j=1}^{M_r} \left\| R_{rm_j}(t) R_{vm_j}^{-1}(t) \right\| \\ + \sum_{k=1}^{J} \left\| P_{aj_k}(t) - P_{rj_k}(q) \right\|_2 \end{pmatrix} \tag{1}$$

where M_p is the number of markers, M_r is the number of distal markers (the hands markers) for which the orientation is taken into account in the criterion, J is the number of joints, P_{aj} is position of actor joint, P_{rj} is position of robot joint and $\alpha = 0.3$ is the weighted factor. Different values for α are tested. Starting from $\alpha = 1$, the value is decreased until the position and orientation errors are not in the same order. Since the joint configuration is found by an optimization technic subject to local minima, the global optimum is believed to be reached by the fact the initial configuration is known and that the optimal solution from the previous sample is the initial guess for the optimization algorithm in the current sample. When the imitation process is achieved for the trajectory, the joint motion is approximated by a polynomial function in order to eliminate measurement noise.

For the case studied, the translation joints of trunk and the joints of neck and head are kept fixed.

4 The Inverse Kinematic Algorithms

The task of each arm is to follow a desired position and orientation for each arm of the humanoid robot obtained in the imitation process. For each motion, the desired position and orientation of the hands are reconstructed based on $q_{imitation}$ and the intermediate model of the humanoid robot.

The general solution of the inverse kinematic with optimization term represented in the differential model is given as:

$$dq = J^{+}dX + (I - J^{+}J)Z \tag{2}$$

where J^{+} is the pseudo inverse of J.

The second term belongs to the null space of Jacobian matrix J and represents optimization term. This term can be used to optimize a desired function $\phi(q)$. Taking $Z = \beta\nabla\phi$ where $\nabla\phi$ is the gradient of function $\phi(q)$ with respect to the q, permits to minimize the function $\phi(q)$ when $\beta < 0$ and to maximize $\phi(q)$ when $\beta > 0$ [6]. In this case, the Eq. (2) can be rewritten as:

$$dq = J^{+}dX + \beta(I - J^{+}J)\nabla\phi \tag{3}$$

where:

$$\nabla\phi = \left[\frac{\partial\phi}{\partial q_1}\cdots\frac{\partial\phi}{\partial q_n}\right]^T \tag{4}$$

The criteria functions that we used are:

- Minimization of the norm of joint velocities $\|\dot{q}\|^2$
  This solution is directly given by the pseudo inverse solution: $dq(t) = J^{+}dX(t)$

- Minimization of the distance between the current position and ergonomic configuration of human $\left|q - q_{ergonomic}\right|^2$
  This solution can be written:

$$dq(t) = J^{+}dX(t) - (I - J^{+}J)(q(t - \Delta t) + J^{+}dX(t) - q_{ergonomic})$$

Studies of the human motion have led to the definition of ergonomic configuration $q_{ergonomic}$ which seems preferred by human to be comfortable during his task [21].

- Minimization of the kinetic energy $\dot{q}^T A(q)\dot{q}$ where $A(q)$ the Inertia matrix of the actor.
  This solution is obtained using weighed pseudo inverse:

$$dq(t) = A^{-1}(q)J^T(JA^{-1}(q)J^T)^{-1}dX(t)$$

- Minimization of the weighted distance to the ergonomic configuration. The weight matrix is defined to include the energetic cost of the displacement, W_A is a diagonal part of the inertia matrix at the initial configuration[1]: $\left(q - q_{ergonomic}\right)^T W_A\left(q - q_{ergonomic}\right)$
  This solution can be written:

$$dq(t) = J^{+}dX(t) - (I - J^{+}J)\left((I - J^{+}J)^T W_A(I - J^{+}J)\right)^{+T}\ldots$$
$$(I - J^{+}J)^T W_A\left(q(t - \Delta t) + J^{+}dX(t) - q_{ergonomic}\right)$$

5 Experiments and Results

The tasks to be achieved are the tracking of desired position and orientation of the wrists motion (see Fig. 4a) defined based on the generalized coordinate from imitation process (see Fig. 4b) as illustrated in Fig. 4 for rotation of the vertical wheel with two hands (see Fig. 1c).

The evaluation of the difference between algorithms is based on the level of achieving the motion like the human.

The results of the IK algorithms for different experiments are given on Table 1 by comparing the motion of the shoulders and elbows in Cartesian space that are not directly controlled by the tasks.

[1]Another configuration can also be chosen.

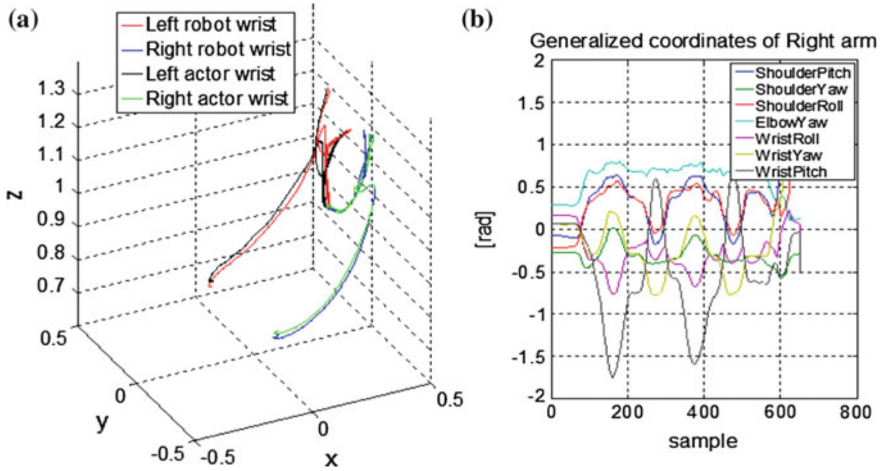

Fig. 4 The motion obtained in imitation process: **a** Cartesian space, **b** Joint space

Table 1 The mean value of cumulative norm of position errors between achieved and desired shoulders and elbows positions, only the cyclic part of the motion is considered without the preparation phase

CumNorm	IK. Al. 1	IK. Al. 2	IK. Al. 3	IK. Al. 4
Hello motion	0.0313	0.0739	0.0901	0.2592
Horizontal wheel	0.0401	0.2644	0.0366	0.1083
Vertical wheel	0.0717	0.1633	0.0614	0.1131
Two valves	0.2315	0.3009	0.3295	0.1763

For comparison the Cumulative trapezoidal numerical integration of position error between the solutions obtained though the IK algorithm and the desired value obtained via the imitation process is used. The results in Table 1 represent the final values of cumulative norm divided by the number of samples expressed in meters.

The results for Hello motion show that IK Algorithm 1 provides the best results. Thus the human seems to minimize joint displacement. The reason for that can be the absence of the contact between the arms and the environment.

The IK Algorithm 3 with minimization of the kinetic energy provides the best results for the tasks Rotation of horizontal wheel and Rotation of the vertical wheel (see Fig. 1b, c). These motions globally have the same characteristics. Looking the results we can say that for the execution of similar motions, the human uses the same strategy. In our case it is minimization of the kinetic energy. Looking at to the position and motion of the arms, the Rotation of the two valves is different in comparison with the two previous motions from the coordination point of view, the two hands have independent tasks. The results also confirm this and show that IK Algorithm 4 seems to be more efficient to reproduce this type of motion. This criterion proposes a compromise between the proximity of the ergonomic configuration and the minimization of energy.

6 Conclusion

In this paper two contributions are developed. A new method for extracting joints trajectory from recorded trajectories of Real Markers is proposed. Virtual Markers are introduced in the humanoid model for following the Real Marker. This imitation process is based on minimization of position error for the frames attached to the joint and the frames attached to Markers, only the orientations of the distal Markers are taken into account. Then, based on comparison of several IK algorithms with different criterions and different motions, we concluded that the IK algorithm providing human like motion may depend on the type of the motion and the contact with environment. In the case of motion without contact with the environment, minimization of joint displacement is a good candidate. In the case of coordinated motion, kinematic energy is a good candidate. Both algorithms can be conceived as a universal methodology for imitation recorded human motion on the adapted model of robot. These preliminary results will be enlarged by the inclusion of several persons and other tasks and other criterions as manipulability and weight between criterions. The long term objective is to be able to detect criterion uses by human and exploit it to produce unlearn human like motion.

Acknowledgments This work is supported by Serbian Ministry of Science under the grant III44008, TR35003, SNSF IP SCOPES, IZ74Z0_137361/1 and ANR project Equipex Robotex.

References

1. ART GmbH (2012) System user manual ARTtrack and TRACKPACK & Dtrack. version 2.8
2. Ayusawa K, Ikegami Y, Nakamura Y (2014) Simultaneous global inverse kinematics and geometric parameter identification of human skeletal model from motion capture data. Mech Mach Theory 74:274–284
3. Baillieul J (1985) Kinematic programming alternatives for redundant manipulators. Proc IEEE Conf Robot Autom 722–728
4. Buss SR (2004) Introduction to inverse kinematics with Jacobian transpose, pseudoinverse and damped least squares methods. IEEE J Robot Autom 17
5. FUI national Romeo project. http://projetromeo.com
6. Khalil W, Dombre E (2004) Modeling, identification and control of robot. Butterworth-Heinemann
7. Kim S, Kim CH, Park JH (2006) Human-like arm motion generation for humanoid robots using motion capture database. In: IEEE/RSJ international conference on intelligent robots and systems, pp 3486–3491
8. Kirk AG, O’Brien JF, Forsyth DA (2005) Skeletal parameter estimation from optical motion capture data. In: IEEE computer society conference on computer vision and pattern recognition, vol 2, pp 782–788
9. Lee D, Nakamura Y (2014) Motion recognition and recovery from occluded monocular observations. Robot Auton Syst 62(6):818–832
10. Mansard N, Chaumette F (2007) Task sequencing for high-level sensor-based control. IEEE Trans Rob 23(1):60–71

11. Nenchev DN, Tsumaki Y, Uchiyama M (2000) Singularity-consistent parameterization of robot motion and control. Int J Robot Res 19(2):159–182
12. Ott C, Lee D, Nakamura Y (2008) Motion capture based human motion recognition and imitation by direct marker control. In: 8th IEEE-RAS international conference on humanoid robots, pp 399–405
13. Park J et al (2001) Multiple tasks kinematics using weighted pseudo-inverse for kinematically redundant manipulators. Proc IEEE Conf Robot Autom 4041–4047
14. Poubel LP, Sakka S, Cehajic D, Creusot D (2014) Support changes during online human motion imitation by a humanoid robot using task specification. ICRA
15. Powell MJD (1978) A fast algorithm for nonlinearly constrained optimization calculations. In: Watson GA (Ed) Numerical analysis. Lecture notes in mathematics, vol 630. Springer, New York
16. Sakka S (2013) Representation of human movement for humanoid applications. Capture and Simulation of Human Motion, Ecole Centrale de Nantes, Nantes
17. Tomic M, Chevallereau Ch (2014) Conversion of captured human motion to the humanoid ROMEO for human imitation. The 1st IcETRAN Conference, Serbia
18. Walker ID (2008) Kinematically redundant manipulators. Springer Handbook of Robotics, pp 245–268
19. Wang Y, Artemiadis P (2013) Closed-form inverse kinematic solution for anthropomorphic motion in redundant robot arms. Adv Robot Autom 2:110
20. Whitney DE (1969) Resolved motion rate control of manipulators and human prostheses. IEEE Trans Man Mach Syst MMS-10(2):47–53
21. Yang J, Marler RT, Kim H, Arora J, Abdel-Malek K (2006) Multiobjective optimization for upper body posture prediction. Virtual soldier research program, center for computer-aided design, the university of Iowa, 111 engineering research facility, Iowa City (IA 52242-1000)

Development of a Virtual Testing Platform Within an Instructor Operation Station

A. Pisla, D. Cocorean, C. Vaida and D. Pisla

Abstract Instructor Operation Station (IOS) is a term usually used in the flight simulators consist in a computer based structure that enables the manual or automatic scenarios generation. The mechatronic system control, the instructor supervision and intervention, together with the instructor assistant in operating, monitoring and evaluation Pîslă et al. (Proceedings in manufacturing systems, (2010) [12]) are the main structural modules. In the initial elaboration stage was starting from the large structure of the International Space Station (ISS) and the docking process of the Dragon fright transporter. The aim of the paper is to present the development of a virtual testing platform (VTP), using a parallel kinematic structure for the propulsion simulation, considering the multibody dynamic (MBD) elements in the detecting the errors and the faults docking maneuver.

Keywords Instructor operation station · Virtual testing platform · Docking maneuver

A. Pisla (✉)
Engineering Design and Robotics Department, Technical University of Cluj-Napoca, Cluj-Napoca, Romania
e-mail: Adrian.Pisla@muri.utcluj.ro

D. Cocorean · C. Vaida · D. Pisla
Research Center for Industrial Robots Simulation and Testing-CESTER, Technical University of Cluj-Napoca, Cluj-Napoca, Romania
e-mail: Dragos.Cocorean@mep.utcluj.ro

C. Vaida
e-mail: Calin.Vaida@mep.utcluj.ro

D. Pisla
e-mail: Doina.Pisla@mep.utcluj.ro

H. Bleuler et al. (eds.), *New Trends in Medical and Service Robots*,
Mechanisms and Machine Science 38, DOI 10.1007/978-3-319-23832-6_20

1 Introduction

Since 2011 Romania is member of the European Space Agency. The necessity to achieve research activity with relevant results is possible only by: correlating the ESA policies in valorizing the Romanian position as ESA member and the development programs of ROSA (ROmanian Space Agency).

On long term it is a must to develop specialized laboratories within the Technical University of Cluj-Napoca (Machine Building Faculty) integrating virtual and physical simulation and testing facilities in order to provide validation and demonstration competences, ensuring also the necessary training solutions.

Within the STAR research framework, the adopted position was to create the concept for an Instructor Operation Station (IOS) as the provider for simulation and testing of products (hardware and/or software) validity, demonstration and training.

The development of an IOS is necessary for training in creating future aerospace applications for service robots and to achieve robust research activity. Following this philosophy in the paper is presented the first stage in the development of a virtual testing platform (VTP) as main component of the IOS.

The general IOS concept is to provide a research and demonstration device for control techniques and devices development, including the necessary training to operate with them based on the ESA regulatory system presented in Fig. 1.

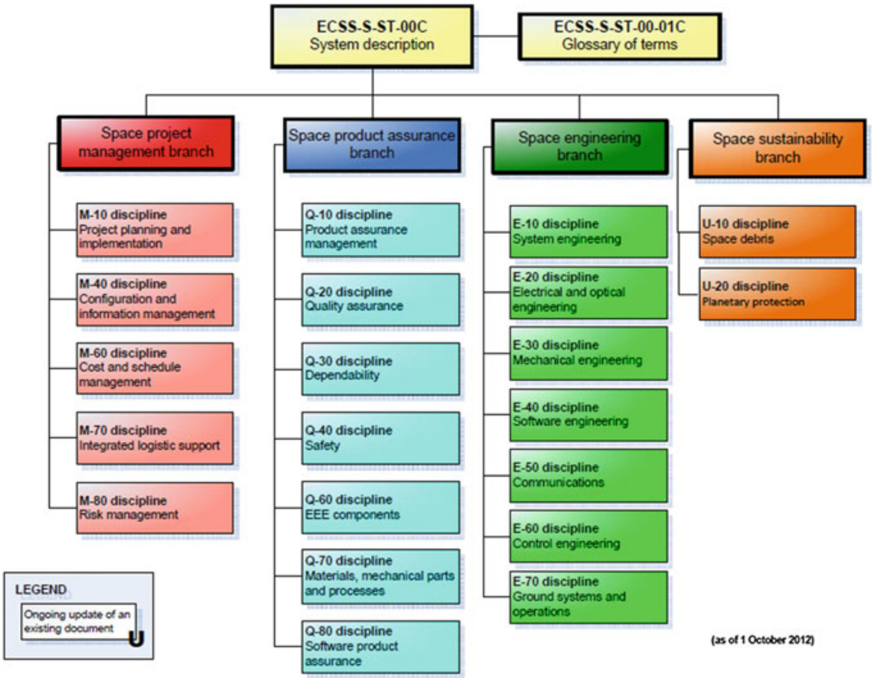

Fig. 1 ESA regulatory system [*Credit* ESA]

In a semi-structured research environment within the new space era, the IOS-STAR project is addressed to the real players that may be active within ESA programs mainly within 3 major domains, each of the them being composed by a set of three specific sub-domains that are suggesting the possible future development.

- Space applications
- Space technologies
- Life science

The basic concept for the IOS functioning is to:

(a) consider a part or a process, generate the part or/and the process with its operation conditions, at the real scale with a virtual reality HS (hardware–software) environment;
(b) generate the part, or components of the process, at a defined scale;
(c) build the physical system;
(d) develop the control system;
(e) provide software interfaces and the similitude coefficients for the scaled physical model (SPM), necessary for the reactions induced by the real scaled model within the virtual reality environment (SSM);
(f) reverse effects generation, within the simulation environment are setting the variables values of the virtual model directly from the physical scaled model operation collisions forces distribution;
(g) develop calibration and optimization process;
(h) develop new mathematical models for the part, process or control systems.

The development and the methodology of the research is considering the PLM elements (product lifecycle management) for the design, implementation and exploitation of the solution, the Siemens PLM software platform being the selected one for the entire project.

Space activity is planned to continue with a lot of space vehicles and service robots, therefore was considered this sort of applications to be on focus as useful components for the IOS structure development.

As example to be modeled and simulated was selected a simplified version of the International Space Station (ISS), as a large inertial structure, combined with the fright module of the first private transporter from SpaceX—the Dragon, as mobile "mini structure" that must be dynamically controlled for the docking process, Fig. 2, [10].

The docking process between the two structures is implying to define a docking trajectory (geometric modeling), a dynamic model for the two spacecrafts (dynamic modeling) and the docking interface (CAD-computer aided design of the geometric and functional characteristics and behavior).

The three components are developed in parallel. Within (a) is the process and parts modeling. The PLM made the link between components and enables an "automatic process" that update all the three components regardless on which of them modifications or developments are made, ensure the safety of the design and

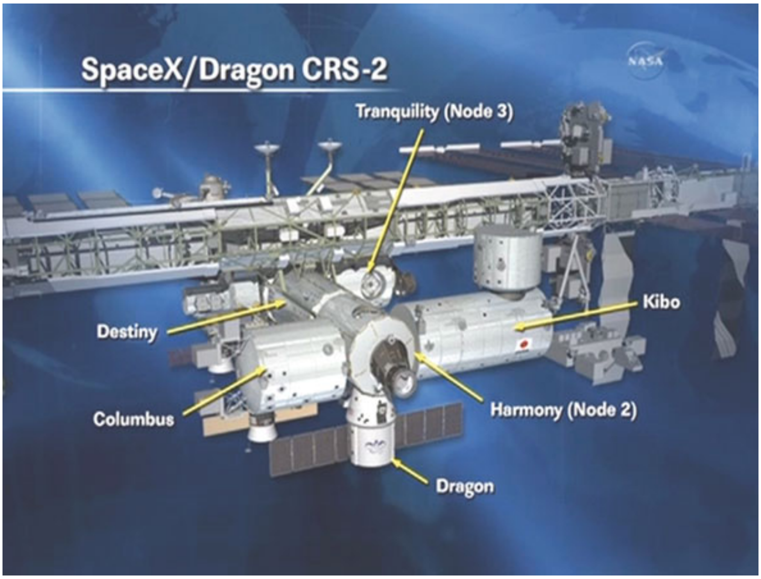

Fig. 2 ISS and Dragon docking systems [*Credit* ESA]

modeling by eliminating revisions and keeping on track the entire process evolution.

The (b) part of the project-scaled generation of the components, considers the scaled Dragon spacecraft module (SDragon), a mobile component within a defined environment, the spacecraft working space.

Actually there are three spacecraft working spaces: the spacecraft working space for the real Dragon module represented in the virtual environment (SWS); the spacecraft working space for the scaled Dragon module, the SDragon, (SDWS); and the spacecraft working space of the scaled module represented in the virtual environment (VSDWS). The three differentiated working spaces are used in parallel within the IOS. In the SDWS is moving the SDragon, actuate by a robotic arm. The motion trajectory is scaled version of the real Dragon path. The scaled speed and accelerations are given from the real model nozzle trust, coupled in a trust vector that can be transferred for the robot arm actuation. The only elements that are not scaled in the SDragon motion are the SDragon orientation and the motion time.

A third element that will be modeled is the entire control chain feedback time, element totally dependent on the used devices and components.

The VSDWS—contains the boundaries of the SDWS and is used for the generation, visualization of the SDragon motion and for the entire scaled system simulation (SDragon + robotic arm + objects in the motion area).

In the SWS is recreated what happens in space with the Dragon shuttle and the ISS. Within the IOS concept the SWS is a “scenarios generator”.

The part (c) of the project-building the physical system, consist in manufacturing the scaled model SDragon, as accurate as possible, together with the simplified ISS model, at the same scale, and select the robotized arm.

Once the robot arm selected, the part (d) of the project—the control system development is made. All together must be encompassed within VSDWS where the motion and the dynamic control are simulated in order to identify the real control parameters of the system.

The link between the real scale model represented in the virtual reality environment (SSM) and the scaled physical model (SPM) is made in the part (e) of the project-interface generation, where the similitude coefficients must be identified to offer a deep immersion of the operator within the virtual reality SWS and a real measurable motion within the SDWS.

The similitude coefficients are used also in part (f) of the project-reverse effects generation for setting variables within the simulation virtual environment.

The validation of the correlated activity is made in the part (g) of the project-calibration and optimization process.

The part (h) of the project-mathematical models development for the part, process or control system definition. This is an optional part, necessary only if the adopted mathematical models provide to be no satisfactory in respect with the demands of the generated IOS.

2 The Startup System

The carrier docking on ISS is not performed by any shuttle pilot but by the Mobile Servicing System (MSS) Canadaram2 robot [8, 9] (a robotic structure derived from Canadarm, Fig. 3. Therefore any person that is planned to work on ISS is trained to operate not only the Canadarm2 but also the European Robotic Arm (ERA) [5], Fig. 4, and the Japanese Experiment Module Remote Manipulator System (JEMRMS), Fig. 5, [7], as a must.

3 The Scaled Model

An innovative element of the project is the IOS hardware structure, formed by an independent computing system, the control interface and the robotic system.

The hardware simulation of the docking conditions is made by placing the ISS scaled model in a “floating” mode and the SDragon attached to the special designed docking places.

The SDragon “thrust actuation” is made with the Stewart-Gough platform in accordance with the trust vector obtained from the simulation within SWS. The robotic arm materialized by the Stewart-Gough platform was used for the possibility to “manipulate the SDragon” in 6 DOF with accurate positioning, speed and acceleration control.

Fig. 3 Canadarm 2 and Mini-Research Module1 [*Credit* ESA]

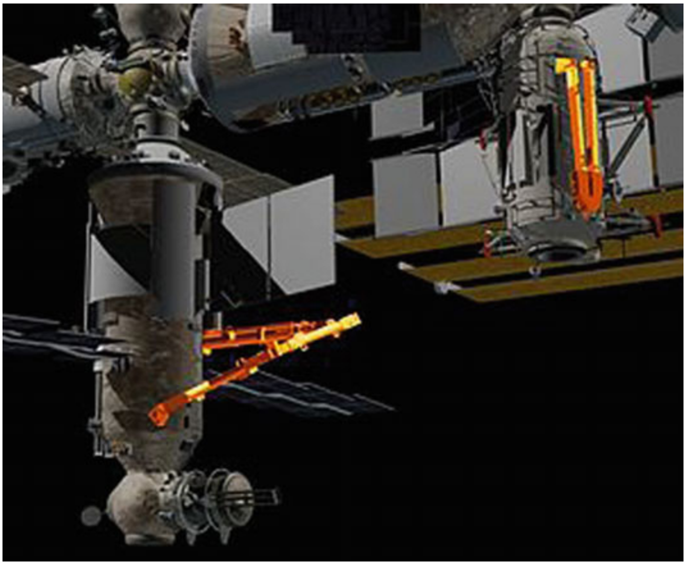

Fig. 4 ERA attached to module Nauka (*left*) and Rassvet (*right*) [*Credit* ESA]

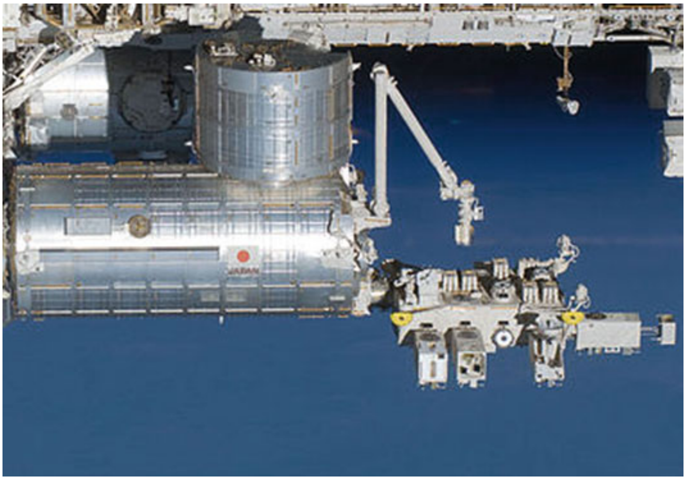

Fig. 5 Japanese—EMRMS [*Credit* ESA]

The parallel kinematics Stewart-Gough platform is considered as an independent system that must be interfaced with the simulation virtual environment, merging the virtual and the real worlds. In this way is introduced the propulsion simulation and the collision effects within the robot control. The errors and faults docking maneuver are visualized firstly in the simulation virtual environment and then observed on the hardware stand. The deviations between the two types of simulations help in calibrating the IOS system.

The effectiveness and the damage avoidance of the human operations depends a lot on: human skills, ergonomic design and control algorithms. Testing these elements represents a target for a virtual testing platform. The use of robotic systems allows not only to simulate a resulted trajectory but also to impose velocities and accelerations offering a feedback reaction for the shuttle position and orientation, improving in the same time the efficiency of the three elements: skills, ergonomics and control.

4 The Methodology

The research methodology selection was made stating from the critical analysis of the latest achievements in the robotic assisted space applications-especially on ISS and the tendencies in spacecrafts design and manufacturing procedures of companies like Space Exploration Technologies Corporation (SpaceX), the Virgin Galactic commercial spaceflights and the ESA (European Space Agency), especially for space tourism.

Fig. 6 Deltalab—Stewart-Gough platform [*Credit* DELTALAB-SMT]

The critical analyses have shown that is little development on IOS structures and therefore the project concept is adopting as default the general Research, Education and Development facilities (RED) as an objectives for the aerospace applications.

The adopted robotized arm is a parallel kinematics platform (Stewart-Gough) mechanical system developed by DELTALAB having 6-DOF, plus one separate redundant DOF for force control and simulation, Fig. 6 [3].

The simulation virtual testing environment uses as reference the DELTALAB parallel kinematic platform but the target is to develop a new control system corresponding to wider control algorithms and next user interface, starting from the identifiable solution applied for Dragon capture and docking structures and the ESA approach in studying simulation and training techniques for the European Robotic Arm (ERA) at JAXA's Tsukuba Space Center, Fig. 7 [6].

The kinematics and dynamics of the Stewart platform mechanism are presented in [2, 11]. The robotic structure sits on a rigid aluminum plate, that forms an horizontal frame that in experimental conditions is meant to have a lateral or un upside-down position for the docking interaction with the SISS.

The active joints of the Stewart platform are of prismatic type. The position, speed, acceleration and axial forces can be estimated and simulated and latter can be compared within the experimental activity.

Fig. 7 JAXA's Tsukuba Space Center [Credit ESA]

5 The Scaled Model Dynamics

The scaled Dragon spacecraft model SDragon was generated also as virtual model [13], within the VSDWS on the Virtual Testing Platform (VTP). The SDragon spacecraft is generated also as experimental model, using a 3D printer to materialize the virtual scaled model, Fig. 8.

Fig. 8 SDragon

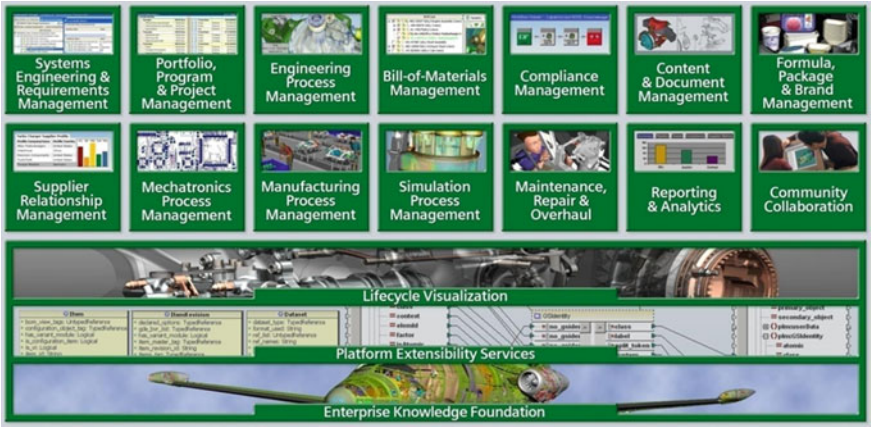

Fig. 9 Siemens PLM, project management modules [Credit Siemens PLM]

A similar procedure was made also to generate the scaled ISS (the SISS). These components are the starting elements for the geometric, kinematic and dynamic simulation of the IOS testing platform.

The purpose of using in parallel the two platforms (the Virtual Testing Platform—VTP and the Mechanical Testing Platform-MTP) is to achieve a scaled virtual environment "the scene" containing the hardware—robotic equipment and the 3D reconstructed model of the spacecrafts. Each model must show the same behavior for the same command or interaction, the Siemens PLM software platform enabling that each development of any of the two models to be reflected on the other one, Fig. 9, [15].

The Motion Simulation module reveals displacements; speeds, accelerations, limits variation for the mobile elements; singular poses, forces and torques.

In the existing model, the behavior definition is using the following simplifying hypotheses: gravity forces are not considered; the bodies and joints are perfectly rigid and without friction. These are valid only for the virtual simulation of the SDragon later on for the real actuating condition the hypothesis will be eliminated.

The considered test-case follows a real situation: the docking procedures. The robot moves from an arbitrary position, to the docking position on ISS. The final linear path must create a clean docking; avoiding the collisions, but any encountered collision will have a feedback reaction on the VTP—simulating a real situation. The profile of the generated trajectory is presented in Fig. 10, [1].

The robot arm must induce to the SDragon a controlled docking motion, as the parameterized trajectory shows the final approach for the docking, Fig. 11.

A kinematic and dynamic simulation was made using Siemens NX, RecurDyn solver [14]. The achieved results are necessary to visualize and validate a chosen trajectory for the Dragon spacecraft that will be reflected in the SDragon, virtual and real motion. The results are the space, speeds and the acceleration diagrams of the SDragon docking point (X, Y, Z, psi, teta, phi, VX, VY, VZ, V_{psi}, V_{teta}, V_{phi},

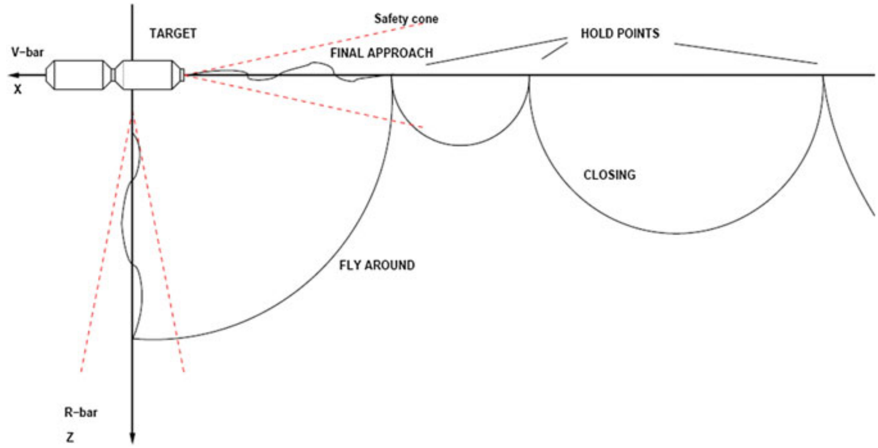

Fig. 10 Representation of the adapted docking trajectory

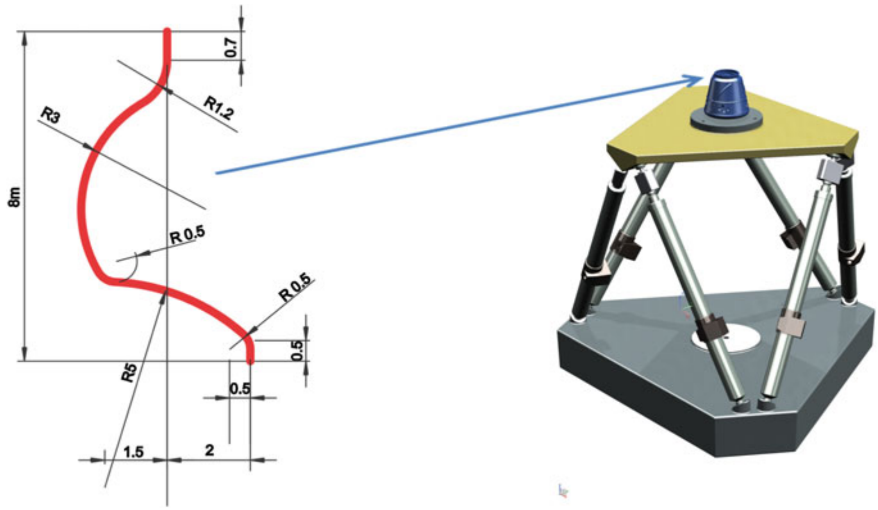

Fig. 11 The design docking trajectory for the spacecraft mock-up placed on the

a_{psi}, a_{teta}, a_{phi}). These are the theoretical positioning parameters defined for the docking, Fig. 12, as reference for establishing the errors in the docking maneuvers, considered as a defined input.

The second simulation results are the actuating parameters (q_i, $V_{qi,}$ $a_{qi,}$ i = 1/6), as output for the robotized arm control, Fig. 13.

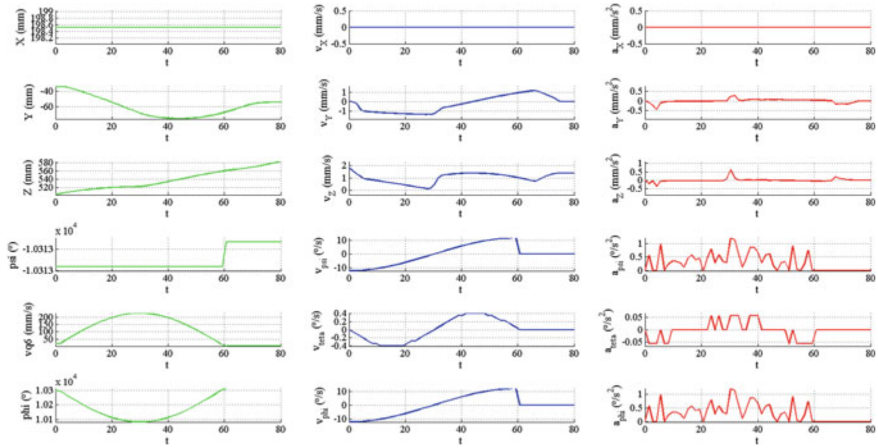

Fig. 12 Representation of the docking robot positional control parameters

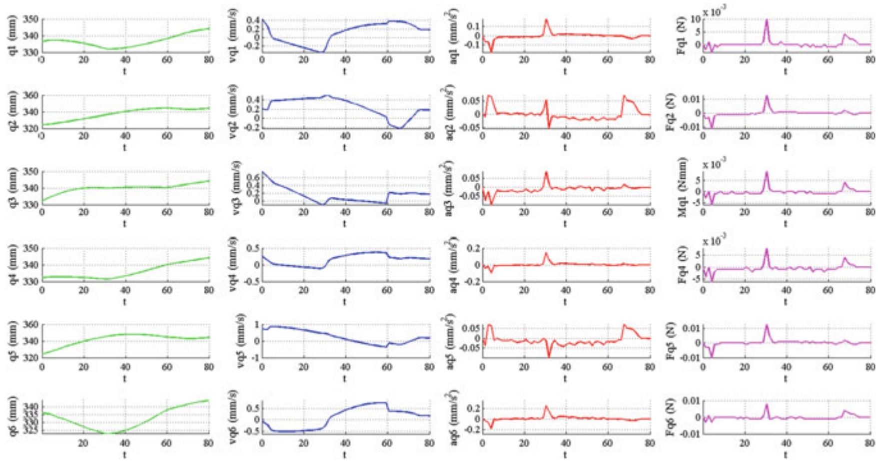

Fig. 13 Representation of the robot actuating control parameters

6 Conclusions

Space technology is in a beginning phase where: safety, cooperation, conformity and the communication compatibility are crucial for new applications. The on-growing sector of space exploration, including the service and space robots, asks for the development of adequate testing and training facilities in Europe and to accommodate the expected large number of pilots travelling in space.

This work is a part of a collaborative project in the framework of ROSA (ROmanian Space Agency), project that intends to provide some IOS (Instructor

Operated System) module as a demonstrator related to space applications, in order to increase the capacity to combine human operation with cognitive and prediction elements.

The setup of an IOS simulator achievement is meant to be a first and smallest solution for future testing and training platform for space missions. Even at this stage, was designed at a reasonable scale (1:12) to be used directly for the testing and training applications. This approach is similar with the one used for the Mars rovers generations, where Sejourner that landed on 4th of July 1997 is 650 mm long and the Curiosity that landed on 6th of August 2012 that is 3000 mm long. If the research conditions will be favorable we intend to provide some IOS modules as demonstrators related to space applications to increase the capacity of combining human operation with cognitive and predictive elements.

A scaled model capable of simulating spacecraft motions in space is under construction. The validation of the scaled model will be achieved on a docking simulation between a Dragon capsule and the International Space Station (ISS). The need for real hardware and mock-up components came from the research framework goal to reach TLR0, TLR1, TLR2, TLR3 and if possible TLR4. Only this type of evolution allowed that continuity for space applications and the capacity to work in other research programs in parallel with the development and use of IOS for real testing and training activities.

The conceptual development of the IOS for Space and the TLR2, has been achieved with three components system:

1. Design of the FA—Final Approach; the generation of the docking trajectory as a result imposed by analyze trajectories from different apace missions.
2. Development of the AGCP—Automated Generation of the Control Parameters, destined to the 6 DOF robotic system that is manipulating the spacecraft mock-up;
3. Design of the virtual and scaled simulation environment, currently under development.

Acknowledgments This work was supported by the Romanian National Authority for Scientific Research grant, Program for research-Space Technology and Advanced Research—STAR, project number 95, the Scopes International Grant IZ74Z0-137361/1, Creative Alliance in Research and Education focused on Medical and Service Robotics-CARE-Robotics and the project "Inter-University Partnership for Excellence in Engineering-PARTING-project coordinated by the Technical University of Cluj-Napoca" contract no. POSDRU/159/1.5/S/137516, project co-founded by the European Social Fund through the Sectorial Operational Program Human Resources 2007–2013.

References

1. Ankersen F Guidance, navigation, control and relative dynamics for spacecraft proximity maneuvers, PhD Thesis. Aalborg University, Denmark
2. Campean E, Pisla A, Pap S (2012) Characteristics of neural network solutions within the parallel kinematic systems control, p 309. QIEM Cluj-Napoca. ISSN 1582-2559
3. Deltalab. http://www.deltalab.fr/
4. Dragon2. http://www.spacex.com/news/2014/05/30/dragon-v2-spacexs-next-generation-manned-spacecraft
5. ERA. http://en.wikipedia.org/wiki/European_Robotic_Arm
6. ESA-S Corvaja ESA and CSA astronauts participate in simulation training at JAXA's Tsukuba Space Center, astronaut André Kuipers blog
7. JEMRMS. http://en.wikipedia.org/wiki/Kibo_(ISS_module)
8. NASA Canadarm 2 and the Mobile Servicing System. http://en.wikipedia.org/wiki/Mobile_Servicing_System
9. NASA ESA Frank De Winne and Nicole Stott at Canadarm 2 workstation for unberthing of HTV
10. NASA mision. www.nasa.gov/mission_pages/station/structure
11. Pîslă A, Irimias T, Muntean R (2010) Elements for modelling change management. In: Proceedings in manufacturing systems, vol 5, no 3, 2010, pp 163–166. ICMAS 2010. 19th international conference on manufacturing systems. University POLITEHNICA of Bucharest, Romania
12. Pîslă A, Itul T, Pîslă D, Szilaghyi A (2012) Consideration upon influence of manufacturing and assembly errors on the kinematic and dynamic behaviour in a flight simulator Stewart-Gough platform. Mechanisms, transmissions and applications, in mechanisms and machine science, vol 3, pp 215–224. Springer Science + Business Media, 2012
13. SDragon. http://www.thingiverse.com/thing:34320
14. Siemens NX, RecurDYN (2014). http://www.plm.automation.siemens.com/en_us/
15. Siemens PLM Teamcenter. http://www.ayokasystems.com/enterprise-systems-solutions/teamcenter-siemens-plm-software/

Index

H. Bleuler et al. (eds.), *New Trends in Medical and Service Robots*,
Mechanisms and Machine Science 38, DOI 10.1007/978-3-319-23832-6